PH.D THESIS

CONTRIBUTIONS TO GROUND-BASED AND UAV SAR SYSTEMS FOR EARTH OBSERVATION

MARC LORT CUENCA

Thesis advisor
Prof. Albert Aguasca Solé

UNIVERSITAT POLITÈCNICA DE CATALUNYA
BARCELONATECH
Departament de Teoria del Senyal
i Comunicacions

UNIVERSITAT POLITÈCNICA
DE CATALUNYA
BARCELONATECH

Contributions to ground-based and UAV SAR systems for Earth observation

Marc Lort Cuenca

ADVERTIMENT La consulta d'aquesta tesi queda condicionada a l'acceptació de les següents condicions d'ús: La difusió d'aquesta tesi per mitjà del repositori institucional UPCommons (http://upcommons.upc.edu/tesis) i el repositori cooperatiu TDX (http://www.tdx.cat/) ha estat autoritzada pels titulars dels drets de propietat intel·lectual **únicament per a usos privats** emmarcats en activitats d'investigació i docència. No s'autoritza la seva reproducció amb finalitats de lucre ni la seva difusió i posada a disposició des d'un lloc aliè al servei UPCommons o TDX. No s'autoritza la presentació del seu contingut en una finestra o marc aliè a UPCommons (*framing*). Aquesta reserva de drets afecta tant al resum de presentació de la tesi com als seus continguts. En la utilització o cita de parts de la tesi és obligat indicar el nom de la persona autora.

ADVERTENCIA La consulta de esta tesis queda condicionada a la aceptación de las siguientes condiciones de uso: La difusión de esta tesis por medio del repositorio institucional UPCommons (http://upcommons.upc.edu/tesis) y el repositorio cooperativo TDR (http://www.tdx.cat/?locale-attribute=es) ha sido autorizada por los titulares de los derechos de propiedad intelectual **únicamente para usos privados enmarcados** en actividades de investigación y docencia. No se autoriza su reproducción con finalidades de lucro ni su difusión y puesta a disposición desde un sitio ajeno al servicio UPCommons No se autoriza la presentación de su contenido en una ventana o marco ajeno a UPCommons (*framing)*. Esta reserva de derechos afecta tanto al resumen de presentación de la tesis como a sus contenidos. En la utilización o cita de partes de la tesis es obligado indicar el nombre de la persona autora.

WARNING On having consulted this thesis you're accepting the following use conditions: Spreading this thesis by the institutional repository UPCommons (http://upcommons.upc.edu/tesis) and the cooperative repository TDX (http://www.tdx.cat/?locale-attribute=en) has been authorized by the titular of the intellectual property rights **only for private uses** placed in investigation and teaching activities. Reproduction with lucrative aims is not authorized neither its spreading nor availability from a site foreign to the UPCommons service. Introducing its content in a window or frame foreign to the UPCommons service is not authorized (framing). These rights affect to the presentation summary of the thesis as well as to its contents. In the using or citation of parts of the thesis it's obliged to indicate the name of the author.

UNIVERSITAT POLITÈCNICA
DE CATALUNYA
BARCELONATECH

Contributions to Ground-based and UAV SAR systems for Earth observation

Author
Marc Lort Cuenca

Thesis Advisor
Prof. Albert Aguasca Solé

A thesis submitted to the Universitat Politècnica de Catalunya (UPC) in
partial fulfillment of the requirements for the degree of
DOCTOR OF PHILOSOPHY

Department of Signal
Theory and Communications

Ph.D. program on Signal Theory and Communications
Remote Sensing Laboratory (RsLab) Group
Barcelona, September 2017

Marc Lort Cuenca

Contributions to Ground-based and UAV SAR systems for Earth observation

Ph.D. program on Signal Theory and Communications

Cover design: Image composition of: (Left) RISKSAR-X SAR sensor in the measurement campaign performed in Montserrat.(Center) SLC image of a stripmap acquisition over the RACBSA airfield. (Right) ARBRES-X SAR system flying in the RACBSA airfield. Copyright ©2017 by Marc Lort Cuenca.

This work has been supported by FPI Research Fellowship Program, Ministerio de Educación, contract BES-2012-060089; by the Spanish Ministry of Science and Innovation (MICINN) under the project TEC2011-28201-C02-01.

UNIVERSITAT POLITÈCNICA DE CATALUNYA
BARCELONATECH
Escola de Doctorat

Curs acadèmic: 2016/2017

Acta de qualificació de tesi doctoral

Nom i cognoms
Marc Lort Cuenca

Programa de doctorat
Teoria del Senyal i Communicacions

Unitat estructural responsable del programa
Teoria del Senyal i Communicacions

Resolució del Tribunal

Reunit el Tribunal designat a l'efecte, el doctorand / la doctoranda exposa el tema de la seva tesi doctoral titulada CONTRIBUTIONS TO GROUND-BASED AND UAV SAR SYSTEMS FOR EARTH OBSERVATION.

Acabada la lectura i després de donar resposta a les qüestions formulades pels membres titulars del tribunal, aquest atorga la qualificació:

☐ NO APTE ☐ APROVAT ☐ NOTABLE ☐ EXCEL·LENT

(Nom, cognoms i signatura) President/a	(Nom, cognoms i signatura) Secretari/ària

(Nom, cognoms i signatura) Vocal	(Nom, cognoms i signatura) Vocal	(Nom, cognoms i signatura) Vocal

______________________, _______ d'/de __________________ de _______________

El resultat de l'escrutini dels vots emesos pels membres titulars del tribunal, efectuat per l'Escola de Doctorat, a instància de la Comissió de Doctorat de la UPC, atorga la MENCIÓ CUM LAUDE:

☐ SÍ ☐ NO

(Nom, cognoms i signatura) President de la Comissió Permanent de l'Escola de Doctorat	(Nom, cognoms i signatura) Secretari de la Comissió Permanent de l'Escola de Doctorat

Barcelona, _______ d'/de ____________________ de _________

To my mother Roser
To my beloved Teresa.

Do not go gentle into that good night,
Old age should burn and rave at close of day;
Rage, rage against the dying of the light.

Though wise men at their end know dark is right,
Because their words had forked no lightning they
Do not go gentle into that good night.

Good men, the last wave by, crying how bright
Their frail deeds might have danced in a green bay,
Rage, rage against the dying of the light.

Wild men who caught and sang the sun in flight,
And learn, too late, they grieved it on its way,
Do not go gentle into that good night.

Grave men, near death, who see with blinding sight
Blind eyes could blaze like meteors and be gay,
Rage, rage against the dying of the light.

And you, my father, there on the sad height,
Curse, bless, me now with your fierce tears, I pray.
Do not go gentle into that good night.
Rage, rage against the dying of the light.

Dylan Thomas

Preface

Finalmente ha llegado el momento en que me veo escribiendo estas líneas que marcan el fin de una etapa. Un fin de recorrido que he imaginado muchas veces y que, como suele suceder, me coge por sorpresa. ¡Qué deprisa fluye el tiempo cuando cada respuesta te abre nuevos interrogantes!

En un momento como éste no puedo dejar de mirar hacia atrás. Por esto, antes de entrar en materia, querría dejar constancia de algunas circunstancias que me han acompañado hasta aquí. Quisiera contaros una historia de ésas de "cómo y por qué?". Una historia que al unir los hitos que la componen permite comprender dónde te encuentras hoy. Una historia de principios pero sin fin, una historia de punto y aparte... una parte de mi historia.

He pensado que sería bueno dejar constancia de lo ocurrido en algún lugar y, por ahora, ningún documento tendrá para mí más relevancia que éste que culmina el esfuerzo de cuatro años de trabajo. Sé que pasado el tiempo estas líneas de carácter introspectivo me ayudarán a evocar cómo sucedió todo, cómo llegué hasta aquí. Espero que, además, ayuden a que me conozcan mejor y a darle sentido al trabajo que les presento, agradeciendo a todos los que me han ayudado a ser el que soy. Creo, por tanto, que no hay mejor momento para plasmar mis vivencias que este punto de inflexión, este fin de trayecto. Intentaré ser breve.

Todo empezó en junio de 2011 con una de ésas llamadas aderezadas con un "no te preocupes, tu madre está bien pero...". Es curioso cómo la típica frase pensada para tranquilizar a alguien consigue el efecto totalmente contrario, cómo te hunde en la incertidumbre, más aún si en ese momento te encuentras lejos de casa. Tódo cambió súbitamente. Al llegar al hospital supe que mi madre había sufrido un ictus devastador que le dejaría secuelas de por vida: hemiplejia derecha y afasia global. Pero creo que he ido demasiado rápido. Permitidme que os sitúe un poco mejor.

Roser, que así se llama mi madre, siempre se ha caracterizado por su espíritu de superación, de sacrificio, de perseverancia y de tenacidad. Una persona auto-disciplinada, de ésas que ponen firmes hasta al apuntador y ante la cual no puedes quedar indiferente. Toda fuerza y temperamento. Una persona de las que, en condiciones adversas, se han hecho a sí mismas y han superado, no sin dolor, muchas adversidades. Provista con la coraza osmótica de los que ayudan con facilidad y reciben poco a cambio. Dura por fuera y todo amor en su interior, siempre ha sido una persona con una gran capacidad para querer. Creedme, jamás he visto a nadie con un sentido de la lealtad y la nobleza tan interiorizado como el suyo. Avanzada a su tiempo, optó por constituir una familia monoparental con ayuda de la ciencia y siempre fuimos una unidad. Me dio todo y me enseñó todo. Y ahora... ahora quisiera haberle preguntado todavía mucho más.

En lo que a mí se refiere, al acabar la licenciatura decidí apartarme del ámbito universitario: ya había tenido bastante con todas esas asignaturas a las que había que sumar un trabajo a tiempo parcial y un entrenamiento deportivo de alto rendimiento, así que opté por orientarme hacia el mercado laboral. Nunca pensé que volvería a reincorporarme a la vida académica y menos aún pude intuir siquiera qué motivaría mi regreso. Normalmente soy incapaz de recordar las fechas importantes, pero el 11 de junio de 2011 me marcó para siempre. Tras la inquietante llamada telefónica, llegado al hospital, una frase demoledora por parte del personal médico se encargó de vapulear cualquier atisbo de optimismo: “tu madre no será ni la sombra de lo que era”. En fin, que el diagnóstico era que permanecería en un estado casi vegetativo.

El caos se afincó en mi mente en los días siguientes. Aquí es donde empiezan los “porqué a nosotros?” y los “estoy soñando, mañana despertaré y no será real”. Qué hacer y cómo actuar en estos casos es algo para lo que normalmente no estamos preparados. Una absoluta inversión de rol: de protegido a protector, con la falta más absoluta de instrumentos para enfrentarme a la situación. El desconcierto no pudo exceder a tres días, pues todo era urgente. Después de una breve tregua mental autoimpuesta, confusa, me vi obligado a reaccionar, a dejar de lamentarme y a comenzar a luchar para abordar todos y cada uno de los interrogantes que se abrían ante mí.

Tuve que afrontar desde problemas laborales, patrimoniales y domésticos hasta tomar decisiones vinculadas a la recuperación y las condiciones de vida de mi madre. Por primera vez en mi vida era mi madre la que dependía de mí. Teníamos que enfrentarnos al que sería nuestro día a día a partir de ese momento. Recuerdo una mañana lluviosa en la que, mientras miraba por la ventana del hospital, tomé conciencia de que muy buena parte de la libertad que hasta ese momento había disfrutado se había esfumado. Que depender había dejado ser un verbo que expresara una relación unilateral y que ahora había cambiado de signo. Tenía 24 años y mucho por hacer.

Se puede imaginar lo que vino después: noches frías de hospital, convivir con el sufrimiento propio y ajeno, abordar un duro proceso de negación, adaptación, superación, toma de decisiones, etc. En definitiva, ver lo que uno no está acostumbrado a ver, hacer lo que uno nunca ha hecho. La prolongada estancia hospitalaria me mostró la cantidad de realidades superpuestas en las que se estratifica esta sociedad y a las que no prestamos atención. Mientras unos vivimos un teatro de inconformismo, de necesidades creadas, de evasión de lo que verdaderamente importa, otros luchan día tras día para, simplemente, seguir existiendo. Qué simple y qué real. Tan real cómo la forma en que apartamos la mirada del dolor. Como si pudiésemos introducir todos esos problemas en un cuarto oscuro y luego tirar la llave al mar.

Supongo que, de alguna manera, nos parecemos a nuestros padres. La genética, la educación y el ejemplo recibido y asumido me impidieron tirar la toalla. Ese mismo verano decidí que no podía hipotecar mi vida. Pasaba días y noches en el hospital. Trabajaba en la recuperación de mi madre; la estimulaba, creaba rutinas, inventaba juegos, movilizaba sus extremidades paralizadas, etc. Y todo siguiendo mi propio instinto, ya que los médicos dijeron literalmente “no vamos a trabajar con tu madre porque no tiene posibilidad de mejorar”. ¡Simplemente con una breve frase aquel médico sentenciaba a mi madre! En aquellos momentos me inquietaba la falta de empatía de algunos médicos, quiénes seguramente tenían muchos conocimientos teóricos pero que no prestaban atención a las personas ni a sus capacidades. Si hubieran intentado conocer a mi madre, indagar sobre su personalidad, hubieran averiguado a quién atendían y sus posibilidades. Sólo yo estaba seguro de que íbamos a ser un caso excepcional. Imagino que ellos pensaban algo así como que yo no aceptaba la realidad. Nada más alejado de la verdad. Así que hice lo que había que hacer; cambiar de médicos.

Conseguimos, no sin esfuerzo y una pizca de suerte, una plaza en el Insitut Guttman, centro pionero a nivel europeo en tratamientos de daño cerebral y allí iniciamos una verdadera actividad recuperadora. Ya empezaba a dar algunos pasos y parecía estar bastante consciente. En el Guttman impera la voluntad de recuperar y de recuperarse, por eso, junto a sus conocimientos y medios, hacen un trabajo excepcional con la gente. Roser, por fin, estuvo en el lugar adecuado y comprendimos que, con calma y perseverancia, aún teníamos mucho margen para la mejora.

Para poder llevar esta nueva vida decidí dejar el trabajo y empezar el master MERIT en UPC. Así podría dedicarme a mi madre y continuar de alguna manera labrando mi futuro. De este modo, a partir de septiembre, compaginé las clases de 8 h a 14 h con mis tareas en el Instituto Guttman de 15 h a 22 h, que era cuando las visitas teníamos que abandonar el centro. Hacia finales de noviembre, volvimos a casa. Fue una decisión controvertida ya que tanto las asistentas sociales como parte de la familia me aconsejaban internarla en una residencia. Visité algun centro y pronto llegué a la conclusión de que de ese modo ni avanzaría en su recuperación ni mejoraría sus condiciones de vida. Mi madre estaba superando todas las expectativas y teníamos ganas de recuperar cierta normalidad. Contraté una persona para que nos ayudara y fuimos estableciendo un pequeño programa de trabajo. No nos asustaba nada.

No habíamos hecho más que restablecer nuestra vida hogareña cuando de pronto acaeció un nuevo desastre. El día antes de navidad, debido a sus ansias por demostrar su independencia, se cayó y se rompió la cadera por el lado paralizado. Fué un duro golpe y creí que mi madre iba a tirar la toalla. No podía permitirlo, debíamos sacar fuerzas de donde las hubiera! Celebramos la navidad en el hospital, nos tomamos las uvas en una cama ortopédica y seguimos luchando para salir de allí. Yo estudiaba entre esas inhóspitas paredes y, cómo tenía trabajos que presentar, los hacía en una incómoda butaca mientras ella dormía. Realmente fue una etapa psicológicamente agotadora. Nos llevó casi un año poder volver otra vez a casa.

Pero lo volvimos a hacer. Yo acabé el master y ella volvió a su hogar. Mi objetivo era conseguir la máxima independencia para ella lo cual implicaba, también, un mayor margen de maniobra para mí. Era importante que mi madre siguiera trabajando en su recuperación. Así que le planifiqué su vida llenándola de tareas que la ayudaran a mantenerse activa; fisioterapia, logopedia, natación, manualidades y, por supuesto, hacerse cargo en la medida de lo posible de la casa. Atender a mi madre me tenía muy ocupado, y hacía prácticamente imposible que me pudiera adaptar a una disciplina laboral normal. Creí que continuar la vida académica era primordial por lo que se convirtió en un objetivo a alcanzar, aunque hay que decir que no era una tarea sencilla. No hace falta recordar que nos encontrábamos en plena crisis económica. Pero, a veces, el esfuerzo tiene su recompensa y la suerte no siempre es esquiva. Surgió la oportunidad de conseguir una beca de doctorado que, por cosas del azar, acabó siendo para mí.

Dicen que las desgracias no vienen solas. Os contaré una anécdota, ahora personal, que nuevamente ha puesto a prueba mi capacidad de respuesta. Como bien dice mi entrenador, “yo nunca pierdo, siempre aprendo”. Después de todo lo vivido, yo estaba dispuesto a aprender. Durante mis años como doctorando sufrí una grave lesión deportiva que ponía en entredicho el que volviera a caminar sin cojear: me rompí el tendón de Aquiles. Me inmovilizaron el pie derecho y me dieron unas muletas. Mi director de tesis, Albert Aguasca, me propuso que hiciese trabajo intelectual desde casa, ya que me lo podía permitir. Aunque le estuve muy agradecido por su proposición, si lo hubiese hecho no habría aprendido nada. Así que decidí levantarme muy temprano cada día y dedicar un par de horas para llegar a la universidad. Entre “muletear”, coger trenes, metros, hacer transbordos y subir hasta el edificio D3 desde diagonal, la verdad es que llegaba bastante agotado. Debo decir que una vez llegaba al edificio aún me faltaba subir al despacho en el primer piso, cosa que SIEMPRE hacía por las escaleras en vez de coger el ascensor. Fueron muchos los que me preguntaban porqué lo hacía y yo siempre contestaba, “así me supero a mí mismo”. Creo que nunca me entendieron. Quizás yo tampoco a ellos. Pero de alguna manera eso me hacía más fuerte. Como en el yin y el yang, de todo lo malo se puede sacar algo bueno.

Con el tiempo, y después de tanto esfuerzo, miro atrás y me doy cuenta de todo lo conseguido. Mi madre volvió a casa y superó con creces todas las expectativas. Ahora puede desplazarse, aunque sea laboriosamente, y ha demostrado tener incluso capacidad artística. Sin embargo, desgraciadamente no ha recuperado la capacidad de comunicarse y necesita ayuda para realizar algunas tareas de la vida diaria, aunque podría decirse que la situación se ha normalizado. Ha aprendido a vivir su nueva vida y no le faltan momentos de felicidad. Yo, por mi parte, he agradecido cada día el poder hacer lo que estaba haciendo y he recibido la solidaridad de otros. Trabajar en mi doctorado ha sido uno de las grandes oportunidades que me ha brindado la vida. Además, paralelamente, conseguí estar en el mejor momento de mi carrera deportiva.

Esta es la historia que acompaña a la Tesis que presento. Creo que a nadie le sorprenderá que este trabajo vaya dedicado a mi madre, Roser Lort. Por el amor que me has dado, por todo lo que hemos vivido, por todo lo que hemos aprendido y por todo lo que me has enseñado. Por creer siempre en mí y aportarme tus valores nunca dejaré de estar en deuda contigo. Porque sin ti nada de esto hubiera sido posible. Gracias Mamá.

Marc Lort

Septiembre 2017

Acknowledgments

En primer lloc vull agrair al meu director de tesi, el professor Albert Aguasca, haver-me donat l'oportunitat de poder realitzar aquest doctorat i el seu recolzament. Sense els seus consells i coneixements res d'això hagués estat possible. Com sempre et dic al acabar les nostres converses des de fa més de quatre anys: "gràcies Albert". Segurament ara, després d'haver llegit el preàmbul, entendràs que aquestes paraules d'agraïment no tan sols responien a cada moment concret, si no a quelcom més profund.

També vull aprofitar aquest espai per agrair als diferents professors del departament el seu recolzament; en especial al professor Carlos López pel seu interès i suport incondicional. Els teus punts de vista, sumats al teu positivisme i empenta, m'han ajudat a millorar en aquesta darrera etapa del doctorat. També voldria fer especial menció al professor Xavier Fàbregas, que desde el començament ha estat disposat a resoldre qualsevol dubte. Finalment voldria donar les gràcies al professor Jordi Mallorquí, que sempre ha estat disponible per qualsevol consulta o discussió.

También quisiera mencionar a todas esas personas que han compartido conmigo parte de este viaje. A Alfred, incansable conseller de la família. Es veu que aquests càrrecs també s'hereten, ja que has passat d'aconsellar a la meva a mare a aconsellar-me a mi. No sé que faria sense les nostres converses i els teus punts de vista. Gràcies pel tot el que has fet i, sobretot, gràcies per tot el que fas.

A mi compañero de despacho e incansable conversador, "el imprescindible" Israel Duran. Gracias por acompañarme en este camino, por nuestras conversaciones y por los consejos transmitidos. Aunque seamos un poco más "robots" y llevemos gafas de pasta, nuestra esencia sigue siendo la misma y nuestra amistad aún más fuerte.

Cómo no mencionar a "Los Intocables" y nuestros "Consejos de Sabios". Sois esa clase de personas que al cruzarse en tu camino sabes que tienes que mantener cerca. Poder contar con cada uno de vosotros es toda una suerte. Cardenas, Heredia, Juaquin y Vallde, espero poder devolveros algún día todo lo que me aportáis. Os quiero chicos.

Debo mencionar también a José Luis Galindo, por compartir conmigo sus conocimientos en economía, su capacidad de análisis y por nuestros debates saboreando las hamburguesas del Foster's. Ah!! Y alguna que otra playa de Formentera.

No me quiero olvidar de Lluís Azorín, por esas comidas semanales en "el estresao" oliendo a fritanga y por nuestras conversaciones arreglando el mundo. Nunca olvidaré ese drone ansioso de libertad. Gracias por ser de los que dan todo sin esperar nada a cambio.

Finalmente, y no por ello menos importante, quisiera dedicar estas últimas palabras a Teresa, que ha tenido que soportar parte de mi historia, así como mis problemas, inquietudes y momentos de agotamiento y estrés. Sé que mi cabezonería te saca de quicio, así que gracias por apoyarme, por ser como eres y por compartir tu vida conmigo. Que nuestros sueños juntos se hagan realidad. Je t'aime!

Official acknowledgments

The author wants to acknowledge the support of the **MICINN** (Ministerio de Ciencia e Innovación) for providing financial support to the research performed in the frame of this thesis under the project TEC2011-28201-C02-01 and contract BES-2012-060089.

Abstract

Mankind's way of life is the main driver of a planetary-scale change that is marked by the growing of human populations demand of energy, food, goods, services and information. As a result, it have emerged new ecological, economic, social and geopolitical concerns that are intended to protect the planet.

In this scenario, Synthetic Aperture Radar (SAR) remote sensing is a potential tool that provides unique information about the Earth's properties and processes that can be used to solve societal challenges of local and global dimension. SARs, which are coherent systems that are able to provide high resolution images with weather independence, represent a suitable alternative for Earth observation (EO) with diverse applications. Some examples of SAR application areas are topography (Digital Elevation Maps (DEM) generation with interferometry), agriculture (crop classification or soil moisture), Moving Target Tndication (MTI), forestry (monitoring biomass or deforestation), geology (monitoring surface deformation) and environment monitoring (oil spills or flooding).

In this framework, the encompassing objective of the present doctoral work has been part of the implementation and the subsequent evaluation of capabilities of two X-band SAR sensors. On the one hand, the RISKSAR-X radar designed to be operated at ground to monitor small-scale areas of observation and, on the other, the AiR-Based REmote Sensing (ARBRES)-X sensor designed to be integrated into small Unmanned Aerial Vehicle (UAV)s. Despite its inherently dissimilar conception, the concurrence of both sensors has been evidenced along this manuscript. By taking advantage of the similarities between them, it has been possible to analogously assess both sensors to obtain conclusions. In this context, the common link has been the development of the polarimetric On-the-Fly (OtF) operation mode of the RISKSAR-X, allowing this sensor to be operated equivalently to the ARBRES-X.

Regarding the RISKSAR-X SAR sensor, several hardware contributions have been developed during part of this Ph.D. with the aim of improving the system performance. By endowing the system with the capability to operate in the fully polarimetric OtF acquisition mode, the relative long scanning time has been reduced. It is of great interest since the measured scatterers that present a short term variable reflectivity during the scanning time, such as moving vegetation, may degrade the extracted parameters from the retrieved data and the SAR image reconstruction. During this doctoral activity, it has been studied the image blurring, the decorrelation and the coherence degradation introduced by this effect. Furthermore, a new term in the differential interferometric coherence γ_{blur} that takes into account the image blurring has been introduced.

Concerning the ARBRES-X SAR system, one of the main objectives pursued during this Ph.D. has been the integration of the sensor into a small UAV Multicopter Platform (MP) overcoming restrictions of weight, size and aerodynamics of the platform. The use of this type of platforms is expected to open up new possibilities in airborne SAR remote sensing, since it offers much more versatility than the commonly used fixed wings UAVs.

Different innovative flight strategies with this type of platforms have been assessed and some preliminary results have been obtained with the use of the ARBRES-X SAR system. During the course of the present doctoral work, much effort has been devoted to achieve the first experimental repeat-pass interfereometric results obtained with the UAV MP together with the ARBRES-X. Moreover, the sensor has been endowed with fully polarimetric capabilities by applying the improvements developed to the RISKSAR-X radar, which is another example of the duality between both systems. Finally, a vertical and a semicircular aperture have been successfully performed obtaining Single Look Complex (SLC) images of the scenario, which envisages the capability of the UAV MP to perform tomographic images and complete circular apertures in the future.

In conclusion, the UAV MP is a promising platform that opens new potentials for several applications, such as repeat-pass interferometry or differential tomography imaging with the realization of almost arbitrary trajectories.

Contents

1

Chapter 1

Introduction

This chapter is devoted to describe the motivations that have led to the study carried out within this doctoral activity and the related main objectives to be fulfilled. The structure of this doctoral dissertation is also presented to point out specifically which are the main contributions of each chapter and how they are linked to the fundamental goals.

1.1 Motivation of the thesis

The Earth is the third planet from the sun in our solar system, a minuscule spot located in the Orion arm at 26000 light years from the center of the Milky Way. Commonly known as "the blue planet", approximately 71% of its surface is water-covered, being the only world known to harbor life [1]. The remaining 29%, with an extension of 148.94 million km^2, has terrain consisting of mountains, plains, deserts, and diverse landforms [2]. Thanks to its particular atmosphere, scientists estimate that 8.7 million species coexist in this hidden place of the universe and, between them, humans [3].

This little grain of sand is the habitat of 7.4 billion people [4], number that has been doubled in the last forty years and that is expected to continue increasing. Due to their way of life, humans have historically altered their environment and according to [5], they are likely the premier geomorphic agent currently sculpting Earth's surface. It can be estimated that human's footprint is imprinted in 83% of Earth's ice-free land area [6]. The "Global change" is a reality, term that refers to changes that alter the land, oceans, atmosphere, polar regions, life, the planet's natural cycles, deep Earth processes and also human society [7]. More into detail, Global change in a societal context encompasses population, economy, transport, communication, land use or pollution among others [8]. In the past, the most important causes of global change were product of natural origin, such as volcanism, solar variation, changes in Earth's orbit around the sun or meteorite impact. But it is evident that nowadays the main driver of planetary-scale change is the growing of human population's demand of energy, food, goods, services and information. This era has been marked by incredible changes in communications, transportation and computer technology that have interconnected the whole world and its societies. These changes are so important that humanity has reached the point where the current rate of land transformation, particularly of agricultural land, seems to be unsustainable.

Such figures and data demonstrate the importance of the human development in the global world. As a result, have emerged new ecological, economic and social concerns that are intended to protect our species while specific requirements are defined to protect the planet. In this framework, the governments of all over the world have pointed out the necessity of setting up specific regulations to human activities to protect the environment and to ensure the related economic outcomes. Some examples could be the Kyoto protocol or the Paris climate accord, which are international agreements linked to the United Nations Framework Convention on Climate Change (UNFCCC) that commits its parties by setting internationally binding emission reduction targets. In a wide sense, these regulations have the aim of control the climate change, the resource depletion, natural hazards or natural and man-made disasters.

In this context, remote sensing provides unique information about the Earth's properties and processes and can be used to solve societal challenges of local and global dimension. In a broad sense, remote sensing can be defined as the science of obtaining information about objects, areas or phenomenon from distance with dedicated instruments. Ground-based, airborne and spaceborne Earth observation (EO) provide information of great value to monitor the Earth's surface, which can be useful to prevent, for example, natural or industrial disasters. Synthetic Aperture Radar (SAR)s, which are coherent systems that are able to provide high resolution images with weather independence, represent a suitable alternative for EO with diverse applications. Some examples of SAR application areas are topography (Digital Elevation Maps (DEM) generation with interferometry), agriculture (crop classification or soil moisture), Moving Target Tndication (MTI), forestry (monitoring biomass or deforestation), geology (monitoring surface deformation) and environment monitoring (oil spills or flooding) [9], [10], [11].

Ground-Based Synthetic Aperture Radar (GB-SAR) sensors represent a cost-effective solution for change detection and ground displacement assessment of small-scale areas in real time early warning applications. The first GB-SAR sensors were based on Vector Network Analyzer (VNA) and had important constraints such as the slow scanning time. The evolution of these sensors and the development of modern GB-SAR systems based on Stepped Linear Frequency Modulated Continuous Wave (SLFM-CW) signals has led to several improvements such as a significant reduction of the acquisition time. Nevertheless, the acquisition time is still long enough to degrade the reflectivity map reconstruction and thus affect in the differential interferometric detection process [12], [13]. Part of this doctoral activity has devoted special effort to understand the mechanisms related with the loss of coherence between images, the duration of the scanning time and the atmospheric phenomena when measuring scenarios containing or surrounded by non-static scatterers that present short term variable reflectivity. To study the degradation of the acquired data as a function of the scanning time and the atmospheric conditions, the different measurements performed with the RISKSAR-X sensor developed by the Universitat Politècnica de Catalunya (UPC) are key to the doctoral activity here presented.

Considering large-scale areas of observation, spaceborne SAR sensors are a well established and recognized technique that have been commonly used during the last decade for monitoring different phenomena, such as surface deformation or coastal surveillance. Compared with orbital platforms, airborne SAR sensors provide higher flexibility in terms of revisiting time of the scenario and higher versatility for short-term variable applications. Despite its advantages with respect to orbital sensors, they share some of the limitations, as the high operational cost of the platform or its deployment difficulties, which limits the capability of the overall systems. Unmanned Aerial Vehicle (UAV) provide the flexibility required in the observation of time-critical applications and are a cost effective alternative for airborne SAR remote sensing. They can be remotely controlled and have less restrictions to take off and land. Otherwise, its reduced autonomy, flight regulations and safety concerns limit the spatial coverage of the UAV SAR missions. Nevertheless, these platforms have some limitations when used in SAR applications. One of the most important is the undesired deviations from the nominal flight trajectory that may cause defocusing, geometric distortions or phase errors in the SAR images. Representative examples of some UAV SAR instruments are nanoSAR (ImSAR Co., Springville, TU, USA), microASAR (Artemis, Inc., Hauppauge, NY, USA), miniSAR (Sandia Nat. Labs, Albuquerque, NM, USA), UAVSAR (National Aeronautics and Space Administration (NASA)/Jet Propulsion Laboratory (JPL), USA) and F-SAR (DLR, Germany).

One of the main objectives of the present thesis is the integration of a short to medium range X-band SAR sensor into a UAV Multicopter Platform (MP) overcoming strong restrictions of size, weight and power consumption. The sensor, called AiR-Based REmote Sensing (ARBRES), is a SAR sensor designed to meet these requirements, which makes it suitable to be integrated in this kind of platforms. The UAV MP presents higher degree of flexibility with respect to conventional UAVs, which combined with the SAR sensor leads to open up new horizons in the capabilities of SAR systems. One of the major advantages of this kind of platforms is the ability to perform three-dimensional flights autonomously, which inherently implies new potentials in airborne SAR observation. Differential tomography imaging or repeat pass interferometry [14], [15] are two examples of challenging objectives that could be accomplished with this kind of platforms in the near future. The present doctoral thesis has dedicated much effort to the development of the ARBRES-X SAR sensor fitted into a UAV MP with repeat pass interferometric and fully polarimetric capabilities.

1.2 Objectives of the thesis

The encompassing objective of the present doctoral work is the study and analysis of the capabilities of two X-Band SAR sensors for EO purposes; one of the sensors has been designed to be operated on ground and the other to be integrated in a UAV MP. The work is based on a transversal study ranging from hardware development, validation and preliminary calibration assessment, passing by the utilization of the sensors in different measurement campaigns and performance evaluation, to the determination of processing strategies to diverse applications. A detailed enumeration of the main objectives of the thesis follows:

- Study and review of state-of-the-art in the SAR field with special emphasis in the frame of GB-SAR systems and airborne SAR systems, providing global insights of the actual systems and applied techniques.
- Hardware development, testing and integration of new elements for the RISKSAR-X system. The main requirements are easy integration, flexibility and modularity. Based on modular commercial elements, the signal generation, the transmitter and the receiver units have to be re-designed to improve the system performance with respect to previous versions. Addition of full polarimetric capabilities to the system.
- Analysis and evaluation of different measurement strategies based on the acquisition time when operating in scenarios containing or surrounded by targets with short term variable reflectivity as, for example, vegetated zones. Assessment of the impact on the retrieved images of measuring scenarios containing distributed scatterers and evaluation of the degradation of the retrieved information, such as for instance the coherence maps. Development of an exhaustive study of the coherence terms involved in this effect with the purpose of characterizing the intrinsic mechanisms that affect to the measurements. Proposal of key parameters to take into account when measuring these kinds of scenarios. Realization of different measurement campaigns to validate the results.
- Hardware development and testing of the ARBRES-X SAR sensor to improve the system performance. Addition of fully polarimetric capabilities to the system by

means of re-designing the transmitter and receiver front-end. Integration of the sensor in a UAV MP overcoming restrictions of weight, size and power consumption. Develop a network of sensors working synchronously with the ARBRES-X SAR sensor to monitor continuously the position of the platform and its instabilities during the acquisition time, including an Inertial Measurement Unit (IMU), a Global Positioning Satellite (GPS), a barometer and the logic of control. Validation and testing of the complete system. Study and implementation of a preliminary calibration procedure for the ARBRES-X SAR sensor to be able to obtain reliable results in fully polarimetric mode in the future.

- Realization of measurement campaigns operating with the ARBRES-X SAR system, being able of flying and acquire data autonomously by pre-programming the flight path, the measurement instant and all the supporting sensors. Study and evaluation of innovative flight strategies in airborne SAR observation to discover new potentials of this type of platforms. Assessment of the key parameters necessary to obtain reliable results. Obtain SLC images of high quality by processing the raw data proportioned by the sensor. Application of MOtion COmpensation (MOCO) techniques and autofocus algorithms to improve the quality of the retrieved images. Perform first studies of feasibility of interferometric repeat pass measurements in order to retrieve interferometric maps. Obtain fully polarimetric measurements. Realization of vertical and circular flights to obtain SAR images.

1.3 Structure of the thesis

This doctoral dissertation is organized in seven chapters. Additional information is also distributed in two appendices at the end of the thesis.

This **first chapter** introduces the motivation and states the main goals of this work. **Chapters 2** to **6** contain the main contributions of this doctoral research. Each chapter focuses on one of the five main objectives previously detailed:

- **Chapter 2** gives a general overview of the SAR framework. A brief review of the general concepts and techniques extracted from the literature is provided.
- **Chapter 3** describes and presents the system architecture of the UPC ground-based RISKSAR-X system. Moreover, its main characteristics of operation are exposed. The most important hardware contributions conducted to the system are presented in this chapter. Besides, the main processing steps necessary to obtain good quality focused images are summarized. The preliminary assessment of the polarimetric calibration of the RISKSAR-X system is briefly addressed in this chapter.
- **Chapter 4** carries out an exhaustive study of the effect in the image reconstruction of having moving scatterers in the scenario that present a short term variable reflectivity. In this context, a detailed mathematical description of the cross-range blurring effect and the reduction of coherence is presented. Furthermore, the image blurring and the image decorrelation are characterized in this chapter. The blurring effect, the decorrelation introduced in the SAR images and the evaluation of the number of coherent pixels in the coherent maps are assessed by means of different experimental results obtained with the SAR sensor.

- **Chapter 5** is devoted to describe the system architecture of the UPC ARBRES-X SAR sensor as well as to expose its main characteristics of operation. Furthermore, the main contributions to the system developed during the course of this doctoral activity are exposed in this chapter. Special attention is given to the different procedures and techniques necessary to process the raw data acquired with the ARBRES-X SAR system. The phase center compensation and a first attempt of polarimetric calibration of the ARBRES-X SAR system is briefly addressed in this chapter.
- **Chapter 6** validates the ARBRES-X system performance by presenting a set of experimental results obtained with the sensor. The initial evaluation of the SAR capabilities in UAV MPs is conducted. Different innovative results obtained with the system can be found along this chapter.

The document is concluded in **Chapter 7**, summarizing the main results and contributions presented along the document as well as providing some insights on the possible future research lines.

2

Chapter 2

SAR Remote Sensing

This chapter is intended to give a general overview of the SAR field framework. In this way, a brief review of the general concepts involved in this field are presented in order to produce a self-contained manuscript. In the first part a brief and up-to-date review of the SAR historical evolution is provided, covering from the first systems to the most recent developments. The second section briefly addresses different SAR basic imaging concepts. The third section focuses on the introduction of SAR polarimetry. Finally, the last section is devoted to introduce the main concepts necessary in SAR interferometry.

2.1 SAR brief historical overview

In the early days of the remote sensing technology, the interaction between different scientific developments allowed the evolution of the basic knowledge of radar systems. A first milestone and the theoretical basis of this technology could be considered when, in 1865, the Scottish physicist James Clerk Maxwell presented his book “A Dynamical Theory of the Electromagnetic Field”. He demonstrated in this piece that electric and magnetic fields travel through space at the speed of light in the form of waves [16]. Despite this great discovery, it was not until 1904 that the German engineer Cristian Hülsmeyer patented his invention called the “telemobiloscope”, which was designed to detect distant objects using electromagnetic waves [17]. Indeed, this is considered the first practical radar test. From then until today radar techniques have evolved considerably, specially during the second Wold War.

Until the 50s, the first airborne systems where called Side-Looking Airborne Radar (SLAR) and were a Real Aperture Radar (RAR) primarily. The main limitation of this systems was the low and range-dependent azimuth resolution determined by the wavelength and the antenna size. This problem was overcome in 1951 when the American Carl Wiley developed the SAR principle, which was patented in 1954 [18]. He proposed the use of a coherent pulsed radar together with the principle of Doppler beam sharpening, which resulted in an improvement of the azimuth resolution. Contrarily to RAR, the azimuth resolution was then independent of the range distance, idea that was extended over time to the concept of synthetic aperture as it is known nowadays [19]. The invention of the SAR principle was a major milestone for the development of airborne and spaceborne imaging radar systems.

During the 50s and 60s several developments in the SAR field were carried out by military research for reconnaissance purposes and man-made target detection. In the 70s and 80s different airborne systems were developed for civilian applications with the main aim of monitoring the Earth’s surface. Airborne SAR systems were always in the vanguard of the technological development that were later introduced in spaceborne SAR systems. A recent compilation of airborne SAR sensors is given in [20].

In 1974, the National Oceanic and Atmospheric Administration (NOAA) and engineers from the Jet Propulsion Laboratory (JPL) contemplated the possibility of using a satellite carrying a synthetic aperture radar for oceanic observations since this systems were ideal for monitoring the Earth’s surface with high accuracy. In this context, the launch of Seasat in June of 1978 was the first civilian application of spaceborne SAR systems and it provided a new powerful tool to scientist studying the Earth. Afterwards, important SAR techniques like polarimetry for improved parameter retrieval, interferometry for deriving the surface topography and differential interferometry for the measurement of Earth surface displacements were developed in the 80s and 90s [21], [9], [22]. The field of synthetic aperture radar changed dramatically in the early 1980s with the introduction of advance radar techniques, such as polarimetry and interferometry. While both of these techniques had been demonstrated much earlier, radar polarimetry only became an operational research tool with the introduction of the NASA/JPL Airborne Synthetic Aperture Radar (AIRSAR) system in the early 1980s. Radar polarimetry was proven from space with the two Spaceborne Imaging Radar C-band and X-band (SIR-C/X) SAR flights on board the space shuttle Endeavour in April and October 1994 [23].

GB-SAR sensors represented an alternative solution to monitor small-scale areas. The aim was to merge the SAR capability to obtain two-dimensional reflectivity images and the advantages offered by a terrestrial platform, such as the high stability, the perfect knowledge of sensor's track and the absence of any revisiting time constrain. Consisting of a Continuous-Wave (CW) radar mounted on a moving platform, they synthesized an aperture longer than the physical dimension of their antennas [24], [25]. Also in the 90s, first in-door experiments were carried out to better understand the microwave backscattering characteristic of vegetations and soils [26]. First GB-SARs were VNA-based but the UPC marked a turning point in the GB-SAR field presenting a system based on a Direct Digital Synthesizer (DDS) [27], [28]. With this prototype, the scanning time was reduced drastically, overcoming the main drawback of GB-SAR VNA-based systems.

In the last 10 years, substantial progress has been achieved with polarimetric SAR interferometry (Pol-InSAR) and tomography for obtaining information of volume scatterers [29], [30]. Most recently, the launch of the bi-static SAR satellites, such as TerraSAR-X (TSX) or TanDEM-X (TDX) (X-band), introduce a new generation of high-resolution SAR satellites [31].

Synthetic Aperture Radar has become one of the most valuable tools for remote sensing of the Earth and its environment. With its high-resolution it is used for innumerable applications, such as sea ice observation, erosion, vegetation structure, disaster management or identification of potential landslide areas.

2.2 Basic principles of SAR

The present section gives a general overview of the SAR field, introducing the necessary theory for the following chapters. The intention is to avoid detailed descriptions and derivations to provide an easy understanding of the subject. An extensive literature on SAR can be found to complement the information [32], such as the tutorial paper by Tomiyasu that gives a very comprehensive view about the SAR principle and image formation [33].

SAR is a coherent radar mounted on a moving platform whose defining characteristic is the use of the relative motion between the sensor and the area under study. The radar transmits pulses with a determined Pulse Repetition Frequency (PRF) and stores the received backscattered echoes in a commonly known *raw data matrix*. The adequate processing of the received echoes at the different positions of the moving platform allows to virtually synthesize a longer antenna. After the SAR processing, a high resolution two-dimensional reflectivity map of the illuminated scenario is obtained. Figure 2.1 shows a simplified example of the SAR geometry with the sensor mounted in a UAV that moves at constant velocity v. The moving direction is denoted as *azimuth* and the observation direction as *slant-range* direction, which should not be mistaken with the ground-range dimension.

The resolution of the system is achieved differently depending on the dimension. In the range direction, the location of a given target is obtained by the time delay between the transmission and reception of a pulse. Thus, the range resolution between two adjacent cells is determined by the duration of the transmitted pulse, which normally is a *chirp*

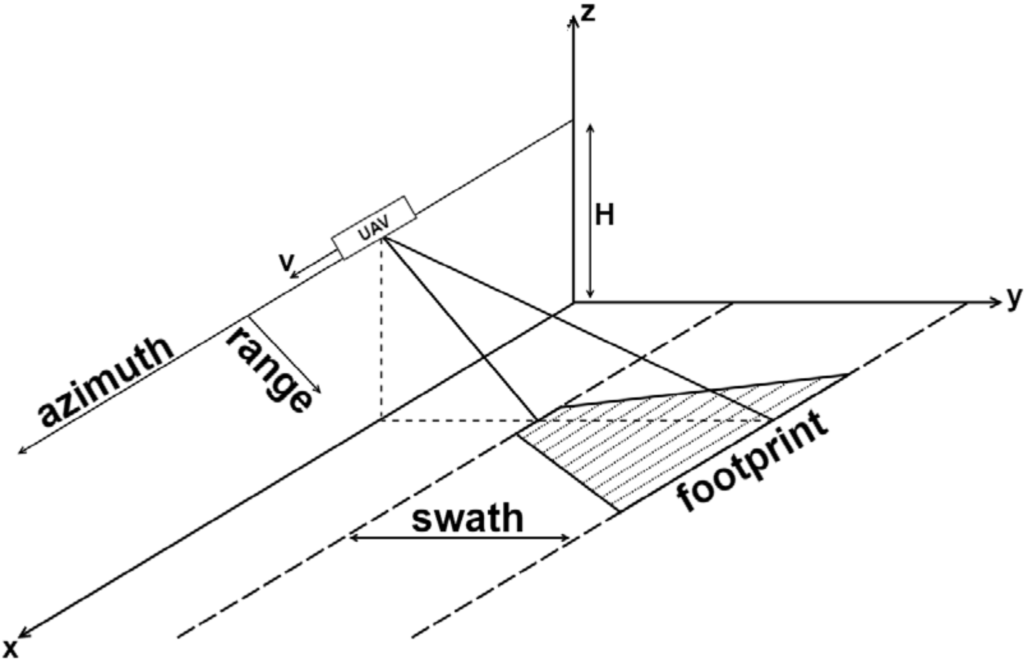

Figure 2.1: Illustration of the SAR imaging geometry.

signal [25]. The range resolution depends on the bandwidth of the transmitted signal B_{rg}

$$\delta_{rg} = \frac{c\tau_p}{2} = \frac{c}{2B_{rg}} \tag{2.1}$$

where c is the speed of electromagnetic waves, τ_p is the pulse duration and the factor 1/2 comes from the two-way path. Therefore, from Equation 2.1 it can be concluded that in order to increase the range resolution the bandwidth must be increased. However, there are usually limitations of availability at the spectrum. An example of range resolution could be the one obtained in the RISKSAR-X and the ARBRES-X SAR sensors with bandwidth $B_{rg} = 100$ MHz, which is $\delta_{rg} = 1.5$ m.

The basic idea of *chirp* signals is that their amplitude is constant during the pulse duration τ_p but the instantaneous frequency is linearly varied over time t according to $f_i = k_r t$, where k_r is the chirp rate that yields the bandwidth $B_{rg} = k_r \tau_p$. The time in the range direction is often denoted as *fast time*, since the electromagnetic waves travel at the speed of light.

Considering Cartesian coordinates (X, Y, Z) oriented such that the X axis is parallel to the flight direction and the Z axis to the normal of the flat surface and being $P_T(X_T, Y_T, Z_T)$ the position of a generic target within the swath, the distance between the moving sensor and the target at time t can be expressed as

$$r_T(t) = \sqrt{(x_T - x_a(t))^2 + y_T^2 + z_T^2} \tag{2.2}$$

where the time t is associated with the movement of the platform and therefore often denoted by *slow time* and $x_a(t)$ is the antenna position in the X axis as a function of t. The time of closest approach, $t = t0 = 0$, is usually referred as *zero-Doppler* distance [10] and is given by the condition

$$r_{T0} = \sqrt{y_T^2 + z_T^2}. \tag{2.3}$$

In the case of narrow-beam antennas, Equation 2.2 can be approximated to a parabolic curve using the Taylor expansion around r_{T0}, yielding

$$r_T(t) = \sqrt{(x_T - x_a(t))^2 + y_T^2 + z_T^2} \approx r_{T0} + \frac{(x)^2}{2r_{T0}} = r_{T0} + \frac{(vt)^2}{2r_{T0}}. \tag{2.4}$$

As the azimuth phase of a given target is directly related to the range variation over time, it also has a parabolic behavior.

$$\varphi(t) = \frac{4\pi}{\lambda} r_T(t). \tag{2.5}$$

To accurately process the data the phase history has to be considered without any approximation. The instantaneous frequency can be calculated as

$$f_i(t) = \frac{1}{2\pi}\frac{d\varphi(t)}{dt} = \frac{2v}{\lambda r_{T0}} t. \tag{2.6}$$

The azimuth or *Doppler bandwidth* B_a, which is the total frequency variation during the synthetic aperture, can be expressed as

$$B_a = -\frac{2v^2}{\lambda r_{T0}} \Delta t_{Lsa} = \frac{2v}{L_{ant}} \tag{2.7}$$

where $\Delta t_{Lsa} = \frac{\lambda}{vL_{ant}} r_{T0}$ is the time interval during which the target is observed by the sensor and L_{ant} is the antenna length.

The basic idea of SAR is to obtain a high resolution in azimuth by means of synthesizing a long antenna in time with the movement of the platform [19]. The beamwidth of an antenna of length L_{ant} can be approximated by $\theta_{az} = \lambda / L_{ant}$. The antenna beamwidth along range determines the *swath* size, while the beamwidth along azimuth results in the length of the synthetic aperture

$$L_{sa} = \theta_{az} r_{T0} = \frac{\lambda r_{T0}}{L_{ant}}. \tag{2.8}$$

A long synthetic aperture is desirable since it results in a narrow virtual beamwidth $\theta_{sa} = \lambda / 2Lsa$ and a high azimuth resolution

$$\delta_{az} = r_0 \theta_{sa} = r_0 \frac{\lambda}{2L_{sa}} = \frac{L_{ant}}{2}. \tag{2.9}$$

Equation 2.9 represents the most important achievement of radar imaging provided by the synthetic aperture technique. It shows that the azimuth resolution for SAR is equal to half the size of the physical antenna and is independent of the distance between the sensor and the target. It also demonstrates that a smaller antenna gives better resolution. This is because the smaller the physical antenna is, the larger its footprint. This allows a longer

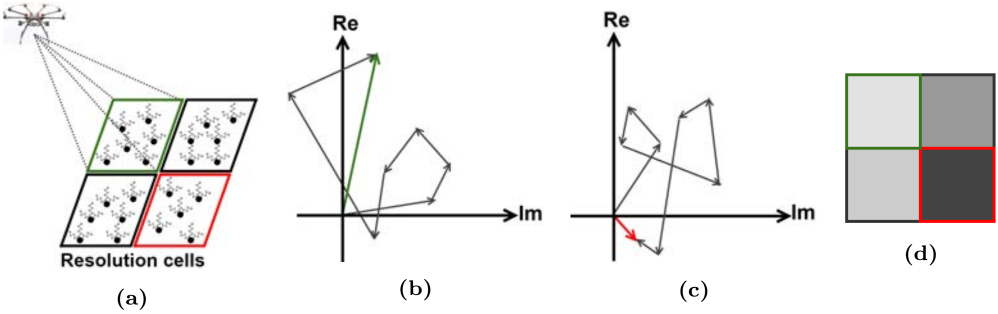

(a) (b) (c) (d)

Figure 2.2: (a) Distributed scatterer scheme. Two-dimensional random walk modelling the returned echo from a distributed scatterer: (b) Constructive combination. (c) Destructive combination. (d) Corresponding pixels on the SAR image.

observation time for each point on the surface, i.e. a longer array can be synthesized. This longer synthetic array allows a larger Doppler bandwidth and, hence, a finer surface resolution. Similarly, if the range between the sensor and the surface increases, the physical footprint increases, leading to a longer observation time and larger Doppler bandwidth, which counterbalances the increase in the range.

The two-dimensional raw data matrix of complex data is formed by the received echo signal, where each sample is composed of a real and an imaginary part, thus representing an amplitude and phase value. The first dimension is associated to the range direction (fast time), where every range line is acquired whenever the sensor travels a distance $v{\cdot}PRI$. This way, it is formed the second dimension of the data matrix, known as azimuth or slow-time. After the SAR processing, the obtained image is commonly displayed in terms of intensity values in the way that each pixel gives an indication of its reflectivity.

Simple geometrical properties are inherently present in most SAR raw data. One of the most importants is the Range Cell Migration (RCM), which accounts from the fact that the distance between the radar and a given point on the image is changing with the movement of the platform along the synthetic aperture. As the RCM is related Equation 2.2, the quadratic behavior of the range distance r_{T0} introduces a curvature in the range compressed response, which makes SAR focusing a two-dimensional space-variant problem. If the RCM is not accurately corrected it will cause azimuth defocusing. Several processors have been developed to efficiently correct the RCM, which the most commonly known are those based on ω - k (or wavenumber domain) processors [34], [35], *range-Doppler* algorithms [36], [37], *chirp scaling* approaches [38], [39] and *Back Projection Algorithm (BPA)* [40], [41].

Another important aspect related to SAR imagery is the so-called *speckle*, which is inherent in coherent radar systems [10], [42]. It is caused by distributed scatterers with a random distribution inside a resolution cell. These scatterers, as shown in Figure 2.2 (a), are opposed to point scatterers in which the scattering behavior is completely deterministic. Thereby, the non-deterministic reflectivity of the final image is given by the coherent addition of the amplitudes and phases off all the scatterers inside the resolution cell, which causes the grainy look to SAR images. Figure 2.2 shows an example of the

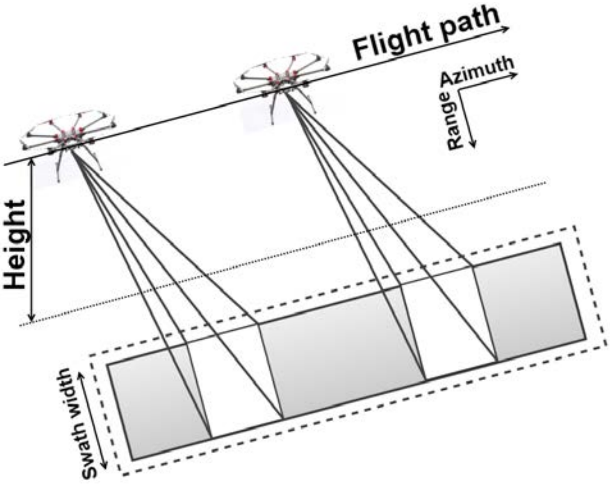

Figure 2.3: Illustration of the Stripmap SAR operation mode.

coherent sum of all the scatterers within the resolution cell and its corresponding pixel in the SAR image. Thus, although speckle is a physical measurement of the scatterers at sub-resolution level, it is normally considered as noise, reason for which it is commonly referred as *speckle noise*. Nevertheless, it cannot be mitigated by increasing the transmitted signal but by using the *multi-look* technique, which basically consists in a non-coherent averaging of the intensity image. The main drawback is the degradation of the resolution due to the averaging, but it improves the visualization of the image. Without entering into detail, it can be pointed out that the multi-look technique can be applied both in frequency or signal domain. More information about the modeling and filtering of speckle noise can be found in the literature [43].

Nowadays, SAR systems are capable of operating in different imaging modes by controlling the antenna radiation pattern. The most conventional one, and used along the present manuscript, is the Stripmap operation mode, in which the pattern is fixed illuminating towards the broadside of the platform trajectory thus imaging a continuous area following the flight path. Figure 2.3 shows an sketch of the Stripmap operation mode. For detailed information, a comprehensive description of other modes, such as Scan-SAR or Spotlight, can be found [24].

2.3 SAR Polarimetry

SAR polarimetry is a widely used technique for the derivation of qualitative and quantitative physical information for land, snow and ice, ocean and urban applications based on the measurement and exploration of the polarimetric properties of man-made and natural scatterers [32], [9]. Measuring the full scattering matrix allows to build up a powerful observation space sensitive to shape, orientation and dielectric properties of the scatterers and allows the development of physical models for the identification and separation of scattering mechanisms occurring inside the same resolution cell [32], [31].

2.3.1 Polarimetric description of the scatterer

The basic concept of SAR polarimetry is given by the 2x2 complex scattering matrix that describes the transformation of the two-dimensional transmitted (e.g., incidence) plane wave vector E^t into the received (e.g., scattered) wave vector E^r (two-dimensional in the far field of the scatterer) performed by the scatterer [9], [23], [31].

$$\begin{bmatrix} E_H^r \\ E_V^r \end{bmatrix} = \frac{e^{-jkr}}{r} \cdot \begin{bmatrix} S_{HH} & S_{HV} \\ S_{VH} & S_{VV} \end{bmatrix} \begin{bmatrix} E_H^t \\ E_V^t \end{bmatrix}^* \tag{2.10}$$

where the matrix $[S]$ is named *scattering matrix* and the S_{ij} are the so-called complex scattering coefficients or complex scattering amplitudes, where the subscripts horizontal (H) or vertical (V) indicate associated received and transmitted polarization. The diagonal elements of the scattering matrix receive the name *"copolar"* terms, since they relate the same polarization for the incident and the scattered fields. The off-diagonal elements are called *"cross-polar"* terms as they relate orthogonal polarization states. The factor $\frac{e^{-jkr}}{r}$, where $k = 2\pi/\lambda$ is the wave number, takes into account the propagation effects both in amplitude and phase.

In monostatic configurations, where receiver and transmitter are co-located, the [S] matrix becomes symmetric, i.e., $S_{HV} = S_{VH}$, for all reciprocal scattering media. In this case, and ignoring the absolute phase, the number of independent parameters in [S] is reduced to five: Three amplitudes and two relative phases. In the bistatic case, where receiver and transmitter are spatially separated, $S_{HV} \neq S_{VH}$ and [S] contains seven independent parameters: Four amplitudes and three relative phases. In SAR remote sensing the majority of the polarimetric systems is operated in a monostatic mode.

As introduced in the previous Section, the concept of distributed target arises from the fact that not all radar targets are stationary or fixed, but generally are situated in a dynamically changing environment and are subject to spatial and temporal variations. In order to fully describe the polarimetric scattering behavior of these type of scatterers a second-order statistical formalism is required, which introduces the concept of space and and time varying stochastic process. The most common formalism to fully characterize distributed scatterers is the 3x3 coherency [T] or covariance [C] matrices. The 3x3 Lexicographic covariance matrix, which is appropriate for system related considerations, is defined as

$$C_3 = \begin{bmatrix} \langle |S_{HH}|^2 \rangle & \sqrt{2}\langle S_{HH}S_{HV}^* \rangle & \langle S_{HH}S_{VV}^* \rangle \\ \sqrt{2}\langle S_{HV}S_{HH}^* \rangle & 2\langle |S_{HV}|^2 \rangle & \sqrt{2}\langle S_{HV}S_{VV}^* \rangle \\ \langle S_{VV}S_{HH}^* \rangle & \sqrt{2}\langle S_{VV}S_{HV}^* \rangle & \langle |S_{VV}|^2 \rangle \end{bmatrix}. \tag{2.11}$$

With respect to the physical information content, the rank of [C] that is normally 3 expresses the number of independent scattering contributions in which [C] can be decomposed. In the most general case both matrices contain nine independent parameters in form of six independent matrix elements: Three real diagonal power elements and three off-diagonal complex cross-correlations.

To simplify the scattering problem and reduce the number of independent parameters of [C], allowing qualitative and quantitative conclusions about the scattering behavior, symmetry assumptions about the distribution of elementary scatterers within the resolution cell can be performed [44]. Besides reciprocity, three special cases of symmetry are important in radar remote sensing applications: Reflection symmetry, Rotation and

Azimuthal symmetry. Further information about the three cases can be found in the literature [9]. Along the manuscript, the concept of reflection symmetry will be considered, idea that was first introduced in the context of calibration by [45]. Reflection symmetric media are characterized by a symmetry plane that contains the line-of-sight so that for any scatterer located at one side of the plane a mirrored scatterer at the other side of the plane exists. In this case the correlation between the co- and crosspolarized elements becomes zero. The resulting [C] matrix contains only five independent parameters in form of three real diagonal elements and one single non-zero complex off-diagonal element (i.e., the correlation between the copolarized elements). The majority of natural distributed scatterers have reflection symmetry [31].
subsectionPolarimetric target decomposition Target decomposition theorems are aimed at providing such an interpretation based on sensible physical constraints such as the average target being invariant to changes in wave polarization basis [9]. Scattering decompositions are widely applied for interpretation, classification, segmentation and as a pre-processing step for scattering parameter inversion. There are many polarimetric compositions that can be classified into four main types:

- Those based on the dichotomy of the Kennaugh matrix K (Huynen, Holm and Barnes, Yang).
- Those based on a “model-based” decomposition of the covariance C_3 matrix or the coherency matrix T_3 (Freeman and Durden, Yamaguchi, Dong).
- Those using an eigenvector or eigenvalues analysis of the covariance C_3 matrix or the coherency matrix T_3 (Cloude, Holm, van Zyl, Cloude and Pottier).
- Those employing coherent decomposition of the scattering matrix S (Kroager, Cameron, Touzi, Pauli).

Detailed information of the different decompositions can be found in [9].

The objective of the coherent decompositions is to express the measured scattering matrix by the radar, i.e. [S], as a combination of the scattering responses of simpler objects

$$S = \sum_{k=1}^{N} c_k S_k \tag{2.12}$$

where S_k stands for the response of the simpler objects, also known as canonical objects, whereas c_k indicates the weight of S_k in the combination leading to the measured S. The coherent target decomposition is useful if only one dominant target component is expected (e.g. dihedral or thihedral edge contributions in urban areas or as calibration targets), and the other components are provided in support for constructing a suitable basis for the whole space of targets.

The Pauli decomposition expresses the scattering S matrix as the complex sum of the Pauli matrices,where an elementary scattering mechanism is associated for each basis matrix, with

$$S = \begin{bmatrix} S_{HH} & S_{HV} \\ S_{VH} & S_{VV} \end{bmatrix} = \frac{a}{\sqrt{2}} \begin{bmatrix} 1 & 0 \\ 0 & 1 \end{bmatrix} + \frac{b}{\sqrt{2}} \begin{bmatrix} 1 & 0 \\ 0 & -1 \end{bmatrix} + \frac{c}{\sqrt{2}} \begin{bmatrix} 0 & 1 \\ 1 & 0 \end{bmatrix} + \frac{d}{\sqrt{2}} \begin{bmatrix} 0 & -j \\ j & 0 \end{bmatrix}. \tag{2.13}$$

The application of the Pauli decomposition to deterministic targets may be considered the coherent composition of four scattering mechanisms: the first being single scattering from a plane surface (single or odd-bounce scattering), the second and third being diplane scattering (double or even-bounce scattering) from corners with a relative orientation of 0° and 45°, respectively, and the final element being all the antisymmetric components of the scattering matrix S. In monostatic systems where reciprocity applies, i.e. $S_{HV} = S_{VH}$, the Pauli basis can be reduced to the first three matrices leading $d = 0$. The span can be expressed as follows

$$Span = |S_{HH}|^2 + 2|S_{HV}|^2 + |S_{VV}|^2 = |a|^2 + |b|^2 + |c|^2. \tag{2.14}$$

The interpretation of the Pauli decomposition must be done according to the matrices in the basis given at Equation 2.13. The matrix S_a corresponds to the scattering matrix of a sphere, a plate or a trihedral. In general, S_a is referred to single- or odd-bounce scattering. The second matrix, S_b represents the scattering mechanism of a dihedral oriented at 0 degrees. In general, this component indicates a scattering mechanism characterized by double or even-bounce, since the polarization of the returned wave is mirrored respect to the one of the incident wave. Finally, the third matrix S_c corresponds to the scattering mechanism of a diplane oriented at 45 degrees. From a qualitative point of view, the scattering mechanism represented by S_c is referred to those scatterers that are able to return the orthogonal polarization, such as for instance volume scattering produced by the canopy.

2.4 SAR interferometry

SAR interferometry is a powerful and well-established remote sensing technique that enables the highly accurate measurement of important geophysical parameters such as surface topography, ground deformation and subsidence as well as glacier movements [9], [46] [12], [11]. The key idea of SAR interferometry is to compare, for a given scene, the phase of two or more complex radar images that have been acquired from slightly different positions or at different times. Since the phase of each SAR image pixel contains range information that is accurate to a small fraction of the radar wavelength, it is possible to detect and measure tiny path length differences with centimetric or even millimetric accuracy. This outstanding accuracy is independent of the distance between the sensor and the scene, which makes SAR interferometry highly relevant for both air and spaceborne remote sensing. Over the last decades numerous terrestrial applications have been demonstrated using either airplanes [29], [47], [48], [49], [15] or satellites [22], [50], [51] [52], [53]. A drawback and fundamental challenge of SAR interferometry is, however, that the measured range difference is ambiguous with the wavelength. This ambiguity is typically resolved by using some external information together with appropriate regularity assumptions about the imaged scene, a process known as phase unwrapping [54].

The radar images for SAR interferometry are typically acquired either from mutually displaced flight tracks or from one and the same flight track but at different times. The former is known as cross-track interferometry and enables, besides several other applications, a precise measurement of the surface topography. The latter is known as along-track or differential interferometry. By varying the temporal baseline between the interferometric acquisitions, velocities ranging from several meters per second down to a few millimeters per year can accurately be measured. Important applications covering the whole range of potential time scales are the detection of moving objects like cars or ships [55], [56], the observation of ocean surface currents [49], [57], the measurement of sea ice drift and glacier flow [58], [59], [60], the study of seismic deformations and volcanic activities [22], [51], as well as the monitoring of land subsidence [53]. Further potential arises from a comparison of the coherence between several data acquisitions, which can be used for land classification and change detection [61], [62], [31].

2.4.1 Cross-track Interferometry

The main objective of cross-track interferometry is to retrieve the height of the illuminated scatterers using only two SAR images. To do so, phase preservation must be ensured in the SAR focusing process. Considering this, the phase of a resolution cell is given by

$$\phi_{slc} = \frac{4\pi}{\lambda} r_{T0} + \phi_{\sigma 0} \tag{2.15}$$

where $\phi_{\sigma 0}$ is the reflectivity of the resolution cell. To retrieve the height of the scatterer, a second SAR image from a different position has to be acquired, as depicted in Figure 2.4. The two acquisition positions are separated by the baseline B with a certain tilt angle α_s. By viewing the same point from two different positions, and knowing both range distances r_1 and r_2, it is possible to obtain the height of the target by solving the parallax. The cosine law yields

$$r_2^2 = r_1^2 + B^2 + 2r_1 B sin(\theta_0 - \alpha_s) \tag{2.16}$$

with θ_0 being the look angle. The *parallel baseline* can be defined

$$B_{\parallel} = Bsin(\theta_0 - \alpha_s) = \frac{r_1^2 + B^2 - r_2^2}{2r_1} = \frac{B^2}{2r_1} - \frac{\Delta r^2}{2r_1} - \Delta r \approx -\Delta r \tag{2.17}$$

where it has been assumed that the baseline B is small compared to the range distance to the target (far-field or parallel-ray approximation [48]). After obtaining θ_0, it is straightforward to compute the height of the target

$$h = H - r_2 cos\theta_0. \tag{2.18}$$

In order to obtain accurate height estimates, it is necessary to know Δr precisely. Effectively, the height accuracy respect to the accuracy in the measurement of the Δr is [21]

$$\sigma_r = \frac{\partial h}{\partial \Delta r} \sigma_{\Delta r} = \frac{r_1 sin(\theta_0)}{Bcos(\theta_0 - \alpha_s)} \sigma_{\Delta r} \tag{2.19}$$

where $B_{\perp} = Bcos(\theta_0 - \alpha_s)$ is normally referred to as the *perpendicular baseline* or *effective baseline*. SAR interferometry can give an accurate measurement of Δr, since the path difference is estimated using the interferometric phase, yielding an accuracy in the order of a fraction of the wavelength. Considering that the phase of the same resolution cell for each image is

$$\begin{aligned} \phi_1 &= \frac{4\pi}{\lambda} r_1 + \phi_{\sigma,1} \\ \phi_2 &= \frac{4\pi}{\lambda} r_2 + \phi_{\sigma,2}, \end{aligned} \tag{2.20}$$

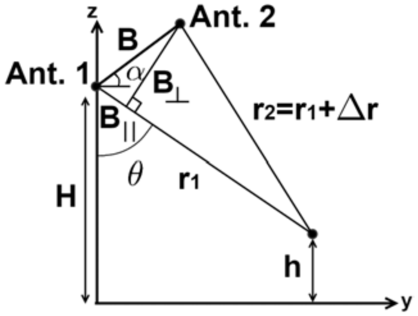

Figure 2.4: Illustration of SAR interferometry geometry.

respectively, an interferogram can be formed by multiplying one image by the complex conjugate of the second one. Assuming that both reflectivities are the same, the Hermitian product yields (omitting decorrelation terms)

$$\phi_{int} = \frac{4\pi}{\lambda} r_{T0} \Delta r. \tag{2.21}$$

Now, the accuracy in the measurement of Δr is related to the accuracy in the measurement of the phase

$$\sigma_{\Delta r} = \frac{\lambda}{4\pi} \sigma_{\phi}. \tag{2.22}$$

It has to be taken into account that the phase values are wrapped between the $[-\pi, \pi]$ interval, while the phase values treated in the previous equations refer to the absolute (unwrapped) ones. Therefore, an unwrapping procedure [63], [50], [64] and absolute calibration is needed in order to properly obtain the topographic height. Analyzing Equation 2.19, it might seem plausible to increase the baseline B to improve the height estimation accuracy. However, there exists a limit in the maximum baseline possible, mainly due to the noise introduced due to baseline decorrelation, which will be used in Subsection 6.3.1 of Chapter 6.

Analyzing the content of the interferometric phase, it can be seen that the so-called flat term introduces a phase pattern in the interferogram. Therefore, this phase pattern is not related to topography and should be subtracted to clearly visualize the topographic one. Both of these components can be approximately obtained analytically. Avoiding the mathematical derivations, the total phase increment between two pixels is

$$\phi_{int} = \phi_{fe} + \phi_{topo} \approx -\frac{4\pi}{\lambda} \frac{Bcos(\theta_0 - \alpha_s)}{rtan\theta_0} \delta_r - \frac{4\pi}{\lambda} \frac{Bcos(\theta_0 - \alpha_s)}{rsin\theta_0} \delta_h \tag{2.23}$$

where δh is the height increment between the two pixels. It is also interesting to introduce the concept of *height of ambiguity*, which refers to the height change that leads to a 2π change in the interferometric phase. From the topographic term of Equation 2.23 the height of ambiguity results in

$$h_{2\pi} = \frac{\lambda r sin\theta_0}{2Bcos(\theta_0 - \alpha_s)}. \tag{2.24}$$

2.4.2 Interferometric acquisition modes

There are two main acquisition modes in SAR interferometry: single-pass and repeat-pass. In the former one, both receiving antennas acquire images at the same time, which allows to obtain inteferograms with very good coherence. However, the baseline is restricted to the dimensions of the platform. Systems working at X-band or higher frequencies normally work in the interferometric single-pass mode, since the antenna dimensions are small enough to be integrated on the aircraft with a reasonable baseline. Due to the high coherence between images, this type of systems are normally preferred for mapping applications.

In the repeat-pass mode the two images are acquired at different time instants. This mode has the advantage that there is not physical restrictions in the baseline, which can be made as large as desired. Nevertheless, different decorrelation effects should be considered. At lower frequency bands, it is normally not possible to integrate two antennas on the same platform due to both the dimension of the antennas and the height sensitivity. This is the case of some polarimetric SAR interferometric applications [21, 95], which usually work with L-band data in order to retrieve useful information like biomass or soil moisture. On the other hand, applications like Differential SAR Interferometry (DInSAR), are based on the acquisition of images at different time instants in order to measure possible displacements of the surface in the observed scene.

2.5 Concluding remarks

In this introductory chapter, a brief review of the main basic concepts that are used along the manuscript are presented, giving a general overview of the SAR field framework.

First of all, a brief up-to-date review of the SAR historical evolution is provided, ranging from the Maxwell equations to the recent high-resolution SAR systems. Moreover, the basic principles of SAR have been introduced avoiding detailed descriptions and derivations. This way, concepts such as for instance the range resolution δ_{rg}, the azimuth resolution δ_{az} or the parabolic behavior of the range distance r_T have been presented. Furthermore, the concept of RCM and the importance of its correction during the focusing process has been commented. Finally, the speckle effect related to SAR imagery has been assessed and the Stripmap operation mode has been introduced.

Regarding SAR polarimetry, the basic concepts concerning the scattering S and covariance C matrices have been assessed, introducing useful concepts such as reflection symmetry, rotation and azimuthal symmetry. The coherent Pauli decomposition is explained, which will be used in this thesis.

Finally, some basic concepts regarding SAR interferometry are introduced, since repeat-pass interferometric measurements will be performed with the ARBRES-X SAR system.

Part I

Contributions to RISKSAR-X system

3

Chapter 3

UPC RISKSAR-X System

This chapter is intended to describe the system architecture of the UPC ground-based RISKSAR-X system as well as to expose its main characteristics of operation. In order to do so, the system will be compared to its previous version with the aim of analyzing the most important contributions conducted to the sensor during the course of the present doctoral work.

In the first part, a brief introduction to the RISKSAR-X sensor is provided assessing the state of the art of the system before this thesis. In the second section, the main hardware contributions to the SAR sensor are exposed, centering the attention to the most relevant elements of the Frequency Generation Unit (FGU), the transmitter and the receiving chain. The third section is intended to briefly describe the way in which the system process the raw data taking into account the new capabilities of the sensor. In the fourth section, the phase centers compensation is described. The fifth section presents the firsts steps to polarimetrically calibrate the system in the future, which is included for completeness purposes. Finally, the main conclusions and major remarks of the chapter are exposed.

3.1 Introduction to the RISKSAR-X sensor

The RISKSAR-X sensor is a fully polarimetric SAR sensor developed by the Remote Sensing Laboratory (RSLab) of the UPC that is under continuous development since 2004 [65], [66]. During the course of this doctoral thesis, some hardware contributions have been introduced to the system with different purposes that will be exposed along the present chapter. The characteristics and the block diagram of the system architecture before the hardware modifications are shown in Figure 3.1 and summarized in Table 3.1, respectively. In previous versions, the system operated with a triangular Stepped Linear Frequency Modulated Continuous Wave (SLFM-CW) ramp signal generated by a Direct Digital Synthesizer (DDS). The FGU of the DDS-based sensor used the chip-set AD9858 from Analog Devices. Its versatility made it possible to digitally generate analogical and digital modulated signals by loading the configuration parameters into its internal registers. For GB-SAR applications, the DDS was set up to generate chirp modulated signals. The output was an L-Band Frequency Modulated (FM) signal that must be band-pass filtered to eliminate spurious replicas generated by the D/A conversion. A final x8 frequency multiplier provided the chirp centered at 9.65 GHz. In the last stage of the transmitter, the delivered power was obtained by a solid state power amplifier. Two electromechanical (EM) switches, one in the transmitter and another in the receiver, endowed the system with fully polarimetric capabilities. The receiver unit consisted of a low-noise chain with a direct Zero-IF demodulator, where a sample of the transmitted signal was used as local oscillator, operating the radar in dechirp-on-receive mode [67].

The sensor was fixed on a linear motion unit and operated in StripMap mode. The scanning technique was the so called *Stop&Go* (*S&G*), which divides the aperture length in different fixed, equally spaced positions where the sensor stops and takes an averaged measurement. This technique is the one used by the first GB-SAR systems and implies the need of several minutes to synthesize a 2 m length aperture. One of its major drawbacks was the long duration of the scanning time that can degrade the quality of the retrieved data when measuring scenarios containing or surrounded by scatterers with short term variable reflectivity, as will be exposed in Chapter 4.

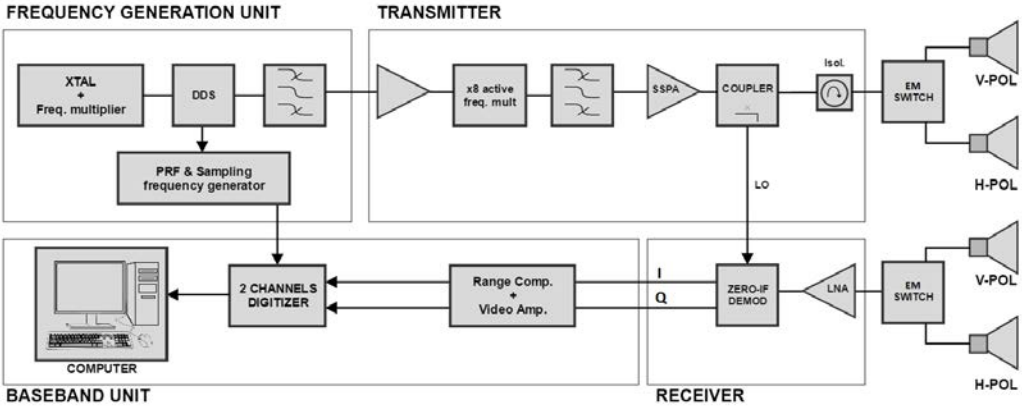

Figure 3.1: RISKSAR-X GB-SAR system architecture before hardware contributions.

3.2 Hardware contributions to RISKSAR-X sensor

In this subsection, the main hardware contributions introduced to the RISKSAR-X sensor during the course of this doctoral work are presented. The setting parameters have remained the same, but the hardware structure has been modified to improve the system performance and capabilities. To this purpose, some new hardware elements have been introduced and some have been modified. The block diagram of the system architecture after the hardware modifications is shown in Figure 3.2. As can be observed, the most important contributions are the introduction of a Phase-Locked Loop (PLL) in the Frequency Generation Unit (FGU) and a solid-state (SS) switch in the transmitter chain. Furthermore, to endow the system with fully polarimetric capabilites, two symmetric receiving chains have been introduced in the receiver, which constitutes an important improvement in the system performance with respect to the version presented in Figure 3.1. As will be explained in detail in Subsection 3.2.2, the electromechanical switches have been removed in the new design.

In this evolved version of the RISKSAR-X sensor the scanning technique could be of

Table 3.1: RISKSAR-X Setting Parameters.

System Parameters	**X-Band**
Carrier Frequency (f_0)	9.65 GHz
Chirp Sampling Frequency (f_s)	50 MHz
Chirp PRF	3.05 KHz
Chirp Bandwidth	100 MHz
Deramped Signal Bandwidth	21 MHz
Transmitted Power	30 dBm
3dB Antenna Beamwidth	27 °
Synthetic Aperture Length	2 m

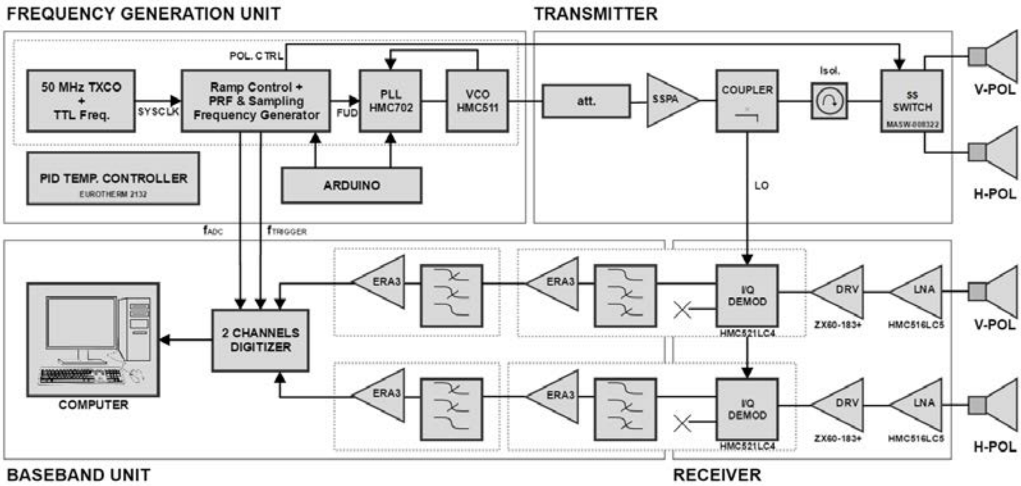

Figure 3.2: RISKSAR-X GB-SAR system architecture after hardware contributions.

two types: *S&G* and On-the-Fly (OtF). The *S&G* operation mode maintain the same philosophy as its predecessor (averaging a determined number of chirp pulses in every azimuth position) but, in the OtF operation mode, the sensor is measuring continuously while the linear unit performs the aperture in a few seconds. This operation mode is analogous to the one used in modern GB-SARs [68]. In both cases, it is important to distinguish between the scanning time and the observation time. The observation time is the effective time in which the radar is illuminating the scenario and it is related with the total amount of energy transmitted, while the scanning time is the time that the system takes to perform the total aperture. The OtF operation mode has the same observation time and scanning time, but the *S&G* mode has not. In our particular case, the observation time can be the same for both operation modes, which ensures the same energy transmitted, but the scanning time in *S&G* mode will be higher. This is due to the computation of the averaging process and the mechanical stop-go-stop movement of the platform. The difference in the scanning times is of great importance because both modes of operation theoretically could have the same Signal-to-Clutter Ratio (SCR), which indeed is related with the quality of the SAR images, but the *S&G* mode is much more affected by the short term variable reflectivity introduced by moving scatterers. Scenarios with moving vegetation by the wind are suitable to be affected by this effect, as it will be demonstrated in Chapter 4.

3.2.1 Frequency generation unit

One of the most important contributions to the RISKSAR-X sensor has been conducted in the generation of the transmitted signal. Concretely, the DDS configuration has been substituted by a PLL configuration. The sensor based on the DDS was developed to optimize the signal generation and transmission in order to obtain a high quality CW-FM signal in a simple way. The sensor based on the PLL maintains the same philosophy but overcoming some limitations of the DDS, together with an improvement of the system performance. Both radar architectures are based on a CW-FM solid-state transmitter designed to be flexible and adaptable to different frequency bands, such as L-, C-, X-, and Ku-bands. The first improvement of the PLL-based sensor resides in the flexibility

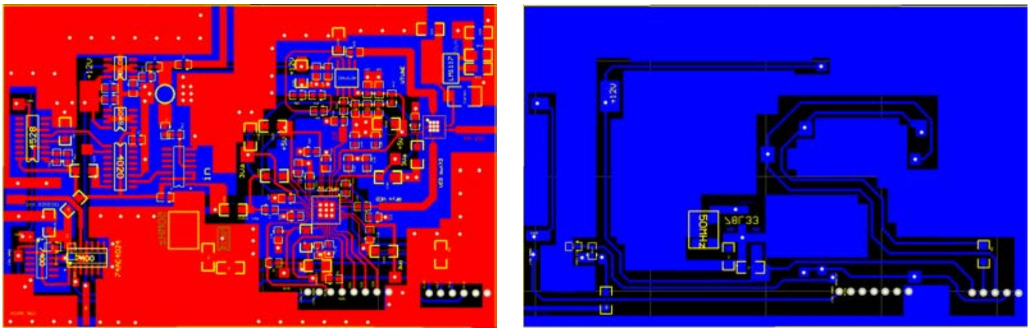

(a) (b)

Figure 3.3: Design of the PLL-based signal generation board. (a) Top side of the board. (b) Bottom side of the board.

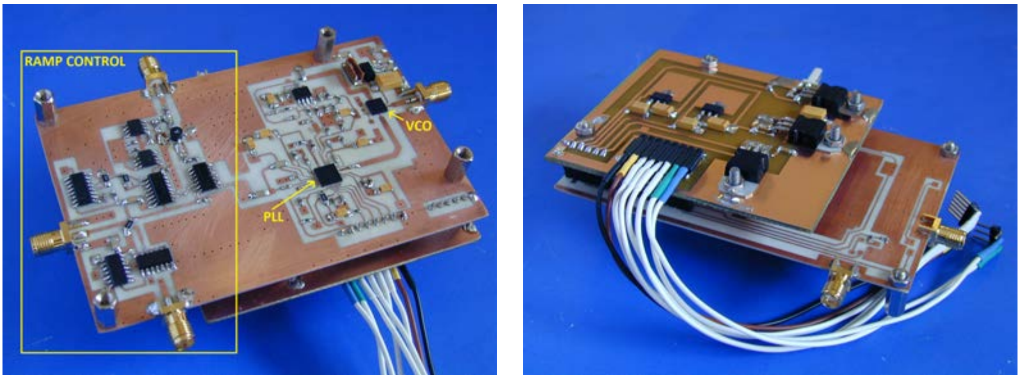

(a) (b)

Figure 3.4: PLL-based signal generation board. (a) Top side of the board. (b) Bottom side of the board.

and adaptability of the system to different signal bandwidths and frequency bands. In the DDS-based sensor, the system is modular and the change of frequency band can be only done by interchanging the frequency multiplication module. This is a tedious task that, in practice, is translated in the necessity of constantly modify the signal generation board at hardware level. Otherwise, the PLL-based system has the capability to change the operation frequency by simply changing the Voltage Controlled Oscillator (VCO) chip and by properly programming the registers of the PLL chip-set at software level. Furthermore, the system is prepared to be easily accessible to be programmed through the Universal Serial Bus (USB) port, as will be explained below. The signal generation based on the PLL and the Monolithic Microwave Integrated Circuit (MMIC) VCO manages the chip-sets HMC702LP6CE and HMC511LP5 from Analog Devices. The PLL chipset is a SiGe BiCMOS fractional-N frequency synthesizer. The fractional synthesizer features an advanced delta-sigma modulator design that allows ultra-fine frequency step sizes. Ultra low in-close phase noise also allows wider loop bandwidths for faster frequency hopping.

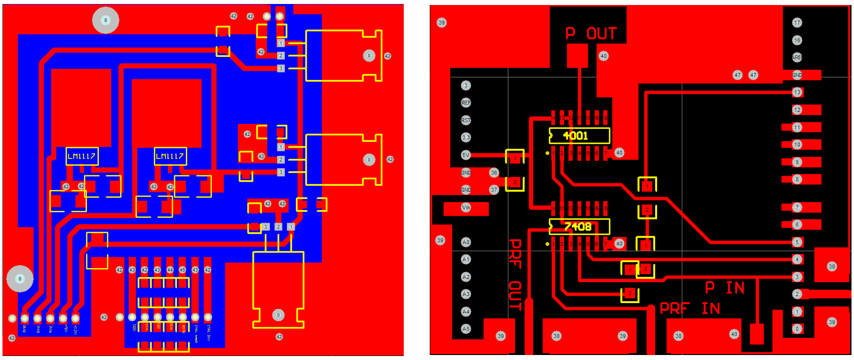

(a) (b)

Figure 3.5: (a) Power supply board. (b) Auxiliar board integrated with the Arduino.

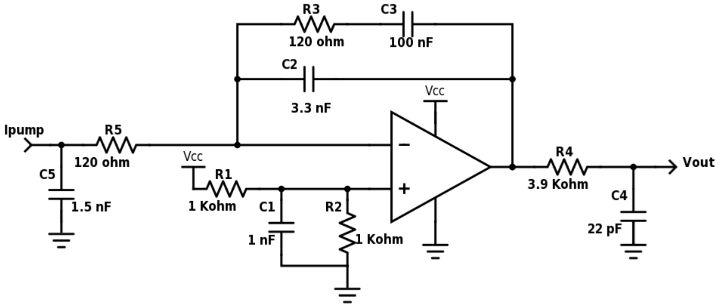

Figure 3.6: Loop filter design with bandwidth of 60 KHz.

The synthesizer contains a built-in linear sweeper function, which allows it to perform frequency chirps with a wide variety of sweep times. On the other hand, the VCO is a GaAs InGaP Heterojunction Bipolar Transistor (HBT), which phase noise performance is excellent over temperature, shock and process due to the oscillator's monolithic structure.

The design of the PLL-based signal generation board developed for the RISKSAR-X sensor can be seen in Figure 3.3 and the built board is shown in Figure 3.4. The top side of the board corresponding to the signal generation contains the PLL chipset, the VCO chipset, the ultra low noise operational amplifier (AD797ARZ) and the loop filter designed of 60 KHz. Besides, the necessary elements to control the frequency ramp generation are integrated in this side of the board. On the other hand, the bottom side of the board has a 50 MHz oscillator used as reference for the signal generation. Moreover, another board containing some voltage regulators and a connector used to communicate the PLL chip-set with a microcontroller has been attached to the bottom side of the PLL board, see Figure 3.5 (a). Besides, it is integrated with another board responsible of managing the different control signals, see Figure 3.5 (b). One of the functions of the microcontroller integrated in the SAR system, which is accessible through a USB port, is the easy programming and configuration of the registers of the PLL. Furthermore, it controls the frequency ramp generation, the trigger that is used in the digitizer to acquire the received signal and the polarimetry by means of the solid-state switch in the transmitter. Another of its functions, together with the solid-state switch that will be presented in Subsection 3.2.2, is to proportionate the flexibility to work in different operation modes. The different possibilities are:

- OtF V POL: transmitting in vertical polarization and receiving in vertical and horizontal polarizations while realizing a measurement in the OtF mode.
- OtF H POL: transmitting in horizontal polarization and receiving in vertical and horizontal polarizations while realizing a measurement in the OtF mode.
- OtF FULL POL: transmitting and receiving in vertical and horizontal polarizations while realizing a measurement in the OtF mode.
- *S&G* V POL: transmitting in vertical polarization and receiving in vertical and horizontal polarizations while realizing a measurement in the *S&G* mode.
- *S&G* H POL: transmitting in horizontal polarization and receiving in vertical and

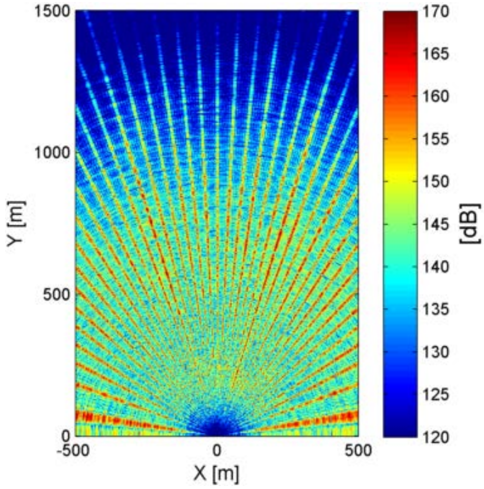

Figure 3.7: SLC of empty space containing undesired spurious due to the oscillation of the operational amplifier.

horizontal polarizations while realizing a measurement in the *S&G* mode.

- *S&G* FULL POL: ransmitting and receiving in vertical and horizontal polarizations while realizing a measurement in the *S&G* mode.

As can be observed, the PLL, the loop filter, the VCO, the trigger control, the polarization control, the ramp control and the needed voltage regulators have been efficiently integrated in a single module. Regarding this module, the part corresponding to the loop filter deserves special attention. The PLL chip-set generates the chirp signal by means of a set of different dividers. Said dividers generate dithering that will affect the system performance if the loop filter is not properly designed. To avoid the noise introduced by the dithering effect, the design of the loop filter shown in Figure 3.6 has been implemented, which corresponds to an active C filter of fourth order. The RC components in the output of the operational amplifier, R4 and C4, are extremely important because they are in charge of suppressing the dithering effect. The final bandwidth of 60 KHz has been selected empirically taking into account the trade-off between the loop response, the equivalent PRF of the system and the noise mitigation. In this context, the operational amplifier introduced in the loop must be properly filtered to avoid the apparition of undesired spurious. It has been observed that if the RC filter at the output is not well designed, the amplifier has the risk of introducing oscillations to the signal. Figure 3.7 shows an example of this effect in the retrieved SLC images. If the chip-set is not properly filtered, the spurious will be present in the final SLC image degrading its quality and masking useful information. On the other hand, the effect of the low-pass and high-pass filters of the receiver chain can also be observable in the image of Figure 3.7. Such effect can be seen in the background noise of the image, which has less intensity for low distances, i.e. low frequencies, than for the higher ones. This frequencies correspond to the cut-off frequency of the filters that will be presented in Subsection 3.2.3.

3.2.2 Solid-state switch in transmitter

Older versions of the sensor had the possibility to perform fully polarimetric measurements by means of two electromechanical switches, one in the transmitter and another in the receiver, as can be seen in Figure 3.1 [69]. One of the main drawbacks was that, with this type of configuration, there was only possible to obtain fully polarimetric results working in the *S&G* operation mode due to the limited switching speed of the electromechanical Radio Frequency (RF) switches. In this context, another distinctive hardware contribution to the RISKSAR-X sensor is the introduction of a solid-state switch in transmission to add fully polarimetric capabilities to the system. This, together with the incorporation of two different reception chains, allows the system to perform fully polarimetric measurements in the OtF mode. Thus, the system front-end is composed by four identical linearly-polarized pyramidal horns and a solid-state switch in transmission, eliminating any electromechanical switch in the transmitting and receiving chains.

The component used to perform the commutation between the two transmitting antennas is the MASW-008322 from Macom. It is a GaAs Single Pole Double Throw (SPDT) device with high isolation and very broadband performance. Figure 3.8 shows the functional schematic of the switch and the board developed with the chip-set integrated. It can be seen that the switch has an input and two outputs called RF1 and RF2, which are directly connected to the two transmitting antennas. Notice that to optimize the performance of the device, some open circuit stubs have been added in the transmission lines, which behave as a simple matching network. The measured insertion losses, return losses and isolation of the board presented in Figure 3.8 (c) are shown in Figure 3.9. As can be seen in Figure 3.9 (a) and (b), in the RF1 port the return losses are -15.2 dB, the insertion losses are -1.3 dB and the isolation between RF1 and RF2 is -66 dB at the desired frequency of 9.65 GHz. Furthermore, in the RF2 port, the return losses are -12.2 dB, the insertion losses are -1.6 dB and the isolation between the two ports is -40 dB. It can be observed that the two ports are not symmetric but in both cases the response is acceptable.

The control of the commutation between the antennas must be performed synchronously with the PRF of the system. With this purpose, the electronic board shown in Figure

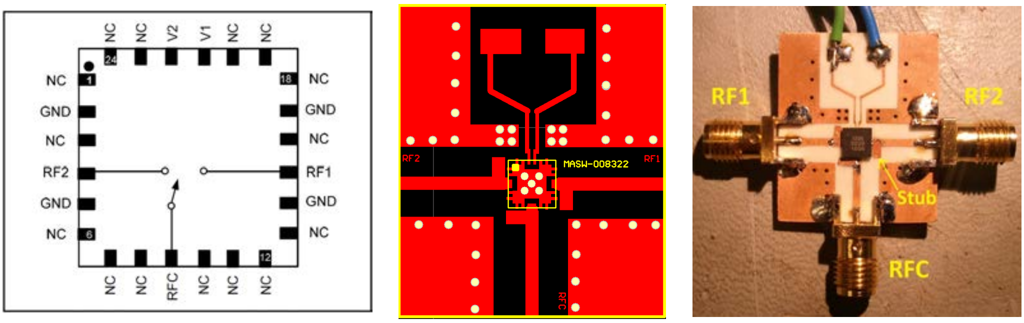

(a) (b) (c)

Figure 3.8: (a) MASW-008322 functional schematic. (b) Design of the board for the switch. (c) Developed board with the MASW-008322 integrated.

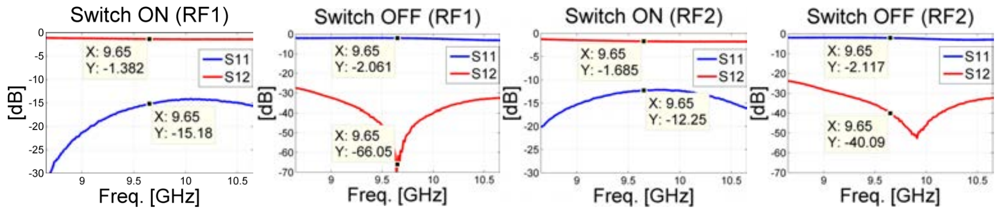

(a) (b) (c) (d)

Figure 3.9: Switch measurement. Insertion losses and return losses in (a) RF1. (c) RF2. Isolation in (b) RF1. (d) RF2.

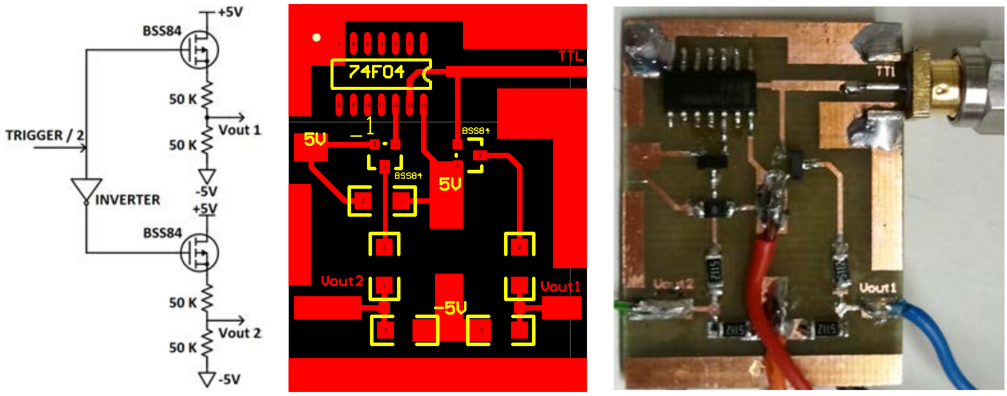

(a) (b) (c)

Figure 3.10: (a) Schematic of the board responsible of the switch commutation. (b) Design of the board responsible of the switch commutation. (c) Developed board.

3.10, which is responsible of the switch commutation, has been designed and developed. The truth table defining the behavior of the switch is shown in Table 3.2. The control inputs of the switch, V1 and V2, are generated by the board shown in Figure 3.10 (c), which consists of two P channel mosfet transistors that are responsible of generating the different states necessary to perform the commutation. The POL CTRL. signal generated in the frequency unit is used to that end. It is a rectangular wave of half the frequency of the PRF that ensures that for every triangular wave of the chirp signal the switch has commuted.

The V1 and V2 control inputs measured with the oscilloscope are shown in Figure 3.11. It is obvious in Figure 3.11 (a) that when one of the signals has 0 V the other has -5V and

Table 3.2: Truth table of the switch.

Input Control		**Switch Condition**	
V1	**V2**	**RF1**	**RF2**
High	Low	Off	On
Low	High	On	Off

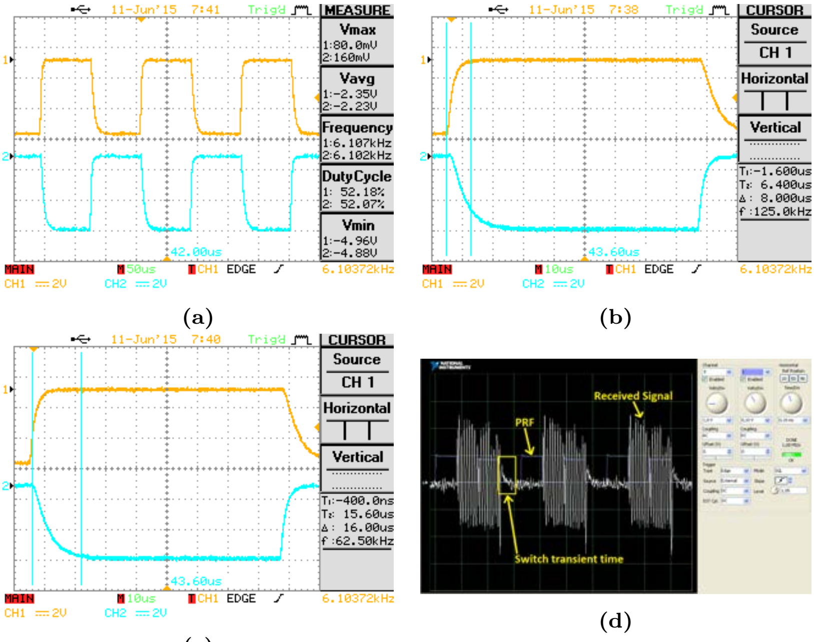

(a) (b) (c) (d)

Figure 3.11: (a) Measured V1 and V2 control inputs. (b) Measured rise time of control input. (c) Measured fall time of control input. (d) Oscilloscope screenshot. Channel 0: received signal in horizontal polarization. Channel 1: system PRF

vice versa. However, there are a rise and fall transient time due to the use of transistors that has been measured and is shown in Figure 3.11 (b) and (c). The measured rise time is 8 μs and the fall time 16 μs, which is fast enough not to affect the system performance. It is possible that the probe of the oscilloscope has masked the measurement, but in any case the response is fast enough to not be taken into consideration. The proper behavior of the switch and its synchronization with the PRF is shown in the screenshot of the oscilloscope in Figure 3.11 (d). To obtain this measurement, the switch is integrated just before the transmitting antennas such that the transmitted signal will change between vertical and horizontal polarization. In reception, just the horizontal polarization is measured. The digitizer uses the rising edge of the PRF to acquire the received data. It can be appreciated in Figure 3.11 (d) that for the first rising edge of the PRF (channel 1) the received signal (channel 0) has no power, since the system is transmitting in vertical polarization and receiving in horizontal. In a complementary way, in the second rising edge of the PRF there is signal, corresponding to transmit and receive in horizontal polarization. After a careful observation of the received signal in channel 0, the falling transient time of the switch can also be seen.

As explained, the fully polarimetric capability of the system is achieved by switching the transmission antennas and storing the data simultaneously with the two reception channels. Figure 3.12 shows a diagram relating the different signals generated in the signal generation board with the way in which the received signal is stored. As can be seen, the GPO3 signal programs the PLL setting the start of the up-ramp and the

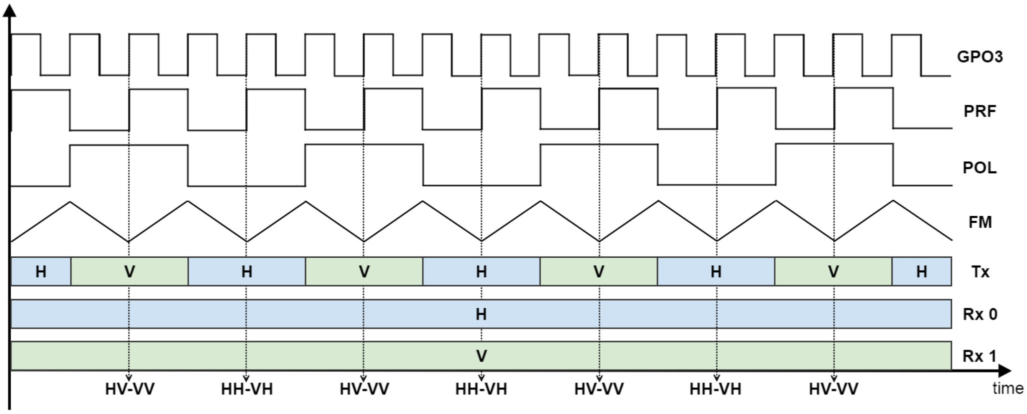

Figure 3.12: Diagram of the signal acquisition in the fully polarimetric case and OtF operation mode with the RISKSAR-X. Tx denotes the transmitting antenna, Rx 0 is the reception channel 0, Rx 1 is the reception channel 1, H denotes Horizontal and V Vertical

down-ramp of the triangular cosine chirp. The rising edge of the PRF is used to digitize the signal, coinciding with the start of the up-ramp of the FM signal. It has to be taken into account that only the positive ramp of the chirp is stored. The POL signal, whose frequency is half of the PRF, determines the commutation of the switch. As can be observed, the commutation coincides with the start of the down-ramp of the chirp, avoiding the fact of starting the acquisition when the switch changes its position. As the digitizer uses two different channels, when the polarization in transmission is vertical it acquires the HV polarization in channel 0 and VV polarization in channel 1. Thus, when the transmitted polarization is horizontal, channel 0 acquires the HH polarization and channel 1 the VH polarization.

3.2.3 Other modular elements in the receiver

During the system tuning, different elements of the receiving chain have been readjusted or modified to improve the RISKSAR-X performance. In the present subsection, a brief summary of the most important contributions during this process is exposed.

Previous versions of the system had the amplification, the down-conversion and the filtering of the received signal grouped in a compact module. This provoked the oscillation of some of the amplification elements, which resulted in the introduction of undesired tones and the apparition of interference in the focused images. Because of that, it has been decided to locate the Low Noise Amplifier (LNA) and the base-band amplifiers in separated modules, as shown in Figure 3.2. In this context, and taking into account the Friis' formula, the first element after the receiving antennas is the LNA. Moreover, three more amplifiers of 20 dB are located at different stages of the receiving chain. One after the LNA, another in base-band after the mixer and the last one after the low-pass filter. The total measured gain of every receiving chain is around 72.5 dB.

One of the designed modules in charge of performing the down-conversion to base-band frequency contains one ERA-3 amplifier, the compact I/Q MMIC mixer (HMC521LC4)

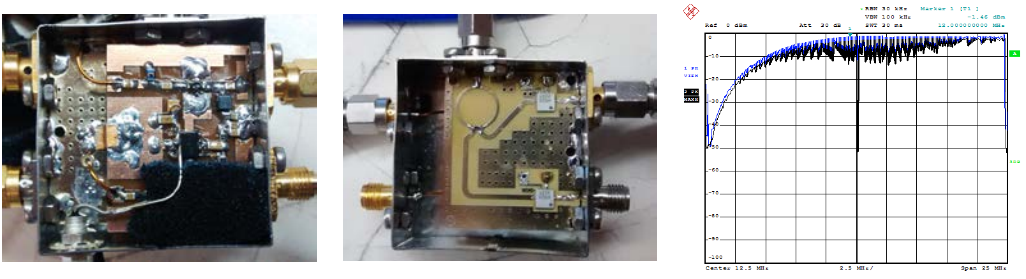

(a) (b) (c)

Figure 3.13: Prototype of the module performing the down-conversion to base-band frequency. (a) Amplifiers and high-pass filters. (b) Mixers HMC521LC4. (c) Measured response of the high-pass filter.

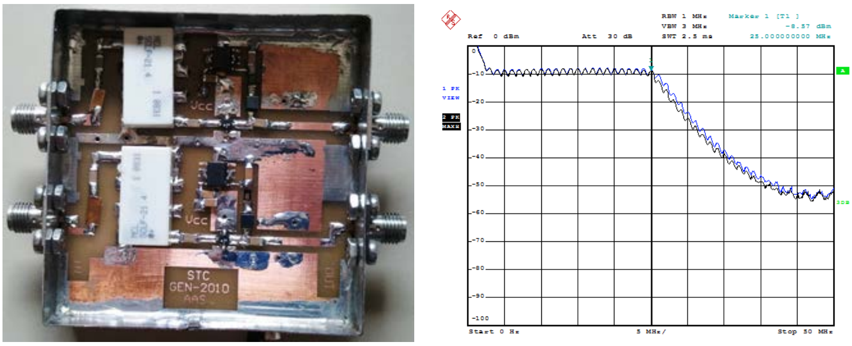

(a) (b)

Figure 3.14: Prototype of the module performing the low-pass filtering and amplification. (a) Low-pass filters and amplifiers. (b) Measured response of the low-pass filter.

from Analog Devices and the high pass RC filter. The complete module can be seen in Figure 3.13. The mixers, which conversion losses are of around 7.5 dB, must be provided of a good Local Oscillator (LO) to perform the down-conversion, in this case a sample of the transmitted signal. Much effort has been devoted to this module to have a good behavior of the mixers and to avoid the apparition of spurious because of the amplifiers. Furthermore, Figure 3.13 (c) shows the measured response of the high pass RC filter, whose cut-off frequency is around 12 MHz, which aims to penalize very close targets with high reflectivity.

The last module before the digitizer contains the low-pass RC filter and the last ERA-3 amplifier of the receiver chain, see Figure 3.14 (a). The cut-off frequency of the filter is approximately 25 MHz, as shown in Figure 3.14 (b).

3.3 RISKSAR-X raw data processing

With the purpose of obtaining high quality focused images from the stored raw data, some processing steps must be conducted. This subsection summarizes the main operations performed in the processing chain, from the raw data storing by means of the acquisition card to the final focused image, passing trough the range compression, the Residual Video Phase Error (RVPE) removal and the application of the Back Projection Algorithm (BPA).

The first step is the data storage and the raw data matrix decomposition, which depends on the selected acquisition card. It is important because the way in which the system stores the retrieved signal in the different operation modes will condition the phase center compensation when applying the BPA, as will be explained in Section 3.4. By means of Figure 3.12 it has been explained how the different polarizations are acquired in the fully polarimetric case and the OtF operation mode, which is one of the most important contributions to the RISKSAR-X sensor.

The digitizer acquires 8192 samples with a sampling frequency of 50 MHz every rising edge of the PRF, which corresponds with the positive slope of the triangular CW ramp signal. As in the previous version of the system, in the *S&G* operation mode and single polarization the resulting raw data matrix dimension is [8192,200], that is 8192 rows and 200 columns. In this case, the number of columns are the total positions were the sensor stops to perform the averaged measurement. Besides, if the systems is operated in the *S&G* operation mode and fully polarimetric case, the raw data matrix will have a dimension of [8192,800], as a matrix for every polarization is stored. On the contrary, for the OtF operation mode and single polarization, the resulting raw data matrix dimension is [8192,N_{chirp}], being N_{chirp} the number of transmitted chirp periods during the

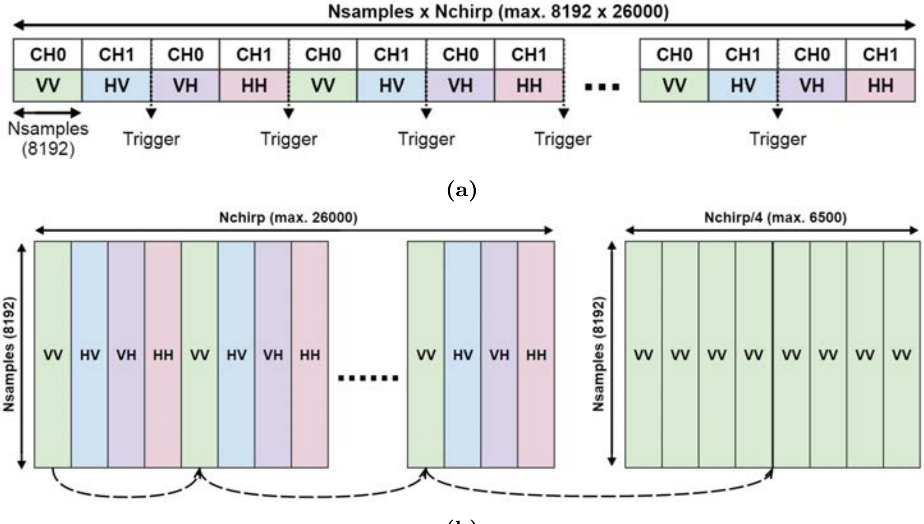

(a)

(b)

Figure 3.15: OtF operation mode and fully polarimatric case: (a) Diagram summarizing the data storage. (b) Exemplification of the raw data matrix generation.

acquisition. The maximum chirp pulses N_{chirp} allowed depend on the memory depth of the acquisition card, which in our system are 13000 chirp pulses per channel, 26000 in total. Thus, in the fully polarimetric case of the OtF operation mode, each polarization will have a maximum raw data matrix size of [8192,6500]. The exposed dimensions of the raw data matrices can give a general idea of the CPU requirements necessary to process the retrieved data.

To graphically exemplify how the data is stored in the OtF operation mode and fully polarimetic case, a simplified scheme of the digitizer performance is shown in Figure 3.15 (a). As can be seen, when a trigger arrives to the acquisition card it stores 8192 samples from channel 0 and consecutively 8192 from channel 1, generating a vector like that of the figure. An example of the matrix decomposition for the VV case is shown in Figure 3.15 (b).

Once the raw data matrices are generated, the first step is to apply the commonly known presuming technique. In the case of the RISKSAR-X sensor, the PRF is much higher than the Doppler bandwidth of the system, which means that the signal is over-sampled. In this case, this step can be considered as a filtering and a decimation in the cross-range frequency domain, which results in a reduction of the raw-data matrix dimension and, consequently, a decrease in the memory and CPU requirements to process the data [70]. This step is of great importance in the OtF operation mode since the stored raw data matrix is very large. In Figure 3.16, an example of presuming applied to a Single Polarimetric (SP) measurement performed in the OtF operation mode is shown. Figure 3.16 (a) shows the raw data matrix after applying the Fast Fourier Transform (FFT)

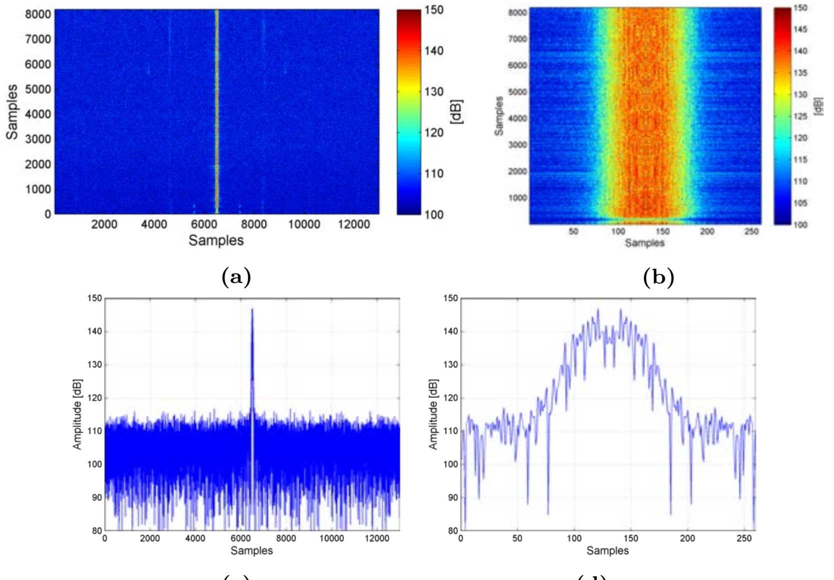

(a) (b)

(c) (d)

Figure 3.16: Example of presuming technique. Raw data matrix: (a) Before presuming. (b) After presuming. Cut along cross-range frequency domain: (c) Before presuming. (d) After presuming.

in the cross-range domain and shifting the zero-frequency component to the center of spectrum. As can be observed, the Doppler bandwidth of the received signal of interest is concentrated in few samples in comparison with the 13000 chirp pulses stored. Thereby, the rest of samples can be considered as noise and can be discarded. Figure 3.16 (b) shows the presumed matrix after selecting just 260 samples of the cross-range frequency domain, which is equivalent to perform a presuming of a factor 50. With this huge presuming the useful data is not altered, being able to perfectly focus the image in further steps managing a matrix of reduced dimensions.

Different techniques have been proposed in the literature for range-domain focusing processes. Probably, the most used one is the matched filter, which is the optimal solution for maximizing the Signal-to-Noise Ratio (SNR) in presence of additive stochastic noise [10]. An alternative approach, which is used by the RISKSAR-X sensor, is the deramping technique [24]. Basically, it consists in multiplying the conjugated received signal by the phase term of the transmitted one. The receiver unit takes advantage of the use of dechirp-on-receive technique to reduce its complexity [67]. It consists of two parallel low-noise chains with a direct zero-IF demodulator, where a sample of the transmitted signal is used as a local oscillator. This step is done at hardware level in the receiver chain of the RISKSAR-X sensor by means of the mixer. Thus, to obtain the range-compressed response from the illuminated scene, just the FFT in the range dimension of the raw data matrix has to be done. The use of the deramping process generates several phase terms that depend on the target's range distance. Moreover, the undesired phase term related with the RVPE, $e^{j(\frac{\alpha}{2}\tau_0(m)^2)}e^{-j(\omega+\alpha\tau_0(m))\tau_0(m)}$, also arise and must be removed. Its origin will be derived in detail in the mathematical description exposed in Chapter 4, Section 4.2 and can be seen in Equation 4.8. RVPE impacts SAR imagery because it varies over a coherent processing interval as the round-trip time delay changes [69].

The next step is to apply a zero-padding, which is performed to improve the reconstruction of the amplitude of the range-compressed signal and estimate more precisely the target's position. Theoretically, the higher the zero-padding factor, the lower the value of the quantification error ΔQ. Practically, negligible improvements have been observed

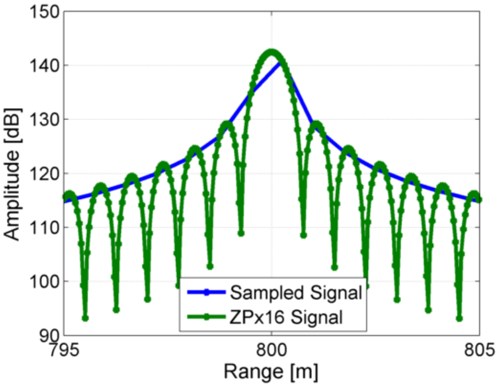

Figure 3.17: Backscattered signal of a simulated target at [0,800,0] m: Range-compressed (blue) and zero-padded x16 range compressed (green). The parameters of the simulated chirp are those of the RISKSAR-X sensor.

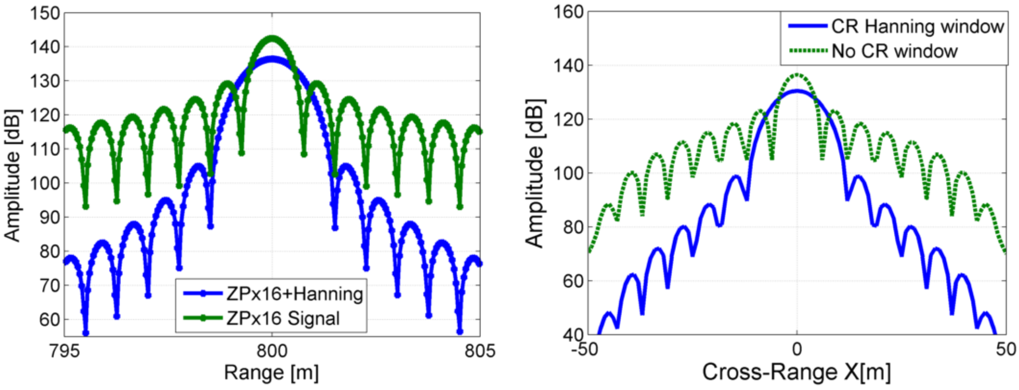

(a) **(b)**

Figure 3.18: (a) Backscattered signal of a simulated target at [0,800,0] m: Zero-padded x16 range compressed and range hanning window (blue) and zero-padded x16 range compressed (green). (b) Cut in azimuth of the target: Before (green) and after (blue) applying the cross-range Hanning window. The parameters of the simulated chirp are those of the RISKSAR-X sensor.

Table 3.3: Simulated azimuth resolution.

	Theoretical Δ_{az} [m]	**Simulated Δ_{az} [m]**
Target [0,800,0] m	8.95	8.96

for a zero-padding higher than 16, as it has been concluded in [69]. An example of the improvement with the zero-padding technique in the amplitude reconstruction can be appreciated in Figure 3.17 where a single target at [0,800,0] m has been simulated. By comparing the two signals in the image, it is noticeable that in the not zero-padded signal (blue line), the maximum of the amplitude does not correspond to the real position of the target. Thus, the improvement of the zero-padding technique in the reconstruction of the amplitude in the range-compressed signal is evident, where the obtained target's position is more accurate.

To reduce the secondary lobes that can degrade the quality of the focused image, a filter window is applied in the range time-domain signal and also in the cross-range domain. Several options can be found in the literature with different properties of the weighting functions [71], [72]. In our case, the Hanning window has been selected because it presents a good suppression of the secondary lobes without compromising excessively the resolution of the main lobe. The effects of applying the Hanning window to the range-compressed signal can be seen in the simulations of Figure 3.18 (a). Furthermore, Figure 3.18 (b) shows the effect of the Hanning window in the azimuth domain. As expected, in both cases the main beamwidth has been spread and the amplitude of the secondary lobes have been considerably reduced. Table 3.3 summarizes the theoretical and measured resolutions of the simulation after applying the cross-range Hanning window. It has to be considered that, in the GB-SAR system, the use of an aperture length shorter than the dimensions of the illuminated scenario implies that the azimuth resolution δ_{az} will

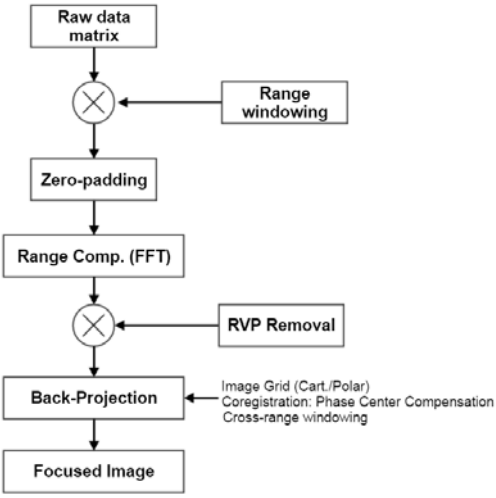

Figure 3.19: Processing scheme of the RISKSAR-X sensor.

depend on the range distance r_T, the length of the synthetic aperture L_{sa} and the squint angle θ as

$$\delta_{az} = \frac{\lambda r_T}{2Lcos^2(\theta)}. \tag{3.1}$$

According to Equation 3.1, the theoretical azimuth resolution of the simulated target located at [0,800,0] m after applying the cross-range Hanning window is 8.95 m. Moreover, the measured 3 dB azimuth resolution after applying the window is 8.96 m.

In order to focus the image, the RCM has to be considered. Basically, it has to be taken into account that the information of a given resolution cell is not contained in a single range line of the raw data matrix, but on an hyperbolic curve. This effect is introduced by the quadratic term $\frac{y_a^2(m)}{2R_{OS}(m)}$ that appears in Equation 4.5 in Chapter 4, Section 4.2. Moreover, it has to be taken into account that this curvatures depend on the range distance to each target, which means that different range positions of the targets have different curvatures. Thereby, this effect has to be included when focusing the image. Another thing that has to be considered when focusing the image is the phase center compensation in the fully polarimetric case, which will be analyzed in detail in Section 3.4.

The last step to obtain the focused image is the application of the BPA. Despite its high computational cost, it is suitable to perfectly focus the image correcting, inherently, the RCM. Besides, it has to be taken into account that the RISKSAR-X sensor works with areas of the image that are outside the SAR zone, since the synthetic aperture of 2 meters is very small and the covered area normally has an extension of 1.2 x $1.5Km^2$. In this sense, the BPA has been selected because it represents an optimal solution for this kind of situations. However, analyzing the focusing algorithm is not the objective of the present doctoral thesis, so for further information about the BPA the following literature may be considered [24], [73], [41], [40]. The whole processing chain of the RISKSAR-X sensor is summarized in the block diagram sketched in Figure 3.19.

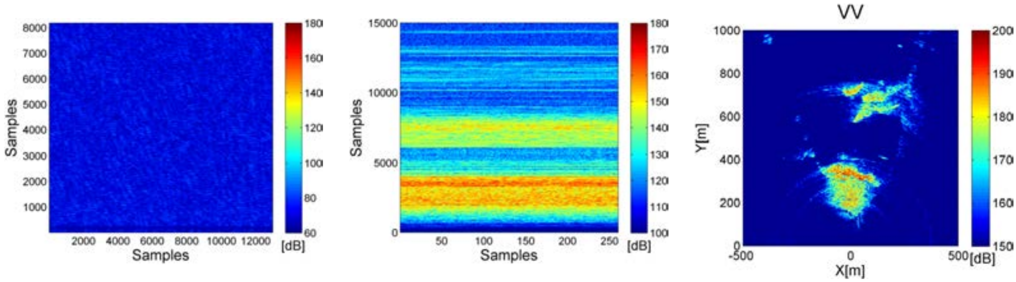

(a) (b) (c)

Figure 3.20: (a) Example of RISKSAR-X raw data amplitude in time domain. (b) After pressuming, x16 zero-padding and range-compression. (c) Example of RISKSAR-X raw data from Montserrat focused on Cartesian grid.

An example of the RISKSAR-X raw data and the amplitude of the presumed, x16 zero-padded and range-compressed data is shown in Figure 3.20 (a) and 3.20 (b), respectively. Finally, Figure 3.20 (c) shows the amplitude of the final focused image in Cartesian coordinates.

3.4 RISKSAR-X phase center compensation

In order to account for phase registration errors between different polarizations in the fully polarimetric case, some comments about the spatial location of the antennas, the data storage and the length of the cables used in the connections have to be addressed.

The location of the transmitting and receiving horn antennas in the radar front-end introduce a registration mismatch between the focused SAR images corresponding to the different polarizations. This registration error affects both the amplitude and phase of the processed data in the two operation modes of the system, *S&G* and OtF, and must be properly compensated. Figure 3.21 (a) shows a photograph of the RISKSAR-X front-end and Figure 3.21 (b) shows the corresponding layout representing the distance between the different antennas and the corresponding phase center of each polarimetric combination.

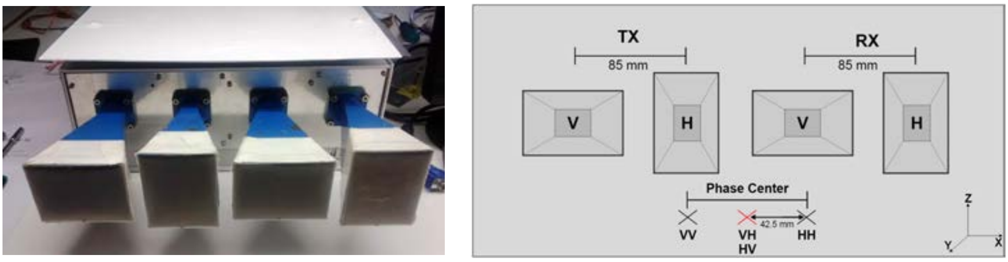

(a) (b)

Figure 3.21: (a) Photograph of the RISKSAR-X front-end. (b) Layout and spatial position of the antennas.

The compensation of the registration error due to the antenna location can be done during the cross-range focusing process taking into account the corresponding spatial separation between the antennas, which in the RISKSAR-X case is 85 mm between V and H polarizations (see Figure 3.21 (b)). The aim of such compensation is to refer the different polarimetric images to the same spatial position, avoiding any phase ramps between the different image combinations. To this purpose, the first step is to select a phase center as a reference, in our case the Cross-polarization Phase Center (CPC) position in the front-end layout, as can be seen marked with a red cross in Figure 3.21 (b). As its name already indicates, the CPC is the center of phase of the cross-polarized SAR images VH and HV. Then, the remaining phase centers VV and HH must be referred to the CPC. To do this, the difference of position has to be measured and introduced in the BPA formulation, concretely in the distance from the sensor to the scatterer. Consistently to Equation 2.2 of Chapter 2, the target's distance to the sensor can be defined in Cartesian coordinates as

$$r_{T_{CPC}}(t) = \sqrt{(x_T - x_a(t) + \Delta x_{CPC})^2 + y_T^2 + z_T^2} \tag{3.2}$$

where Δx_{CPC} is the spatial difference between the phase center taken as reference and the phase center corresponding to another combination of antennas. In the case of the RISKSAR-X sensor, Δx_{CPC} is -42.5 mm to compensate the VV polarization and +42.5 mm for the HH polarization. Another option to compensate this phase registration error is to multiply the resulting SAR image by a correction phase term that considers the antennas separation

$$\varphi_{CPC}(t) = e^{j\frac{4\pi}{\lambda}\Delta r_{CPC}} \tag{3.3}$$

where $\Delta r_{CPC} = r_{T_{CPC}}(t) - r_T(t)$, being $r_T(t)$ the distance from the sensor to the target without considering the term Δx_{CPC}, see Equation 2.2. This process can be done because the antenna difference is so small that does not implies any displacement of the pixels between images, i.e there is no important registration errors between the images. Thus, it can be considered that only the phase is affected.

Another source of registration error arises in the way in which the system stores the received data in the OtF operation mode. According to Figure 3.12 and Figure 3.15 (a), to complete a fully polarimetric measurement the digitizer needs two periods of the trigger. In the first trigger, for instance, the system stores the VV and HV polarizations and in the second one the VH and HH polarizations. As the platform has been moving during the acquisition, the position of the platform in the second trigger has been displaced a distance $T_{PRF} * velo_{antenna}$ with respect to the first one. This provokes a registration error that must be considered. However, in the case of the RISKSAR-X sensor this effect is negligible since the velocity of the moving platform is too slow, approximately 0.468 m/s, and the distance error is about 153.4 μm. Up to this point it has to be mentioned that there is also a Doppler component due to the velocity of the platform that is not taken into account, assuming that the received pulse is at the same position than the transmitted one. For higher velocities of the platform, as is the case of the ARBRES SAR system that will be presented in Chapter 5, the effect associated to the data storage could be noticeable. In this case, a cross-range phase ramp that must be compensated will appear between the different polarimetric combinations.

Finally, according to [69], the effect of the length of the cables from the feeding points to the switch in the transmitter must be analyzed, as well as the effect of the different

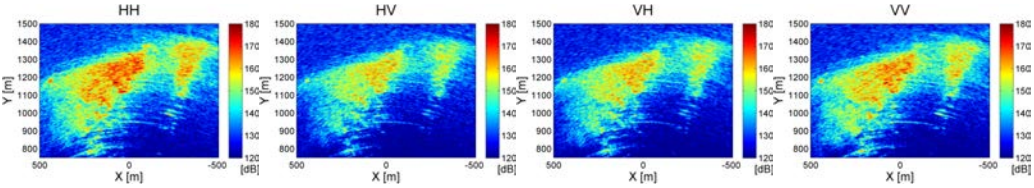

(a) **(b)** **(c)** **(d)**

Figure 3.22: Fully polarimetric measurement in Collserola test site. SLC images: (a) HH. (b) HV. (c) VH. (d) VV.

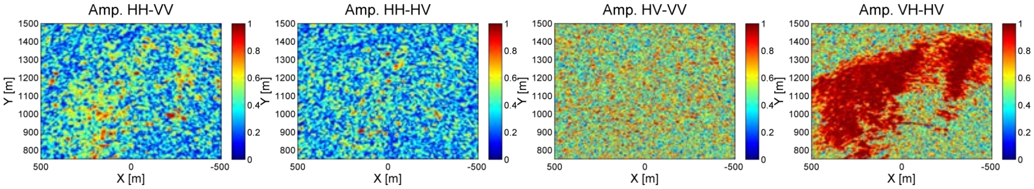

(a) **(b)** **(c)** **(d)**

Figure 3.23: Polarimetric correlation analysis. Coherence without any phase compensation (Multilook 15x15 m): (a) HH-VV. (b) HH-HV. (c) HV-VV. (d) VH-HV.

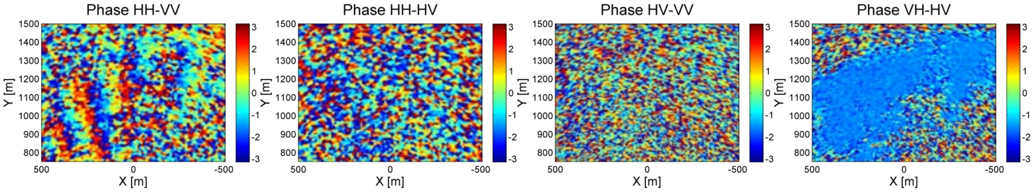

(a) **(b)** **(c)** **(d)**

Figure 3.24: Polarimetric correlation analysis. Phase difference without any phase compensation (Multilook 15x15 m): (a) HH-VV. (b) HH-HV. (c) HV-VV. (d) VH-HV.

lengths of the cables in the receiving chain. These effects are manifested as a phase ramp in the range direction and must be also compensated. To avoid it, a range correction function must be applied to each range profile in the time domain. Nonetheless, that problem is also negligible in the RISKSAR-X sensor, since the two transmitting and receiving channels are symmetric and the total length of the cables are almost the same.

To exemplify the effect in the phase of the commented registration errors a measurement campaign has been conducted in the Collserola test site, see Subsection 4.3.1. Figure 3.22 show the SLC images corresponding to the different polarizations. As expected, the area corresponding to the Collserola mountain present higher reflectivity values for the co-polar terms HH and VV. A trihedral corner reflector and different Polarimetric Active Radar Calibrator (PARC)s have been placed in the scenario to be used as references.

Figure 3.23 and 3.24 show the polarimetric correlation analysis of the coherence and the phase difference, respectively, for the HH-VV, HH-HV, HV-VV and VH-HV com-

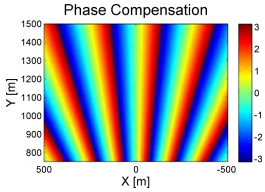

Figure 3.25: Simulation of the azimuth phase ramp introduced by an antennas separation of 85 mm.

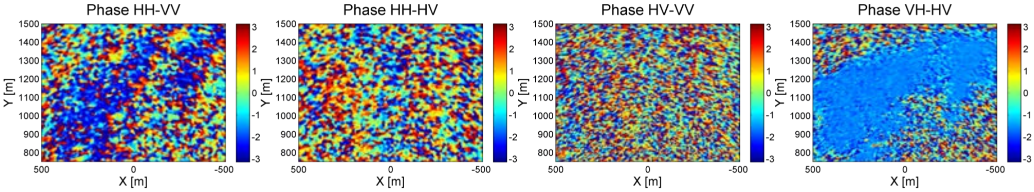

(a) (b) (c) (d)

Figure 3.26: Polarimetric correlation analysis. Phase difference compensating antenna position (Multilook 15x15 m): (a) HH-VV. (b) HH-HV. (c) HV-VV. (d) VH-HV.

binations prior any phase center compensation. Some comments might be done after analyzing the phase differences of Figure 3.24:

- **HH-VV** combination presents a phase ramp in the azimuth direction corresponding to the distance of 85 mm between H and V antennas. Figure 3.25 shows the simulated azimuth phase ramp considering this separation. Intuitively, it can be appreciated that the repetition of the simulated and measured azimuth phase patterns correspond to each other.
- **HH-HV** and **HV-VV** present a noisy phase distribution. Assuming reflection symmetry, which is a feasible acceptance when measuring distributed targets like the natural scenario of the image, one would not expect to find any phase pattern in these combinations [45].
- **VH-HV** presents a constant phase distribution in the area with high coherence corresponding to the vegetated area. Furthermore, it can be also concluded that there is not a phase ramp in the range direction associated to the length of the cables.

The effect of the misregistration due to the antenna separation has been compensated when applying the BPA, which can be appreciated in Figure 3.26 (a) were the cross-range phase ramp has disappeared.

3.5 RISKSAR-X polarimetric data calibration

Once the system has the capability to acquire fully polarimetric data, a calibration step is mandatory to extract reliable information from the polarimetric RISKSAR-X focused images. The calibration of the system is not under the scope of this dissertation, but some points are assessed here for completeness purposes, pointing out the first steps to polarimetrically calibrate the system in the future. In this context, the results presented in this section are very preliminary and must be improved. The methods applied here are based on the work presented in [69].

It is known that the transmission and reception channels of the radar system modify the scattering information of the illuminated area. A contrasted description of such process linearly relates the desired scattering matrix [S] of a target to the measured matrix [M] in the following way

$$[M] = \begin{bmatrix} M_{hh} & M_{hv} \\ M_{vh} & M_{vv} \end{bmatrix} = \begin{bmatrix} R_{hh} & R_{hv} \\ R_{vh} & R_{vv} \end{bmatrix} \begin{bmatrix} S_{hh} & S_{hv} \\ S_{vh} & S_{vv} \end{bmatrix} \begin{bmatrix} T_{hh} & T_{hv} \\ T_{vh} & T_{vv} \end{bmatrix} + [N] = [R][S][T] + [N] \tag{3.4}$$

where [N] accounts for the additive noise contribution and [R] and [T] consider the distortion introduced in each polarimetric channel by the receiver and the transmitter respectively [74]. Basically, any procedure used to calibrate polarimetrically the system aims at obtaining an estimation of [S] from inverting Equation 3.4, which proposes a system of 4 equations with 12 unknowns. Further equations are then needed to obtain the solution. To do this, three main approaches may be used [75]:

- Use man-made targets with known scattering matrices.
- Make assumptions regarding the general properties of the scatterers being measured.
- Make assumptions about the radar system parameter

Without entering into details, most techniques split the calibration problem into two steps: the cross-talk unbalance compensation and the radiometric calibration. In this sense, the correction of the cross-talk unbalance has been performed by using a strong cross-polar target present in the scenario, whereas the radiometric calibration has been carried out using a trihedral corner reflector. The use of PARCs has been excluded since they are an active element that does not fulfill the Reciprocity Theorem [74]. Moreover, its high sensitivity to alignment errors and the fluctuations in the signal amplification make this kind of calibrators unsuitable for long-time calibration purposes [76].

Regarding the specific case of the RISKSAR-X sensor it can be considered that, as the polarization purity of the horn antennas and the isolation between channels is good enough, the off-diagonal terms of [R] and [T] may be neglected

$$R_{hv} = R_{vh} = T_{hv} = T_{vh} = 0. \tag{3.5}$$

Accordingly, Equation 3.4 can be written in a vectorial form as

$$\begin{bmatrix} M_{hh} \\ M_{hv} \\ M_{vh} \\ M_{vv} \end{bmatrix} = \begin{bmatrix} R_{hh}T_{hh} & 0 & 0 & 0 \\ 0 & R_{hh}T_{vv} & 0 & 0 \\ 0 & 0 & R_{vv}T_{hh} & 0 \\ 0 & 0 & 0 & R_{vv}T_{vv} \end{bmatrix} \begin{bmatrix} S_{hh} \\ S_{hv} \\ S_{vh} \\ S_{vv} \end{bmatrix}. \tag{3.6}$$

Different measurements have been conducted in the Collserola test site, see Subsection 4.3.1 in Chapter 4, for calibration purposes, where different calibrators have been introduced in the scenario. The distinct elements are a trihedral corner reflector to perform the radiometric calibration and three different PARCs with different orientations to be used as references. One of the PARCs is oriented in horizontal position, another is tilted -45°

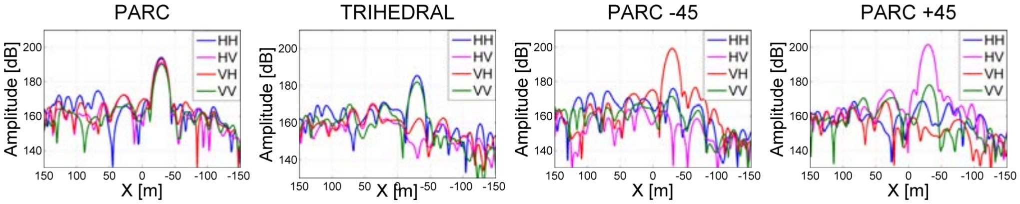

(a) **(b)** **(c)** **(d)**

Figure 3.27: Measured RCS with the uncalibrated RISKSAR-X of: (a) Horizontal PARC. (b) Trihedral. (c) PARC tilted -45°. (d) PARC tilted +45°.

with respect to the ground and the last one is tilted +45°. The trihedral corner reflector is expected to have identical horizontal and vertical backscattering sections, HH=VV, while no cross-polarizations components are generated, HV=VH=0. The PARC in horizontal position is expected to have cross-polarizations and co-polarizations components. The PARC tilted -45° is expected to have only the cross-polarization component VH and the PARC tilted +45° only the cross-polarization component HV. Equation 3.7 shows the theoretical scattering matrices of the calibrators and Figure 3.27 shows the measured uncalibrated Radar Cross Section (RCS) of the trihedral and the different PARCs.

$$\begin{aligned}
&S = \begin{pmatrix} S_{HH} & S_{HV} \\ S_{VH} & S_{VV} \end{pmatrix}; \\
&S_{PARCFP} = \begin{pmatrix} 1 & 1 \\ 1 & 1 \end{pmatrix}; \; S_{TRIHEDL} = \begin{pmatrix} 1 & 0 \\ 0 & 1 \end{pmatrix}; \\
&S_{PARC-45^\circ} = \begin{pmatrix} 0 & 0 \\ 1 & 0 \end{pmatrix}; \; S_{PARC+45^\circ} = \begin{pmatrix} 0 & 1 \\ 0 & 0 \end{pmatrix}.
\end{aligned} \tag{3.7}$$

As mentioned before, the usage of PARCs has been excluded for calibration purposes. The equality of the cross-polar channels can only be ensured when orientated at exactly 45° with respect to the line of sight of the target. Taking this into account, the measured uncalibrated scattering matrix of a different trihedral corner reflector is

$$S_{TRI_{Uncal}} = \begin{pmatrix} 1 & 0.75 \\ 0.87 & 0.98 \end{pmatrix}. \tag{3.8}$$

By means of one reference target with known scattering matrix such as the trihedral and a strong cross-polarized scatterer from the scenario, the linear equations in 3.6 can be solved by the polarimetric calibration technique proposed in [77]. Such technique is suitable to radar systems with good polarization isolation as is the case of the RISKSAR-X sensor. Figure 3.28 shows the polarimetric correlation after the system calibration. It can be appreciated in Figure 3.28 (b) and (d) that the residual phase is mostly zero (green) instead of the offset present in Figure 3.26 (a) and (d) (blue).

Moreover, the measured scattering matrix of the trihedral after this preliminary calibration is analyzed, obtaining

$$S_{TRI_{Cal}} = \begin{pmatrix} 1 & 0 \\ 0.06 & 1 \end{pmatrix}. \tag{3.9}$$

The comparison between the theoretical, the uncalibrated measured and the calibrated measured polarization signatures of the trihedral corner reflector is shown in Figure 3.29. As can be observed in Equation 3.9 and Figure 3.29, the measured scattering matrix and the polarization signature before the system calibration does not correspond to the theoretical ones. Nevertheless, after the calibration procedure they are very similar.

Figure 3.30 shows the evolution of the Red, Green and Blue (RGB) Pauli's composition of the images, ranging from the system without applying the CPC compensation to the system applying the first attempt of calibration. Figure 3.30 (a) shows the Pauli's composition before applying any CPC compensation. As can be observed, the azimuth phase ramp is appreciated alternating red and green lines and masking the results. Moreover, Figure 3.30 (b) shows the Pauli's image after compensating the phase centers. As can be observed, the azimuth pattern has been removed but the response of the agricul-

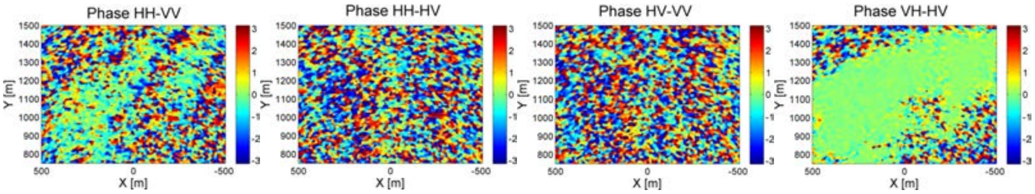

(a) (b) (c) (d)

Figure 3.28: Polarimetric correlation analysis after the system calibration. Phase difference compensating antenna position (Multilook 15x15 m): (a) HH-VV. (b) HH-HV. (c) HV-VV. (d) VH-HV.

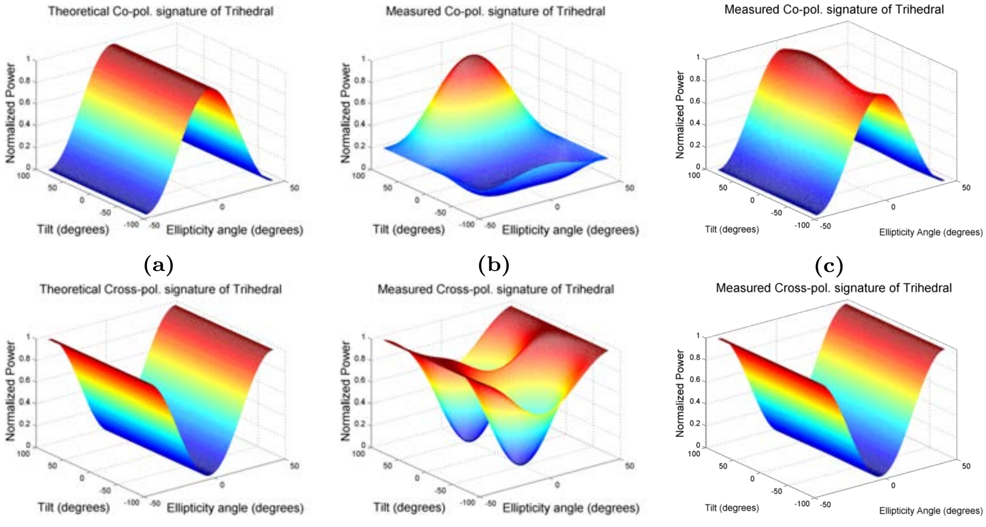

(a) (b) (c) (d) (e) (f)

Figure 3.29: Polarimetric signature of the trihedral. Theoretical (a) Co-polarimetric. (d) Cross-polarimetric. Measured before the calibration: (b) Co-polarimetric. (e) Cross-polarimetric. Measured after the calibration: (c) Co-polarimetric. (f) Cross-polarimetric.

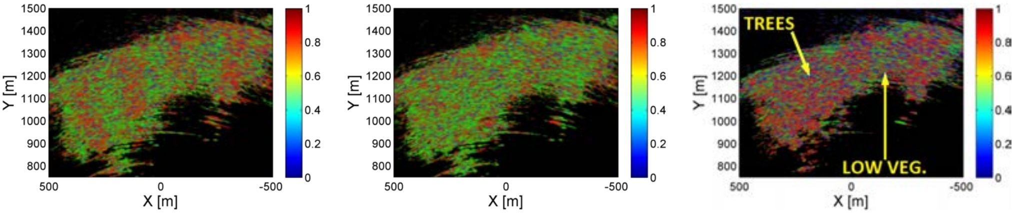

(a)

(b)

(c)

Figure 3.30: Pauli composition of the scenario using $|HH + VV|$, $|HH - VV|$ and $|HV|$ as red, green and blue, respectively. (a) No CPC compensation. (b) After compensating antenna location. (c) After preliminary calibration of the system.

Figure 3.31: Zoom to the vegetated area of the Collserola mountain.

tural field is mostly green, which is equivalent to a dihedral-like response (double-bounce). In the scenario, it can be identified two areas with different types of vegetation, one of them mainly composed by trees and the other by low vegetation, see Figure 3.31. In the calibrated Pauli's image of Figure 3.30 (c), these two areas can be identified in green and red, corresponding to double-bounce and single scattering, respectively.

It is worth noting again that the polarimetric calibration of the system is out of the scope of the present doctoral activity. Nevertheless, a first attempt of calibration of the RISKSAR-X sensor has been assessed with the sole intention to set the basis to thoroughly calibrate the system in the future. Taking this into account, the results presented in this section must be accurately analyzed and improved.

3.6 Concluding remarks

The RISKSAR-X system has accumulated nearly thirteen years of continued development. During the realization of this doctoral activity some hardware contributions have been conducted to the system with the aim of improving its performance and its capabilities. One of the main contributions is related with the way in which the transmitted signal is generated. Concretely, a PLL board has been designed and developed to optimize the signal generation and transmission to offer a higher degree of flexibility and adaptability to the system. An example of such versatility is the endowment to the system with the capability to operate in different operation modes and different polarizations.

Another distinctive element incorporated to the system is the solid-state switch that permits, together with the use of two symmetric reception channels, to acquire fully polarimetric data in the OtF operation mode. The solid-state switch united with the capability to acquire data in the OtF operation mode deserves special attention since it works analogously to the ARBRES-X SAR system that will be exposed in Chapters 5 and 6. Thus, the developments conducted to this GB-SAR sensor are directly applicable to the airborne sensor integrated in the UAV Multicopter Platform (MP).

On the other hand, the main steps necessary to process the raw-data obtained with the RISKSAR-X sensor have been summarized in this chapter. The way in which the system stores the data has been analyzed in order to decompose the raw data matrices corresponding to the different polarizations. The importance of the presuming technique and the zero-padding of the range-compressed signal has been evidenced, as well as the range and cross-range signal windowing.

The RISKSAR-X phase center compensation has been assessed, evaluating the intrinsic registration errors of the system. It has been concluded that the spatial separation between the antennas location must be compensated to avoid phase errors. Moreover, it has been observed that the phase miss-registration due to the data storage in the OtF operation mode is negligible since the velocity of the platform is too slow (on the order of 0.468 m/s). However, this phase error will be extremely important in the case of platforms moving at higher velocities, as the ARBRES-X SAR system where the velocity of the platform can be up to 25 m/s. Finally, the fact of having two symmetric receiving chains avoids the necessity to compensate for phase miss-registrations introduced by different lengths of the cables.

Since the system has good polarization isolation, a first attempt of calibration has been done applying the technique proposed in [77], obtaining first preliminary results. The intention of this process is just to set the basis to thoroughly calibrate the system in the future. In this context, a trihedral corner reflector and an strong cross-polarized target of the scenario have been used for calibration purposes. After the preliminary calibration, the measured response of the trihedral has been improved and is similar to the theoretical one.

During the course of this doctoral work, the RISKSAR-X sensor has been used in different measurement campaigns, as for instance, in the Collserola and Montserrat test site. This has been extremely useful to develop the prototypes and to validate the system performances to be able to obtain reliable results, such as the ones presented in Chapter 4.

4

Chapter 4

Impact of short term variable reflectivity scatterers on GB-SAR imagery

---

This chapter is intended to characterize the effect in the GB-SAR image reconstruction of moving scatterers that have a short term variable reflectivity during the scanning time. In scenarios where the area of interest contain or is surrounded by vegetation, this is normally related to the wind. During this chapter, it is evaluated the blurring effect, the decorrelation introduced in the SAR images and the degradation of the extracted parameters, such as the coherence maps. In order to validate the results, the study assesses different GB-SAR images obtained with the RISKSAR-X sensor developed in the UPC.
In the first part, it is provided a brief introduction to the defocusing problem in the GB-SAR images and their causes. The second section is intended to derive a mathematical description of the cross-range focusing process in GB-SAR. In the third section, the experimental results are presented and a general description of the test site and the data set employed in this study is given. The main conclusions and major remarks of the chapter are exposed in the last section. [a]

---

[a] The following sections contain portions, sometimes verbatim, of the author's publication [JA3].

4.1 Introduction

Data retrieved from Orbital SARs has been used during the last decades to monitor deformation episodes in large-scale areas of observation by means of Differential SAR Interferometry (DInSAR) [12], [13]. An alternative strategy to monitor small-scale areas is based on GB-SARs, which are increasingly being used as Early Warning systems [78], [79]. The main differences between GB-SARs and classical Orbital or Airborne SARs are the way in which the aperture is synthesized, the transmitted signal waveform and its power. In GB-SARs, the radar sensor is placed on a mechanical platform of linear displacement, transmitting a triangular Frequency Modulated Continuous Wave (FMCW) signal of few watts of output power. Despite its flexibility in terms of rapid deployment and easy operability some limitations have to be considered, as the reduced length of the aperture that could degrade the cross-range resolution or the long scanning time. High rate SLFM-CW GB-SAR sensors are capable to perform faster scans, reducing the scanning time in the order of seconds. This reduction has led to important improvements in GB-SAR performances for the monitoring of surface deformations by means of coherence maps analysis and Persistent Scatterer Interferometry (PSI). An example of such systems is the experimental polarimetric RISKSAR-X sensor developed by the UPC. Even though the scanning time has been reduced, it is still long enough to take into account the reflectivity changes in the scenario during the scan time. These changes are related to atmospheric phenomena, as wind, that may modify the reflectivity of the scenario in short periods of time, especially if the observed area contains or is surrounded by vegetation [80]. As a result, the quality of the focused images and the extracted parameters are degraded. Some examples of studies performed with GB-SARs in this type of scenarios can be found in the literature [78], [81], [82], [83], [84].

The purpose of the present Chapter is to identify and to understand the phenomena that may reduce the GB-SAR system performances by evaluating the retrieved data, such as coherence and interferometric phase maps. In order to do so, different measurements with the OtF and *S&G* operation modes will be presented, analyzing the importance of the scanning time in SAR measurements. As mentioned in Chapter 3, the two operation modes can be programmed to have the same observation times and transmitted energy, but the scanning time is higher in the *S&G* mode. Besides, it is intended to provide a mathematical description of the image blurring by means of the study of the cross-range focusing. The study presented in the chapter takes into account the limited aperture length and the time to perform an acquisition by the GB-SAR. Some of the conclusions presented could be directly applicable to other types of SAR systems, either airborne or orbital.

4.2 Mathematical description of the cross-range blurring effect and the reduction of coherence

To understand and to quantify the effect in the image reconstruction process of having vegetation with short term variable reflectivity surrounding the area of interest, the mathematics of the cross-range focusing process have been reformulated. The simplified expression of the transmitted signal in a SAR system working with FMCW chirp signals is

$$s_T(t) = a(t)e^{j(\omega_0 t + \frac{1}{2}\alpha t^2)} \tag{4.1}$$

where $\omega_0 = 2\pi f_0$, being f_0 the center frequency, α is the signal chirp rate and t is the rapid time related with the propagation of the signal. The rectangular function $a(t)$ can be expressed as

$$a(t) = \prod((t - T_p/2)/T_p) \tag{4.2}$$

where $a(t) = 1$ for $0 \leq t \leq T_p$ and zero otherwise and T_p is the chirp duration. The complex reflectivity function Γ describing the scenario depicted in Figure 4.1, where a single scatterer is considered, can be written as

$$\Gamma(t, m) = \sigma(m)e^{j\phi(m)}\delta(t - \tau_0(m)). \tag{4.3}$$

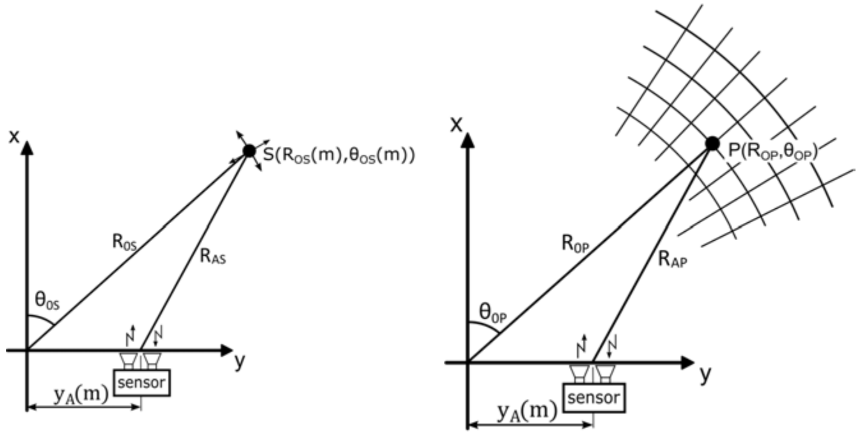

(a)

(b)

Figure 4.1: Geometry in polar coordinates where the GB-SAR position is $y_A(m)$. (a) The scatterer is located at $(R_{OS}(m), \theta_{OS}(m))$. (b) The pixel associated to the scatterer is (R_{OP}, θ_{OP}).

Notice that in this particular definition of the imaging geometry, the sensor is moving along the Y axis. In OtF mode operation, m corresponds to the transmitted chirp period number. The complex reflectivity of the scatterer is $\sigma(m)e^{j\phi(m)}$ and $\tau_0(m)$ is the round trip delay from every antenna position $y_A(m)$ along the aperture to the scatterer. The antenna position is defined as $y_A(m) = v \cdot t = v \cdot T_{PRF} \cdot m$, where v is the speed of the linear unit and the slow time $t = T_{PRF} \cdot m$. The slow time t is related with the mechanical movement of the platform and is a function of m and the PRF. In case of *S&G* operation mode, T_{PRF} and v have to be readjusted to an equivalent longer T_{PRFeq} and slower v_{eq}, that takes into account the temporal averaging and the slower motion velocity. The normalized received signal from the illuminated scenario can be expressed as the convolution between Equation 4.1 and Equation 4.3, $s_T * \Gamma(t, m)$, as follows

$$s_R(t, m) = \sigma(m)e^{j\phi(m)}a(t - \tau_0(m))e^{j(\omega_0(t-\tau_0(m)) + \frac{\alpha}{2}(t-\tau_0(m))^2)}. \tag{4.4}$$

The transmitter and receiver are moving along the y axis as shown in Figure 4.1. The round trip delay $\tau_0(m)$ can be expressed as

$$\begin{aligned}
\tau_0(m) &= \frac{2R_{OS}(m)}{c}\sqrt{1+\frac{y_a^2(m)-2R_{OS}(m)\cdot y_A(m)\cdot sin(\theta_{OS}(m))}{R_{OS}^2(m)}} \\
&\approx \frac{2}{c}\left(R_{OS}(m)+\frac{y_a^2(m)}{2R_{OS}(m)}-y_A(m)\cdot sin(\theta_{OS}(m))\right) \qquad (4.5)
\end{aligned}$$

where the scatterer position $(R_{OS}(m), \theta_{OS}(m))$ can be defined as

$$\begin{aligned}
R_{OS}(m) &= \hat{R}_{OS}+\Delta R_{OS}(m) \\
\theta_{OS}(m) &= \hat{\theta}_{OS}+\Delta\theta_{OS}(m) \qquad (4.6)
\end{aligned}$$

where $(\hat{R}_{OS}, \hat{\theta}_{OS})$ is the nominal position of the scatterer and $\Delta R_{OS}(m)$ and $\Delta\theta_{OS}(m)$ are the variation in the position of the scatterer during the slow time t. Note that the quadratic term $\frac{y_a^2(m)}{2R_{OS}(m)}$ in Equation 4.5 is responsible of the range dependent hyperbolic curve corresponding to the RCM mentioned in Chapter 3, Section 3.3.

As mentioned in Chapter 3, in a dechirp-on-receive system the received and transmitted signals are directly mixed. This technique notably reduces the required baseband signal sampling rate [85]. The mixing process generates a Zero IF frequency signal that is low pass filtered

$$s_{IF}(t,m)=\frac{1}{2}\sigma(m)e^{j\phi(m)}a(t-\tau_0(m))e^{j(-\alpha t\tau_0(m)-\omega_0\tau_0(m)+\frac{\alpha}{2}\tau_0^2(m))}. \qquad (4.7)$$

Notice that the dependence with the transmitted power, antenna gain, receiver power gain and propagation losses are not included for simplicity. The range compressed version of the received signal is the Fourier transform of s_{IF} in rapid time

$$\begin{aligned}
S_{IF}(\omega,m) &= \mathcal{F}(s_{IF}(t,m))=\frac{1}{4}\sigma(m)e^{j\phi(m)} \\
&\quad e^{j(-\omega_0\tau_0(m)+\frac{\alpha}{2}\tau_0(m)^2)}e^{-j(\omega+\alpha\tau_0(m))\tau_0(m)}A(\omega+\alpha\tau_0(m)) \qquad (4.8)
\end{aligned}$$

where $A(\omega)$ is the Fourier transform of $a(t)$

$$A(\omega)=T_P sinc(\frac{T_p}{2}\omega)e^{-j\omega\frac{T_p}{2}}. \qquad (4.9)$$

If it is assumed that the energy is mainly around the maximum in the point spread function, which can be expressed as $\omega=-\alpha\tau_0(m)$, the term $e^{-j(\omega+\alpha\tau_0(m))\tau_0(m)}$ in Equation 4.8 can be neglected. After the range compression, the cross-range image reconstruction is performed by means of the BPA. Any pixel $p(R,\theta)$ of the image is reconstructed as follows

$$p(R,\theta)=\sum_{m=0}^{M-1}S_{IF}(\omega,m)e^{j(\omega_0\tau_p(m)-\frac{\alpha}{2}\tau_p^2(m))} \qquad (4.10)$$

where ω is a function of R_{OS}, $\tau_p(m)$ is the round trip delay from every antenna position $y_a(m)$ to the pixel at (R,θ) and M is the total number of antenna positions or transmitted chirp periods along the aperture. The round trip delay $\tau_p(m)$ is derived in the same way that $\tau_0(m)$ but depending on the position of the pixel. Indeed, Equation 4.10 corresponds to the matched filter for a given pixel at (R,θ), i.e., the convolution of the received signal with the complex conjugated of the expected response for a given pixel. The expression of the $p(R,\theta)$ function can be employed to find the equivalent cross-range response of the GB-SAR. Assuming that there is only one scatterer located at (R_{OS},θ_{OS}), the reconstructed pixel $p(R_{OP},\theta)$ along the θ axis can be evaluated

$$p(R_{OP},\theta) \cong K\sum_{m=0}^{M-1}\sigma(m)e^{j\phi(m)}e^{j\omega_0(\tau_0(m)-\tau_p(m))} \tag{4.11}$$

where the terms $e^{(j\frac{\alpha}{2}\tau_0^2(m))}$ and $e^{(-j\frac{\alpha}{2}\tau_p^2(m))}$, which are related with the Residual Video Phase Error (RVPE), have not been included because their contribution to the reconstruction of p is negligible. It has been assumed that $K=\frac{1}{4}A(\omega+\alpha\tau_0(m))$ is constant during the evaluated scanning time. This is equivalent to assume no RCM in the cross-range dimension, which is a feasible approximation if the total aperture length is a fraction of the scatterer range. The reconstructed pixel in Equation 4.11 can be expressed as

$$\begin{aligned} p(R_{OP},\theta) \quad \cong \quad & \sum_{m=0}^{M-1}K\sigma(m)e^{j\phi(m)}e^{j\frac{4\pi}{\lambda}(R_{OS}(m)-R_{OP})}e^{j\frac{4\pi y_a^2(m)}{\lambda}(\frac{1}{R_{OS}(m)}-\frac{1}{R_{OP}})} \\ & e^{j\frac{4\pi y_A(m)}{\lambda}(sin\theta-sin\theta_{0S}(m))}. \end{aligned} \tag{4.12}$$

Assuming that the pixels under study are at the same range as the scatterer $R_{OP}=\hat{R}_{OS}$, the expression of Equation 4.12 can be rewritten as

$$\begin{aligned} p(\hat{R}_{OS},\theta) \quad \cong \quad & \sum_{m=0}^{M-1}K\sigma(m)e^{j\phi(m)}e^{j\frac{4\pi}{\lambda}\Delta R_{OS}(m)}e^{j\frac{4\pi y_a^2(m)}{\lambda}(\frac{1}{\hat{R}_{OS}(m)+\Delta R_{OS}(m)}-\frac{1}{R_{OP}})} \\ & e^{j\frac{4\pi y_a(m)}{\lambda}(sin\theta-sin\theta_{0S}(m))} \end{aligned} \tag{4.13}$$

where the term $\frac{1}{\hat{R}_{OS}(m)+\Delta R_{OS}(m)}$ can be expressed as

$$\begin{aligned} \frac{1}{\hat{R}_{OS}(m)+\Delta R_{OS}(m)} \quad &= \quad \frac{1}{\hat{R}_{OS}}\left(\frac{1}{1+\frac{\Delta R_{OS}(m)}{\hat{R}_{OS}}}\right) \cong \frac{1}{\hat{R}_{OS}}\left(1-\frac{\Delta R_{OS}(m)}{\hat{R}_{OS}}\right) \\ &= \quad \frac{1}{\hat{R}_{OS}}-\frac{\Delta R_{OS}(m)}{\hat{R}_{OS}^2}. \end{aligned} \tag{4.14}$$

Substituting Equation 4.14 into 4.13 and assuming that $\hat{R}_{OS}^2 \gg \Delta R_{OS}(m)$, yields the simplified expression

$$p(\hat{R}_{OS},\theta) \cong \sum_{m=0}^{M-1}K\sigma(m)e^{j\phi(m)}e^{j\frac{4\pi}{\lambda}\Delta R_{OS}(m)}e^{j\frac{4\pi y_A(m)}{\lambda}(sin\theta-sin\theta_{0S}(m))}. \tag{4.15}$$

Taking into account that for long $\hat{R}_{OS}$ the equivalent angle variation of the scatterer position $\Delta\theta_{OS}(m)$ is negligible, the expression of Equation 4.15 can be considered as follows

$$p(\hat{R}_{OS}, \theta) \cong \sum_{m=0}^{M-1} K\sigma(m) e^{j\phi(m)} e^{j\frac{4\pi}{\lambda}\Delta R_{OS}(m)} e^{j\frac{4\pi y_A(m)}{\lambda}(sin\theta - sin\hat{\theta}_{0S})}. \tag{4.16}$$

Defining $G(m) = K\sigma(m)e^{j\phi(m)}e^{(j\frac{4\pi}{\lambda}\Delta R_{OS}(m))}$ and considering the total length of the aperture $L_{sa} = M \cdot T_{PRF} \cdot v$, Equation 4.16 can be rewritten as

$$p(\hat{R}_{OS}, \theta) \cong \sum_{m=0}^{M-1} G(m) e^{j\frac{4\pi \cdot m \cdot L_{sa}}{\lambda \cdot M}(sin\theta - sin\hat{\theta}_{0S})}. \tag{4.17}$$

Assuming a new polar coordinate system, the following two variables can be defined

$$\begin{aligned} \beta_{OS} &\cong \frac{2L}{\lambda} sin\hat{\theta}_{OS} \\ \beta &= \frac{2L}{\lambda} sin\theta \end{aligned} \tag{4.18}$$

where the β coordinate is a sinusoidal function of the polar angle θ. Applying the new polar coordinate system, the reconstructed pixel is

$$p(\hat{R}_{OS}, \beta) \cong \sum_{m=0}^{M-1} G(m) e^{j\frac{2\pi \cdot m}{M}(\beta - \beta_{OS})} \tag{4.19}$$

where the pixel reconstruction along the equivalent β axis in Equation 4.19 has an equivalent expression of a Discrete Fourier Transform (DFT) of the sequence $G(m)$. In case of having multiple scatterers at the same range R and different β_{OSn}, the expression of Equation 4.19 can be rewritten as

$$p(\hat{R}_{OS}, \beta) \cong \sum_{m=0}^{M-1} \sum_{n=0}^{N-1} G_n(m) e^{j\frac{2\pi \cdot m}{M}(\beta - \beta_{OSn})} \tag{4.20}$$

where N is the total number of scatterers at different angles (different β_{OSn}). In case of having an stable scatterer, $G(m) = constant$, the cross-range response along the β axis is a *sinc* function and its extension depends on the ratio λ/L_{sa}. As expected, the cross-range resolution of a GB-SAR depends on the length of the aperture. On the other hand, a moving scatterer means that $G(m) \neq constant$ and, as it will be demonstrated mathematically and experimentally in the present section and Section 4.3, respectively, it implies image blurring and decorrelation between images due to the movement of the vegetation.

4.2.1 Image blurring characterization

Starting from the mathematical description developed previously, the present subsection studies the blurring effect in the retrieved SAR images. The simulations presented in Figure 4.2 are intended to provide a graphic illustration of the effect that produces in the Single Look Complex (SLC) images the fact of having moving scatterers with variable complex reflectivity during the acquisition time. As will be shown, the neighbouring cells of a moving scatterer may be altered depending on its motion, which could be analogous

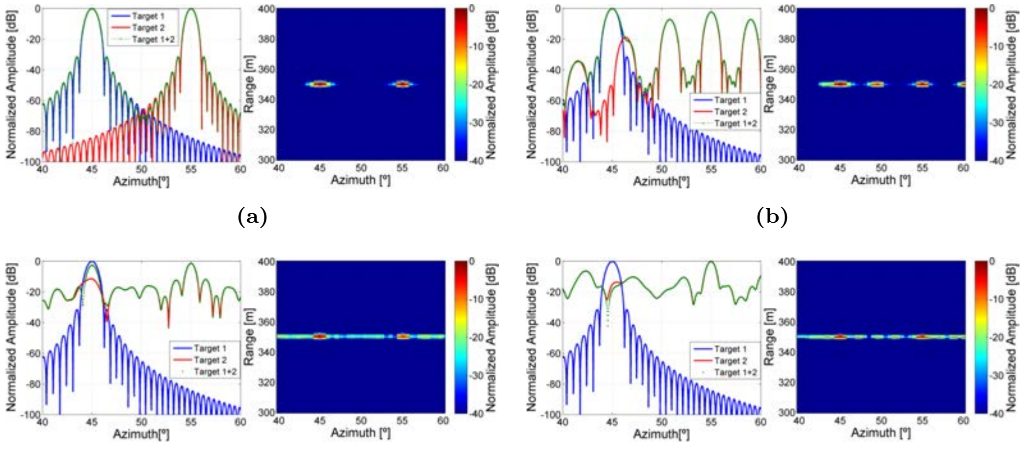

(a) (b)

(c) (d)

Figure 4.2: Two simulated targets. Left: cut of the targets in Polar coordinates. Right: SLC images obtained with BPA in Polar coordinates. Scatterer 1 is a static target and scatterer 2 is a (a) static target, (b) target with a sinusoidal motion, (c) target with a random motion in range and (d) distributed target inside the resolution cell modeled as a stochastic process.

to have vegetation around the area of interest altering the pixels under study. Taking advantage of the similarity of the pixel reconstruction to a DFT, the qualitative effect of a moving scatterer in slow time can be studied by means of the mathematical description presented in this section. Figure 4.2 (a) shows the simulation along the β axis of Equation 4.20, where two static scatterers are located at $\hat{\theta}_{OS1} = 45°$ and $\hat{\theta}_{OS2} = 55°$. As expected, two sinc functions are obtained. Thus, for this particular case, the reconstructed pixel in Equation 4.20 can be expressed as

$$\begin{aligned} p(\hat{R}_{OS}, \beta) &\cong \sum_{m=0}^{M-1} G_{perm1}(m) e^{j\frac{2\pi \cdot m}{M}(\beta - \beta_{OSperm1})} + \sum_{m=0}^{M-1} G_{perm2}(m) e^{j\frac{2\pi \cdot m}{M}(\beta - \beta_{OSperm2})} \\ &= sinc(\beta - \beta_{OSperm1}) + sinc(\beta - \beta_{OSperm2}) \end{aligned} \tag{4.21}$$

where $G_{perm1}(m)$ and $G_{perm2}(m)$ are constant during the aperture, generating the two *sinc* functions centered at $\beta_{OSperm1}$ and $\beta_{OSperm2}$, respectively. In another way, it is particularly interesting the case of considering one scatterer that presents a short oscillating periodic movement in the range direction. The recovered complex reflectivity of the associated pixel, and also the reflectivity of neighbouring pixels, will be affected in amplitude and phase. Figure 4.2 (b) shows the result of two simulated scatterers; Scatterer 1 is a static target while Scatterer 2 presents a sinusoidal motion in range with a period shorter than the total time of the acquisition. The phase $e^{j\phi_{periodic}(m)}$ of the complex reflectivity of Scatterer 2 has been modelled as a sinusoidal function. It can be observed, as it was pointed in [86], that this range motion has an equivalent phase modulation in the complex reflectivity that introduces replicas along the β axis. This causes the appearance of non-existing scatterers (ghost scatterers) in the SLC image. Since the reflectivity map is changed due to the apparition of ghost scatterers, which depends on the periodic movement of the scatterer during the acquisition time, the coherence maps may be modified. In practice, this may provoke an alteration in the number of coherent pixels. In this case, Equation 4.20 can be rewritten as

$$\begin{aligned} p(\hat{R}_{OS},\beta) &\cong \sum_{m=0}^{M-1} G_{perm}(m)e^{j\frac{2\pi\cdot m}{M}(\beta-\beta_{OSperm})} + \sum_{m=0}^{M-1} G_{periodic}(m)e^{j\frac{2\pi\cdot m}{M}(\beta-\beta_{OSperiodic})} \\ &= sinc(\beta-\beta_{OSperm}) + is(\beta-\beta_{OSperiodic}) \end{aligned} \quad (4.22)$$

where the term $G_{perm}(m)$ is constant during the aperture while the term $G_{periodic}(m) = K_{periodic}\sigma_{periodic}(m)e^{j\phi_{periodic}(m)}e^{j\frac{4\pi}{\lambda}\Delta R_{OSperiodic}(m)}$ varies with the movement of Scatterer 2. Thus, the reconstruction of a pixel associated to a scatterer can be expressed as the sum of the response of the desired scatterer and an interference signal $is(\beta-\beta_{OSperiodic})$, which is the result of a phase modulation in the frequency domain that introduces spatial replicas in the SLC image. The separation of the replicas depends on the periodic movement of the target during the acquisition time.

In contrast, in case of non-periodic motion of the scatterers, the complex reflectivity of moving scatterers in a resolution cell can be modelled as a Brownian motion affecting to its amplitude and phase [87]. Nevertheless, if the scatterer presents a stochastic motion during slow time t, the amplitude and phase of the reflectivity $\sigma(m)e^{j\phi(m)}$ will be modified, not only affecting the resolution cell but also the neighbouring cells at the same equivalent range. This means that the fact that neighbouring cells are affected may introduce a blurring effect in the cross-range direction. Figure 4.2 (c) shows two simulated scatterers; Scatterer 1 is a static target while Scatterer 2 presents a random motion in slow time and its complex reflectivity $\sigma_{random}(m)e^{j\phi_{random}(m)}$ has been modeled as a stochastic process. The energy tails of Scatterer 2 have been increased because of its inherent stochastic motion. This causes the blurring effect in the cross-range of the SLC images due to the dispersion of the energy along the β axis. It is equivalent to the effect of defocusing and blurring in SAR images for scenarios with oceanic waves [88]. This effect is only present in the cross-range direction because the Doppler bandwidth of the system is on the order of tens of Hz, which is comparable to the frequency spreading of the energy of moving scatterers. On the contrary, the increment in frequency that justifies a change of cell in the range direction is on the order of tens of KHz, which is too high compared to the frequency spreading of the energy of moving scatterers. Besides, as the observed reflectivity is the sum of the contributions of all the scatterers (in this case Scatterer 1 and Scatterer 2), the energy dispersion implies that adjacent cells in the same range, although being associated to static scatterers, will show a variable reflectivity between images. It can be appreciated in the simulation of Figure 4.2 (c), where a reduction in the main lobe of the static scatterer is observed by comparing the blue and the green lines. Consequently, a decorrelation between images arises and degradation in the coherence maps between consecutive images can be observed. For the case of having a permanent scatterer and a scatterer that moves randomly, Equation 4.20 can be expressed as

$$\begin{aligned} p(\hat{R}_{OS},\beta) &\cong \sum_{m=0}^{M-1} G_{perm}(m)e^{j\frac{2\pi\cdot m}{M}(\beta-\beta_{OSperm})} + \sum_{m=0}^{M-1} G_{random}(m)e^{j\frac{2\pi\cdot m}{M}(\beta-\beta_{OSrandom})} \\ &= sinc(\beta-\beta_{OSperm}) + is(\beta-\beta_{OSrandom}) \end{aligned} \quad (4.23)$$

where $G_{random}(m) = K_{random}\sigma_{random}(m)e^{j\phi_{random}(m)}e^{j\frac{4\pi}{\lambda}\Delta R_{OSrandom}(m)}$ varies during the aperture, generating the uncorrelated interference signal $is(\beta - \beta_{OSrandom})$ along the β axis, which is related with the cross-range frequency spreading.

Finally, Figure 4.2 (d) shows the case in which Scatterer 2 is a distributed target, consisting of different elements inside the resolution cell that move randomly during the acquisition time. This is analogous to the example shown in Figure 4.2 (c) and Equation 4.23, where the amplitude and phase of the reflectivity $\sigma_{random}(m)e^{j\phi_{random(m)}}$ is modeled stochastically, but in this case the complex reflectivity is modeled as the sum of the complex reflectivities of the different elements inside the resolution cell

$$\begin{aligned} p(\hat{R}_{OS},\beta) &\cong \sum_{m=0}^{M-1} G_{perm}(m)e^{j\frac{2\pi\cdot m}{M}(\beta-\beta_{OSperm})} + \sum_{k=0}^{K-1}\sum_{m=0}^{M-1} G_{random}(m)e^{j\frac{2\pi\cdot m}{M}(\beta-\beta_{OSrandom})} \\ &= sinc(\beta - \beta_{OSperm}) + \sum_{k=0}^{K-1} is(\beta - \beta_{OSrandom}) \end{aligned} \tag{4.24}$$

where K is the number of elements in the resolution cell that conform the distributed scatterer.

4.2.2 Image decorrelation characterization

The decorrelation between images, which is introduced by the fact of having a short term variable reflectivity during the acquisition time, is analyzed in this section by means of the complex coherence. The complex coherence is defined as the correlation coefficient of two SAR images S_1 and S_2 [89]

$$\gamma = \frac{E\{S_1 S_2^*\}}{\sqrt{E\{|S_1|^2\}E\{|S_2|^2\}}} \tag{4.25}$$

where $E\{x\}$ is the mathematical expectation of x and $*$ is the complex conjugate. The magnitude of Equation 4.25, $|\gamma|$, is called coherence and its argument is the effective phase difference between reflectivity maps. The simplified expression for the differential interferometric coherence has to include a new term, γ_{blur} , to take into account the blurring effect

$$\gamma = \gamma_t \gamma_{th} \gamma_{other} \gamma_{blur}. \tag{4.26}$$

The term γ_{other} takes into account other decorrelation factors as exposed in [90] and γ_t considers the changes in the backscattered signal due to different instants of measurement. The thermal noise contribution γ_{th} depends on the SNR and γ_{blur} accounts for the cross-range image blurring. As γ_{th} is negligible because of the high power transmitted and the reduced dimensions of the illuminated scene [91], the degradation of the coherence γ can be related to the temporal decorrelation occurred between different acquisitions and the blurring effect in the cross-range direction during the scanning time. It can be assumed that the scenario has not changed during the short period of time between measurements, which means that there is no temporal decorrelation between images. Thus, the blurring effect γ_{blur} is in our case the main responsible of the decorrelation between images and the largest contributor to the degradation of the coherence. This term, in contrast with γ_t, shows a correlation with the wind conditions. Besides, as it is seen in Figure 4.2 and assessed from Equation 4.20, the effect of energy spreading along the cross-range axis can be considered as an interference signal. In this case, the correlation between the response of two signals $z_1 = s$ and $z_2 = s + is$, where s is the signal and is the interference signal, can be evaluated as

$$\gamma = \frac{E\{z_1 z_2^*\}}{\sqrt{E\{|z_1|^2\}E\{|z_2|^2\}}} = \frac{E\{s(s+is)^*\}}{\sqrt{E\{s^2\}(E\{s^2\}+E\{is^2\})}} = \frac{1}{\sqrt{1+\frac{1}{SIR_e}}} \tag{4.27}$$

where $SIR_e = E\{s^2\}/E\{is^2\}$ is the Signal to Interference Ratio (SIR) and s is uncorrelated with the interference signal is. It can be seen from Equation 4.27 that the higher the equivalent interference of the adjacent cells, the lower the SIR_e, which implies a reduction of γ_{blur}.

To assess the image blurring effect, the study of the evolution of the decorrelation along a temporal sequence of acquisitions constitutes the subject of the measurement campaign presented in Section 4.3. The appearance of ghost scatterers and the cross-range blurring effect introduced by the motion of the scatterers is also analyzed in that section.

4.3 Experimental Results

In this section, the most important results of two different measurement campaigns are presented. They will facilitate the analysis of the blurring effect and the coherence degradation between images pointed out previously. These two main effects, due to moving scatterers in the scenario during the scanning time, have a direct relationship with the atmospheric phenomena, concretely the wind. The instrument employed for the measurements is the RISKSAR-X GB-SAR sensor, which has been used in different applications, such as the monitoring of rock falls in the Montserrat mountain (North-Eastern Spain), the characterization of urban subsidence in Sallent (North-Eastern Spain) or the monitoring of landslides in Canillo (Andorra) [92], [93].

4.3.1 Test site description and data set

4.3.1.1 Collserola test site

The test site is the Eastern side of the Collserola hill, surrounding the city of Barcelona, Spain (41°23′N, 2°06′E). It is a heterogeneous scenario including low vegetation, wooded and urban areas, see Figure 4.3. The yellow lines in Figure 4.3 define the observable area with an extension of approximately 1.2×1.5 Km^2.

During the measurement campaign, the UPC GB-SAR sensor was operated in two different modes, *S&G* and OtF, performing measurements of different scanning times. A sequence of 68 measurements was acquired from 18:00 h local time in July 26th, to 18:00 h in July 27th, with a time step of 40 minutes. Each measurement was composed of three different scans with an aperture length of 2 m. The first scan was performed in the OtF mode with a duration of 6 seconds and the following two scans were performed in the *S&G* MID and *S&G* SLOW modes with a duration of 60 and 600 seconds, respectively. It has been ensured that the three different scans have the same total transmitted energy.

During the measurement campaign, the weather conditions were typical of summer

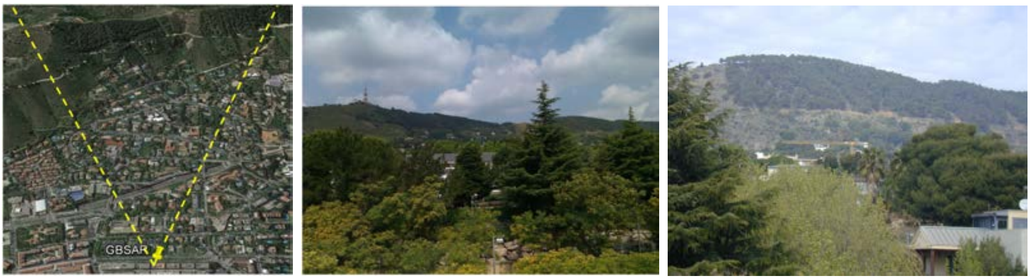

(a) (b) (c)

Figure 4.3: Test site: (a) Aerial view of the test site from Google Earth. (b) Photograph of the field of view of the GB-SAR. (c) Photograph of a crane in the test site.

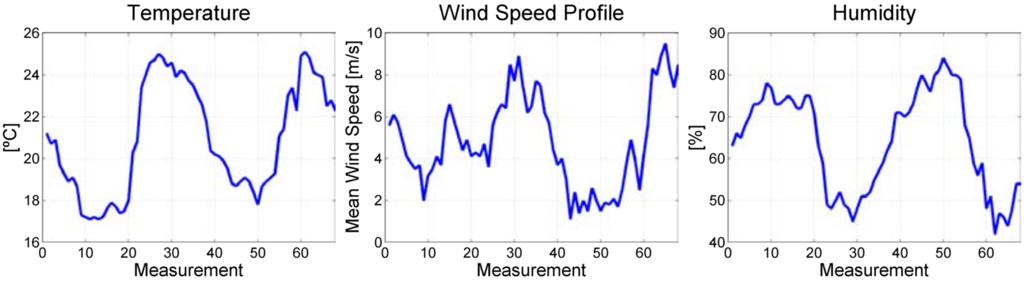

(a) (b) (c)

Figure 4.4: Atmospheric parameters information during the measurement campaign (www.meteo.cat): (a) Temperature. (b) Mean wind speed. (c) Humidity.

season in the west Mediterranean. The most important atmospheric parameters are represented in Figure 4.4: temperature, relative humidity and mean wind speed.

Two periods of strong wind together with high temperatures and low humidity can be noticed.

4.3.1.2 Montserrat test site

Another measurement campaign has been conducted in Montserrat, Catalonia, Spain. It is located 50 km southwest of Barcelona between the regions of Anoia, Baix Llobregat and Bages (41°36′N, 1°49′E). The area under study is mainly composed by rocks and dense vegetated areas containing low vegetation and trees. In the center of the illuminated area there is a rock cliff, as can be seen in Figure 4.5 (b). The yellow lines in Figure 4.5 (a) define the observable area with an extension of roughly 1×1.5 Km^2.

In this campaign, the RISKSAR-X sensor was operated in the $S\&G$ and OtF modes, performing measurements of different scanning times. A sequence of 27 measurements were acquired from 10:53 h to 12:28 h local time in July 23th. Figure 4.6 show the wind information during the measurement campaign. The vertical red lines define the time interval of the measurements, between 11 h and 12:30 h.

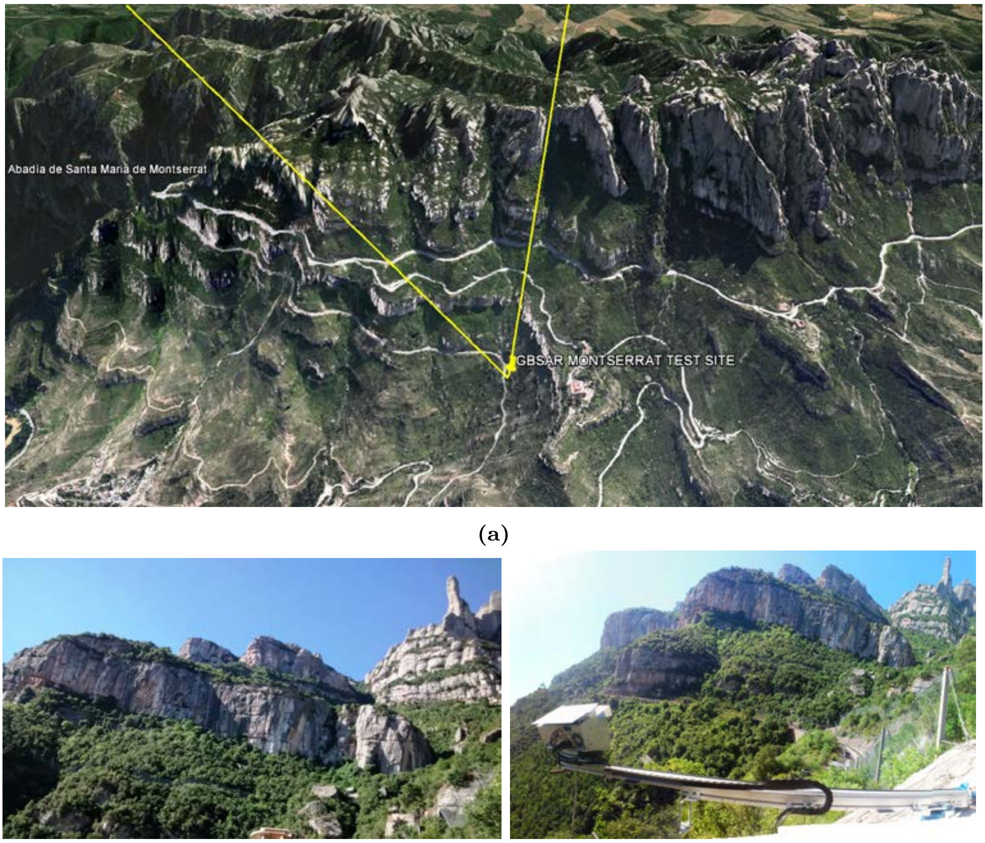

(a)

(b) **(c)**

Figure 4.5: Test site: (a) Aerial view of the test site from Google Earth. (b) Photograph of the field of view of the GB-SAR. (c) Photograph of the GB-SAR in the test site.

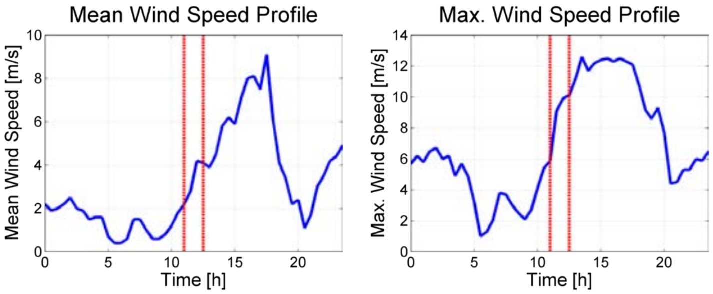

(a) **(b)**

Figure 4.6: Wind information during the measurement campaign (www.meteo.cat): (a) Mean wind speed. (b) Maximum wind speed.

4.3.2 Effect of oscillating scatterers in the retrieved images

4.3.2.1 Oscillating scatterers simulation

In this subsection, some simulations are presented to assess the impact in the retrieved data and the focused images of oscillating scatterers during the SAR acquisition. For this purpose, it has been developed a simulator that reproduces the equivalent of a real raw data matrix and applies the BPA to obtain the focused image, providing an extension of the study presented in Figure 4.2 in Section 4.2.1. The parameters considered for the simulator are those of the RISKSAR-X with an aperture length of 2 m. Figure 4.7 shows an static simulated target located at 350 m from the sensor in the range distance and at zero Doppler in the azimuth position. The grid resolution of the image is 2x2 m.

To evaluate the effect of the oscillating scatterers in the SLC images, different oscillatory displacements of the target have been introduced in the range and cross-range direction. It has been observed that oscillatory displacements in the azimuth direction have a negligible impact in the retrieved data and the processed images. On the other hand, targets presenting an oscillatory displacement in the range direction during the acquisition time present a variation in the phase of its complex reflectivity. As concluded in Section 4.2.1, this leads to the apparition of ghost scatterers in the SLC images.

Figure 4.8 shows the simulated target of Figure 4.7 with an oscillatory movement in the range direction during the acquisition time. Two different oscillation periods and two amplitudes have been considered. The scatterer in Figure 4.8 (a) and (b) present a cosine shape oscillation of 2 periods with a displacement amplitude of 15 mm and 30 mm, respectively. Otherwise, the target in Figure 4.8 (c) and (d) oscillated 20 periods with a displacement amplitude of 15 mm and 30 mm, respectively. It is observed that, as the number of periods increases, the response of the target is spread along the azimuth direction in the same radial range. If the oscillation becomes too fast with respect to the acquisition time, i.e. there are several oscillation periods, the received signal is sub-sampled leading to the apparition of ghost scatterers, see Figure 4.8 (c) and (d). Furthermore, the higher the amplitude of the oscillation, the more accentuated is the spreading, see Figure 4.8 (b).

In order to evaluate the behavior of the phase of an oscillating scatterer, a set of simulations assuming that the sensor is in a fixed position have been performed, which

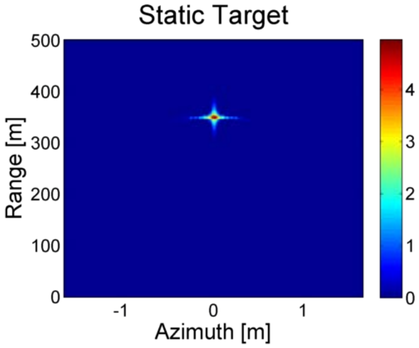

Figure 4.7: SLC image in Cartesian coordinates: Simulated static target.

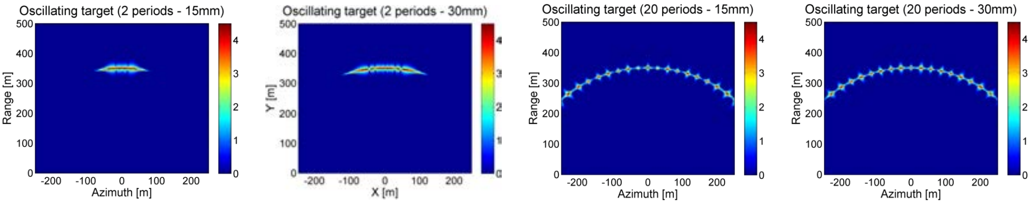

(a) **(b)** **(c)** **(d)**

Figure 4.8: SLC images obtained with BPA in Cartesian coordinates. Oscillating target in the range direction: (a) 2 periods oscillation, 15 mm amplitude. (b) 2 periods oscillation, 30 mm amplitude. (c) 20 periods oscillation, 15 mm amplitude. (d) 20 periods oscillation, 30 mm amplitude.

is equivalent to perform a radar cut. By not implementing the synthetic aperture, the simulated signals are transmitted and received from the same position and the phase of the retrieved data does not need compensation relative to the movement of the SAR. Because of that, the focused image of a one dimensional simulation or measurement concentrates all the information in the center of the image, corresponding to the zero Doppler in the azimuth position. According to Equation 4.19, the pixel reconstruction has an equivalent expression of a DFT, reason for which the azimuth focusing of the image can be conducted by applying the FFT in the cross-range dimension. This is a feasible approximation in this simulations since the aperture length is too small and the RCM is negligible. In Figure 4.9 it can be seen the SLC image of an ideal simulated static target that has been focused applying the FFT in the azimuth direction after the range compression. As expected, the target appears concentrated in one pixel in the focused image. Figure 4.10 (a) shows the spectrogram of the scatterer varying its position with an oscillatory movement of 10 mm in the cross-range direction. The phase associated to the pixel corresponding to the target is also represented in Figure 4.10 (b). As it has been previously advanced, the effects of an oscillation in cross range dimension are negligible in the focused image. As stated in Equation 2.5 of Section 2.2 in Chapter 2, the phase of the pixel of the target is

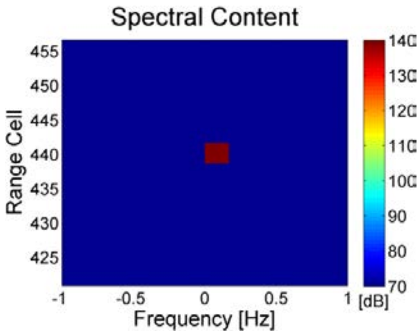

Figure 4.9: Spectrogram of the range cells of a simulated static target.

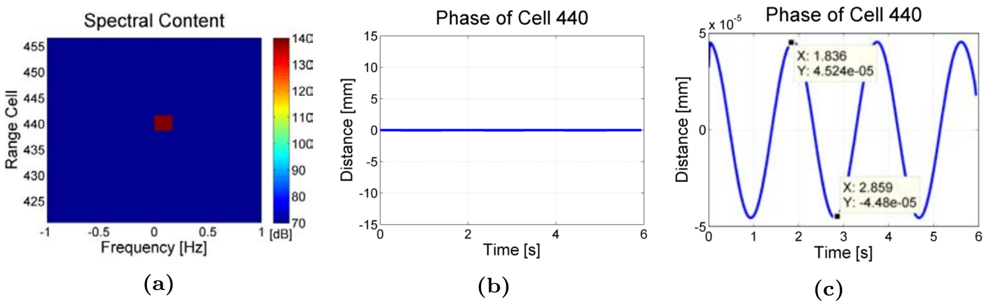

Figure 4.10: (a) Spectrogram of the range cells of a simulated oscillating target in the azimuth direction. (b) Evolution of the phase associated to the range cell of the target. (c) Zoom to the phase.

related with the distance $r_{AS}(m)$ from the sensor to the scatterer as follows

$$\varphi_{target} = \frac{4\pi}{\lambda} r_{AS}(m). \tag{4.28}$$

According to Equation 4.28, the evolution during the simulated acquisition time of the phase of the range cell of the target is evaluated in Figure 4.10 (b) and (c). The Y axis has been converted to relative distance in millimeters to show the absolute movement of the scatterer. In this case, during the simulated acquisition time, the phase of the range cell 440 equivalent to the target has an oscillation of very small amplitude ($4.5e^{-5}$ mm).

On the other hand, the target has been simulated oscillating in the range direction. Figure 4.11 shows the focused SLCs for two different oscillation amplitudes of the target of 10 mm and 100 mm with only one period during the acquisition time. As can be observed, it is enough to present the blurring effect in the azimuth direction. As expected, the SLC of Figure 4.11 (b), with an oscillation of 100 mm, has an stronger blurring effect than the SLC with an oscillation of 10 mm of Figure 4.11 (a). Besides, as can be appreciated in Figure 4.12, the evolution of the phase associated to the scatterer represents the range

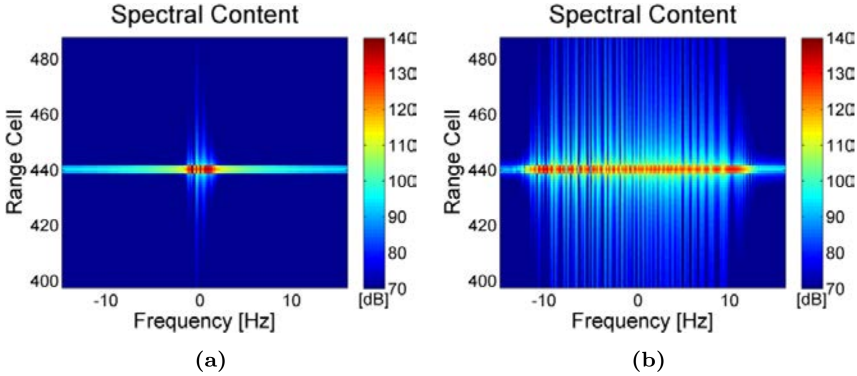

Figure 4.11: Spectrogram of the range cells of a simulated oscillating target in the range direction: (a) 10 mm oscillation amplitude. (b) 100 mm oscillation amplitude.

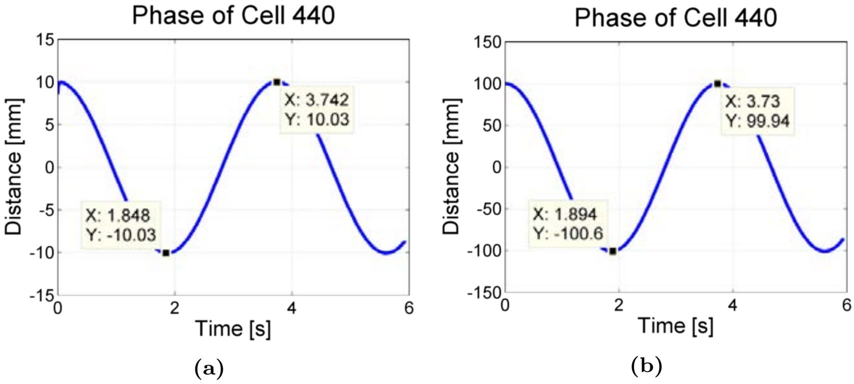

(a) **(b)**

Figure 4.12: Evolution of the phase associated to the range cell of the oscillating target: (a) 10 mm oscillation amplitude. (b) 100 mm oscillation amplitude.

oscillation of the target in time and amplitude. Thus, the retrieved phases have an amplitude of 10 mm and 100 mm approximately.

With the simulations exposed in the present subsection, apart of the blurring effect it has been evidenced the capability of the system to retrieve the range movement of a given pixel during the acquisition time. This capability, together with the blurring effect, is analyzed in different parts of this chapter.

4.3.2.2 Oscillating scatterers in a controlled experiment

The purpose of this subsection is to corroborate the previous simulations with an experiment carried out in a controlled scenario. The aim of the measurements was to detect very little oscillations of a scatterer taking advantage of the W-band UPC SAR sensor operating at 94 GHz. This system has been used in different measurements for high resolution imaging and deformation control and for security screening applications [94], [CA3], [CA5], [CA6]. As this radar operates at very high frequencies, little displacements of an object show its impact on the retrieved phase, being able to detect range changes on the order of micrometers. This is analyzed in detail by measuring a controlled oscillating target in the anechoic chamber of the UPC.

Before studying the phase of an oscillating scatterer, both the stability of the system and the minimum displacement in range that this sensor is able to resolve have been experimentally analyzed. Due to the extremely high frequencies of the the W-band sensor, little disturbances on the atmosphere, such as a change of temperature or humidity, may affect the measurements. With the purpose of studying the stability of the system, two trihedral corner reflectors have been located at a range distance of approximately 4.5 m and 7 m from the sensor in the anechoic chamber. The sensor is programmed to perform 100 measurements every 10 seconds (T1=16.6 minutes), then 100 more measurements every 30 seconds (T2=50 minutes) and finally 150 measurements every 300 seconds (T3=12.5 hours) and has been located in a fixed position to perform one dimensional radar cuts. The evolution of the retrieved phase of the two trihedrals along the T1, T2 and T3 intervals of measurement is shown in Figure 4.13.

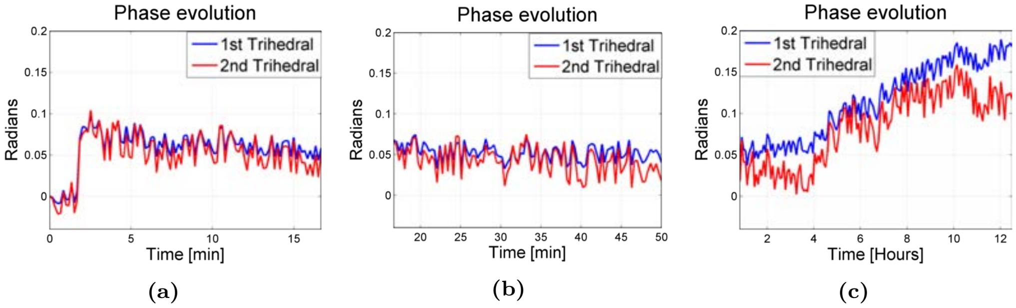

Figure 4.13: Evolution of the phase: (a) During T1 (16.6 min). (b) During T2 (50 min). (c) During T3 (12.5 h).

In Figure 4.13 it can be seen that the retrieved phase evolution of the two trihedrals is similar. Because of that, it is concluded that the phase drift does not depend on the targets and its location but on the electronics of the sensor. During the two first minutes, the system needs to be stabilized in temperature, which is evidenced by an abrupt change of the phase of the targets, see Figure 4.13 (a). In this sense, the fact that the sensor does not have a Proportional Integral Derivative (PID) temperature controller has to be taken into account. After the thermal stabilization of the system, the phase remains almost constant during the following five hours, see Figure 4.13 (b). Finally, as it was dawning, the temperature and conditions of the atmosphere in the anechoic chamber changed and the phase started to increase its value, as it can be seen in Figure 4.13 (c). In conclusion, it has to be taken into account that due to changes in the atmospheric conditions of the scenario a phase drift of approximately 0.2 radians may be introduced.

To evaluate the maximum increment in range that the W-band GB-SAR system is able to resolve through the analysis of the evolution of the phase, two experiments have been performed carrying out a set of one dimensional measurements. In both experiments, a trihedral has been located inside the UPC anechoic chamber at a certain distance in range from the radar. Said trihedral in turn has been mounted above a micrometric positioner in order to control the increment of distance in every measurement. In experiment 1, increments in range from 50 μm to 400 μm have been introduced while in experiment 2 the increments are comprised between 5 μm and 100 μm. Table 4.1 and Table 4.2 show the relative range and the range increment for experiment 1 and experiment 2,

Table 4.1: Relative range and range increment between measurements in experiment 1

	Meas 1	**Meas 2**	**Meas 3**	**Meas 4**	**Meas 5**	**Meas 6**	**Meas 7**	**Meas 8**	**Meas 9**	**Meas 10**
Relative range [μm]	0	0	0	50	100	200	500	800	1200	1600
Range increment [μm]	-	0	0	50	50	100	300	300	400	400

Table 4.2: Relative range and range increment between measurements in experiment 2

	Meas 1	**Meas 2**	**Meas 3**	**Meas 4**	**Meas 5**	**Meas 6**	**Meas 7**	**Meas 8**	**Meas 9**	**Meas 10**	**Meas 11**	**Meas 12**	**Meas 13**
Relative range [μm]	0	0	0	5	10	15	20	30	40	50	70	100	200
Range increment [μm]	-	0	0	5	5	5	5	10	10	10	20	30	100

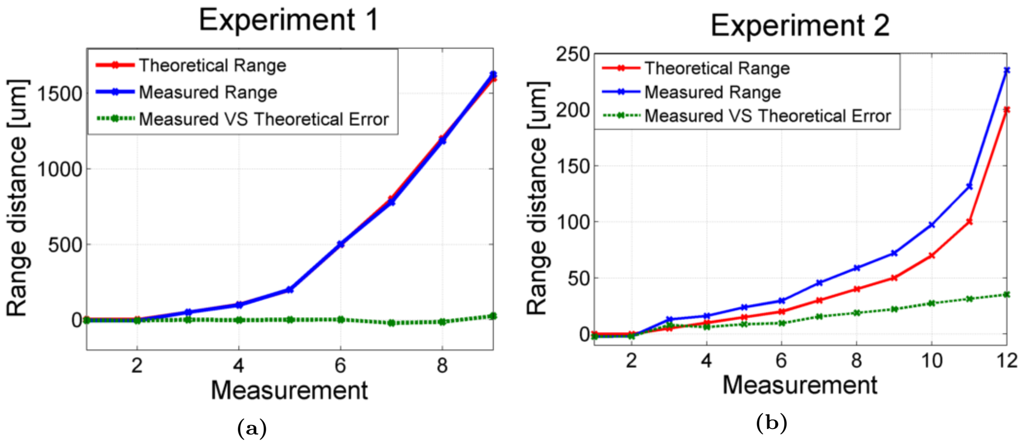

Figure 4.14: Range measurements for: (a) Experiment 1. (b) Experiment 2.

respectively. The relative range is considered as the displacement with respect to the range of the first measure and the range increment is the increment in range with respect to the previous measure. In both experiments, the first measure is the reference one, the second measure is a redundant measure without any displacement and the third measure is a redundant measure without any displacement but entering in the anechoic chamber to analyze if some disturbance is created by only entering to move the trihedral. Figure 4.14 shows graphically the results presented in both tables, comparing the theoretical with the measured range and the error between them.

It can be observed in experiment 1, see Figure 4.14 (a), that for range increments of 50 μm and above the theoretical and measured range curves are almost identical. Thereby, the error between both curves is nearly 0, which means that range increments of 50 μm are easily detectable with the W-band UPC sensor. In the case of experiment 2, Figure 4.14

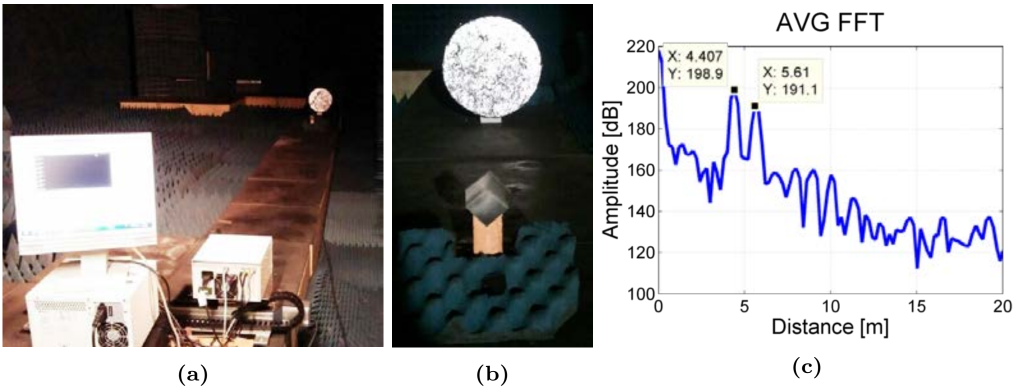

Figure 4.15: (a) Recreating an oscillating target in the UPC anechoic chamber and measuring it with the W-band GB-SAR. (b) Trihedral and oscillating target in the anechoic chamber. (c) Average range FFT of the received signal.

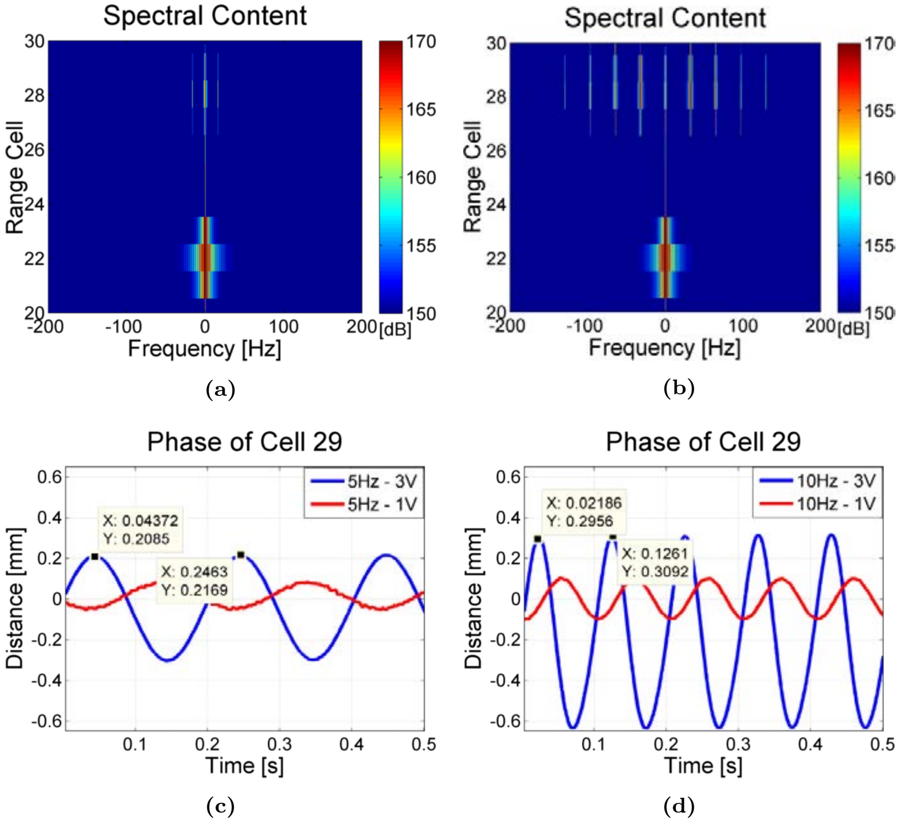

(a)

(b)

(c)

(d)

Figure 4.16: Spectral content with the speaker oscillating at: (a) 5 Hz and 1 V amplitude. (b) 10 Hz and 3 V amplitude. Measured phase of the speaker oscillating at: (c) 5 Hz and 1-3 V amplitude. (d) 10 Hz and 1-3 V amplitude.

(b) shows slightly differences between the theoretical and measured range, but both have the same tendency. This means that a cumulative error is introduced when displacing the trihedral with the micrometric positioning system, since it is extremely difficult to displace 5 μm accurately by hand. According to the results, it can be concluded that the W-band UPC GB-SAR is able to detect displacements in range on the order of 5 μm.

In order to analyze the effects of an oscillating permanent scatterer inside the anechoic chamber, the experiment shown in Figure 4.15 has been performed. Two scatterers have been located at approximately 4.4 m and 5.6 m in range from the radar, see Figure 4.15 (a) and (b); a trihedral corner reflector and an oscillating target. The oscillating target is implemented by sticking a flat surface with reflective material to the membrane of a conventional speaker. When a sinusoidal function of a determined frequency and amplitude is introduced to the speaker its membrane oscillates and so does the flat surface adhered on it. This way, a controlled oscillating scatterer is recreated. In Figure 4.15 (c) it can be seen the average range FFT of the total transmitted chirp periods during the acquisition time. As expected, the response of the two scatterers correspond to a range of 4.4 m and 5.6 m.

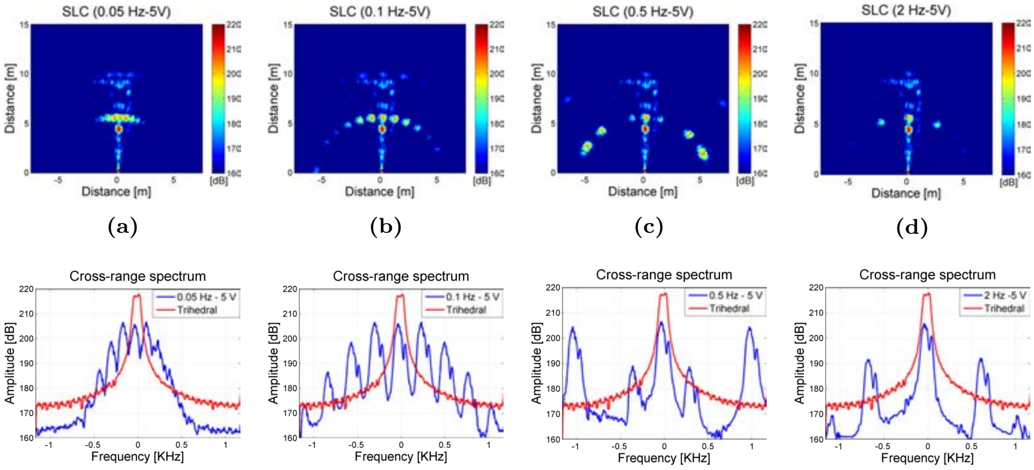

(a) (b) (c) (d)

(e) (f) (g) (h)

Figure 4.17: SLC image and cross-range spectrum with the speaker oscillating at: (a), (e) 0.05 Hz -5 V. (b), (f) 0.1 Hz -5 V. (c), (g) 0.5 Hz -5 V. (d), (h) 2 Hz -5 V.

A set of one dimensional measurements have been performed to analyze the evolution of the phase of the oscillating target, which has been recreated introducing sinusoidal functions with different amplitude and periods to the speaker. Figure 4.16 (a) and (b) shows the spectral content of two measurements where the speaker oscillated at 5 Hz and 10 Hz with amplitudes of 1 V and 3 V, respectively. According to the simulations presented in Figure 4.8, as the frequency and amplitude of the oscillation increases, the replicas of the scatterer begin to appear. Furthermore, in Figure 4.16 (c) and (d) it can be seen the retrieved phase of the range cell associated to the oscillating scatterer, which has the same sinusoidal behavior introduced to the speaker. Besides, the period of the retrieved phase is 5 Hz and 10 Hz and its amplitude is higher when introducing 3 V than when introducing 1 V, fact that is related to a major displacement of the membrane of the speaker for higher input amplitudes.

After analyzing the evolution of the retrieved phase in the one dimensional measurements, a synthetic aperture of 2 m length was performed maintaining the same scenario with the aim of analyzing the impact of the oscillating target in the focused SLC images. With this purpose, four different oscillating periods of the sinusoidal function with a fixed amplitude of 5 V have been introduced to the speaker: 0.05 Hz, 0.1 Hz, 0.5 Hz and 2 Hz. Figure 4.17 shows the focused SLC images and the cross-range spectrum associated to the trihedral and the speaker for all the cases. It can be observed that, as the oscillating period of the speaker increases, the replicas in the image appear more spatially separated along the same radial range. However, there comes a point where the ghost scatterers disappear beyond the limits of the image and the process starts again, as is the case of Figure 4.17 (d). On the other hand, the cross-range spectrum associated to the trihedral remains constant, while the spreading of the spectrum and the apparition of ghost scatterers is evidenced for the case of the speaker. All these results are consistent with the simulations of Subsection 4.3.2.

4.3.2.3 Oscillating scatterers in Collserola test site

To evaluate the effect in the retrieved images of having an scatterer oscillating in the range direction during the scanning time, the behaviour of a crane located in the Collserola test site has been studied, see Figure 4.3 (c). During the measurements, it evidenced oscillatory movements due to the effect of the wind and normal operation of a flexible structure.

The RISKSAR-X sensor was located in a fixed position to perform an equivalent radar cut. The scanning time of the system was approximately 6 seconds. Figure 4.18 (a) shows the spectrogram of the range cut of a measurement where the range cell 434 corresponds to the crane. During the measurement there was strong wind, which can be noticed by the energy spreading along the frequency axis in the spectrogram. In Figure 4.18 (b) it can be seen a zoom to the range cells corresponding to the crane in the normalized spectrogram. It can be noticed that the response of the crane has been spread along the frequency axis due to its motion during the acquisition time. According to Equation 4.28,

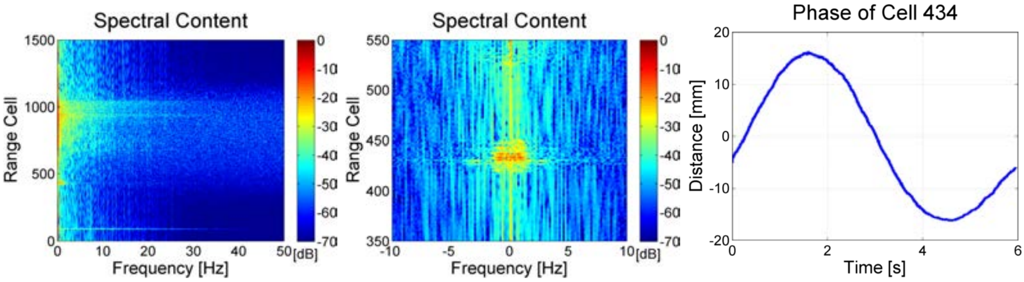

(a) (b) (c)

Figure 4.18: (a) Normalized Spectrogram of the range cells. (b) Zoom to the range cells of the crane in the normalized spectrogram. (c) Phase of the cell 434 corresponding to the crane during the scanning time.

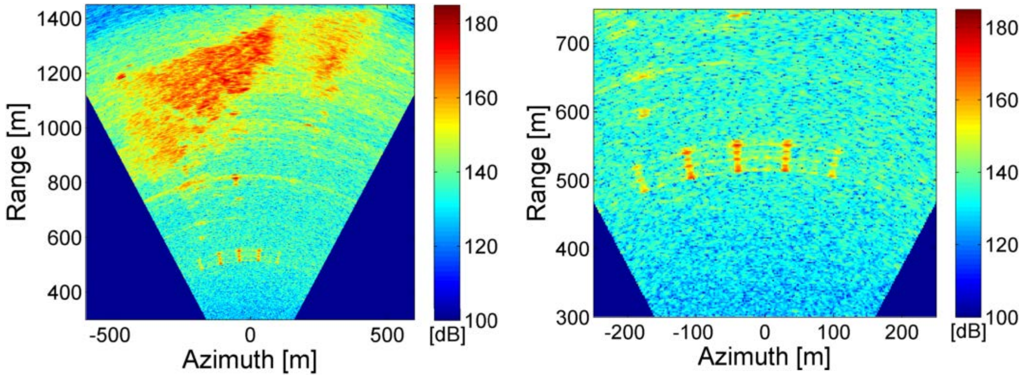

(a) (b)

Figure 4.19: (a) SLC image in Cartesian coordinates with replicas along the cross-range of an oscillating crane in the scenario. (b) Zoom of the replicas of the crane in the SLC image.

the phase of the pixel of the crane is related with the distance $r_{AS}(m)$ from the sensor to the scatterer. Thereby, the phase evolution during the scanning time of the range cell of the crane was extracted and evaluated in Figure 4.18 (c). It reveals that the center of phase of the pixel associated to the crane was oscillating around 30 mm in the range direction during the scanning time and, hence, a sinusoidal curve has been obtained.

Figure 4.19 shows the SLC image obtained operating the system in the *S&G* operation mode, where the effect of the movement of the crane in the focused image is clearly seen. Since the scanning time is 60 seconds, the phase of the pixel corresponding to the crane presents several periods of oscillation during the measurement. This introduces a phase modulation in its complex reflectivity that results in the appearance of replicas along the cross-range direction, as it is illustrated in the simulations of Figure 4.2 (b) in Subsection 4.2.1 and Figure 4.8 in Subsection 4.3.2.1. The number of replicas and their angular separation depends on the oscillating period of the scatterer with respect to the acquisition time.

4.3.3 Effect of windblown in the retreived images

In order to evaluate the effect in the quality of the image of the random, short term variable complex reflectivity $\sigma(m)e^{j\phi(m)}$ of a generic scatterer, a specific experiment was performed. The RISKSAR-X sensor was again used as one dimensional radar using a pair of high directive antennas with equivalent radar beamwidth of approximately 2 degrees. The antennas were pointed towards the wooded area, see Figure 4.20 (a). The scans were of short intervals of time of roughly 6 seconds and were performed in different moments of the same day with contrasted wind conditions. Figure 4.20 (b) and (c) show the spectrogram of the range cut in two times of the day, with different mean wind speed of 0.8 m/s and 4.9 m/s, respectively. The normalized spectrogram under higher wind speed presents an important energy dispersion in the frequency domain with respect to the one with lower wind speed, which is consistent with the simulations of Figure 4.2 (c) in Subsection 4.2.1.

The power spectral density of the range-compressed signal from two different cells (no. 351 and 800) are studied under distinct wind conditions. The first cell is identified as

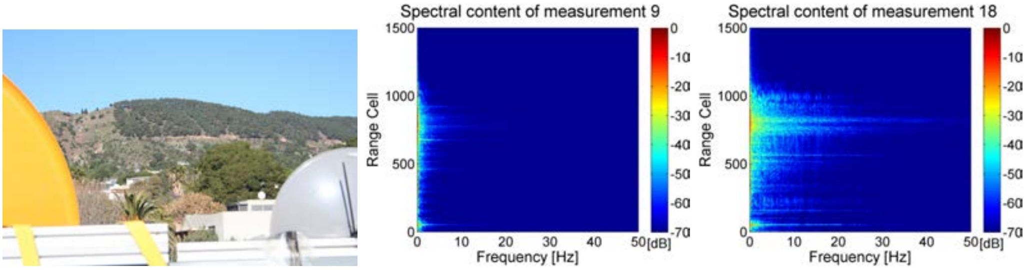

(a) **(b)** **(c)**

Figure 4.20: (a) High directive parabolic antennas pointing towards the wooded area of the Collserola test site. Normalized Spectrograms of the range cells for two different mean wind speeds: (b) $v_{wind} = 0.8$ m/s. (c) $v_{wind} = 4.9$ m/s.

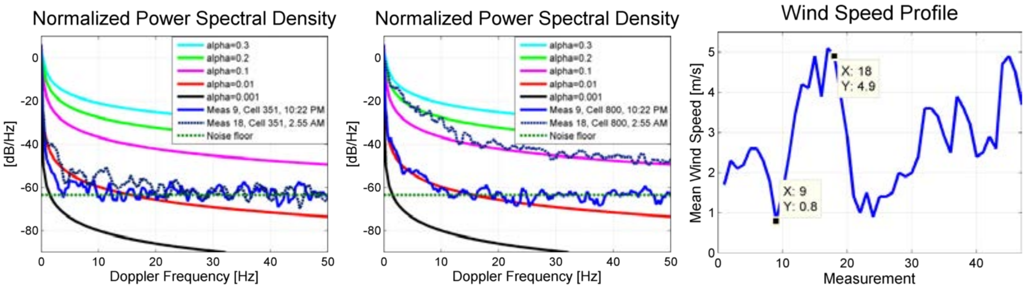

(a) **(b)** **(c)**

Figure 4.21: Comparison of K-PSD model distribution with PSD of cells no. (a) 351 corresponding to a static scatterer and (b) 800 corresponding to a wooded area for (c) two different instants of the day with different average wind speed, 0.8 m/s and 4.9 m/s.

a permanent scatterer, while the second corresponds to a vegetated, wooden, area. In Figure 4.21, the Power Spectral Density (PSD) of these cells is compared with the model for the Doppler spectrum of windblown radar ground clutter called K-PSD [80]. The K-PSD model is highly appropriate for characterizing clutter spectra from windblown vegetation. Different PSD shapes are obtained for different values of α_{KPSD}, which are related with the movement of the vegetation. The parameter α_{KPSD}, which has been adjusted to match the wind strength, controls the scaling of the exponential slope, the shape of the peak and the global variance of the clutter PSD.

The PSD of both cells in Figure 4.21 (a) and (b) is quite different. While cell 351 shows a delta shape, as expected for a prominent static scatterer, cell 800 presents an exponential decay response with notable influence of the measurement instant. In both images, it is also clearly seen the equivalent frequency bandwidth of the PSD, which is wide enough to ensure a change in the backscatter reflectivity of the cell during the typical scanning time of the GB-SAR. Besides, in the images it is evidenced the noise floor of the system (green dashed line). The energy dispersion of the equivalent reflectivity of the distributed scatterers is wide enough, on the order of tens of Hz, to degrade the focusing process with an equivalent cross-range blurring effect, as it is pointed in Section 4.2. The focusing degradation because of the variable reflectivity during the scanning time will be higher if the scenario includes dense vegetated areas that are shaken by the wind. In this case, the main GB-SAR parameters (transmitted power, transmitted signal bandwidth, chirp rate, chirp period, scanning method and time of observation, etc.) must be accurately chosen to minimize the cross-range blurring effect. In this sense, it is obvious that it is mandatory to reduce the scanning time, but the transmitted energy has to be maintained to have the same SCR.

4.3.3.1 Blurring effect on the images obtained in Collserola test site

To assess the effect of the energy dispersion associated to the movement of the vegetation in the final image, a compilation of SLC images taken in the Collserola test site is shown in Figure 4.22. These images were obtained under different windblown condition, with one OtF and two *S&G* scans, each with different scanning times. The mean wind speed for the measurements is 2 m/s (light wind) and 8.9 m/s (strong wind), corresponding to measurement 9 and 30 of the data set. As introduced in Section 4.2, there is a correlation between the scanning time and the blurring effect on the final image. The top row shows the SLCs taken with light wind (low temperature and high humidity) while the bottom row is showing SLCs taken under strong wind (high temperature and low humidity).

The best focused image corresponds to light wind and OtF scan, where the contours of different reflective surfaces can be clearly distinguished. On the other hand, a blurred image is obtained under strong wind blow and long aperture time. An indicative that the cross-range blurring effect is affecting the quality of the images is the fact that in the SLCs corresponding to strong wind, the energy of the pixels associated to the back side of the mountain is increased when it should remain constant. As it is marked in the *S&G* SLOW measurement in Figure 4.22 (b), the pixels of the left part of the image beyond 1200 m correspond to a shaded area. By comparing the measurements taken with the two *S&G* modes, it can be seen that there are no significant differences between them. It is noticeable the relevance of the moment of measurement according to the type of scenario. In this case, the scenario contains static high reflective (buildings and urban structures) and distributed scatterers (trees and bushes). These last have a short term variable reflectivity due to the wind during the scanning time, which is normal in scenarios used for GB-SAR applications. Short term variable reflectivity together with long scanning time strongly increases the image cross-range blurring, as previously seen in the simulations of Figures 4.2 and 4.8.

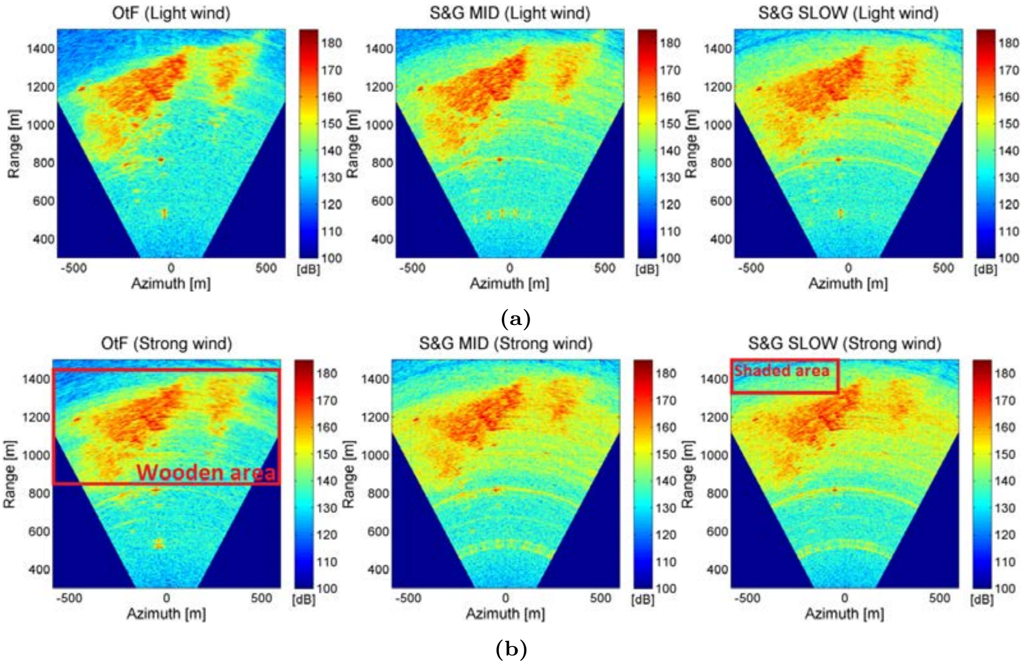

(a)

(b)

Figure 4.22: SLC images in Cartesian coordinates for different operation modes and different wind blown speed: (a) Light mean wind speed of 2 m/s. (b) Strong mean wind speed of 8.9 m/s.

4.3.3.2 Blurring effect on the images obtained in Montserrat test site

The same procedure has been conducted in the Montserrat test site but operating the RISKSAR-X sensor only in the OtF and *S&G* MID modes, since it has been observed that the difference between the results with both *S&G* modes is not significant. As can be noticed in Figure 4.5, the scenario has a rock cliff surrounded by dense vegetation, which makes it ideal to evaluate the blurring effect in the SLC images with different wind conditions and different acquisition times. A compilation of SLC images taken in the Montserrat test site under different windblown conditions is shown in Figure 4.23.

The mean-max. wind speed for the measurements is 2.2-5.9 m/s for light wind and 4.1-10.1 m/s for strong wind, corresponding to the measurement taken at 11 h and 12:30 h of the data set, see Figure 4.6. Figure 4.23 (a) and (b) correspond to the SLCs taken under light wind while Figure 4.23 (c) and (d) shows SLCs taken under strong wind. As it happened in Figure 4.22, the best focused image correspond to light wind and OtF scan. In this case, the contours of the rock cliff and the different rocks in the scenario can be clearly distinguished. On the other hand, the most blurred image is again obtained under strong wind blow and long scanning time. The cross-range blurring effect is obviously

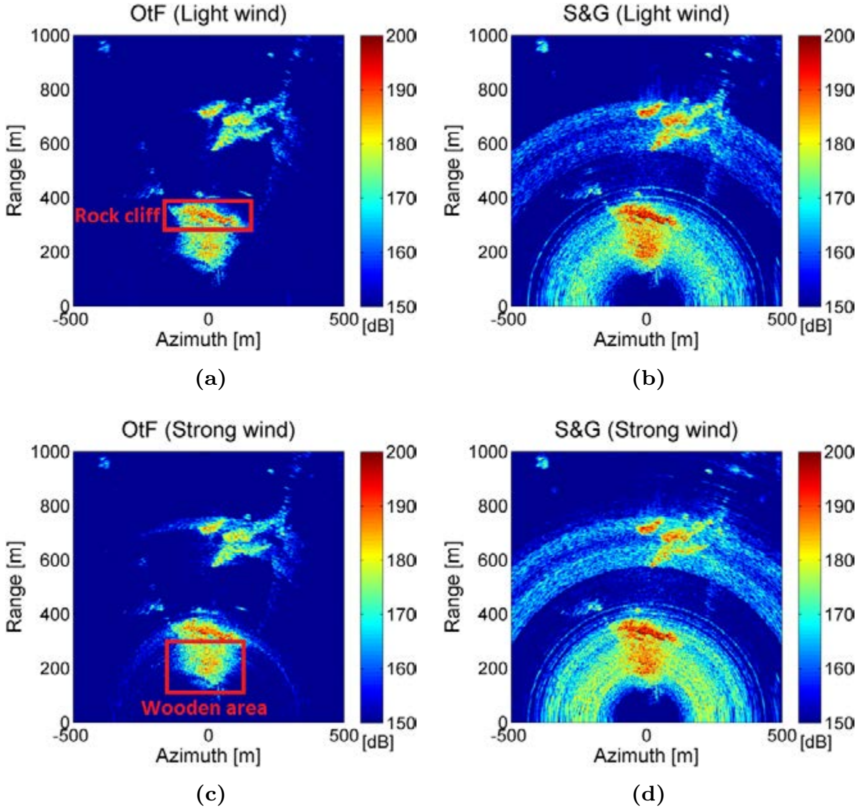

(a) (b) (c) (d)

Figure 4.23: SLC images in Cartesian coordinates for different operation modes and different wind blow speed. Light mean wind speed of (a) and (b): 2.2-5.9 m/s. Strong mean wind speed of (c) and (d): 4.1-10.1 m/s.

Table 4.3: Evaluation of the number of coherent pixels.

	LIGHT			STRONG		
	OtF	*S&G* MID	*S&G* SLOW	OtF	*S&G* MID	*S&G* SLOW
Pixels with coherence amplitude>0.6	90342	74305	70112	37174	34758	34571
Reduction respect OtF[%]	-	17.75	22.39	-	6.5	7

evidenced in the two *S&G* measurements where the distributed scatterers corresponding to low vegetation and trees have been moving during the acquisition time. The results obtained in the Montserrat test site are consistent with those of Collserola presented in Subsection 4.3.3.1.

4.3.4 Coherence map evaluation

After analyzing the different SLC images, some temporal differential interferometric images based on the same master image have been generated. The aim was to evaluate how the coherence is affected by the fact of having an scenario with high coherent scatterers surrounded by vegetated areas containing distributed targets with short term variable reflectivity.

4.3.4.1 Coherence map evaluation in Collserola test site images

Figure 4.24 shows the normalized coherence $|\gamma|$ of six differential interferometric images obtained with the OtF, *S&G* MID and the *S&G* SLOW operation modes for two different mean wind speeds of 2 m/s and 8.9 m/s. It can be observed that for light wind speed the number of coherent pixels, which are the ones that maintain a constant reflectivity over the time, are reduced as the duration of the scanning time increases, overcoat between the OtF and the *S&G* mode. In the measurements with strong wind speed, the number of coherent pixels has been drastically reduced for the three operation modes. This information is shown in Table 4.3, which summarizes the evolution of the number of coherent pixels for the different operation modes and wind speeds.

In Table 4.3 it can be seen that, for the light wind measurements, the coherence map corresponding to the *S&G* MID operation mode has a reduction of the 17.75 % with respect to the OtF case in the density of coherent pixels with a coherence amplitude greater than 0.6. The *S&G* SLOW mode has a reduction of the 22.39 % with respect to the OtF case. For the strong wind the *S&G* MID and the *S&G* SLOW have a reduction of 6.5 % and 7 %, respectively, with respect to the OtF case. Besides, the measurements under strong wind have a reduction in the number of coherent pixels with respect to the measurements under light wind of 58.8 %, 53.2 % and 50.69 % for the OtF, *S&G* MID and *S&G* SLOW, respectively.

Figure 4.25 shows the histogram of the coherence $|\gamma|$ for two different mean wind speed and the three different operation modes. It is clearly evidenced that for light wind conditions the OtF scan method offers the highest number of pixels with an elevated coherence, while the two *S&G* scans are almost indistinguishable. On the other hand,

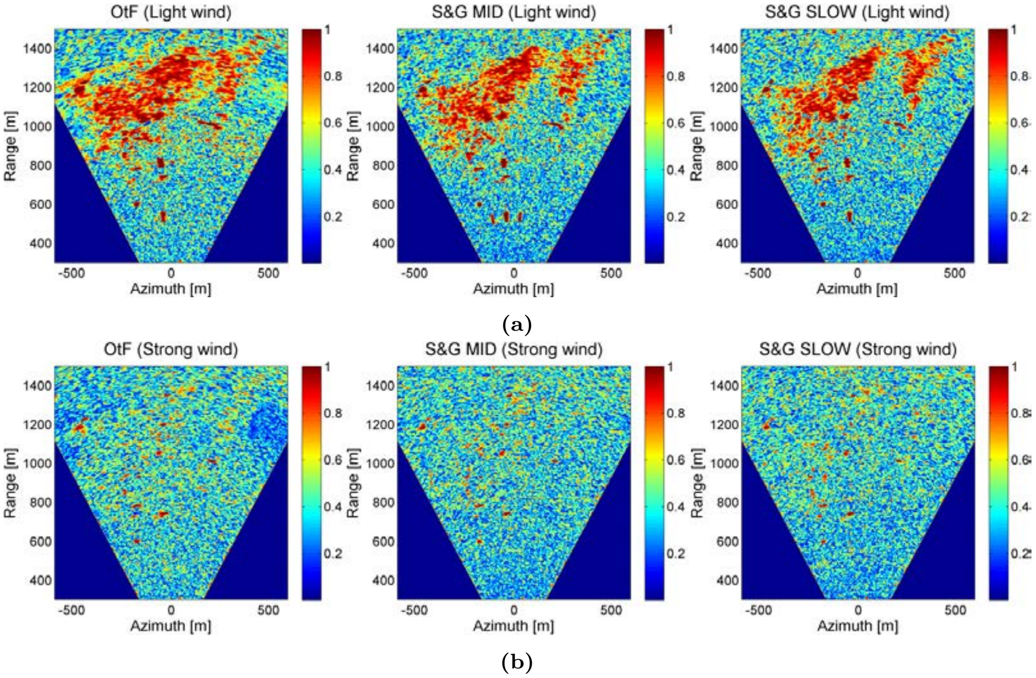

(a)

(b)

Figure 4.24: Coherence $|\gamma|$ of differential interferometric images for different operation modes and different wind blow speed: (a) Light mean wind speed of 2 m/s. (b) Strong mean sind speed of 8.9 m/s.

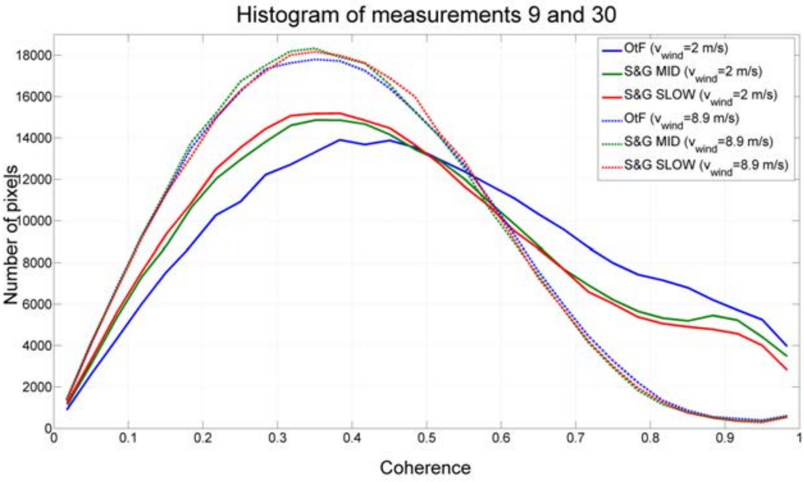

Figure 4.25: Histogram of the coherence $|\gamma|$ for two different mean wind speed, $v_{wind} = 2$ m/s and $v_{wind} = 8.9$ m/s, and the three different operation modes.

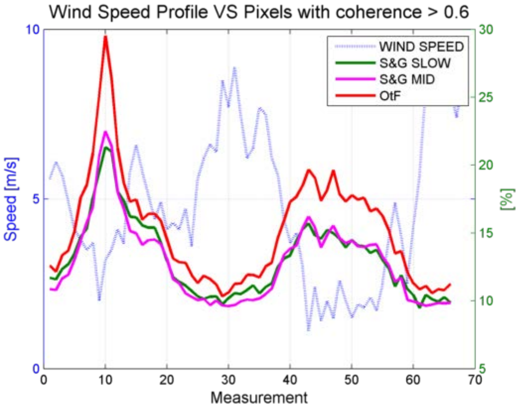

Figure 4.26: Superposition of mean wind speed and the evolution of pixel density with coherence higher than 0.6. The highest density is close to the master image. A strong correlation between coherent pixel density and mean wind speed is detected.

under strong wind conditions, the three scanning modes have a similar performance and present a higher number of pixels with low coherence with respect to the light wind case. Thus, after analyzing the results shown in Figure 4.24 and Figure 4.25, it has been concluded that for scenarios containing or surrounded by vegetation and strong wind conditions, the reduction of the scanning time between the tree operation modes is not enough to avoid the blurring effect and the decorrelation between images.

After analyzing the differential interferometric images of the measurements realized during the two days of campaign, Figure 4.26 exposes the evolution of the density of pixels in the image with coherence value over a certain threshold, in this case 0.6. The plot clearly shows that the density of coherent pixels is higher for short aperture times and that there is a strong correlation with the atmospheric activity, in particular with the wind. The test site is in part composed by vegetated areas in which the foliage moves with the effect of the wind varying its reflectivity. Thus, the higher the wind speed during the acquisitions, the lower the number of density pixels with coherence over a certain threshold.

4.3.4.2 Coherence map evaluation in Montserrat test site images

Figure 4.27 shows the coherence $|\gamma|$ of four differential interferometric images obtained with the OtF and *S&G* MID modes for two different mean-max. wind speeds of 2.2-5.9 m/s and 4.1-10.1 m/s. In the same way as in Subsection 4.3.4.1, the number of coherent pixels decreases with the increase of the acquisition time and the wind speed. Table 4.4 shows a summary of the evolution of the number of coherent pixels for the different cases.

As it is shown in Table 4.4, for the light wind measurements the coherence map corresponding to the *S&G* MID operation mode has a reduction of the 3.7 % with respect to the OtF case in the density of coherent pixels with a coherence amplitude greater than 0.6. For the strong wind case, the *S&G* has a reduction of the 37.4 % with respect to the OtF case. Furthermore, the measurements under strong wind have a reduction in

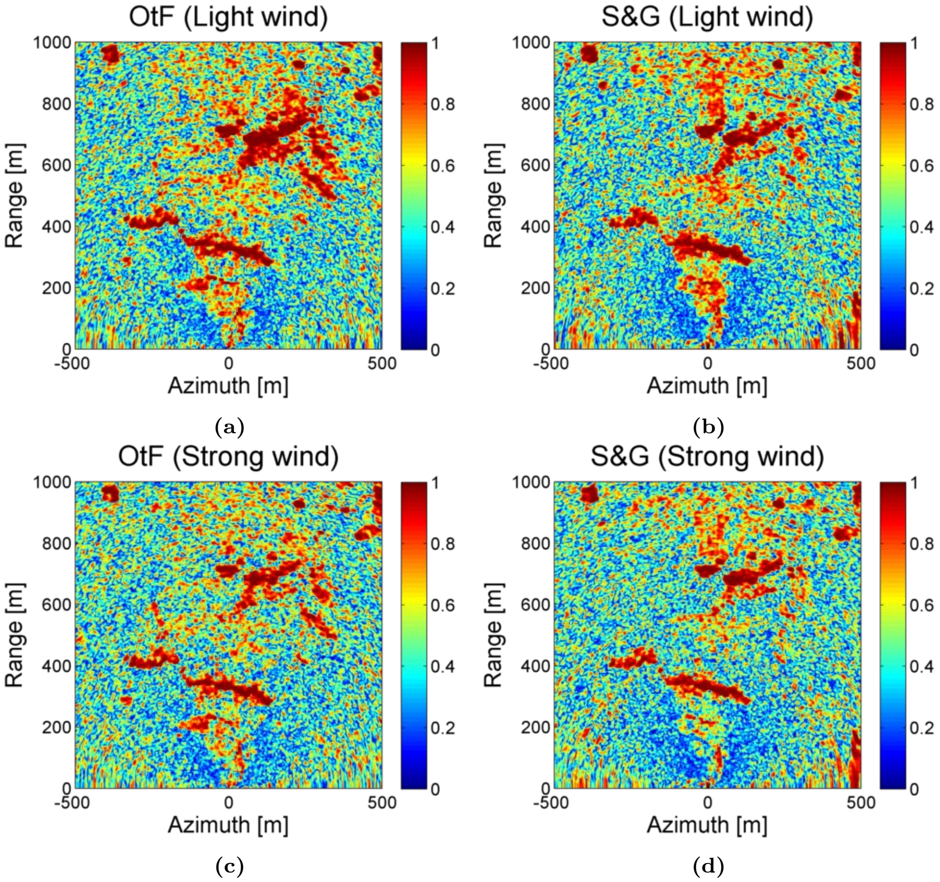

(a) (b) (c) (d)

Figure 4.27: Coherence $|\gamma|$ of differential interferometric images for different operation modes and different wind blow speed: (a) and (b) Light mean-max. wind speed of 2.2-5.9 m/s. (c) and (d) Strong mean-max. wind speed of 4.1-10.1 m/s.

Table 4.4: Evaluation of the number of coherent pixels.

	LIGHT		**STRONG**	
	OtF	*S&G* MID	OtF	*S&G* MID
Pixels with coherence amplitude>0.6	62925	60926	49954	31257
Reduction respect OtF[%]	-	3.7	-	37.4

the number of coherent pixels with respect to the measurements under light wind of 20.6 % and 48.69 % for the OtF and *S&G* MID, respectively. Comparing these results with the ones presented in Subsection 4.3.4.1, it can be noticed that the reduction of coherent pixels between both operation modes is less accentuated in this case. This may be due the fact that the velocity of the wind has been much more moderate during this measurement campaign.

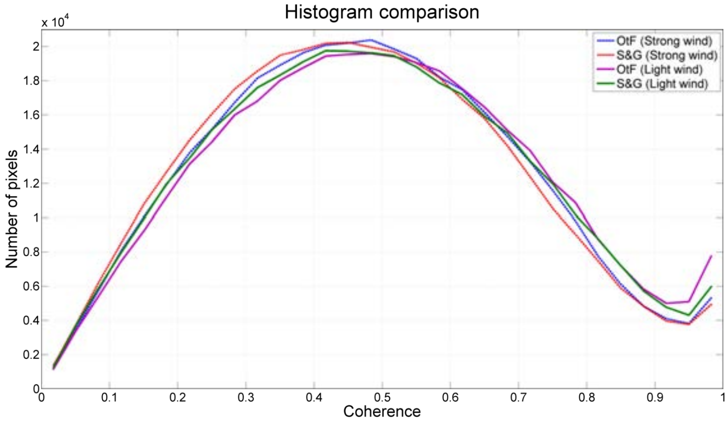

Figure 4.28: Histogram of the coherence $|\gamma|$ for two different mean/max. wind speed, $v_{wind} = 2.2 - 5.9$ m/s (light wind) and $v_{wind} = 4.1 - 10.1$ m/s (strong wind), and the two different operation modes.

Figure 4.28 shows the histogram of the coherence $|\gamma|$ for two different mean wind speed and the two different operation modes. It can be seen that the operation mode with the highest number of pixels with an elevated coherence is the OtF under light wind conditions, followed by the *S&G* under light wind conditions, the OtF under strong wind conditions and finally the *S&G* under strong wind conditions. This denotes the importance of reducing the acquisition time to obtain, for instance, good interferometric results when measuring scenarios containing or surrounded by wooded areas.

In GB-SAR systems, the effect of the energy spreading along cross-range of adjacent cells must be taken into account because it can degrade the quality of the retrieved information. This can be seen, for instance, in the reduction of the amount of coherent pixels in the coherence maps. The spreading effect can be explained in terms of the equivalent Doppler bandwidth of the illuminated scene. For long scanning time, the particular geometry of the scenario forces a reduced Doppler bandwidth of a fraction of a cycle, while the equivalent frequency spreading of the variable scatterers are hundreds of Hz. Because of that, these systems are affected by the blurring effect and the decorrelation between images can arise.

The blurring effect is not present in the same way in orbital SARs, but it could be noticeable in airborne SARs, depending on the Doppler bandwidth and the frequency

Table 4.5: Evaluation of the Doppler bandwidth

RESOLUTION [m]	**DOPPLER BANDWIDTH (Hz)**		
	GB-SAR (v=0.5 m/s)	AIRBORNE (v=100 m/s)	ORBITAL (v=7500 m/s)
15	0.03	6.6	500
1.5	0.3	66	5000

spreading of the energy of the scatterers. In orbital SARs, the equivalent Doppler bandwidth is wider than the energy frequency spreading of deterministic and random moving scatterers. This is summarized in Table 4.5, which shows the evaluation of the Doppler bandwidth for a given range resolution as a function of the different SAR topologies.

4.4 Concluding remarks

The potentials of GB-SAR sensors to monitor deformation episodes have been demonstrated during the last years. The high stability and flexibility of the sensor platform, in addition to their reduced cost compared to orbital platforms, makes them ideal to detect changes in small-scale areas of observation by means of GB-SAR interferometry. Nevertheless, some limitations in the performance of GB-SAR systems have to be pointed out. This chapter has studied some of these limitations, directly related with the short aperture length together with the relative long scanning time and the change in the reflectivity of the scenario during the measurement. These changes of reflectivity due to moving vegetation can be forced by atmospheric phenomena as wind. The main effects assessed in the present chapter are image blurring, decorrelation and, hence, an important coherence degradation. In this context, it has been concluded that the retrieved information from scenarios surrounded or containing vegetation can be deteriorated, since pixels associated to moving scatterers also alter the reflectivity of neighbouring pixels in the same radial range.

Taking into account that GB-SAR systems are mainly used to detect and monitor changes in heterogeneous scenarios by means of the coherence maps, the degradation of the quality of these maps is an important drawback that has to be minimized. By means of working with the OtF and *S&G* operation modes, it has been confirmed that to reduce the blurring effect in the cross-range direction it is necessary to reduce the scanning time, while maintaining the total transmitted energy. Thus, a readjustment of the Chirp Repetition Pulse (CRP) is mandatory to ensure that the spatial Nyquist criterion is accomplished. Nevertheless, despite an important reduction of the scanning time to seconds, under some atmospheric conditions (strong wind) no improvement is reached, so it is clearly preferable to take measurements under stable atmosphere.

A mathematical description of the GB-SAR cross-range focusing process has been developed, which has permitted the analysis and characterization of the effect in the image reconstruction process of having moving vegetation surrounding the area under study. Periodic changes in scatterer reflectivity imply the apparition of cross-range replicas of the scatterer, while the random ones force image blurring and image decorrelation. A new term in the differential interferometric coherence γ_{blur} that takes into account the image blurring has been introduced. This effect can be considered as noise, having a direct dependence with the SIR_e. It is beyond the scope of this work to characterize the interference signal SIR_e as a function of the moving scatterers, but some general explanations to different particular cases have been pointed out.

The RISKSAR-X GB-SAR sensor has been used to experimentally validate the effect of the wind on the retrieved data while measuring scenarios containing urban and vegetated areas. The experimental results have shown a decorrelation at X-Band between data acquired at different instants, which implies a decrease of the coherence of the overall image.

Part II

Contributions to ARBRES-X SAR system

5

Chapter 5

UPC ARBRES-X SAR System

This chapter is intended to describe the system architecture of the UPC ARBRES-X SAR sensor as well as to expose its main characteristics of operation. Furthermore, the different elements of the complete system comprising the SAR sensor, the UAV MP and other electronics are analyzed and the main contributions to the system developed during the course of this doctoral activity are exposed. Moreover, the most important processing steps are assessed, such as the use of the autofocus algorithm or the phase center compensation prior to the system calibration. In the first section, a brief introduction to the ARBRES-X SAR sensor is provided. In the second section, the main hardware contributions to the SAR sensor are exposed and the complete integrated system is analyzed. The third section is intended to briefly describe the way in which the system process the raw data taking into account the new capabilities of the sensor. The fourth section aims to describe the phase centers compensation and a first attempt of polarimetric data calibration for the ARBRES-X. Finally, the main conclusions and major remarks of the chapter are exposed. [a]

---

[a] The following sections contain portions, sometimes verbatim, of the preliminary results exposed in [CA2], [CA4].

5.1 Introduction to the ARBRES-X SAR system

The experimental fully polarimetric ARBRES-X SAR sensor has been entirely developed by the RSLab of the UPC. Originally it was designed to be fitted in small UAVs for testing innovative SAR concepts, since this type of platforms are particularly interesting due to its low cost and requirements. For that purpose, the emphasis was put on weight and volume reduction. In previous versions of the system, the radar was mounted on a radio controlled fixed wings UAV that had the capability to flight at speeds up to 40 m/s and high altitudes [95]. This platform constituted a good solution since its flight was very stable, offering the possibility to perform straight apertures at constant speed. Even so, this UAV was limited by its low versatility while flying and the lack of control of the flight trajectory. These constraints were of great importance as they restricted the capabilities of the SAR sensor, such as for instance making it difficult to perform repeat-pass interferometric measurements.

During the realization of the present doctoral work and with the aim of overcoming some of the exposed drawbacks, the radio controlled plane has been substituted by a UAV MP. In this process, some parts of the radar have had to be re-designed to fulfill the space requirements of the MP, as is the case of the RF front-end. The migration in the typology of the platform is intended to explore new potentials in airborne SAR observation, which is one of the objectives of this doctoral activity. The initial SAR capabilities of these type of platforms will be exposed in Chapter 6.

5.2 ARBRES-X SAR system description

In the present section, the system description, the architecture and the setting parameters of the ARBRES-X SAR sensor are presented, including the hardware contributions conducted to the radar during the course of this doctoral thesis. Furthermore, the UAV MP used to integrate the radar is introduced, analyzing its main advantages and drawbacks. Finally, the different electronics necessary to obtain satisfactory SAR measurements are detailed and assessed throughout this chapter.

5.2.1 The UAV multicopter platform

The Spreading Wings S1000 from DJI, designed for professional aerial photography and cinematography, has been chosen to integrate the ARBRES-X SAR sensor. UAV MPs have several advantages compared with a fixed wings airplane UAV that makes them suitable to integrate the sensor to perform SAR measurements. The main advantage of the UAV MP is that it does not need a long landing strip. Due to its vertical lift capability, it only needs a small area, such as a forest clearing, to take off and to land, making it operational in almost any location. Besides, its capacity to hover and perform agile maneuvering makes this type of platforms well suited for many applications in airborne SAR observation. Some examples could be object detection or urban structure characterization, where precision flights and the ability to maintain the observation on a single target for extended periods of time may be required.

Another important advantage is that the UAV MP can perform three dimensional flights due to its ability to move in almost any direction, opening a wide range of new

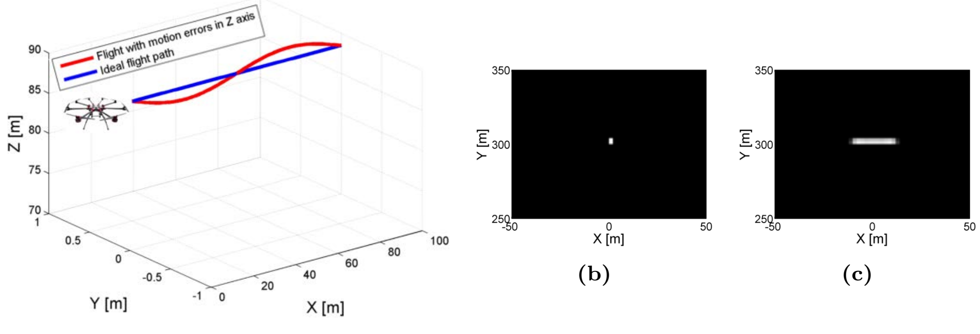

(a) (b) (c)

Figure 5.1: (a) Representation of the geometry of a non-ideal flight path with deviations in the Z axis (height). SLC of a simulated target obtained with: (b) Ideal flight path. (c) Non-ideal flight path with deviations in the Z axis (height).

possibilities in airborne SAR measurements. Vertical and circular flights can be combined, for example, to define new strategies to obtain three dimensional measurements of structures. Vertical flights may be used to perform vertical apertures and also to think about high resolution tomography in the future. On the other hand, circular flights might be used, for instance, to obtain high resolution Circular SAR (CSAR) images with the UAV MP in the future [96]. Finally, some pre-programmed flights with auto-trigger can be performed with the autopilot function of the UAV MP. It is important because it gives the capability to pre-define different strategies of flight, such as repeat pass interferometry in airborne SAR, thanks to the fact of having a good control of the route and the measurement instant. All these advantages make the UAV MP a versatile platform that gives a greater degree of operational flexibility with respect to conventional UAVs.

Despite the important advantages of the UAV MP, some drawbacks have also to be pointed out. It is inherently unstable if compared with the fixed wings UAVs, so its capability to perform constant velocity, straight linear trajectories is reduced. This is extremely important because errors in positioning and velocity of the platform during the acquisition time affect drastically to the measurements performed with the ARBRES-X SAR sensor. In this context, Figure 5.1 is intended to provide a graphical description of the effects of having non-uniform trajectories during the realization of the measurements. How to compensate these effects when focusing the images will be studied in detail in Subsection 5.3.1 and a real case will be exposed in Section 6.2 of Chapter 6.

Figure 5.1 (a) shows the example of a geometry considering an ideal flight path and a flight with deviations in height from the nominal track. In Figure 5.1 (b) and Figure 5.1 (c) the focusing of a Permanent Scatterer (PS) has been simulated considering an ideal flight path and a flight path with deviations in height, respectively. The focused SLC image of the PS obtained with the non-ideal flight, Figure 5.1 (c), presents an important defocusing in the azimuth direction due to the deviations of the platform from the nominal track. For this reason, these effects must be compensated when focusing the images, taking into account that the deviations from the ideal track can be present in the three spatial coordinates X, Y and Z.

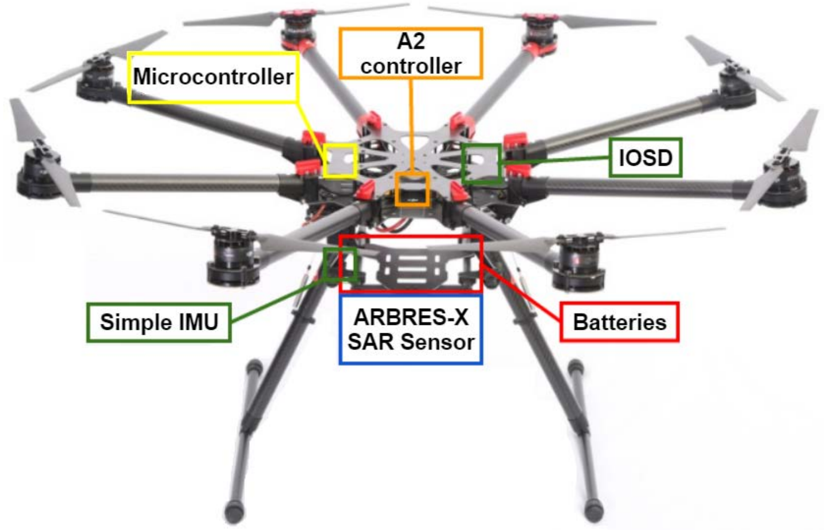

Figure 5.2: ARBRES-X SAR system complete schematic.

Another drawback of the UAV MP is the short flight autonomy with respect to the fixed wings UAVs, which reduces the total area that can be covered. The flight time, which depends on the power consumption of the system, is related with the total weight of the platform. This imposes several restrictions in weight for the integration of the ARBRES-X SAR sensor and all the additional electronics that will be analyzed along this chapter, such as the trigger control or the IMU.

The whole system requires the integration of the ARBRES-X SAR sensor, the RF front-end bar, the IMU, the electronics of control and the batteries into the UAV MP platform without exceeding the maximum takeoff weight. The SAR sensor, with a weight of approximately 2 Kg, has been placed in the lower part of the UAV MP together with the batteries of the platform and a simple IMU. It can be seen in Figure 5.2, which shows the schematic of the complete system and the location of the main components in the UAV MP. The A2 flight controller, which is responsible of the multi-rotor stabilization, is integrated in the top of the platform together with the microcontroller and the IOSD. The IOSD is the device from DJI in charge of logging the data from the IMU of the platform. The total payload is around 6.5 Kg and the whole integrated system weights around 10.5 Kg, slightly below the maximum takeoff weight of 11 Kg.

5.2.2 The ARBRES-X SAR sensor and the developed hardware contributions

The ARBRES-X SAR sensor here presented is an evolution of a previous version developed by the RSLab of the UPC [95], [97]. During the course of this doctoral activity, different hardware contributions to the system have been conducted with the aim of improving its performance. The most important contributions to the radar are exposed in this section.

The ARBRES-X is a SAR sensor operating at 9.65 GHz that works with a SLFM-CW

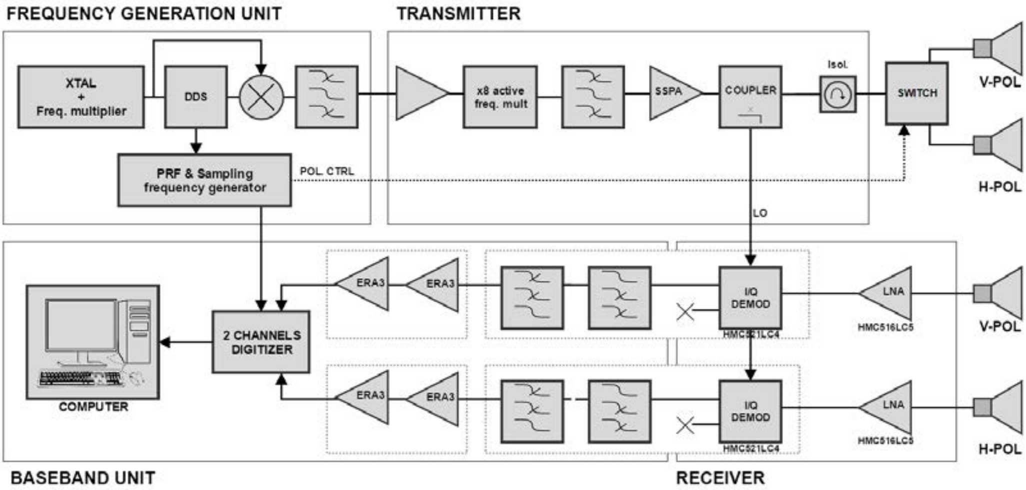

Figure 5.3: ARBRES-X system architecture.

signal. The complete system has been designed to be fitted in small UAVs. This has imposed strong constraints in its design in terms of weight, power consumption, compactness and robustness. The main characteristics of the sensor are summarized in Table 5.1 and the block diagram of the system is shown in Figure 5.3.

As mentioned before, the general architecture of the sensor is based on a previous version of the GB-SAR [65], reason for which it maintains the DDS philosophy in the signal generation. The DDS synthesizes the triangular FM with the stepped frequency technique. Normally, a PLL is used after the DDS in order to multiply and filter the base-band signal. To reduce weight and space, the PLL has not been introduced in the sensor. In the same way as the GB-SAR, the system can be divided into four units: The FGU, the transmitter, the receiver and the baseband units. The SLFM-CW signal generated in the FGU is up-converted by means of a x8 active frequency multiplier that generates the desired frequency of 9.65 GHz. Before the Radio Frequency (RF) front-end, a solid-state power amplifier generates 1 Watt of output power. The last element before the transmitting antennas, which constitutes the main hardware contribution to

Table 5.1: ARBRES-X SAR Sensor Parameters.

System Parameters	**X-Band**
Carrier Frequency (f_0)	9.65 GHz
Chirp Sampling Frequency (f_s)	44.62 MHz
Chirp PRF	5.44 KHz
Chirp Bandwidth	100 MHz
Transmitted Power	30 dBm
Range Resolution (nominal)	1.5 m
Weight	≈ 2 Kg
Power Consumption	29.3 $Watt$

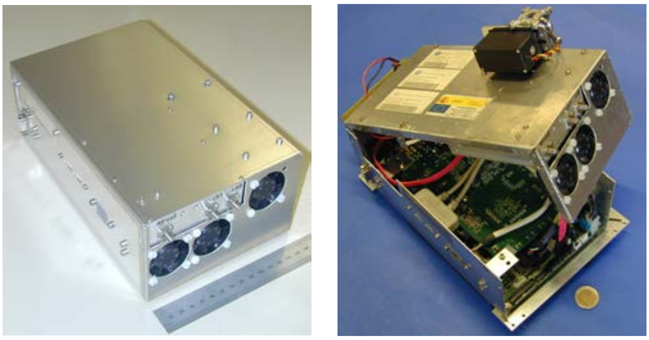

(a) (b)

Figure 5.4: (a) Closed and (b) opened ARBRES-X SAR sensor.

the sensor, is the solid-state switch responsible for providing fully polarimetric capabilities to the system.

The receiver unit takes advantage of the use of dechirp-on-receive technique to reduce its complexity [67]. It consists of two parallel low-noise chains with a direct zero-IF demodulator, where a sample of the transmitted signal is used as a local oscillator. To reduce the noise figure and to amplify the signal in the receiver, an LNA is directly connected to the antenna. After the baseband conversion, the signal acquisition in the baseband unit is performed by a commercial high speed digitizer controlled by a single board computer with a solid state hard disk drive. The two baseband signals are synchronously digitized using trigger and clock references that are coherently generated in the FGU. Figure 5.4 shows the compacted lightweight ARBRES-X SAR sensor.

5.2.2.1 The RF front-end.

Taking advantage of the work developed for the RISKSAR-X sensor, see Section 3.2, the endowment of fully polarimetric capabilities to the ARBRES-X radar has been implemented extrapolating the design performed for the GB-SAR system. Since the OtF operation mode of the RISKSAR-X radar is analogous to the way in which the ARBRES-X sensor acquires the data, the design regarding the solid-state switch is almost directly applicable, see Subsection 3.2.2. As in the RISKSAR-X sensor, the switch is used to change between the two transmitting antennas, varying the polarization for every transmitted chirp signal. The measured insertion losses, return losses and isolation of the switch integrated in the ARBRES-X sensor are shown in Figure 5.5. Figure 5.5 (a) and (b) show that in the RF1 port the return losses are -31 dB, the insertion losses are -1.3 dB and the isolation between RF1 and RF2 is -33.8 dB at the desired frequency of 9.65 GHz. Furthermore, in the RF2 port, the return losses are -24.6 dB, the insertion losses are -1.4 dB and the isolation between the two ports is -37.8 dB. It can be observed that the two ports are not symmetric but in both cases the response is acceptable.

Figure 5.6 shows the design of the board responsible of the switch control and a photograph of the board integrated in the RF front-end. This board is analogous to the one developed for the RISKSAR-X and presented in Figure 3.10 of Chapter 3, but

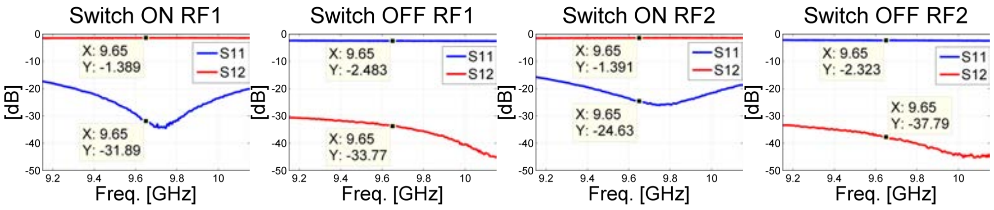

(a) **(b)** **(c)** **(d)**

Figure 5.5: Switch measurement. Insertion losses and return losses in (a) RF1. (c) RF2. Isolation in (b) RF1. (d) RF2.

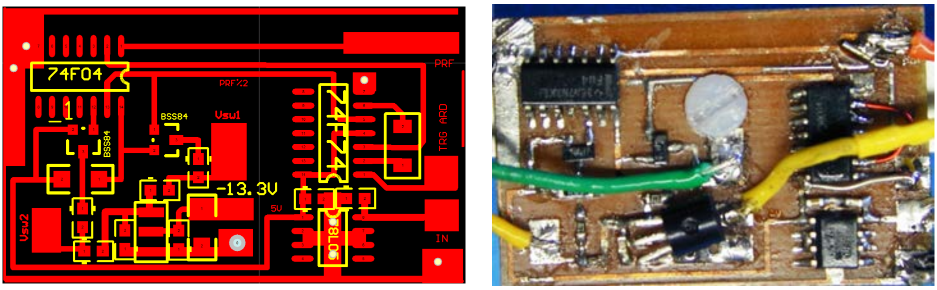

(a) **(b)**

Figure 5.6: Board responsible of the polarization control: (a) Schematic. (b) Developed prototype of the board.

with some slight modifications to adapt it needs of the ARBRES-X. The main goal when designing the board has been the integration of all the elements in the minimum space to reduce size and weight, achieving dimensions of 4x2.5 cm. The fully polarimetric capability is obtained with an array of 2x2 patch antennas transmitting and receiving in both vertical and horizontal channels. The microstrip antennas follow the same principles as its predecessor, prioritizing the reduced dimensions and weight to easily integrate them in the MP without compromising the aerodynamics. This patch radiators present reduced sidelobes with acceptable antenna efficiency. On the contrary, due to its reduced dimensions, they have a wide antenna beamwidth [95]. Figure 5.7 shows the measured antenna patterns where the blue line correspond to the normalized radiation diagram cut and the red line correspond to the Cross Polarization Discrimination (CPD) factor, which is approximately -22 dB. It can be seen that the microstrip antennas present a beamwidth of approximately 36° in the E plane and 42° in the H plane.

Regarding the composition of the receiving antennas, they have been re-designed incorporating the LNA and making them an active element as a whole. This way, the RF front-end is compacted, achieving a reduction of the total weight of the system in addition to saving space. Furthermore, the noise factor is reduced since the LNA is placed just after the antenna. Figure 5.8 shows a photograph of a prototype of the receiving antenna where the different elements can be seen, including the integrated LNA.

Unlike the previous platform based on the fixed wings UAV, where the patch radiators were fixed directly in the aircraft fuselage, the structure of the UAV MP does not have

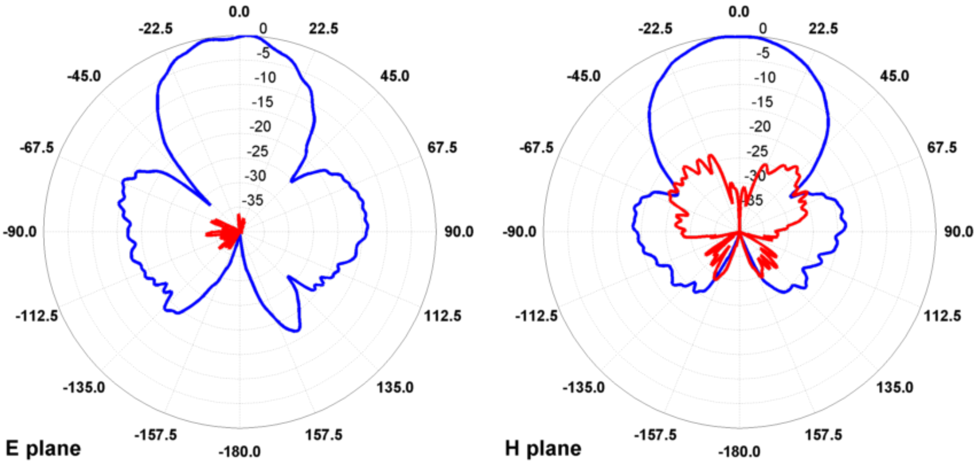

(a) **(b)**

Figure 5.7: Measured antenna patterns. Normalized radiation diagram cuts in dB. (a) E-plane. (b) H-plane.

this kind of flat surfaces necessary to effectively integrate the antennas. As a result, a new RF front-end has been specifically designed and developed to be integrated into the UAV MP. It consists of a light-weight aluminum bar together with the microstrip antennas, the switching board presented in Figure 5.6 and the solid-state switch. Furthermore, it has also attached a connector responsible of carrying the power supply and the polarization control. All together aims to have low inertia and not to affect the aerodynamics of the platform. Finally, a servo motor fixed to the system and controlled by a simple Inertial Measurement Unit (IMU) holds the RF front-end. Its purpose is to maintain the antennas in horizontal position with respect to the ground, compensating the inherent tilt angle of the platform while flying. Figure 5.9 (a) shows the schematic of the RF front-end and Figure 5.9 (b) shows a photograph of the lightweight aluminum bar integrated in

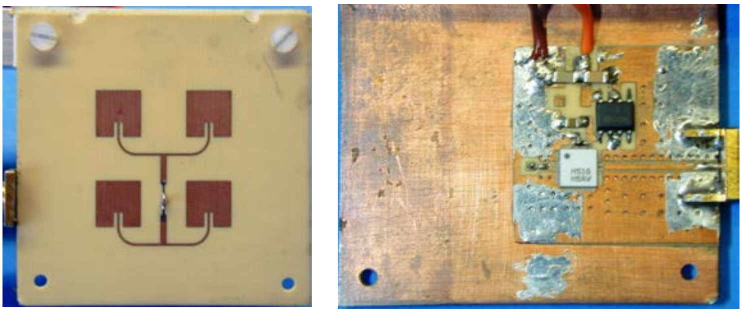

(a) **(b)**

Figure 5.8: Picture of the prototype of the active receiving microstrip antenna: (a) Front part consisting of the radiating elements. (b) Back part with the LNA incorporated.

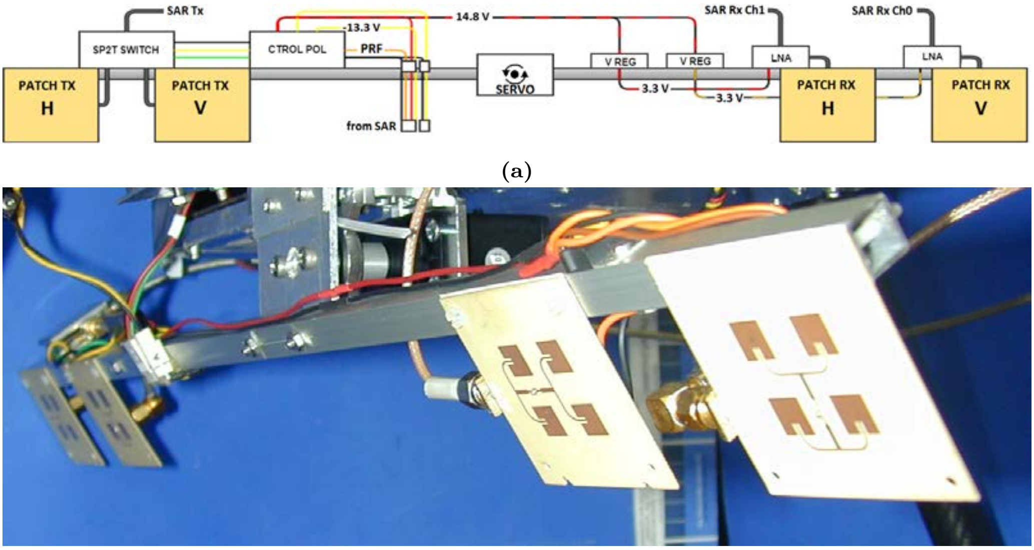

(a)

(b)

Figure 5.9: Transmitter/receiver RF front end: (a) Schematic of the light-weight aluminum bar. (b) Photograph of the light-weight aluminum bar together with the patch antennas.

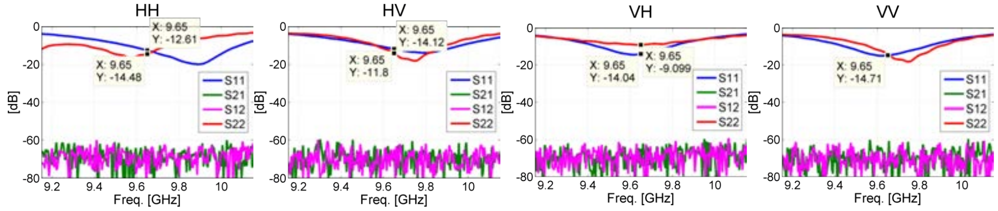

(a) (b) (c) (d)

Figure 5.10: Measured S parameters of the patch antennas for each polarization: (a) HH. (b) HV. (c) VH. (d) VV.

the system and attached to the servo motor. In the image, the abbreviations SP2T and VREG correspond to Single-Pole Double-Throw and Voltage Regulator, respectively.

The separation between the cross-polar transmitting and receiving antennas is approximately 43 cm for the VH polarization and 58.6 cm for the HV polarization. Besides, the co-polar separation is around 50.8 cm. This separation between antennas is enough to ensure good isolation between them, as can be seen in Figure 5.10, where the S parameters of the patch antennas measured in the anechoic chamber of the UPC are shown. The isolation between the antennas for the different polarizations is around -70 dB and the return losses are acceptable, ranging from -9 dB in the S_{22} for the VH polarization to -14.71 dB in the S_{22} for the VV polarization.

It has to be considered that the array of antennas is not placed in the center of gravity of the platform but on a displaced position, as it is shown in Figure 5.11. Concretely, the phase center of the cross-polarization antennas is displaced from the center of the platform 9.5 cm and 1.5 cm in the Y and the X axis respectively. Moreover, it is displaced 30 cm in the Z axis from the top of the platform. This implies that the rotation movements of the platform roll, pitch and yaw are related with this displacements in the three axis and the variation of the position of the antennas. Moreover, the location of the sensor in the lower part of the platform favors the apparition of undesired motion errors of the antennas, such as for instance an oscillatory movement like a pendulum. To compensate

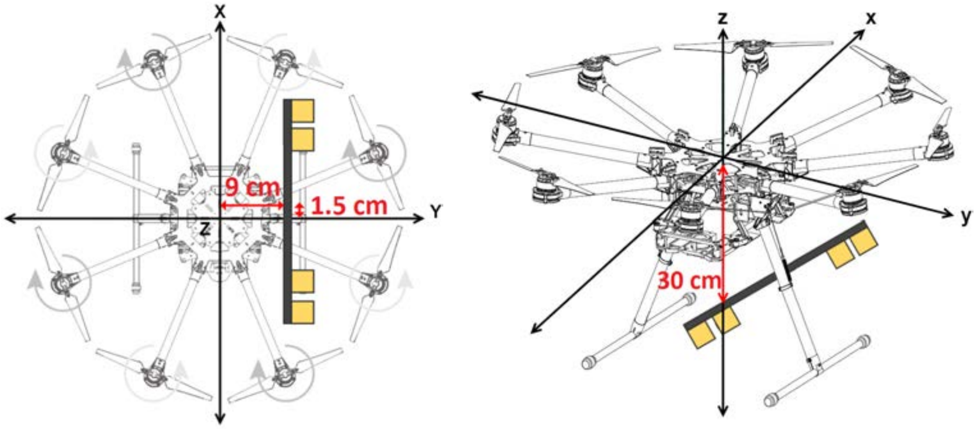

(a)

(b)

Figure 5.11: Displacement of the antenna arm position in the UAV MP: (a) X and Y axis. (b) Z axis.

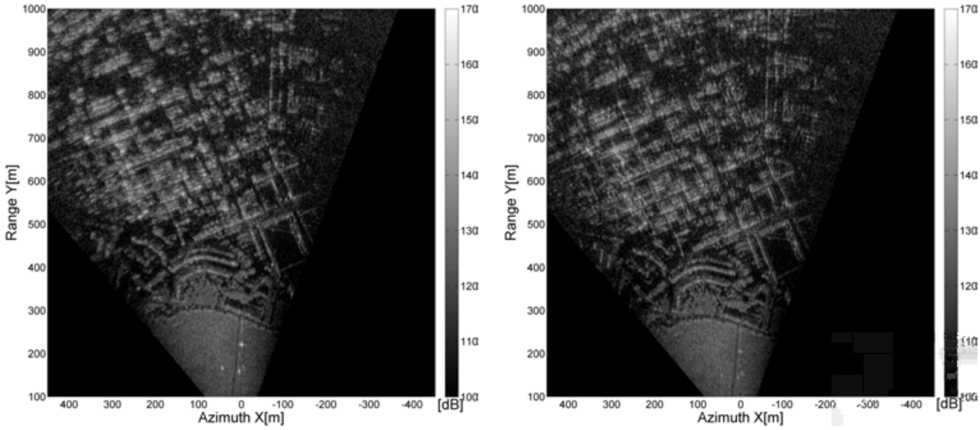

(a)

(b)

Figure 5.12: Yaw deviation in SLC images in Cartesian coordinates. (a) Before autofocus. (b) After autofocus. Flight conditions: Aperture= 40.9 m, 100 m height, $v_{UAV} = 8.9 m/s$, VV Pol.

for the undesired motion errors applying MOCO techniques, the position of the antennas with respect to the location of the IMU should be characterized.

An example of the relation between the rotation errors and the positioning of the antennas can be seen in Figure 5.12 where it is shown an example of SLC image obtained with a deviation in the yaw angle when performing a measurement illuminating the scenario of the Real Aero Club Barcelona-Sabadell (RACBSA) airfield in Ripollet (described in Section 6.1). In this example, the 2x2 patch antennas were substituted by ones with a smaller azimuth beamwidth that better evidenced the effect of the yaw error. As can be observed, there was an error in the yaw dimension during the acquisition time, which provoked a deviation of the antenna mean beamwidth. For that reason, the reflective area is not centered in the image. This is of great importance because it can degrade, for instance, the quality of repeat-pass interferometric measurements. In that case, if the yaw angle varies between the two different passes, the SLC images could not be correctly registrated, affecting the interferometric process.

5.2.3 Other electronics

Auxiliary electronics are necessary to perform SAR measurements. On the one hand, a IMU in charge to monitor all the movements of the platform while measuring is mandatory. As previously exposed, the UAV MP is relatively unstable compared with a fixed wings UAV. For that reason, flight deviations from the nominal track and the undesired motion errors must be measured with great precision to be compensated in processing steps. The device responsible of logging the inertial data is the IOSD MARK II from DJI, see Figure 5.13 (a). It has been selected for its compact size (52x41x11 mm), low weight and high compatibility with the UAV A2 controller. Besides, the system incorporates a barometer, which is indispensable to know the altitude of the platform with much higher accuracy with respect to the one given only by the GPS. Another advantage of this system is that, being combined with the A2 flight controller, the moment in which the SAR system starts the measure can be stored together with the inertial data. This would be necessary to be able to use the inertial data to apply MOCO techniques.

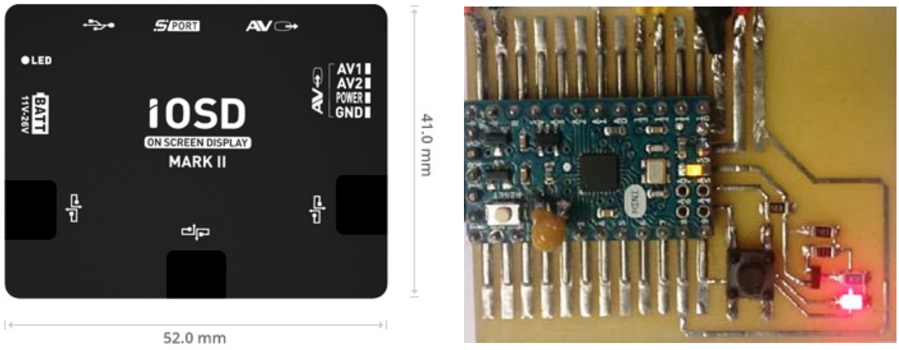

(a)

(b)

Figure 5.13: (a) IOSD MARK II IMU from DJI. (b) Board of the microcontroller responsible of triggering the SAR system.

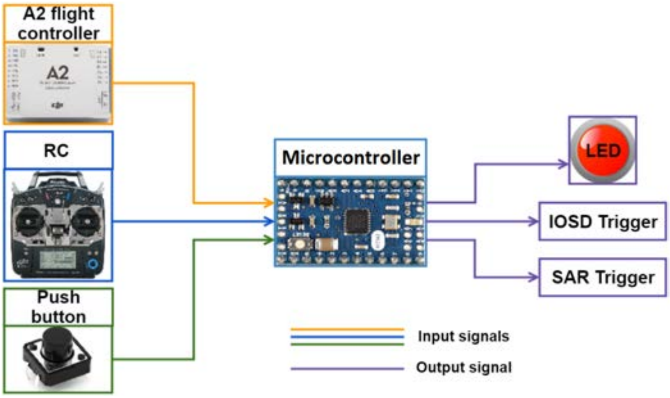

Figure 5.14: Diagram of the trigger generation with the microcontroller.

On the other hand, a microcontroller responsible to manage the start of the acquisition is also integrated in the UAV MP, see Figure 5.13 (b). It has been chosen because of its reduced dimensions and low power consumption. The system has been designed to be triggered in three ways; manually by pressing a push button integrated in the microcontroller board, manually by activating a button in the radio controller of the platform and automatically with the A2 controller. The push button in the microcontroller board, see Figure 5.13 (b), is intended to test the trigger system. The button in the radio controller is useful in manual flights of the platform, when the start of the acquisition has to be manually activated. Finally, the most interesting solution is triggering the system automatically. One of the channels of the A2 controller can be programmed to send the order to trigger the system. This can be done in automatic flights of the platform, where the system stores the inertial data together with the raw data of the SAR acquisition. Figure 5.14 shows the diagram of the trigger generation with the microcontroller contemplating the different possibilities.

5.3 ARBRES-X raw data processing

In the same way as in Section 3.3 for the RISKSAR-X case, this subsection is intended to provide an overview of the different processing steps that must be conducted to focus a SAR image obtained with the ARBRES-X SAR system. Basically, the procedure is analogous to the one conducted in the GB-SAR but with some peculiarities that will be discussed below.

The data storage and raw data matrix decomposition varies from the RISKSAR-X system since in the ARBRES-X system it is used a different acquisition card. Concretely, it is used the PCI 9820 from Adlink technology. In this case, the digitizer is programmed to acquire 4096 samples with a sample frequency of 44.625 MHz every rising edge of the PRF. As shown in Figure 5.15, the system stores 1 sample for each channel alternatively. In the fully polarimetric case, the switch changes its position every 8192 samples, following the same philosophy as explained in Figure 3.12. The maximum number of chirp pulses stored is 60000, which will limit the maximum processable aperture length. From the stored vector, the raw data matrices must be decomposed as in Figure 3.15 (b), which

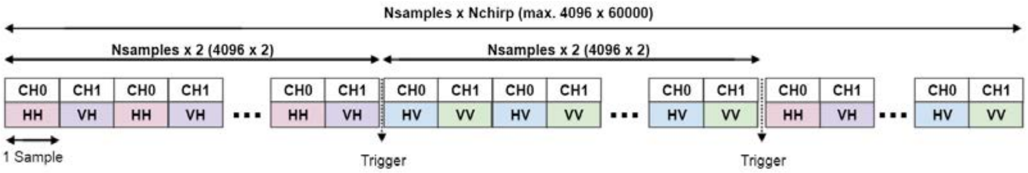

Figure 5.15: Diagram summarizing the data storage of the ARBRES-X SAR system operating in the fully polarimetric case.

means that every polarization matrix will have a maximum size of [4096,15000] samples.

As an example, some numbers can be given about the maximum attainable aperture length. With the PRF of the system of 5.445 KHz and assuming a constant velocity of the platform of 9 m/s, the maximum aperture length that can be performed is 99.17 m in the SP case and 44.58 m in the fully polarimetric (FP) case. In the latter, the maximum aperture length is half that in the SP case, since every PRF the digitizer stores the data with 2 channels.

Once the raw data matrices are generated, the processing steps are the same that in the GB-SAR. First the presuming technique is applied reducing the amount of data to be processed and then the range-compression is applied by means of the FFT. The zero-padding and the use of filtering windows are exactly the same as in the RISKSAR-X. The area illuminated by the ARBRES-X SAR sensor is extended to approximately 1500 m in range and 900 m in azimuth. Analogously to the RISKSAR-X sensor, the SLC images obtained from the retrieved data are processed off-line. In this context, the range compressed signal is focused in the azimuth domain with the BPA [24]. In this case, the range resolution obtained with the parameters used by the ARBRES-X SAR sensor is approximately 1.5 m and the cross-range resolution depends on the type of measurement. The application of the BPA in UAV airborne SAR represents an optimal solution since it can directly include in the focusing process the movement compensation, which is essential when focusing images taken with this type of platforms. The algorithm inherently compensates the motion errors since the position of the sensor is used during the process. As will be discussed in Chapter 6, if the GPS together with the IMU provides high precision information, this step is easily applicable.

5.3.1 Autofocus algorithm

Another alternative to compensate the motion errors of the UAV MP is the application of an autofocus algorithm. This could be very useful in the case of lack of high precision inertial data which permits the application of MOCO techniques. Different techniques have been proposed in the literature that are used to compensate for motion errors in UAV SAR imagery [98], [99]. In our case, an algorithm based on the retrieved phase history of different PS has been selected [100]. The objective is to derive the deviations of the platform in the three axes by means of the retrieved phase history of three PSs. Since in real measurements it is difficult to find three natural PS in the scenario with good reflectivity response, normally three different PARCs are placed in visible and accessible locations.

According to Equation 2.5 of Section 2.2 in Chapter 2, the phase evolution of a given PS along the aperture can be expressed as a function of the slant range distance $r_{PS}(t)$ from the sensor to the PS during the slow time t, which i.e. is the distance from the sensor to the PS for every antenna position during the acquisition time. The relative distance $r_{PS}(t)$ can be expressed by the quadratic function as

$$r_{PS}(t) = \sqrt{(x_{PS} - x_a(t) - u_x(t))^2 + (y_{PS} - u_y(t))^2 + (z_{PS} - u_z(t))^2} \tag{5.1}$$

where x_{PS}, y_{PS} and z_{PS} correspond to the ideal position of the PS in the X, Y and Z axis respectively, $x_a(t)$ is the azimuth antenna position during the slow time and $u_x(t)$, $u_y(t)$ and $u_z(t)$ are the positioning errors of the platform in the three axis with respect to the nominal flight path. Figure 5.16 illustrates the described ARBRES-X SAR geometry with deviations from the nominal flight track were it can be seen an example of the nominal flight track compared with the real one. It should be noted that the real track not only follows a different trajectory, but also has superimposed a motion error due to the platform instability.

Having three PSs, a system of three non-linear equations and three unknowns can be solved for every azimuth position of the platform. Thus, the deviations of the platform $u_x(t)$, $u_y(t)$ and $u_z(t)$ can be derived to refocus the image. In order to do so, the retrieved deviations can be directly introduced in a second iteration of the BPA to obtain a better focused image. It has to be taken into account that, normally, the retrieved motion errors must be filtered to avoid undesired effects of blurring in the compensated image. This is necessary because the retrieved parameters can present some noise that could be

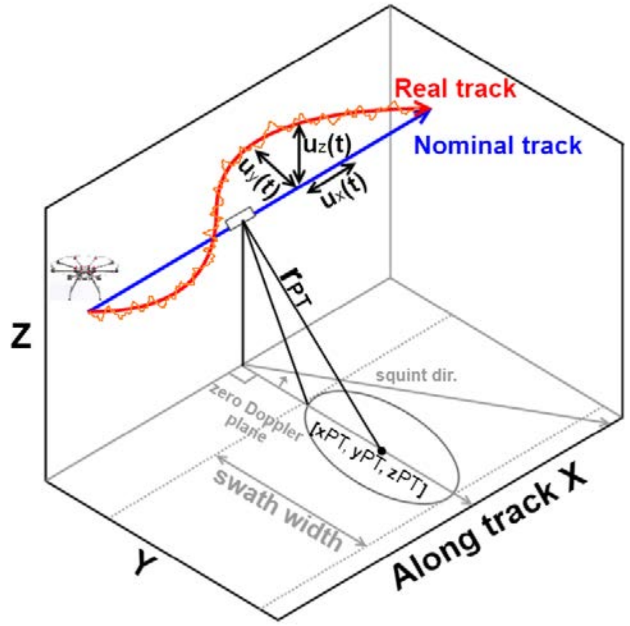

Figure 5.16: Illustration of the ARBRES-X SAR geometry. Blue: Ideal flight track. Red: Flight track with deviations.

introduced by irregularities in the phase or by inaccuracies when solving the equations. Because of that, they must be filtered to prevent the SLC images from being degraded when introducing the coefficients in the BPA. In our case, to perform the filtering, a moving average low-pass filter is used. Figure 5.21 (a) summarizes the different steps of the autofocus processing for the ARBRES-X SAR sensor.

To assess the capability of the autofocus algorithm to compensate undesired motion errors in the three different axes, some simulations have been performed. Since there are several cases to be taken into account, it has been considered appropriate for completeness to add an appendix with different simulations and conclusions (see Appendix A). In each simulation, 5 PSs that reproduce the response of PARCs located at different ranges and with different squint angles are introduced. The targets positions are [0,200], [0,350], [0,450], [-50,300] and [-100,400] meters, respectively. Then, different types of motion errors have been introduced in the generation of the raw data, analyzing the effect of such deviations in the SLC images. After that, the autofocus algorithm is applied using the Newton Raphson method to solve the set of non-linear equations [101]. Once the positioning errors are derived, they are introduced in a second iteration of the focusing process to compensate for the undesired deviations.

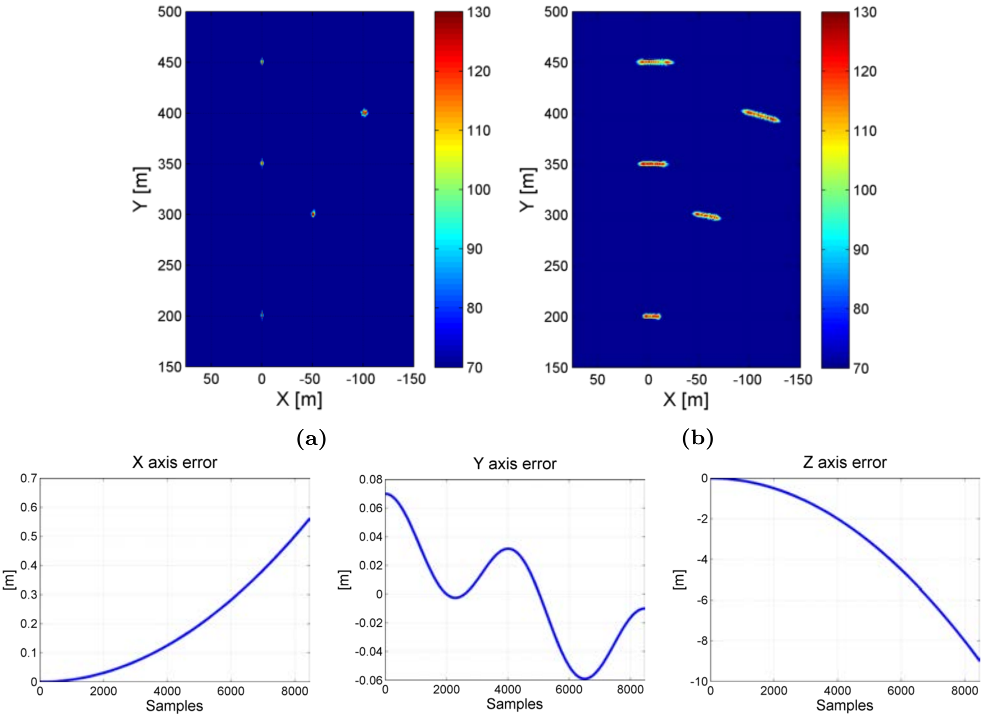

(a) (b)

(c) (d) (e)

Figure 5.17: Simulated aperture of 14 m. (a) SLC with an ideal flight path. (b) SLC with deviation errors in the flight path. Deviation errors introduced in the: (c) X (d) Y and (e) Z axis.

Figure 5.17 (a) shows the simulated SLC image without any deviation error while Figure 5.17 (b) shows the simulated SAR image introducing the errors represented in Figure 5.17 (c), (d) and (e) for the X, Y and Z axis, respectively. The targets in the SLC image with errors present an important spreading in the azimuth direction that is accentuated with the range distance and the squint angle. It has to be commented that the deviations from the nominal track introduced in the simulations are typical of the UAV MP and have been extrapolated from the observation of several flights of the platform. Nevertheless, in the proposed simulation those deviations have been pushed to the extreme to maximize their effect on the focused images. Figure 5.17 (c) shows the error in the X axis related to an acceleration of the platform during the acquisition time. In Figure 5.17 (d) a decreasing periodic error en the Y axis is observed, which is related to two different phenomena. First, the platform is not following an straight path but a curved line that is approaching to the target. Moreover, as in the case of a pendulum, the radar located in the lower part of the UAV MP is oscillating, moving closer and away from the illuminated scenario. Finally, Figure 5.17 (e) shows a decreasing in the height of the platform due to the inclination of the UAV, which is typical in this type of drones when they are accelerating.

Figure 5.18 (a), (b) and (c) show the simulated measured and ideal slant range from the sensor to the targets extracted from the retrieved phase of each simulated PS. In the images, the difference between the ideal and the measured curves is given by the introduced deviations of the platform from the nominal flight path. After solving the non-linear equations with the Newton Raphson method, the deviations in the three axis are retrieved and shown in Figure 5.18 (d), (e) and (f). It is important to remark that,

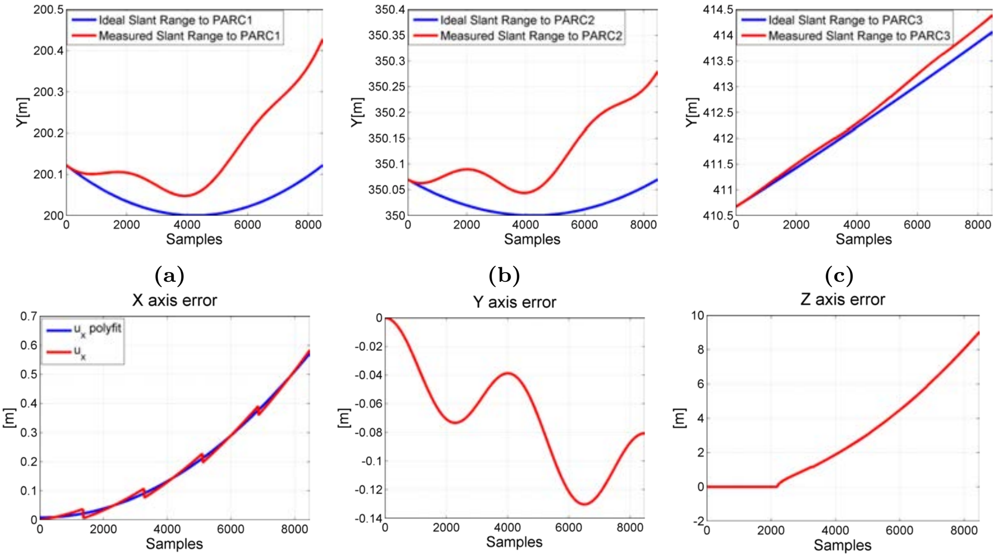

(a) (b) (c)

(d) (e) (f)

Figure 5.18: Retrieved slant range distance from the sensor to (a) PARC1 [0,200]. (b) PARC2 [0,350] (c) PARC3 [-100,400]. Retrieved motion errors in (d) X, (e) Y and (f) Z axis.

to obtain good results with this method, the retrieved phase from the selected target must be of high quality. Otherwise, the retrieved deviations will not be good enough to be introduced in the focusing process, provoking a defocusing effect in the compensated SAR images, see Appendix A. In this context, it has been concluded that the targets presenting better phase information are those centered in the middle of the aperture, which are preferable to obtain the deviation errors in the Y and Z axis. The high quality of the phase of this targets may be due to its optimal illumination during the complete aperture, since normally they present an anisotropic behavior.

Despite being preferable to select centered targets, in the case of the $u_x(t)$ error associated to the velocity of the platform it is necessary to select a squinted scatterer. The main reason is that the velocity errors affect mainly to those targets that are not centered in the aperture. The more squinted the target, the more defocused it appears in the SLC image in presence of velocity errors. But the problem is that the phase information of squinted targets is normally of low quality and also normally present discontinuities due to problems with the phase unwrapping, reason for which the Newton Raphson method does not work optimally. This provokes that the retrieved parameters $u_x(t)$, $u_y(t)$ and $u_z(t)$ from squinted targets also present some discontinuities and must be approximated, as is the case shown in Figure 5.18 (d). In this cases, the retrieved deviation must be approximated to avoid discontinuities that may degrade the focusing process. However, this approximation might penalize the azimuth resolution of the focused image.

On the other hand, it can be seen in Figure 5.18 (f) that the retrieved error $u_z(t)$ is nearly 0 for the first 2200 samples approximately, which corresponds to an error in height of roughly 0.6 m (almost half of the resolution cell). This is because small height errors does not affect too much to the focused image. The resulting SLC image obtained after introducing the retrieved deviations represented in Figure 5.18 to the BPA is shown in Figure 5.19 (b). Comparing Figure 5.17 (b) with Figure 5.19 (b), it can be seen that, even introducing heavy deviations in the trajectory of the platform, the simulated targets have been compensated minimizing the spreading effect.

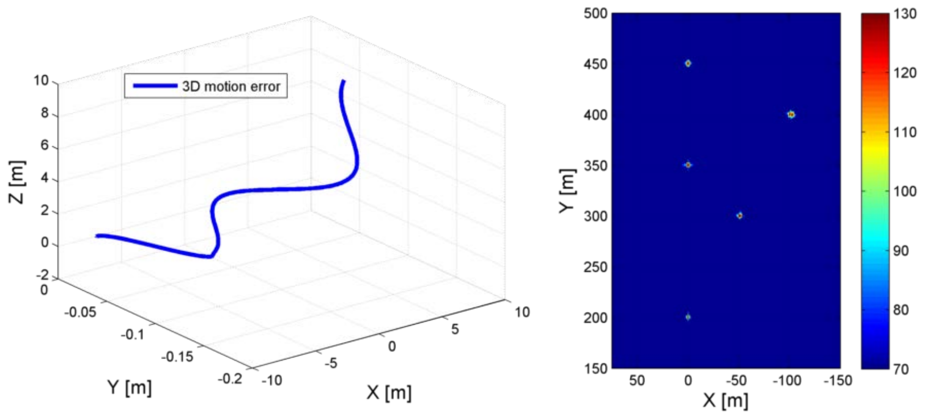

(a)

(b)

Figure 5.19: (a) 3D representation of the platform deviations introduced in the BPA. (b) Compensated SLC image.

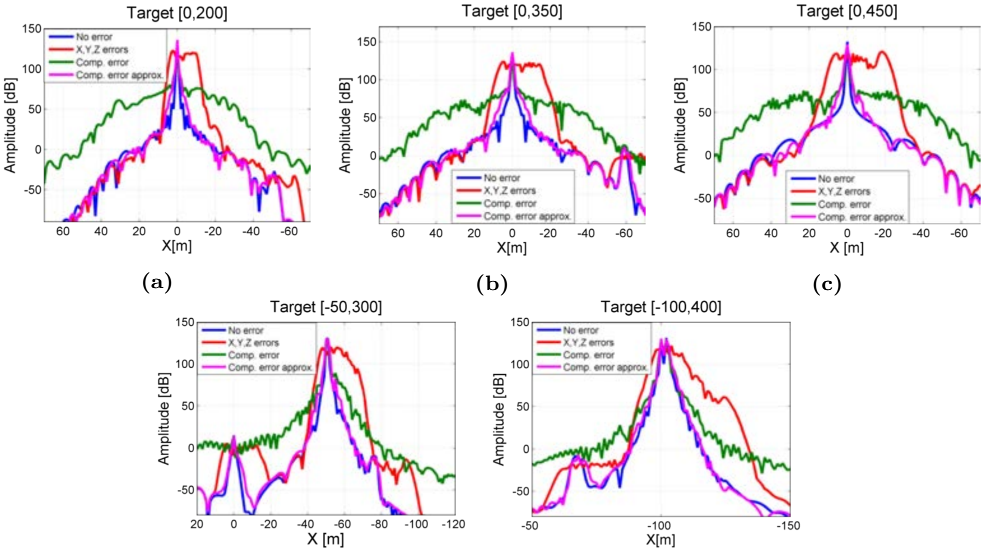

(a) (b) (c)

(d) (e)

Figure 5.20: Cut in azimuth of the PARCs: (a) PARC1 [0,200] m. (b) PARC2 [0,350] m. (c) PARC3 [0,450] m. (d) PARC4 [-50,300] m. (e) PARC5 [-100,400] m. Blue: No deviation errors. Red: X,Y,Z deviation errors. Green: Compensated error without approximating X deviation. Magenta: Compensated error approximating X deviation.

To evaluate the azimuth resolution of the simulated targets before and after the application of the autofocus algorithm, the cut in azimuth of the different targets has been analyzed. Figure 5.20 shows the cut in azimuth of the different PSs where the results for the different cases of the autofocus algorithm can be analyzed. In blue it is represented the cut of the simulated PSs focused without any motion error and in red the cut is presented after introducing the extreme deviations in the three axis. It is observable a noticeable spreading effect in the response of all the simulated targets, which means a loss of the azimuth resolution due to the simulated deviations. Moreover, the green and magenta lines represent the response of the targets after applying the autofocus algorithm. In green it is shown the azimuth cut without approximating the retrieved $u_x(t)$ deviation and the magenta line after approximating it. As expected, when comparing the two responses in Figure 5.20, the first one presents a higher value of noise floor for all the targets with differences of up to around 50 dB. Nevertheless, the cut in azimuth of the targets after approximating the $u_x(t)$ parameter might present a slight worsening in the obtained azimuth resolution, see magenta line. This can be observed in Table 5.2, which summarizes the theoretical and the measured 3 dB resolutions after the autofocus algorithm for the different cases.

As the performed aperture lengths are shorter than the dimensions of the illuminated scenario, the theoretical azimuth resolution δ_{az} is computed according to Equation 3.1. In this context, it is worth mentioning that the theoretical azimuth resolution presented in the in Table 5.2 does not consider the azimuth windowing. In the same way as in the RISKSAR-X case, in order to reduce the secondary lobes that can degrade the quality

Table 5.2: Azimuth resolution

	Azimuth resolution [m]				
	Theoretical	**No Error**	**X,Y,Z errors**	**Comp. error**	**Comp. approx. error**
Target[0,200]	0.22	0.39	13.1	0.39	0.44
Target[-50,300]	0.34	0.69	25.7	0.78	0.97
Target[0,350]	0.38	0.49	20.5	0.45	0.71
Target[-100,400]	0.44	0.56	34.35	0.57	0.57
Target[0,450]	0.48	0.49	25.18	0.86	0.82

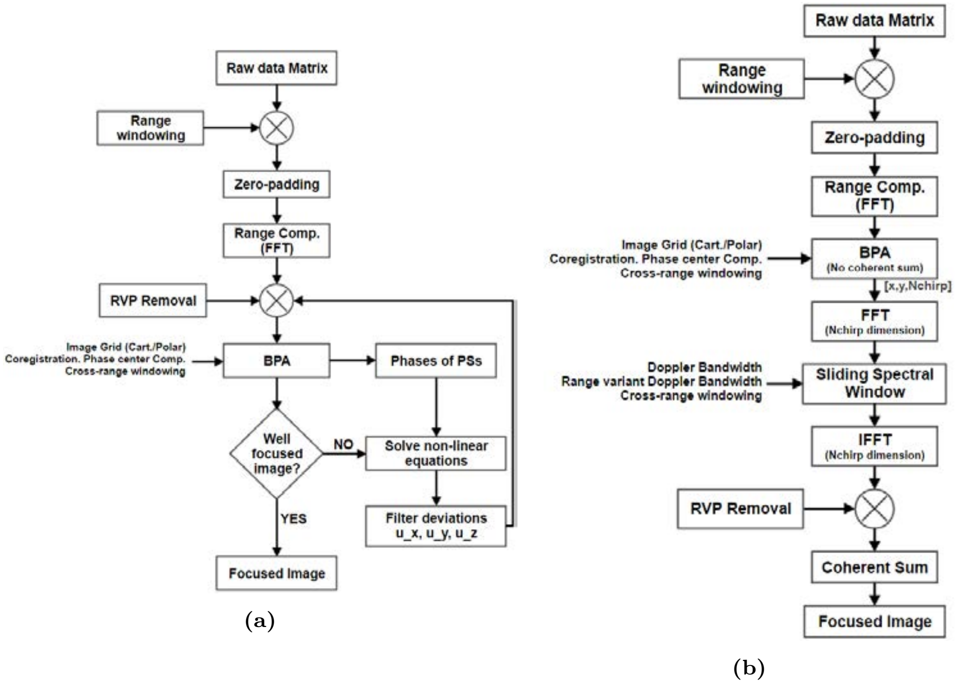

(a)

(b)

Figure 5.21: Processing flowchart for the ARBRES-X SAR sensor: (a) Autofocus processing scheme. (b) Advanced processing scheme.

of the focused image, a Hanning filter window is applied in the cross-range domain. In agreement with [102], the main lobe resolution is worsened by the effect of the Hanning window. Taking this into account, the measured azimuth resolutions after the autofocus algorithm are quite acceptable compared with the theoretical ones.

5.3.2 Advanced Processing

To improve the results obtained with the ARBRES-X SAR sensor some advanced processing can be conducted. The objective of this additional steps is to retrieve better quality focused images by means of applying a sliding spectral window during the processing, filtering the signal in the cross-range domain. Although the implementation of this procedure is very time consuming and requires a lot of CPU resources, it could be of interest in applications where a high quality of the retrieved phase is important, such as in interferometric measurements. The advanced processing steps are detailed in the present subsection and Figure 5.21 (b) summarizes the processing flowchart applied to the ARBRES-X focusing process.

As shown in the processing scheme of Figure 5.21 (b), once the image grid of the resulting image is defined, each pixel is associated to a sample of the range compressed zero-padded data by means of the BPA. But in this case, the RVPE is not yet compensated and the coherent sum of every azimuth position of the antenna is not done. Instead of that, a matrix for every azimuth position of the platform is stored. This way, the evolution of the pixels during the entire aperture can be analyzed, which is a vector of N_{chirp} samples for every pixel. As explained in Section 3.3 in Chapter 3, the length of the vector can be reduced by applying the presuming technique. The next step is to perform the FFT for later application of the sliding spectral window. From now on and for the sake of simplicity, only a particular pixel associated to a PS will be considered. According to [103], if the target is seen by the radar under an angle φ_{az}, the Doppler bandwidth of the synthetic aperture can be expressed as

$$B_a = \frac{2v}{\lambda}\Delta_{\varphi} \tag{5.2}$$

where $\Delta_{\varphi} = sin(\varphi_{az_{max}}) - sin(\varphi_{az_{min}})$ is the difference between the minimum and maximum angle under which the target is illuminated, as can be seen in Figure 5.22.

Considering an aperture length shorter than the dimensions of the focused images, Δ_{φ} can be approximated as

$$\Delta_{\varphi} \approx \frac{L_{sa}}{r_T} \tag{5.3}$$

yielding the range variant Doppler Bandwidth

$$B_a \approx \frac{2vL_{sa}}{\lambda r_T}. \tag{5.4}$$

The range variant Doppler Bandwidth is converted to samples by means of the Doppler frequency resolution $dx = \frac{PRF}{N_{chirp}}$ to know the size of the spectral window. Once the spectral window is defined it is applied to the data in the frequency domain, discarding

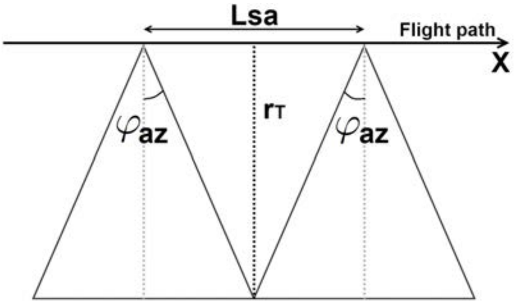

Figure 5.22: Sketch illustrating the SAR observation geometry.

the unnecessary samples. After that, the Inverse Fast Fourier Transform (IFFT) in the azimuth direction is performed to recover the temporal signal, being able to obtain a better quality of the information of the pixel. Finally, the last step to obtain the focused image is to compensate the RVPE and coherently sum the contributions of every antenna position to the pixel.

To exemplify the processing steps, the procedure is applied to a measurement performed in the RACBSA airfield in Ripollet. The selected pixel under study corresponds to a PARC located at [-2.6, 265] m in the scenario. Figure 5.23 shows the amplitude and phase evolution of the pixel before and after the application of the sliding spectral window. As can be observed in Figure 5.23 (a), the window only selects the samples corresponding to the response of the PARC and discards the rest. Besides, in Figure 5.23 (b) it can be appreciated how after the application of the sliding spectral window the retrieved phase is filtered and is less noisy than the phase before the application of the window.

On the other hand, Figure 5.24 (a) shows the RVPE compensation function applied to the pixel evolution after the spectral windowing, which should be complementary to

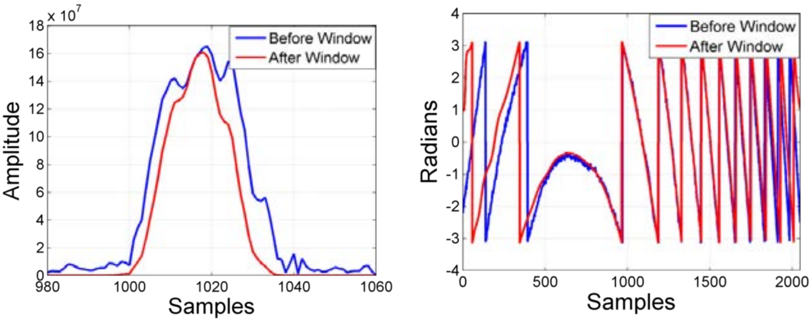

(a) (b)

Figure 5.23: Evolution of the pixel before and after the application of the sliding spectral window: (a) Amplitude. (b) Phase.

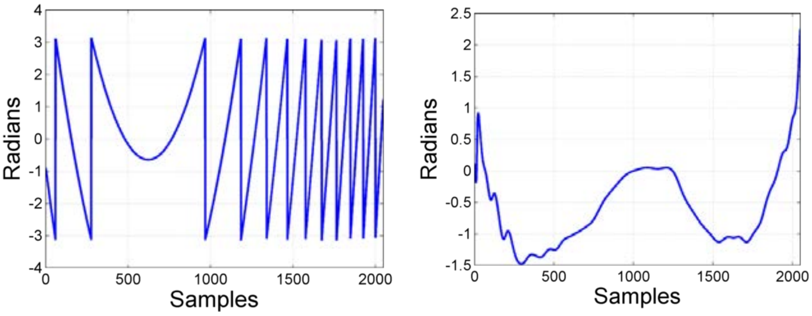

(a) (b)

Figure 5.24: (a) RVP compensation function. (b) Unwrapped phase after RVP compensation.

the phase of Figure 5.23 (b). Moreover, Figure 5.24 (b) shows the unwrapped phase after the RVPE compensation, which should be nearly zero. As can be observed, it is not perfectly compensated and there are errors that may be related with the velocity of the platform. In this sense, analyzing the unwrapped phase after compensating the RVPE is a good indicative to know if the selected velocity of the platform is correctly done, which can be used as complementary information to the data stored by the IMU. In a case like the one chosen in the example, the focusing process could be optimized by dividing the complete aperture into small sub-apertures. Each sub-aperture can be processed adjusting the velocity of the platform to improve the RVPE compensation. Finally, the resulting azimuth spacing obtained for the different sub-apertures can be integrated together to perform the complete aperture and complete the results.

The advanced processing has been introduced in the focusing algorithm to improve the results obtained in Chapter 6, such as for instance in the measurements performing repeat pass interferometry. It has been concluded that, even improving the quality of the retrieved phase, the results remain the same. This is because the most important errors are introduced by the flight instabilities and the deviations from the nominal trajectory, which should be improved as the main objective.

5.3.3 Coregistration for interferometry

Once the image has been focused, some steps might be necessary before the formation of the interferogram. Coregistration is needed in almost any kind of interferometric applications related with airborne and orbital SARs. It is intended to ensure that the information of a given resolution cell is associated to the same pixel in both the master ans slave images.

Considering the ideal case in which the two passes of the platform were perfectly parallel and with aligned acquisitions, coregistration would only need to account for the difference in the geometry due to different illumination angles. The two images would have different projections of the observed scene, which requires over-sampling and interpolation to locate the correlation peaks and match the slave image with the master image. If not, the interferometric phase could be noisier or even completely decorrelated. Normally, a coregistration error smaller than 10 % of the resolution cell is acceptable. One possibility to estimate the offset between images is to use the cross-correlation of the amplitude or the intensity.

However, perfectly parallel and aligned passes are difficult to achieve in the case of the ARBRES-X SAR sensor due to the inaccuracy of the navigation system, which causes that the two passes of the platform are normally far from the ideal case. It has been observed that different effects can degrade the interferometric process:

- Variation of the platform altitude during the acquisition, resulting in a non constant baseline during the aperture.
- Different platform attitudes. Errors in roll, pitch and yaw angles alter the trajectory of the platform and the illuminated scenario. An example could be the variation in the yaw angle shown in Figure 5.12 of the present chapter.
- Different velocities of the platform. This affect the azimuth sampling and the proper alignment of the trajectories, provoking an undesired shift between the two passes.

To assess the effects of non-aligned passes, an experiment with the ARBRES-X SAR sensor has been conducted in the Collserola test site. To that purpose, the radar has been mounted in the linear unit used by the GB-SAR performing an aperture of 2 m and with the aim of performing single pass interferometric measurements. The first measurement has been done with one of the receiving antennas (antenna 1) connected to the first channel of the acquisition card and the second antenna (antenna 2), with a vertical baseline of approximately 50 cm, connected to the second channel. Figure 5.26 shows the obtained SLC images as well as the coherence and the interferometric phase. As expected, the interferometric phase presents some fringes in the zone with reflectivity corresponding to the Collserola mountain. Then, another measurement has been performed but displacing antenna 2 approximately 14 cm in the azimuth direction. Figure 5.27 shows the coherence and the interferometric phase before and after the image rough coregistration. The location of the antennas in the geometry of the experiment can be visualized in the scheme presented in Figure 5.25.

Before coregistering the images, the interferometric phase shown in Figure 5.27 (b) presents fringes in the azimuth direction introduced by the horizontal separation of the antennas. These fringes have been compensated in Figure 5.27 (d) after the image coregistration, but the number of coherent pixels and the quality of the interferogram have been reduced. This could be due to an azimuth spectral shift introduced by a variation in the Doppler centroid between the two antennas resulting in a less common bandwidth between the two acquisitions. Prior to the interferometric cross-product generation, the uncorrelated contributions that behave like noise could be filtered, keeping the common bandwidth to improve the results.

After these results, where it has been observed a degradation of the quality of the interferometric phase and a reduction of the coherence, a new experiment has been performed to better understand the effect of having non-aligned passes. To do that, it has been used a measurement conducted by the RISKSAR-X sensor in the Montserrat test site. This measurement has been selected because of the robustness and reliability of the GB-SAR sensor, since the conclusions obtained can be directly applicable to the ARBRES-X SAR sensor. The idea was to obtain the coherence and the interferometric phase of two images

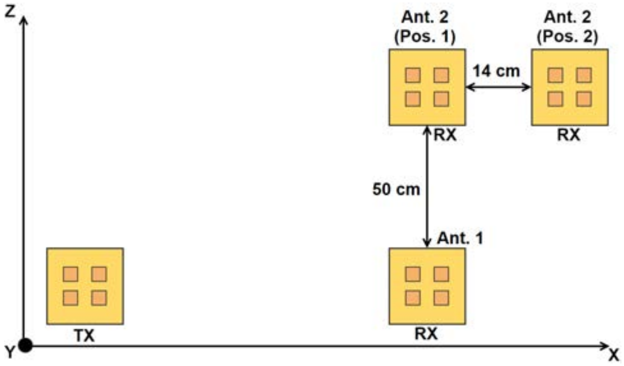

Figure 5.25: Scheme representing the location of the antennas in the geometry of the experiment conducted to assess non-aligned passes.

focused from the same aperture including a variable Horizontal Separation (HS) between them. From the original 2 m aperture of the GB-SAR, only 1.22 m will be used to focus the image to permit an increasing variable HS of half of the aperture. The master image has been processed from the origin of the aperture and the slave images are focused varying the HS from 0 to 76.8 cm, as shown in the scheme of Figure 5.28. In Figure 5.29 it can be seen the SLC focused image with a zoom to the most reflective areas corresponding to a vertical cliff of the mountain.

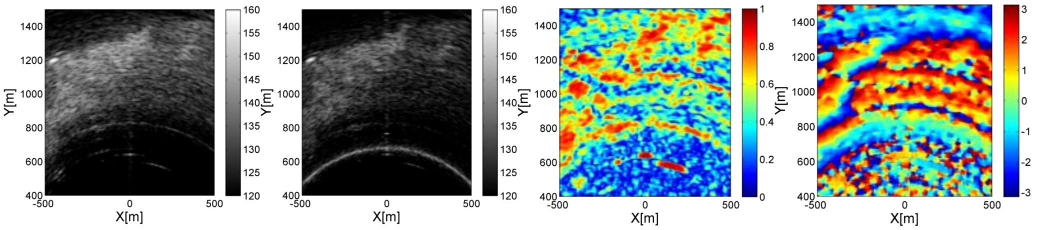

(a) **(b)** **(c)** **(d)**

Figure 5.26: Single pass interferometric measurement in the Collserola test site with a vertical baseline of approx. 50 cm: (a) SLC antenna 1. (b) SLC antenna 2. (c) Coherence. (d) Interferometric phase.

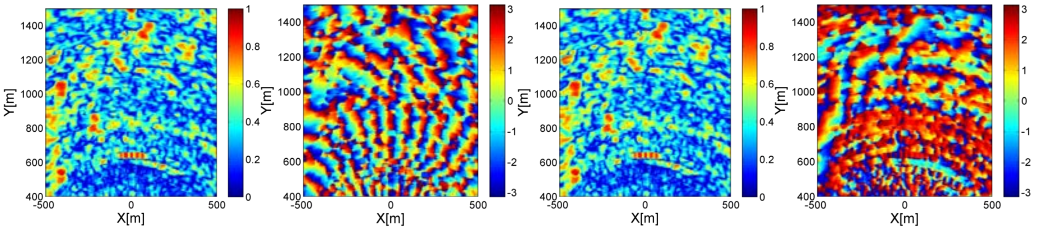

(a) **(b)** **(c)** **(d)**

Figure 5.27: Single pass interferometric measurement in the Collserola test site with a vertical and horizontal baseline of approx. 50 cm and 14 cm, respectively. Coherence and interferometric phase before (a) (b) and after (c) (d) rough coregistration.

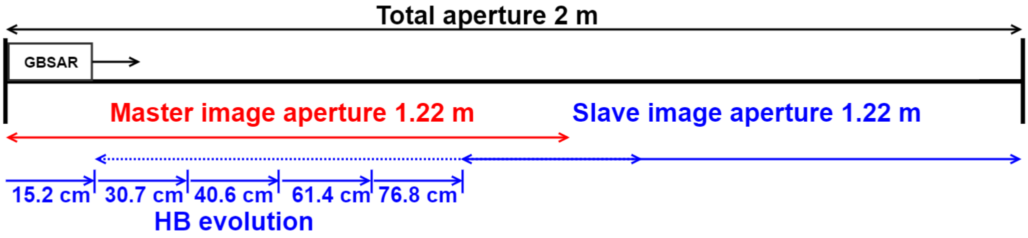

Figure 5.28: Scheme representing the Horizontal Separation (HS) evolution between the master and slave images of the experiment.

In order to analyze the decorrelation between images with the increase of the HS, Figure 5.30 shows the evolution of the coherence and the interferometric phase as the HS increases. As expected, for the HS=0 the coherence is 1 and the interferometric phase is 0, since the same image is compared and it is totally correlated. Furthermore, it can be observed that the number of coherent pixels decrease as the HS increases. Table 5.3

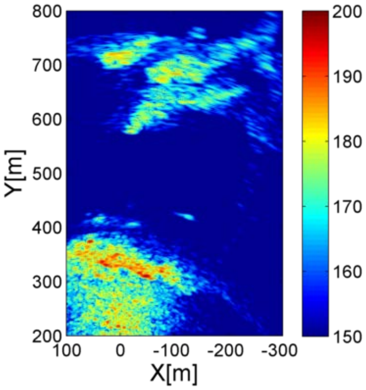

Figure 5.29: SLC image of the Montserrat test site.

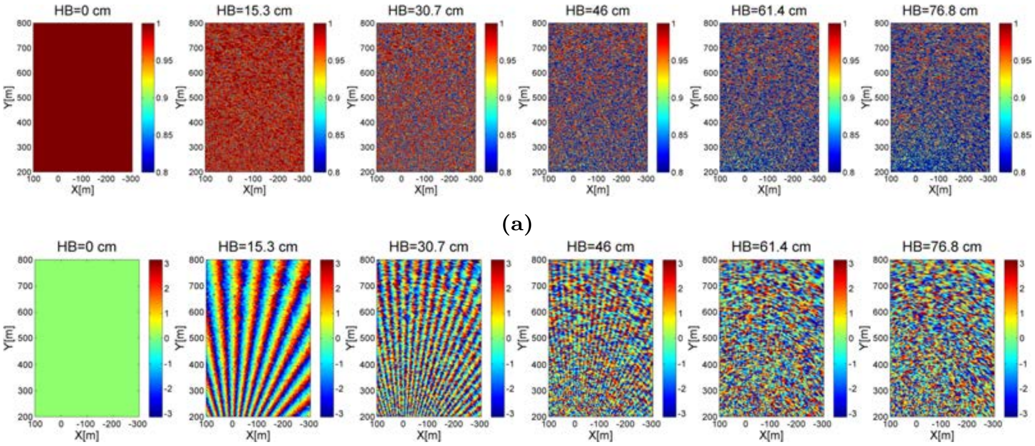

(a)

(b)

Figure 5.30: Evolution of the (a) coherence and (b) the interferometric phase with the increase of the Horizontal Separation (HS) for an aperture of 1.22 m. HS from left to right: 0, 15.3, 30.7, 46, 61.4 and 76.8 cm.

Table 5.3: Evaluation of the number of coherent pixels with the increase of the HS.

Horizontal Baseline (cm)	**0**	**15.3**	**30.7**	**46**	**61.4**	**76.8**
Pixels with coherence amplitude>0.8	6005001	5499369	4518316	3891513	3583911	3416238
Percentage of the total pixels [%]	100	91.57	75.24	64.8	59.68	56.88

shows a summary of the evolution of the number of pixels with a coherence greater than 0.8 as the HS increases. As can be observed, for an HS of 76.8 cm the number of pixels with high coherence have been reduced by almost half.

Regarding the interferometric phase, it presents an azimuth offset due to the miss-registration between images, presenting several fringes in the cross-range direction associated to the horizontal separation of the antennas. To remove this effect, a rough coregistration is applied obtaining the results shown in Figure 5.31. As can be seen, although having coregistrated the images, the interferometric phase is not well compensated, i.e. is not 0 for HSs greater than 0. The histograms in Figure 5.31 (b) demonstrate that there is a degradation in the interferometric phase as the HS increases, which may be related to an azimuth decorrelation of the azimuth spectrum. To assess this effect, the cross-range spectra of the different images is analyzed, observing an spectral shift proportional to the HS between the apertures, see Figure 5.32. This causes the spectra to be totally decorrelated for high HSs. As previously mentioned, filtering the common

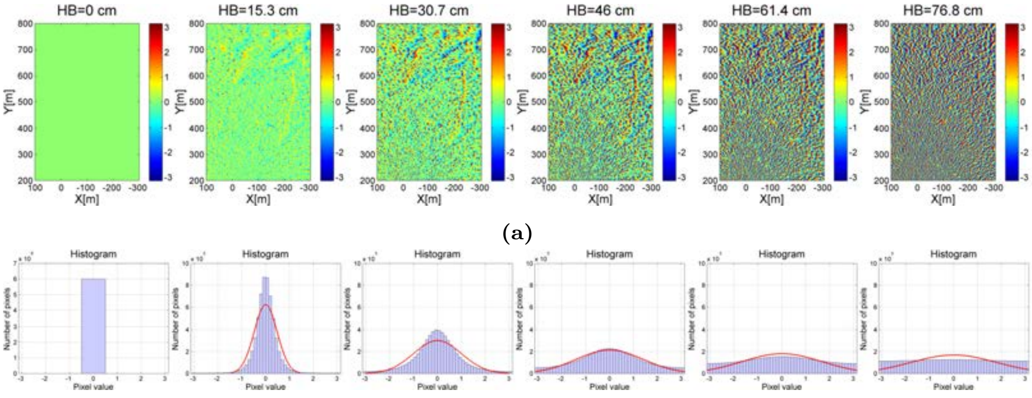

(a)

(b)

Figure 5.31: Evolution of (a) the interferometric phase and (b) the phase histograms with the increase of the Horizontal Separation (HS) for an aperture of 1.22 m after rough coregistration. HS from left to right: 0, 15.3, 30.7, 46, 61.4 and 76.8 cm.

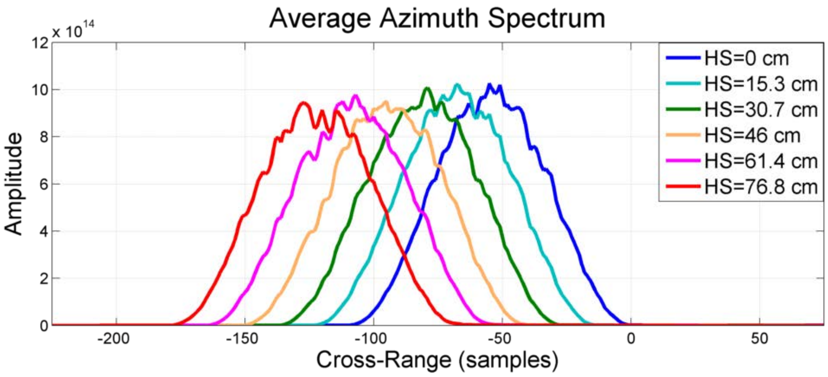

Figure 5.32: Comparison of the azimuth spectra for different HS.

bandwidth could improve the results if the spectra are not very decorrelated. Nevertheless, for the most extreme cases this would not be useful. Then, a possible solution to be analyzed in the future would be to shift the spectra so that they are centered in the same Doppler centroid.

Analyzing the results of Figure 5.31, it can be also observed that approximately for a HS half of the length of the complete aperture, the two images are completely decorrelated. In this sense, it can be concluded that the larger the aperture length, the less sensitive the coherence and the interferometric phase to an HS between passes. This is shown in the comparison of Figure 5.33, where the coherence, the interferometic phase and the phase histogram can be seen for two apertures of 1.22 m and 1.68 m and the same HS. The larger aperture has 82.43 % of the total pixels with a coherence value greater than 0.8, while the shorter aperture has the 75.25 %, which implies an increase of the 7.18 %. Moreover, the histograms of the interferometric phase reveal that the larger aperture is much more correlated than the shorter one. Analyzing the azimuth spectra of the different apertures, see Figure 5.34, it has been observed that the larger aperture presents wider azimuth spectra. For that reason, for the same HS the azimuth spectra are more overlapped for the aperture of 1.68 m than for the one of 1.22 m.

The main conclusion of the experiments presented in this subsection is relative to the importance of the alignment between the two passes in repeat-pass interferometric measurements conducted by the ARBRES-X SAR system. Due to the lack of accuracy of the UAV MP navigation system, the velocity and the trajectory might not be ideal while measuring, fact that can introduce an important decorrelation between the different passes due to the azimuth spectral shift. In this sense, the larger the aperture the wider

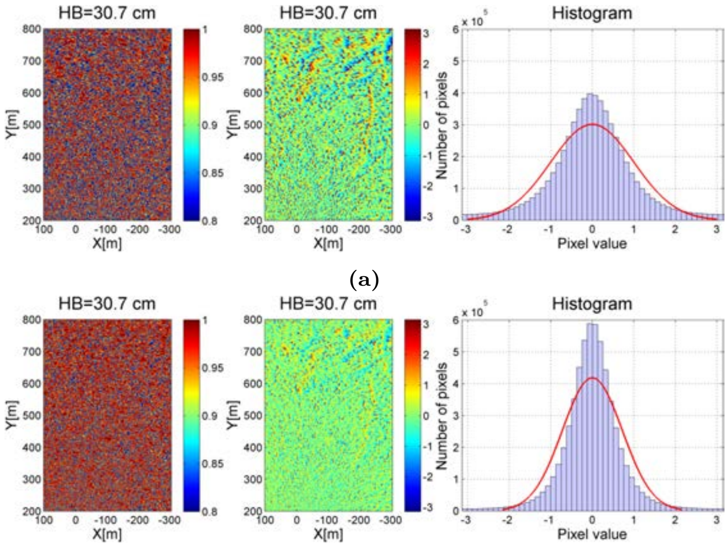

(a)

(b)

Figure 5.33: From left to right: Coherence, interferometric phase and phase histogram after rough coregistration for an aperture of (a) 1.22 m and (b) 1.68 m and a HS between passes of 30.7 cm.

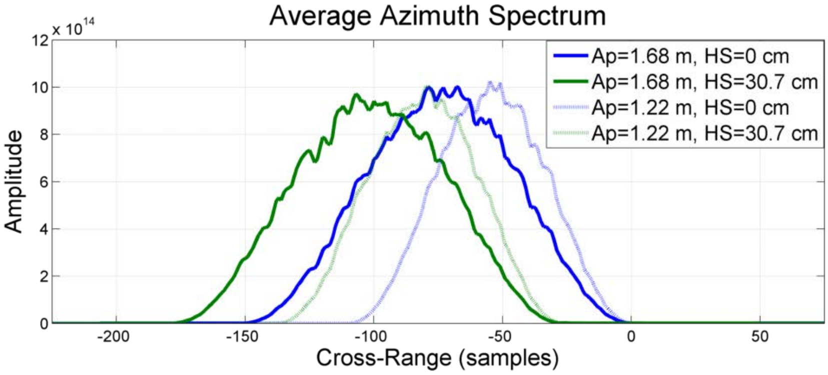

Figure 5.34: Comparison of the azimuth spectra for two different aperture lengths, 1.22 m and 1.68 m, and a HS of 30.7 cm.

the spectra, which is preferable to have more overlapped responses. However, as will be stated in Chapter 6, it has to be taken into account that larger apertures present more motion errors and deviations from the nominal track due to the inherent instability of the platform, which imposes restrictions in the maximum processable aperture length. Moreover, the vertical accuracy of the GPS together with the barometer is not able to guarantee a constant flight altitude, being an important inconvenient when trying to maintain a non-variable baseline between the two passes. Added to this, there are several motion errors that can also affect the interferometric process, complicating the fact of obtaining good interferometric results. Errors in roll, pitch an yaw can completely degrade the results, reason for which the different processing steps exposed in the present chapter are mandatory. The technical feasibility of acquiring SAR data with the ARBRES-X SAR system will be analyzed in detail in Chapter 6.

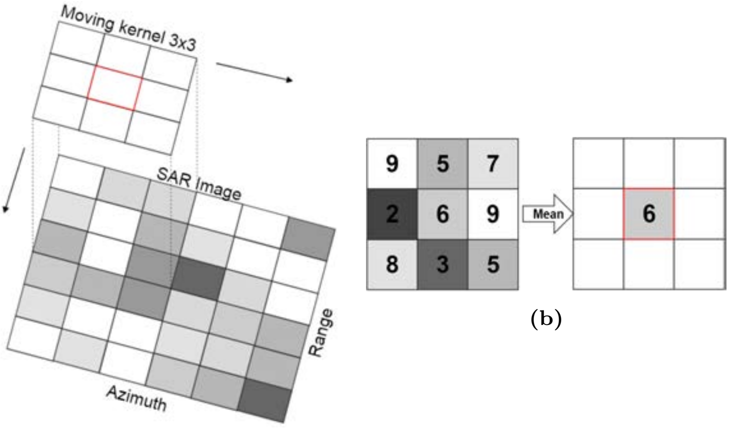

(a)

(b)

Figure 5.35: (a) Representation of the 3x3 moving filtering window applied to the SLC images. (b) Example of the new value assigned to the center pixel in a 3x3 mean filter.

5.3.4 Speckle Filtering

As introduced in Section 2.2 of Chapter 2, in order to reduce the speckle in SAR, a filtering step must be applied in the processed images. The aim of this process is the reduction of speckle with minimum loss of information and spatial resolution. The filter applied in the images obtained during this doctoral activity are the mean and median filter. They are non-adaptive filters in spatial domain that use a moving kernel. Depending on the moving filtering window, which processes the entire SAR image, a new value is assigned to the center pixel. Figure 5.35 (a) shows a representation of how the moving filter is applied in the focused images and Figure 5.35 (b) shows an example of the computation of the value of the center pixel with the mean filter. The value of the center pixel is obtained by computing the mean or median of all the pixels forming the filter window.

Figure 5.36 (a) shows an SLC image obtained in the RACBSA airfield of Ripollet, see Section 6.1 of Chapter 6, and Figure 5.36 (b) and (c) shows the same image after applying the mean and median filters, respectively. The grid of the image is 0.2x0.5 m and the moving filtering window is 10x10 pixels. Besides, Figure 5.36 (a'), (b') and (c') show a zoom to the area between -200 and 200 m in azimuth and 250 and 700 m in range to better visualize the effect of the moving filters. As can be observed, the granular noise related to speckle has been considerably reduced.

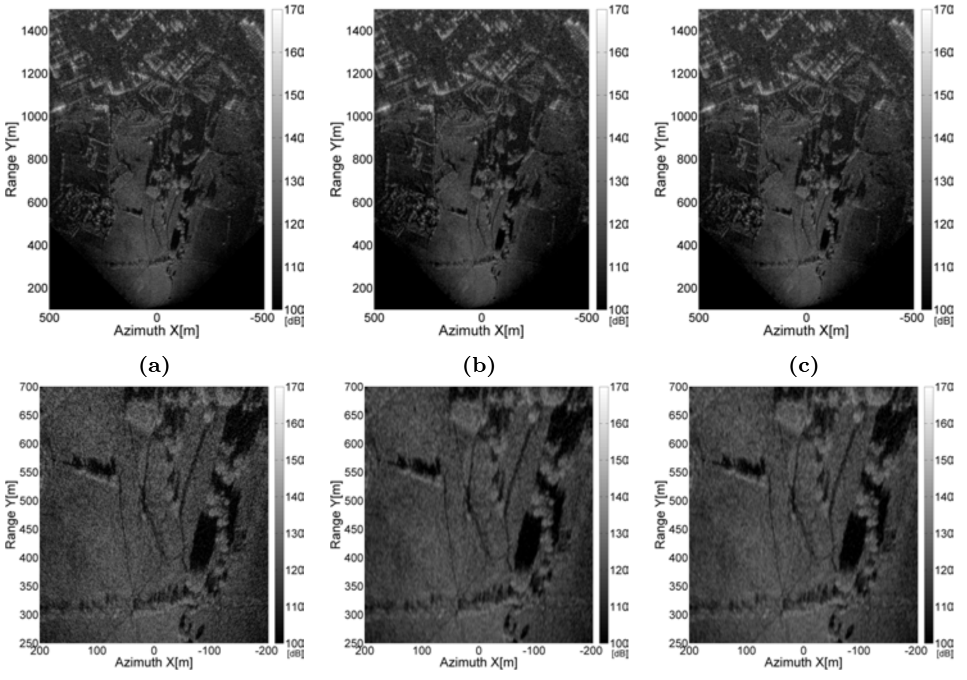

(a) **(b)** **(c)**

(a') **(b')** **(c')**

Figure 5.36: SLC images in Cartesian coordinates: (a) No filter, (b) Mean filter 10x10 pixels and (c) Median filter 10x10 pixels. Zoom: (a') No filter, (b') Mean filter 10x10 pixels and (c') Median filter 10x10 pixels. Flight conditions: 100 m height, $v_{UAV} = 8m/s$, VV Pol.

5.4 ARBRES-X phase center compensation and polarimetric data calibration

In the same way as in the case of the RISKSAR-X system studied in Section 3.4, the phase registration errors must be considered in the ARBRES-X SAR system. In this context, the spatial location of the antennas and the data storage have to be taken into account.

The ARBRES front-end with the microstrip antennas located in the lightweight aluminum bar introduce a registration mismatch as happened with the horn antennas in the RISKSAR-X sensor. Again, this effect must be compensated. Figure 5.37 shows the layout of the antenna arm seen in Figure 5.9 (b). The distance between the different antennas and the corresponding phase center of each polarimetric combination is represented in the schematic. As can be observed, the separation between both transmitting and receiving antennas is 78 mm. As in the GB-SAR system, the phase centers of each polarization must be referred to the same position, in this case the CPC location marked with a red cross in the image. According to the layout, a distance Δx_{CPC} of +39 mm and -39 mm must be considered in Equation 3.2 to compensate the VV and HH polarization respectively.

Differently from the RISKSAR-X sensor, in the ARBRES-X SAR system it is important to consider the way in which the system stores the received data. According to the diagram shown in Figure 5.15, the acquisition card needs two triggers to complete a fully polarimetric measurement, see Figure 5.38. This introduces a registration error between the first stored polarizations (HH and VH) and the following ones (HV and VV) that correspond to the displaced distance $T_{PRF} * velo_{antenna}$. In the GB-SAR case, the velocity of the platform is too slow (on the order of 0.468 m/s), but the velocity of the UAV MP can be programmed to be up to 25 m/s. Normally, to perform the SAR acquisitions the velocity of the UAV is set at around 9 m/s, which is equivalent to a distance error of approximately 1.65 mm. This distance is approximately 11 times greater than the 153.4 μm of the RISKSAR-X case, reason for which it has to be considered and compensated. Regarding the effect in the phase of the length of the cables, it can be also negligible in the ARBRES-X SAR sensor. The two reception channels are identical and the total length of the cables for the two channels can be considered equal.

To exemplify the effect in the phase of the registration errors that must be compensated in the ARBRES-X SAR system, a measurement performed in the RACBSA airfield

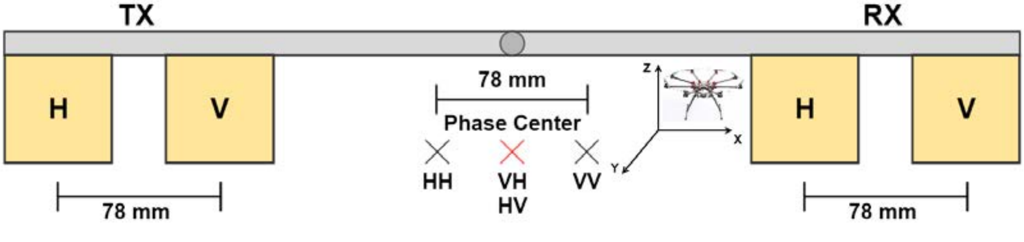

Figure 5.37: Layout representing the spatial position of the antennas and the phase centers in the ARBRES-X SAR sensor.

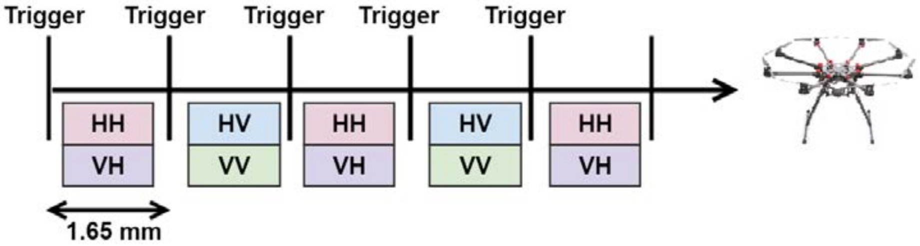

Figure 5.38: Diagram representing the data storage registration error for the fully polarimetric case in the ARBRES-X SAR sensor.

(described in Section 6.1) is analyzed. In this acquisition, the UAV MP was flying at 150 m height and at a constant speed of approximately 7 m/s, performing an aperture length of around 21 m. Figure 5.39 shows the SLC images of the scenario corresponding to the different polarizations. Three PARCs and a trihedral corner reflector were placed in the agricultural field of the scenario forming a triangular shape for focusing purposes and polarimetric evaluation. It can be appreciated that the co-polar images present higher reflectivity values than the cross-polar ones.

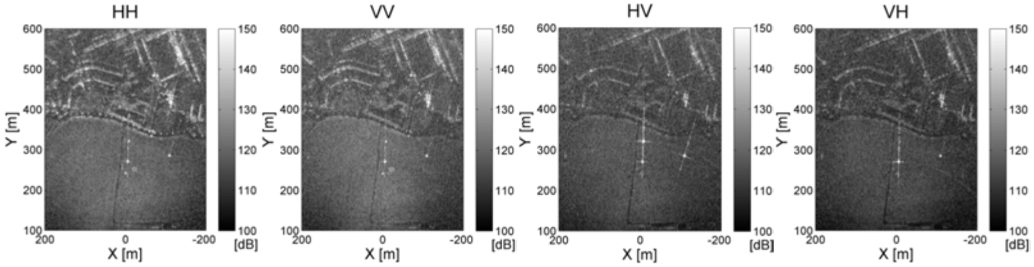

(a) (b) (c) (d)

Figure 5.39: Fully polarimetric SLC images of the RACBSA airfield. (a) HH pol. (b) VV pol. (c) HV pol. (d) VH pol. Flight conditions: 150 m height, $v_{UAV} = 7$ m/s, Ap=20 m.

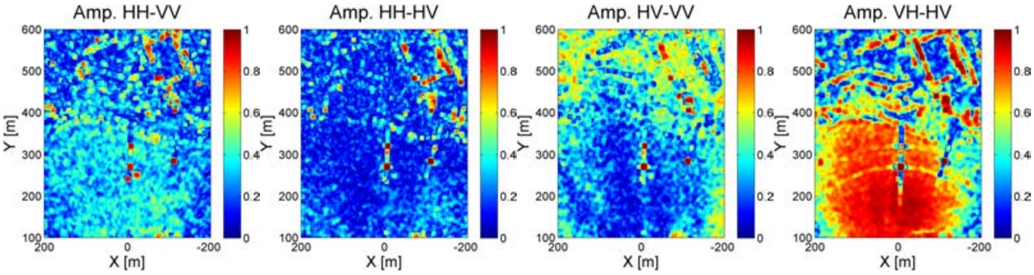

(a) (b) (c) (d)

Figure 5.40: Polarimetric correlation analysis. Coherence without any phase compensation (Multilook 10x10 m): (a) HH-VV. (b) HH-HV. (c) HV-VV. (d) VH-HV.

Figure 5.40 and 5.41 show the polarimetric correlation analysis of the coherence and phase difference respectively for the HH-VV, HH-HV, HV-VV and VH-HV combinations before any phase center compensation. Several comments can be done after analyzing the phase differences of Figure 5.41:

- **HH-VV** combination presents a phase ramp in the azimuth direction corresponding to the distance of 78 mm between H and V antennas. Figure 5.42 (a) shows the

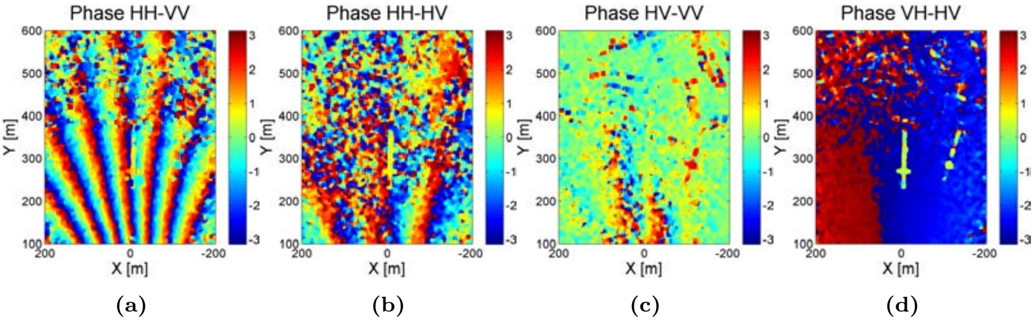

(a) **(b)** **(c)** **(d)**

Figure 5.41: Polarimetric correlation analysis. Phase difference without any phase compensation (Multilook 10x10 m): (a) HH-VV. (b) HH-HV. (c) HV-VV. (d) VH-HV.

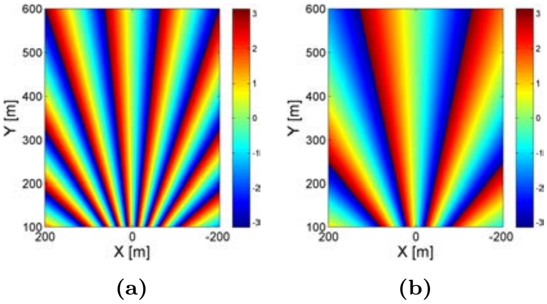

(a) **(b)**

Figure 5.42: Simulation of the azimuth phase ramp introduced by an antennas separation of: (a) 78 mm. (b) 39 mm.

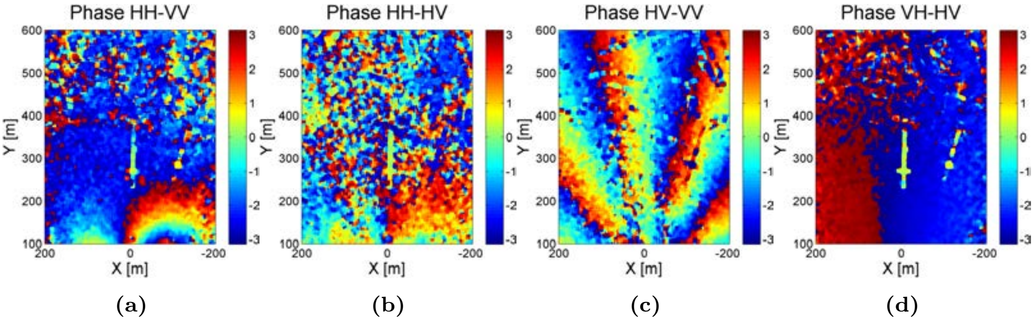

(a) **(b)** **(c)** **(d)**

Figure 5.43: Polarimetric correlation analysis. Phase difference compensating antenna position (Multilook 10x10 m): (a) HH-VV. (b) HH-HV. (c) HV-VV. (d) VH-HV.

simulated azimuth phase ramp considering this separation. Intuitively, it can be appreciated that the simulated and measured azimuth patterns correspond one to the other.

- **HH-HV** and **HV-VV** present an azimuth phase ramp proportional to the separation between the phase centers of the co-polar and cross-polar polarizations, which is 39 mm. Figure 5.42 (b) shows this simulated azimuth phase ramp separation, which is similar to the one in Figure 5.41 (b) and (c). As stated in Section 2.2 of Chapter 2, reflection symmetry can be assumed, which is a feasible acceptance when measuring distributed targets like the field of the image, and one would not expect to find any phase pattern in these combinations [45]. Instead, a noisy phase distribution should be found. Then, it can be concluded that there are cross-talk effects introduced by the diagonal terms of the covariance matrix, see Equation 5.10, that are degrading the quality of the phase measurements.
- **VH-HV** presents a light phase jump that is associated to the data storage displacement. Furthermore, it can be also concluded that there is not a phase ramp in the range direction associated to the length of the cables.

Figure 5.43 shows the phase difference for the different combinations after compensating the antenna separation, from which some conclusions can be extracted:

- **HH-VV**: the azimuth phase ramp has been compensated. However, a residual pattern can be appreciated in the bottom-right part of the image. Further analysis of the system must be conducted to determine the origin of this error, but a first hypothesis points to the patch antennas.
- **HH-HV**: the azimuth phase ramp proportional to the separation between the HH-HV combination has been compensated. Nevertheless, the remaining phase distribution is similar to the retrieved in the HH-VV combination, reason for which it is believed that the HH polarization predominates over the others.
- **HV-VV**: in this combination the phase not only has not been well compensated but also the phase pattern represented Figure 5.42 (b) has been introduced. This effect is analyzed carefully below to understand the mechanisms that degrade the quality of the retrieved phase.

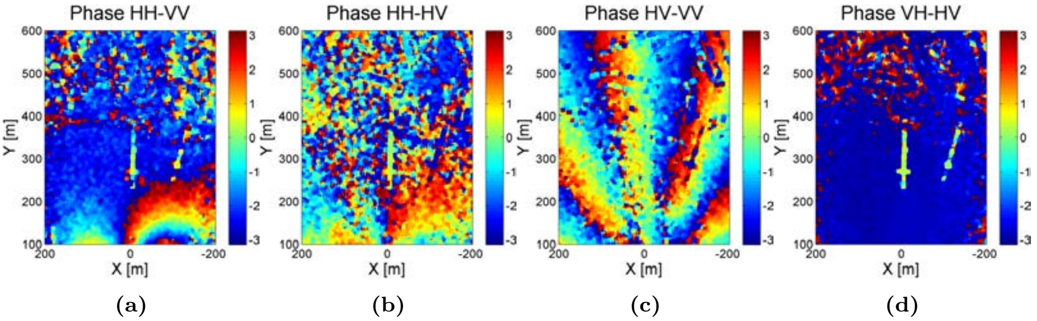

(a) **(b)** **(c)** **(d)**

Figure 5.44: Polarimetric correlation analysis. Phase difference compensating antenna position and data storage (Multilook 10x10 m): (a) HH-VV. (b) HH-HV. (c) HV-VV. (d) VH-HV.

- **VH-HV**: this combination is not affected by the antennas separation compensation, since their CPCs are not altered during the process. The phase jump has to be compensated by taking into account the data storage of the system.

Finally, after compensating the data storage, see Figure 5.44, the most noticeable effect can be appreciated in the removal of the phase jump in Figure 5.44 (d).

To understand the different inconsistencies found during the phase center compensation and to assess the necessity to improve the system performance, a deepest analysis of the cross-talk parameters is conducted. Following the nomenclature used in [104], the most general form of the system model relating the real [S] and the measured [M] scattering matrix including system distortions in the measurements can be expressed in vector form as [23]

$$\begin{pmatrix} M_{HH} \\ M_{VH} \\ M_{HV} \\ M_{VV} \end{pmatrix} = K(\gamma) \begin{pmatrix} \alpha_r & v_t + \alpha_r w_r & v_t w_r \\ \alpha_r u_r & \alpha_r & v_t \\ \alpha_r z_t & 1 & w_r \\ \alpha_r u_r z_t & u_r + \alpha_r z_t & 1 \end{pmatrix} \begin{pmatrix} k_r^2 & 0 & 0 \\ 0 & k_r & 0 \\ 0 & 0 & 1 \end{pmatrix} \begin{pmatrix} S_{HH} \\ S_{HV} \\ S_{VV} \end{pmatrix} \quad (5.5)$$

where

$$\begin{array}{ll} w_r = R_{HV}/R_{VV} & z_t = T_{HV}/T_{HH} \\ k_r = R_{HH}/R_{VV} & \alpha_r = R_{VV}T_{HH}/R_{HH}T_{VV} \\ u_r = R_{VH}/R_{HH} & K(\gamma) = R_{VV}T_{VV} \\ v_t = T_{VH}/T_{VV} & \end{array} . \quad (5.6)$$

Equation 5.5 can be expressed in the form

$$\begin{pmatrix} M_{HH} \\ M_{VH} \\ M_{HV} \\ M_{VV} \end{pmatrix} = K(\gamma)[X][Q] \begin{pmatrix} S_{HH} \\ S_{HV} \\ S_{VV} \end{pmatrix} . \quad (5.7)$$

The covariance matrix of the measured vector in Equation 5.7 can be written as

$$[C]_{measured} = |K(\gamma)|^2 [X][Q][C]_{actual}[Q^\dagger][X^\dagger]. \quad (5.8)$$

where the superscript † denotes the adjoint (transpose complex conjugate) of the matrix. To analyze the distortion matrix [X] it is assumed that the image exhibits reflection symmetry, which means that the co- and cross-polarized components of [S] are uncorrelated for random distributed targets with azimuthal symmetry [45]. This is the case of the agricultural field of the scenario composed of natural distributed targets. Mathematically, this means that

$$\begin{array}{c} \langle S_{HH}^* S_{HV} \rangle = 0 \\ \langle S_{VV}^* S_{HV} \rangle = 0. \end{array} \quad (5.9)$$

where $\langle . \rangle$ denote spatial averaging of the image data over an area and * denotes the conjugate. Thus, assuming reciprocity, whereby $S_{VH} = S_{HV}$, the averaged actual covariance matrix that fully describes the scattering properties of the target is

$$[C]_{actual} = \begin{pmatrix} \langle S_{HH} S_{HH}^* \rangle & 0 & \langle S_{HH} S_{VV}^* \rangle \\ 0 & \langle S_{HV} S_{HV}^* \rangle^2 & 0 \\ \langle S_{HH} S_{VV}^* \rangle & 0 & \langle S_{VV} S_{VV}^* \rangle \end{pmatrix} . \quad (5.10)$$

Thus, Equation 5.8 can be rewritten

$$[O] = [Q][C]_{actual}[Q^{\dagger}] = \begin{pmatrix} |k_r^2|^2\langle S_{HH}S_{HH}^*\rangle & 0 & k_r^2\langle S_{HH}S_{VV}^*\rangle \\ 0 & |k_r|^2\langle S_{HV}S_{HV}^*\rangle^2 & 0 \\ k_r^{2*}\langle S_{HH}S_{VH}^*\rangle & 0 & \langle S_{VV}S_{VV}^*\rangle \end{pmatrix}. \tag{5.11}$$

The following multiplication is done to estimate the cross-talk parameters

$$[T] = [X][O][X^{\dagger}]. \tag{5.12}$$

Performing the multiplication of Equation 5.12, the cross-talk parameters of the most relevant combinations presented in the polarimetric correlation analysis performed in this subsection will be assessed. The aim of this process is to find the source of error related to the cross-talk parameters. In our particular case, those terms that are of second order compared to the other terms in the same element will be neglected. The measured scattering elements for HV, VV and HH can be expressed as

$$\begin{aligned} M_{HV} &= K(\gamma)(\alpha_r z_t k_r^2 S_{HH} + k_r S_{HV} + w_r S_{VV}) \\ M_{VV} &= K(\gamma)(\alpha_r u_r z_t k_t^2 S_{HH} + k_r(u_r + \alpha_r z_t)S_{HV} + S_{VV}) \\ M_{HH} &= K(\gamma)(\alpha_r k_r^2 S_{HH} + (v_t + \alpha_r w_r)k_r S_{HV} + v_t w_r S_{VV}). \end{aligned} \tag{5.13}$$

Thus, the correlation between the different polarimetric combinations that seems to present cross-talk errors in Figure 5.41 can be computed. Lets first analyze the HV-VV combination to justify the apparition of the undesired phase pattern

$$\langle M_{VV}M_{HV}^*\rangle = \underbrace{\alpha_r^* z_t^* \langle S_{VV}S_{HH}^*\rangle}_{1} + \underbrace{w_r^* \langle S_{VV}S_{VV}^*\rangle}_{2} + \underbrace{(u_r + \alpha_r z_t)\langle S_{HV}S_{HV}^*\rangle}_{3}. \tag{5.14}$$

Equation 5.14 presents three distortion elements involved in the correlation between VV and HV, two in reception (w_r and u_r) and one in transmission (z). Each of them can be considered as a combination between the error introduced by the antenna itself and the error introduced by the isolation between channels. This way, the different parameters can be decomposed introducing the following phase patterns

$$\begin{aligned} &1 \rightarrow z_t : T_{HV} = T_{HV}^{ant} + T_{HV}^{isol} \longrightarrow \boxed{VV \cdot HV^*} + VV \cdot HH^* \\ &2 \rightarrow w_r : R_{HV} = R_{HV}^{ant} + R_{HV}^{isol} \longrightarrow \boxed{VV \cdot HV^*} + VV \cdot VV^* \\ &3 \rightarrow u_r : R_{VH} = R_{VH}^{ant} + R_{VH}^{isol} \longrightarrow \boxed{VV \cdot HV^*} + HV \cdot HV^* \\ &3 \rightarrow z_t : T_{HV} = T_{HV}^{ant} + T_{HV}^{isol} \longrightarrow \underbrace{HV \cdot HV^* + HH \cdot HV^*}_{eq.\quad phase\quad pattern} \end{aligned} \tag{5.15}$$

where the combinations at the right of the arrow represent the equivalent phase patterns introduced by the cross-talk parameters. For instance, the separation between the CPC of $VV \cdot HV$ combination introduces an azimuth phase pattern proportional to the one simulated in Figure 5.42 (b). If there are cross-talk errors due to the antennas or the isolation between channels, a residual pattern due to this combination may appear in the images, as is the case under study.

It has to be mentioned that the isolation in transmission obtained from the solid-state switch is 33.8 dB and 37.8 dB for the two channels, see Subsection 5.2.2.1. Besides, the isolation between the reception channels is of around 37 dB. Considering these values, the phase pattern that could be introduced by the cross-talk due to a bad isolation between channels can be neglected. To validate this hypothesis, a measurement with low isolation between the reception channels has been evaluated, obtaining similar results as the ones presented in this section.

Thus, it is concluded that the important cross-talk errors are introduced by the patch antennas. In this case, the phase error observed in Figure 5.41 (c) could be introduced by the phase patterns from the cross-talks framed in Equation 5.15. As can be observed, the z term associated to T_{HV}^{ant} in 3 does not introduce a phase pattern since VH and VH have the same CPC. This could be the reason why when compensating the antennas location it appears the phase pattern in Figure 5.43 (c). This means that, implicitly, when compensating the CPC other phase patterns are introduced through the cross-talk elements of the antennas.

At this point it is interesting to repeat the same procedure with the HH-HV polarization, since it presents an azimuth phase pattern that is removed after the antenna position compensation.

$$\langle M_{HV} M_{HH}^{*} \rangle = \underbrace{|\alpha_r|^2 z_t \langle S_{HH} S_{HH}^{*} \rangle}_{1} + \underbrace{\alpha_r^{*} w_r \langle S_{VV} S_{HH}^{*} \rangle}_{2} + \underbrace{(v_t^{*} + \alpha_r^{*} w_r^{*}) \langle S_{HV} S_{HV}^{*} \rangle}_{3} . \tag{5.16}$$

Equation 5.16 presents three distortion elements involved in the correlation between HV and HH, two in transmission (z_t and v_t) and one in reception (w_r). The phase patterns that can be introduced due to the cross-talk effects are

$$\begin{aligned}
&1 \rightarrow z_t : T_{HV} = T_{HV}^{ant} + T_{HV}^{isol} \longrightarrow \boxed{HV \cdot HH^{*}} + HH \cdot HH^{*} \\
&2 \rightarrow w_r : R_{HV} = R_{HV}^{ant} + R_{HV}^{isol} \longrightarrow \boxed{HV \cdot HH^{*}} + VV \cdot HH^{*} \\
&3 \rightarrow v_t : T_{VH} = T_{VH}^{ant} + T_{VH}^{isol} \longrightarrow \boxed{HV \cdot HH^{*}} + HV \cdot HV^{*} \\
&3 \rightarrow w_t : T_{HV} = T_{HV}^{ant} + T_{HV}^{isol} \longrightarrow \underbrace{\boxed{HV \cdot HH^{*}} + VV \cdot HV^{*}}_{eq. \quad phase \quad pattern} .
\end{aligned} \tag{5.17}$$

In this case, considering Equation 5.17, all the elements introduce an azimuth phase pattern corresponding to the antennas separation of Figure 5.42 (b). Because of that, when compensating the CPC corresponding to the antennas location the azimuth phase pattern is removed in Figure 5.43 (b) and no other patter is introduced in consequence.

As a conclusion it can be determined that there are several cross-talk effects that seems to be introduced by the antennas. Although the patch antennas have been measured in the anechoic chamber and present enough CPD factor, see Figure 5.7, the RF front-end is not working properly. Moreover, the aluminum bar with the attached patch antennas suffers from undesired motion errors due to the vibrations and the inertia of the platform. This could introduce important polarimetric errors that must be avoided by improving the system hardware. Then, instead of devoting much effort to calibrate the system, further steps should include reviewing the hardware to find the origin of the cross-talk effects and solve the problem. Thus, reliable polarimetric measurements may be carried out in the future.

Despite the exposed cross-talk errors, a first attempt of calibration is conducted based on the method presented in Section 3.5 of Chapter 3, [77], with the sole intention of setting the basis for a suitable future calibration. It has to be stressed that the purpose of part of the present doctoral work was to demonstrate the technical feasibility of acquiring SAR data with the UAV MP, without focusing on the necessary algorithms or in the calibration of the system.

Having said this, and although it is not true in our particular case, a good polarization isolation of the system is considered, calibrating the system using the trihedral corner reflector of the image and a strong cross-polarized scatterer, as in the RISKSAR-X case. In this sense, the Pauli decomposition is here presented with the aim of analyzing the impact of the cross-talk effects in the RGB images. Figure 5.45 shows the evolution of the Pauli's composition of the images, ranging from the system without applying the CPC compensation to the system applying a first attempt of calibration. Two different spans are considered as weight factor to stress, on the one hand, the agricultural field and on

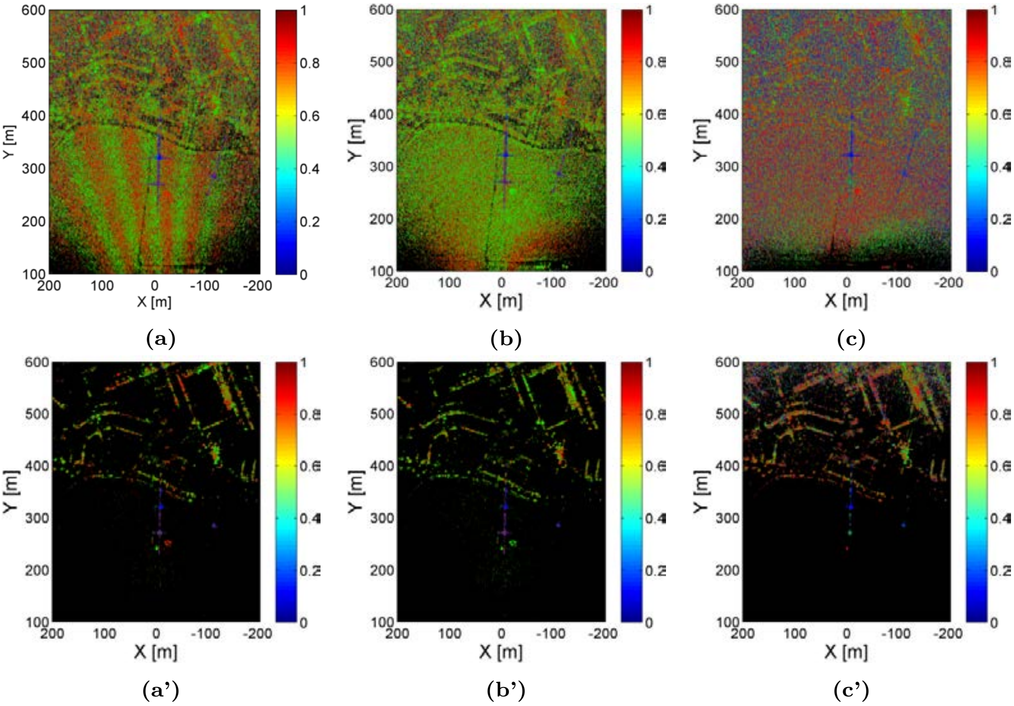

(a) (b) (c)

(a') (b') (c')

Figure 5.45: Pauli composition of the scenario with two different spans using $|HH+VV|$, $|HH-VV|$ and $|HV|$ as red, green and blue, respectively. No CPC compensation: (a) Span 1. (a') Span 2. After compensating antenna location and data storage: (b) Span 1 . (b') Span 2. After calibration: (c) Span 1. (c') Span 2.

the other the position of high-reflectivity urban scatterers. Figure 5.45 (a) and (a') show the Pauli's composition before applying any CPC compensation. As can be observed, the azimuth phase ramp is appreciated alternating red and green lines and masking the results, stressing the importance of compensating the phase centers.

Figure 5.45 (b) and (b') show the Pauli's image after compensating the phase centers. As can be observed, the azimuth pattern has been removed but the response of the agricultural field is mostly green, which amounts to a dihedral-like response (double-bounce). This response is not expected for the agricultural field, which should be more blue (volumetric) and red (single-bounce). As will be exposed in detail in Section 6.3 of Chapter 6, three PARCs and a trihedral corner reflector are placed in the agricultural field of the scenario. After the first calibration, the trihedral corner reflector in the RGB image of Figure 5.45 (c') appears in red, which accounts for single-scattering. Besides, PARC 2 and 3 are represented in blue (targets returning orthogonal polarization), which is feasible due to the orientation of the calibrators. Finally, PARC 1 appears in green, which accounts for double-bounce response.

5.5 ARBRES assistant

During the course of this doctoral work, part of the research activity has required the development of different specific codes and algorithms to process the data acquired by the ARBRES-X SAR sensor. In this context, much effort has been devoted to the implementation of this functional codes according to the processing steps and algorithms exposed in Section 5.3. In order to take advantage of this effort, it has been developed a tool that collects the main procedures to process the raw data from the radar, which is called ARBRES assistant. Figure 5.46 shows a picture of the main menu where the different capabilities of the application can be seen. The main menu of the ARBRES assistant is divided in different sections:

- **Parameters.** The different parameters of the sensor can be introduced: the center frequency f_0, the sampling frequency f_{sample}, the chirp bandwidth A_{chirp}, the PRF PRF, the total number of chirp pulses to process related to the aperture length N_t, the number of digitized samples per frequency ramp N_{samps}, the presuming factor PF, the aperture length offset N_{offset} and the zero padding factor *Zero padding.*

F0 9.65e9
Fsample [Hz] 44.625e6
A chirp 100e6
Tprf 5.445e3
Nt 8192
Nsamps 4096
PF 4
N offset 25000
Zero Padding 16

● Constant Velocity [m/s] 8
○ Linear variable velocity [m/s] Initial velo 0 Final velo 0
Altitude of the platform [m] 0

● Cartesian coordinates X [m] -300 300; Y [m] 0 1500; X Resolution [m] 1; Y Resolution [m] 1; Ant. beamwidth [°] 40
○ Polar coordinates Theta [°] -20 20; Range [m] 0 1500; Theta Resolution [°] 0.02; Range Resolution [m] 1
Colormap axis [dB] 100 160

MeasurementType Single Pol
Focusing Altgorithm ● BPA
☐ Focused image
☐ Autofocus parameters
☐ Autofocus
☐ Import focused image
☐ Pomnent target Polyfit
N prominent targets 2

Figure 5.46: Main menu of the ARBRES assistant.

- **Platform info.** The velocity and the height of the platform can be introduced to properly process the data.
- **Imaging info.** In this section the parameters related to the grid of the image can be selected, being able to choose between Polar and Cartesian coordinates. The image size, the azimuth and range resolution and the antenna beamwidth can be introduced, as well as the colormap scale of the final image in dB.
- **Data processing.** The options of data processing allow the selection between the different operation modes: Single Pol., Half Pol. Rx., Half Pol. Tx and Full Pol. The Half Pol. operation modes have been very useful while evaluating the system during its development, reason for which has been included in the software. The focusing of the images is performed by the BPA and the autofocus algorithm can be applied to improve the focusing process in large apertures. Regarding the autofocus algorithm, it is capable to find automatically the PARCs in a given area of the image to extract the phase information, which is useful if the targets are close to each other. If not, the introduction of the PARCs position can be performed manually. On the other hand, if the evolution of the extracted phase presents discontinuities due to the unwrapping process, it can be approximated. Furthermore, the GPS location of the calibrators and the UAV MP are required in order to derive the distance from the sensor to the PARCs, as explained in Subsection 5.3.1 of the present chapter. A section called utilities is added, which comprises the different procedures to perform the speckle filtering with the median and mean filter, the polarimetric correlation analysis of the focused images and the Pauli RGB decomposition.

Finally it has to be commented that, as the ARBRES assistant tool is in early stages of development, it can be optimized and many functions can still be added, such as for instance the automatic polarimetric calibration of the system.

5.6 Concluding remarks

The main objective of the hardware contributions conducted to the ARBRES-X SAR sensor has been the improvement of its performances and capabilities. To that purpose, the migration from a fixed wings UAV to a MP has constituted the core of the work developed in this doctoral thesis, improving the versatility of the overall system. During the present chapter, the system architecture and main characteristics of operation of the ARBRES-X SAR have been exposed. Furthermore, the main hardware developments conducted to the system in order to integrate the sensor into the UAV MP have been assessed. In this sense, the fundamental goal when designing the system has been overcoming restrictions of weight, size and aerodynamics of the platform. Finally, the integration of the ARBRES-X SAR sensor into a small multicopter platform has been presented, opening new possibilities in airborne SAR remote sensing as will be assessed in Chapter 6.

In Section 5.3, the different steps necessary to process the raw-data have been summarized. One of the most important procedures correspond to the autofocus algorithm, which will be applied in real measurements in Section 6.2 of Chapter 6. It is extremely important to retrieve the possible motion errors of the platform in absence of a high precision IMU in order to obtain well focused SAR images. During the simulations it has been concluded that, when solving the set of non-linear equations, some inaccuracies in the method can arise. Because of that, the retrieved parameters can present some noise that must be properly filtered prior to its introduction to the focusing process. It has been observed that, if this is not done, the image can be defocused. Furthermore, for efficient operation of the algorithm it has been concluded that the retrieved phase of the selected PSs must be of high quality. Sometimes, if the selected target is squinted or its reflectivity is not optimum during the acquisition, the retrieved parameters might present some anomalies that, again, can deteriorate the focusing process. In such cases, the retrieved parameters must be approximated to eliminate the discontinuities and minimize the impact in the focusing process, although this implies to assume a certain degree of error and a possible loss of resolution.

On the other hand, the importance of the coregistration procedure for interferometry has been studied. It has been pointed out the great difficulty in the ARBRES-X SAR system to have perfectly aligned and parallel passes due to the inaccuracy of the navigation system, which complicates a lot obtaining good interferometric results. It has been observed that the misalignment between passes due to velocity errors provokes decorrelation between images due to a shift of the azimuth spectra. Moreover, the fact of not having constant baselines during the acquisitions and the attitude errors of the platform further difficult the situation. The difficulty of obtaining good interferometric results will be highlighted in the experimental results presented in Chapter 6. Due to all these considerable undesired errors, it has been concluded that the application of the sliding spectral window proposed in Section 5.3.2 does not improve the obtained results.

Regarding the phase center compensation in the ARBRES-X SAR sensor, it has been concluded that the compensation of the spatial location of the antennas is mandatory to avoid any phase ramp between the different polarizations. Furthermore, the misregistration due to the way in which the system stores the data becomes relevant in this system, since the velocity of the platform is much higher than in the RISKSAR-X case. By means of analyzing the polarimetric correlation between different combinations, it has been determined that in the actual version of the system there are cross-talk effects due to the antennas that are degrading the performance of the sensor. In the future, it is mandatory to fix the problem at hardware level to be able to obtain reliable polarimetric measurements. Moreover, further steps also comprise an exhaustive calibration of the system.

6

Chapter 6

Initial evaluation of SAR capabilities in UAV Multicopter Platforms

The purpose of this chapter is to validate the ARBRES-X SAR system performance and to conduct an initial evaluation of the SAR capabilities in UAV MPs. The use of this platform introduces new possibilities in airborne SAR observation due to its inherent flight capabilities and characteristics. Along the chapter, different innovative results obtained with the UAV MP are shown. It can be found, for instance, repeat-pass interferometric and fully polarimetric measurements, as well as acquisitions from vertical and circular trajectories.

In particular, the first Section briefly introduces the main objectives of the chapter and the test site used to evaluate the system. Section two assesses the stability of the UAV MP and the application of the autofocus algorithm to obtain good quality SAR images. In Section three some innovative flight strategies in airborne UAV MP multidimensional SAR are presented. Finally, the chapter is ended summarizing the main conclusions obtained.[a]

---

[a] The following sections contain portions, sometimes verbatim, of the author's publication [JA2].

6.1 Introduction

In the previous chapter the ARBRES-X SAR system description as well as the different steps necessary to process the retrieved data have been exposed. The main hardware developments conducted to the sensor have been shown and the main difficulties when integrating the radar into the UAV MP have been commented. Furthermore, the different drawbacks of the platform that can affect the overall system performance have been introduced. In this context, the present chapter is devoted to assess the initial capabilities of the ARBRES-X SAR sensor integrated in the UAV MP. To that purpose, the system has been tested in the Real Aero Club Barcelona-Sabadell (RACBSA) Radio Control Airfield (Ripollet, Barcelona, Spain). Several measurements have been performed in this scenario that is characteristic for its heterogeneous nature, since it contains agricultural fields surrounded by an urban area with smooth topography. Figure 6.1 shows an aerial photograph of the scenario obtained from Google Earth. In the bottom of the photograph it can be seen the landing strip of the airfield where the platform can be safely operated following local regulations. As can be observed, in the urban area the scenario is mainly composed by elements with high reflectivity, such as buildings, roads, pylons or parked cars, which makes it suitable to validate the system performances. Figure 6.2 shows a picture of the complete system at take-off time during one of the many measurement campaigns performed in the test site.

The aim of the different measurement campaigns conducted with the ARBRES-X SAR system during the course of this doctoral activity can be divided into different significant points:

- Test and validation of the system performances.

Figure 6.1: Aerial photograph of the scenario from Google Earth.

Figure 6.2: Fully polarimetric ARBRES-X SAR integrated in the UAV MP and flying in the RACBSA airfield during a measurement campaign.

- Evaluation of the initial SAR capabilities in UAV MP.
- Evaluation of the technical challenges and limitations of operating a SAR sensor on a UAV MP.
- Realization of innovative flight strategies in airborne UAV MP multidimensional SAR and obtainment of first results.
- Establishment of a future line of work to improve the overall system performance and results.

6.2 Stability of the UAV MP and application of the autofocus algorithm

In Subsection 5.3.1 of Chapter 5, the inherent instability of the platform has been mentioned, which can degrade the quality of the retrieved data from the ARBRES-X SAR sensor. The deviations with respect to the nominal flight track impose severe restrictions on the maximum processable aperture length. The larger the aperture, the greater the cumulative positioning error of the platform with respect to the ideal flight path and the greater the degree of defocusing in the retrieved images. In the same way, when processing small azimuth sub-apertures, it can be assumed that the motion errors and the deviations are negligible, since they are too small compared with the slant range distance $r_T(t)$. Figure 6.3 shows a comparison of three SLC images of the scenario obtained with different aperture lengths, where Cartesian coordinates are used because it is visually easier to compare the focused images with the picture of the real scenario. In Appendix B it can be seen the different focused images of the scenario after applying the autofocus algorithm and with a higher grid and size to better visualize the different elements.

It is evident in Figure 6.3 that the defocusing increases for larger apertures, where the flight path is more susceptible to have deviations from the nominal trajectory. For instance, it can be noticed in Figure 6.3 (c) the loss of resolution of the three Prominent Target (PT) corresponding to PARCs located in the near range center of the image, together with the blurring effect in far range. Considering the coordinate system presented in Figure 5.1 (a), an error in the positioning in the X axis is due to errors in the velocity of the platform, which is equivalent to a non-uniform azimuth sampling of the signal. Errors in the Z axis are related with the height of the platform and in the Y axis with the lateral deviation of the platform with respect to the scenario. Besides, and bearing in mind the schematic of Figure 5.11 and the SLC image of Figure 5.12 in Chapter 5, the rotation movements of roll, pitch and yaw angles are also translated in displacements in the three axis.

The aperture length is related with the SCR of the focused images since the energy emitted, i.e. the number of transmitted chirp pulses, is greater for larger apertures. Thus, in order to process larger apertures, it is necessary to compensate for the undesired effects of the non-idealities in the platform flight path. In this context, the first attempt was to incorporate an IMU integrated with a Global Positioning Satellite (GPS) receiver and a position accuracy of 2.5 m and an angular dynamic accuracy of 1 degree RMS. The position and attitude information of the platform were logged simultaneously with the radar raw data for a proper image geocoding. At first, the information provided by the IMU was intended to be used to apply MOtion COmpensation (MOCO) techniques in the focusing process. Thus, the possible motion errors might be compensated and the defocusing, the geometric distortions and the phase errors of the retrieved images could be

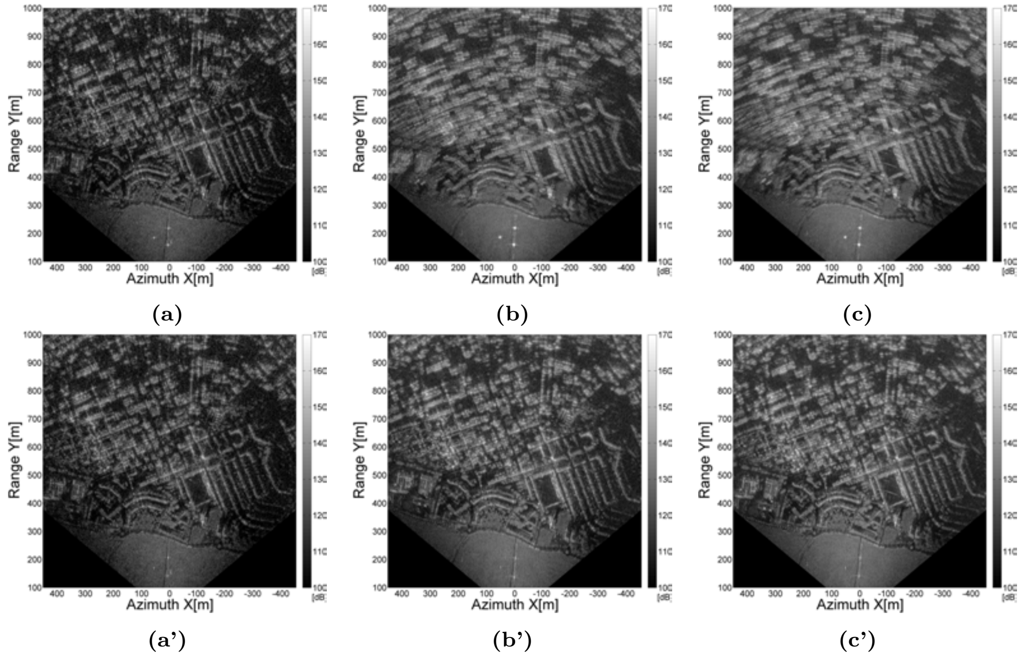

(a) (b) (c)

(a') (b') (c')

Figure 6.3: SLC images in Cartesian coordinates for different aperture lengths. Before autofocus: (a) 13.4 m, (b) 40.9 m and (c) 55.6 m. After autofocus: (a') 13.4 m, (b') 40.9 m and (c') 55.6 m. Flight conditions: 150 m height, $v_{UAV} = 8.9 m/s$, VV Pol.

Figure 6.4: Example of PARC location in the agricultural field of the scenario.

minimized. Nevertheless, this option was discarded because the accuracy of cost-effective devices that are suitable to be integrated in the UAV MP, overcoming restrictions of size and weight, is not enough to meet the necessary requirements. In this sense, the accuracy of these systems is too low in terms of the wavelength. Besides, the vibrations of the platform are another important drawback that degrades the quality of the measurements performed by the IMU.

To overcome the defocusing problem due to the instabilities of the UAV MP when processing long apertures, the autofocus algorithm proposed in Section 5.3 of Chapter 5 has been applied. Since it is difficult to find three natural PS in the scenario with good reflectivity response, three different PARCs have been placed in visible and accessible locations of the scenario in order to retrieve its phase history to apply the autofocus algorithm. Figure 6.4 shows one of the PARCs placed in the agricultural field of the scenario surrounded by growing vegetation. Their pointing angles (azimuth and elevation) are adjusted to maximize their visibility with the sensor during the measurements. They can be recognized in Figure 6.3 as the three PS forming a triangle between 150 m and 220 m in the range axis and centered in the azimuth direction.

Analyzing the evolution of the phase of the PARCs during the acquisition time $\varphi_{PARC}(t)$, the relative distance variation from the sensor to the PARCs $R_{PARC}(t)$ can be obtained from Equation 2.5, but not the nominal value of the distance. In practice, it can be extrapolated for the entire aperture knowing the slant range distance at the first instant of measurement $R_{PARC}(t=0)$. Despite not having the real value $R_{PARC}(t=0)$, it can be approximated by its ideal value taking as reference the position of the platform given by the GPS together with the barometer. This approximation is valid because the positioning errors of the platform are small in comparison with the distance from the sensor to the scatterer. Figure 6.5 shows the retrieved information from the PARC's phase and the computed parameters obtained by the autofocus algorithm to refocus the image in a second iteration.

Figures 6.3 (a'), (b') and (c') show the three different SLC images after applying the autofocus algorithm to Figures 6.3 (a), (b) and (c), respectively. The correction parameters $u_x(t)$, $u_y(t)$ and $u_z(t)$ obtained in Figure 6.5 are introduced in the focusing process to generate the images. Comparing, for instance, Figures 6.3 (c) and (c') it

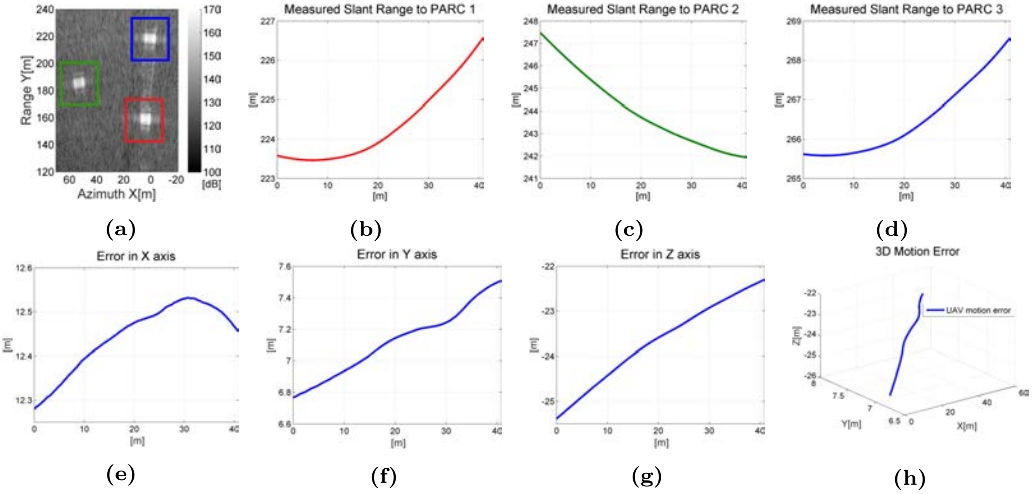

Figure 6.5: Autofocus parameters for an aperture of approx. 40.9 m and flight conditions: 150 m height, $v_{UAV} = 8.9m/s$, VV Pol. (a) SLC image in Cartesian coordinates with zoom to PARCs. Relative measured slant range to: (b) PARC 1, (c) PARC 2 and (d) PARC 3. Filtered deviation: (e) $u_x(t)$, (f) $u_y(t)$ and (g) $u_z(t)$. (h) 3D representation of the platform deviations.

is clearly visible the reduction of the azimuth defocusing after the application of the autofocus algorithm. Thus, larger apertures can be processed minimizing the effect of the motion errors in the processed images. Moreover, the fact of processing larger apertures implies a higher transmitted energy, i.e higher SCR, and an improvement in the quality of the SLC images.

The improvement in the azimuth resolution after applying the autofocus algorithm can be clearly seen in Figure 6.6, where it is shown a zoom to the area containing the PARCs in the SLC images. Even the track in the scenario is well defined in the image of Figure 6.6 (b), while in Figure 6.6 (a) is not easily recognizable. The cut in azimuth of the three PARCs is presented in Figure 6.6 (c), were it is noticed that the response of the three PSs is clearly spread before applying the autofocus algorithm and gets better focused after applying it. Thus, the redistribution of the energy in the focusing process results in higher values of amplitude, in particular 2.31 dB, 10.2 dB and 6.08 dB, for PARCs 1, 2 and 3, respectively.

As stated in Chapter 5, Subsection 5.3.1, the use of a sub-optimal aperture length implies that the azimuth resolution δ_{az} varies with r_T, L_{sa} and θ. According to Equation 3.1, the theoretical azimuth resolutions of PARCs 1, 2 and 3 are 0.14 m, 0.16 m and 0.16 m, respectively, and the measured 3 dB azimuth resolutions after applying the autofocus algorithm are 0.39 m, 0.22 m and 0.20 m. Again, it has to be considered the Hanning filter window applied in the cross-range domain that degrades the main lobe. Taking this issue into account, the measured azimuth resolutions after the autofocus algorithm are quite near to the theoretical ones, although the autofocus algorithm could still be improved. Table 6.1 summarizes the theoretical and measured resolutions after the autofocus algorithm for the aperture of 40.9 m.

At this point and regarding the autofocus processing, it is worth mentioning that the calibrators presented in this subsection have been placed too close to each other to compensate for the possible deviations in the entire image. Because of that, the autofocus compensation works better near the PARCs and worse as we move away from them. In the future, it is recommendable to place them much more separated and encompassing the urban area. Two of them should be aligned in the boresight direction and a third one much more squinted, forming a triangular shape. This way, the deviations in the three axes could be better extracted and compensated in the whole image.

In conclusion, the capability of the ARBRES-X SAR sensor integrated in the UAV MP to obtain good quality SLC images in stripmap configuration has been demonstrated in this subsection, since different focused images of the urban area of Ripollet obtained with linear trajectories have been exposed.

Table 6.1: Azimuth resolution

	δ_{az} **Theoretical [m]**	δ_{az} **Measured [m]**
PARC 1	0.14	0.39
PARC 2	0.16	0.22
PARC 3	0.16	0.20

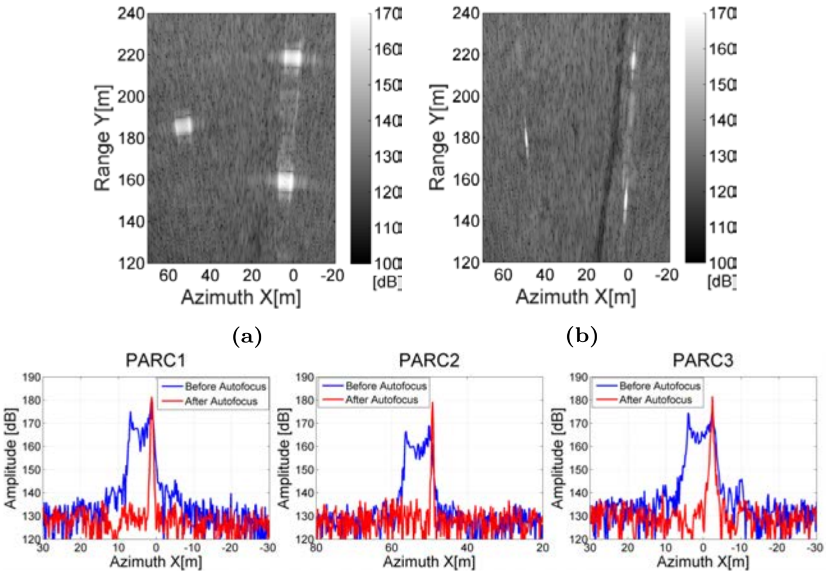

(a)

(b)

(c)

Figure 6.6: Aperture length of 40.9 m. Zoom to PARCs in SLC image before (a) and after (b) application of autofocus algorithm. (c) Cut in azimuth of the PARCs RCS before and after the application of the autofocus algorithm.

6.3 Innovative flight strategies in airborne UAV MP multidimensional SAR

As it has been pointed out previously, the flight versatility of the UAV MP open new possibilities in airborne SAR observations. The present subsection exposes the following innovative results obtained with the ARBRES-X SAR sensor integrated in the UAV MP, which can be divided in four groups:

- Repeat-pass interferometric results.
- Fully polarimetric results.
- SLC images of implementing vertical apertures.
- SLC images of implementing circular apertures.

The aim of this subsection is to assess the system performances and the initial SAR capabilities of the UAV MPs while evaluating the technical challenges and limitations of operating the sensor in this type of platforms.

6.3.1 UAV MP SAR repeat pass interferometry

SAR interferometry exploits the phase differences between two sets of complex SAR data to derive, for example, topographic information. Differential Interferometry (DInSAR) is a particular configuration in which the interferometric data is obtained in different passes separated by a short baseline for deformation measurements [21]. The antenna position that defines the baseline during the two passes is of great importance to have a good accuracy in the interferometric process. In the UAV MP, the baseline depends on the precision in positioning to perform the required flight paths and the undesired motion errors. Having a good control of the trajectory, together with the minimization of the instabilities of the platform, is mandatory to obtain interferometric results. According to [105], the total baseline decorrelation is reached in correspondence with the critical baseline

$$\mid B_{nc} \mid = \left| \frac{\lambda r_T tan(\theta_0 - \alpha_s)}{2\delta_{rg}} \right| \tag{6.1}$$

where λ is the wavelength of the system, r_T is the sensor to target distance, θ_0 is the off-nadir angle, α_s is the local terrain slope (range) and δ_{rg} is the slant range resolution. Figure 6.7 shows the evolution of the critical baseline as a function of θ_0 for different r_T.

In our particular case, it has to be stressed that due to the fact of performing short-range images with the considered geometry, the angles and distances are quite varied, complicating the determination of the optimum baseline. Taking this into account, the off-nadir angle of the ARBRES-X SAR system integrated in the UAV MP has been considered of approximately 45° and the local terrain slope of the illuminated scenario is approximately 4.6° with an inclination of the 8% up to 300 m. In Figure 6.7 it can be seen that, for $r_T = 100$ m and $r_T = 750$ m the critical baseline ranges from 0.88 m to 6.6 m, respectively.

Taking advantage of the possibility offered by the UAV MP to perform pre-programmed routes, repeat pass interferometry strategies can be assessed. Figure 6.8 shows an aerial view of the scenario with the flight path information, where two different passes of approximately 96 m in stripmap configuration can be seen. Three PARCs and a trihedral corner reflector were placed in the agricultural field to be used as references. The UAV MP was programmed to fly at 100 m with an interferometric baseline between passes of 0.8 m, which is under the critical baseline calculated by Equation 6.1 for $r_T = 100$ m. The programmed baseline should be on the order of 1/10 of the critical one to ensure sufficient coherence and range resolution of the interferogram. This would mean that the value of 0.8 m is too close to the critical one since the passes should be separated by around 8 cm. In this sense, the lack of accuracy of the navigation system constitutes the main limitation of the platform to perform interferometric baselines on the order of magnitude required. For the GPS together with the barometer, the vertical positioning of the platform is on the order of 0.5 m, which is too far from the 8 cm.

Figure 6.9 (a) and (b) show the evolution of the barometric altitude and the inter-

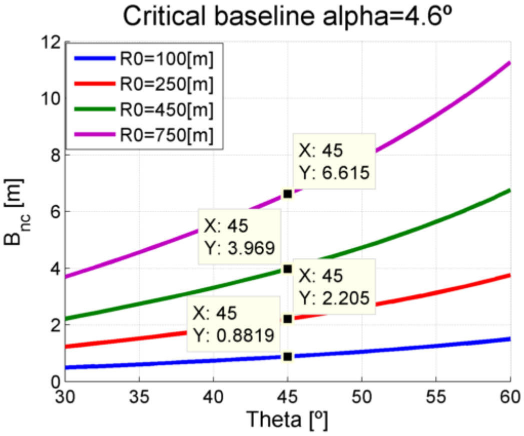

Figure 6.7: Critical baseline as a function of the off-nadir angle for different r_T.

Figure 6.8: Image of the scenario taken from Google Earth with the flight path information and the different calibrators.

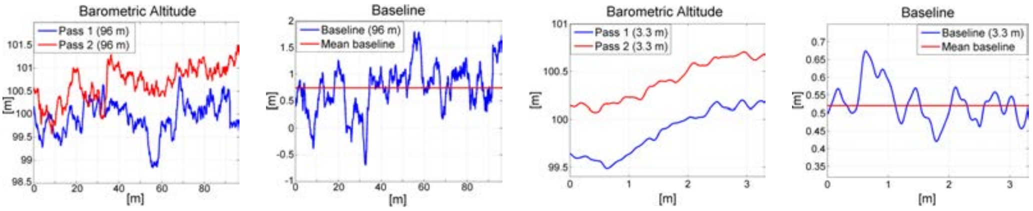

(a) **(b)** **(c)** **(d)**

Figure 6.9: (a) Barometric altitude and (b) baseline for the two passes of different apertures of approx. (c) 96 m and (d) 3.3 m.

ferometric baseline of the UAV MP, respectively, during the complete aperture of 96 m. The mean baseline of the aperture is 0.74 m, which is under the critical baseline. As it is clearly visible, the height of the platform was not constant during the acquisition time, which introduces a lot of focusing errors in the processing. This, together with the flight deviations and the instabilities of the platform, requires processing short apertures in order to minimize the defocusing of the images and the phase errors. In this sense, the autofocus algorithm cannot be applied yet to compensate this motion errors in long apertures preserving the phase information, which could be due to a lack of precision in the correction in terms of the wavelength.

Figure 6.9 (c) shows the barometric altitude for an aperture of approximately 3.3 m, where the measurements are less affected by the instabilities of the UAV MP during the flight path. Furthermore, the selected part of the aperture for the two passes have a similar ascending behavior. Finally, Figure 6.9 (d) shows the interferometric baseline evolution for this shorter aperture, where the largest difference of distance between the maximum and the minimum is 0.25 m and the mean baseline is 0.52 m. At this point it is worth mentioning that the theoretical accuracy of the navigation system in the positioning of the platform is ±0.5 m in vertical and ±1.5 m in horizontal. Furthermore, the velocity accuracy of the UAV MP is 0.1 m/s, which is determined by the GPS. Moreover, the barometer of the system has a vertical accuracy of nearly 25 cm. Despite these values, the parameters retrieved from the IMU of the platform do not have enough accuracy to quantify the precision of the flights. This can be observed, for instance, in the data shown in Figure 6.9, where the response of the IMU represents unreal dynamics of the platform. An example can be seen in the barometric altitude shown in Figure 6.9 (a), where it can be appreciated impossible variations in the height of the platform of 1.25 m in 0.15 seconds.

Figure 6.10 (a) and (b) show the SLC images obtained with the two different passes. Besides, the coherence and the retrieved interferometric phase are shown in Figure 6.10 (c) and Figure 6.10 (d), respectively. In this case, the velocity during the short aperture has been assumed constant, which is a feasible approximation, since the acquisition time of 0.3 seconds is too short to allow great velocity deviations.

As it can be seen in Figure 6.9, the motion errors of the platform in each pass are independent during the interferogram generation. In this case, differently from single-pass systems, the baseline has a time-varying error that may cause significant phase errors in range and azimuth direction. Nevertheless, Figure 6.10 shows that, despite having a non-constant baseline during the selected part of the aperture, the first interferogram with a UAV MP has been obtained. However, it has to be admitted that it is extremely difficult to obtain interferometric maps, since perfectly parallel and aligned passes are difficult to achieve with the UAV MP. This is due to the lack of the required accuracy in the positioning of the platform and the inherent motion errors of UAV MPs. For other interferometric results obtained with the platform see Appendix B.

As the accuracy of the GPS and the IMU is not sufficient to retrieve the flight deviations that permit to let us know the correct baseline during the acquisition time, future steps include putting some effort on the estimation and correction of time varying baseline errors from the interferometric SAR data to improve the results, applying methods such as the one proposed in [106]. Moreover, a better navigation system operating with Real Time Kinematic (RTK) GPS together with an IMU should be used, which would permit an accuracy of few centimeters both in vertical and horizontal. This way, larger apertures might be processed and better interferometric results could be achieved.

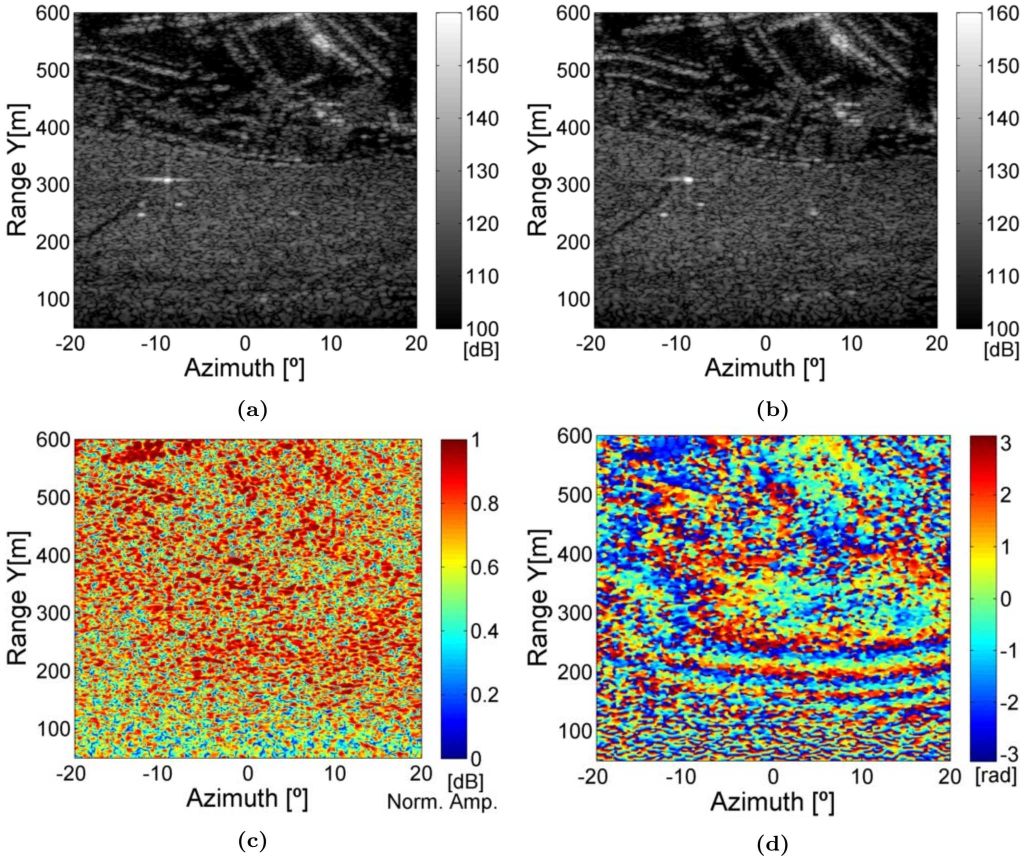

(a)

(b)

(c)

(d)

Figure 6.10: Polar coordinates. (a) SLC pass 1. (b) SLC pass2. (c) Coherence multilook 4m x 0.4 deg. (d) Interferogram multilook 4m x 0.4 deg. Flight conditions: 100 m height, $v_{UAV} \approx 8.7m/s$, 0.52 m mean baseline, VV Pol.

6.3.2 Fully polarimetric UAV MP SAR measurements

To evaluate the fully polarimetric capabilities of the ARBRES-X SAR sensor, some measurements have been performed in the RACBSA airfield. To analyze the results it has to be taken into account that, as said in Section 5.2.2, four patch antennas have been used in the system. They have been selected for their simplicity, low weight, low size and easy integration into the system, but they usually offer low levels of cross-talk as it has been demonstrated in Subsection 5.4 in Chapter 5. Despite this difficulty, the CPD factor of the patch antennas is approximately -22 dB. Furthermore, the isolation between the two receiving channels is approximately -37 dB. Considering this, the first preliminary results presented in this section are not polarimetrically calibrated but, as will be shown, the theoretical and measured results are consistent. In any case, the results here presented constitute the first evidence that it is possible to perform fully polarimetric measurements with a SAR sensor integrated in a UAV MP. However, as mentioned in the previous chapter, to obtain reliable fully polarimetric results a hardware improvement is mandatory to remove the antenna cross-talk effects prior the calibration of the system.

Figure 6.11 shows the flight path performed by the UAV MP and the disposition of different calibrators in the scenario. To assess the different polarizations, three PARCs and a trihedral corner reflector have been placed in the agricultural field of the area. Figure 6.12 (a) and (b) show the photograph of PARC 1 and 2, respectively. Figure 6.12 (c) shows PARC 3, which has been rotated 45 degrees with respect to PARC 2. Finally, the trihedral corner reflector is shown in Figure 6.12 (d). The orientation of the different PARCs in the scene is detailed in Figure 6.13, where it can be observed that the antennas of PARC 2 are rotated 90 degrees with respect to the antennas of PARC 1, but both are expected to return the same polarizations.

The theoretical scattering matrices of the different elements are shown in Equation 6.2

Figure 6.11: Disposition of the calibrators in the scenario and flight path performed by the UAV MP. Image from Google Earth.

and the theoretical polarization signatures are shown in Figure 6.14. The trihedral corner reflector is expected to have identical horizontal and vertical backscattering sections, HH=VV, while no cross-polarizations components are generated, HV=VH=0. PARC 1 and PARC 2 are expected to have cross-polarizations and co-polarizations components and, finally, PARC 3 is expected to have only the cross-polarization component HV.

$$
\begin{gathered}
S = \begin{pmatrix} S_{HH} & S_{HV} \\ S_{VH} & S_{VV} \end{pmatrix}; \\
S_{P1-2} = \begin{pmatrix} 1 & 1 \\ 1 & 1 \end{pmatrix}; S_{P3} = \begin{pmatrix} 0 & 1 \\ 0 & 0 \end{pmatrix}; S_{TRI} = \begin{pmatrix} 1 & 0 \\ 0 & 1 \end{pmatrix};
\end{gathered}
\tag{6.2}
$$

Figure 6.15 shows the SLC images of the four polarizations HH, HV, VH and VV. As expected, PARC 1 and PARC 2 can be perfectly seen in all the polarizations, while the cross-polar polarization HV is the most important component of PARC 3. Besides, the most important components of the measured trihedral are HH and VV polarizations. To evaluate the response of the calibrators to the different polarizations, the measured Radar Cross Section (RCS) is shown in Figure 6.16 and the retrieved scattering matrix of the calibrators, derived from the measured RCS, can be seen in Equation 6.3.

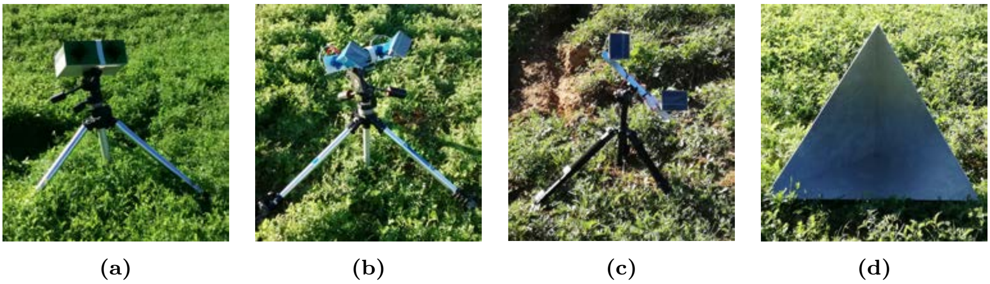
(a) (b) (c) (d)

Figure 6.12: Photograph of the calibrators placed in the scenario. (a) PARC 1. (b) PARC 2. (c) PARC 3. (d) Trihedral corner reflector.

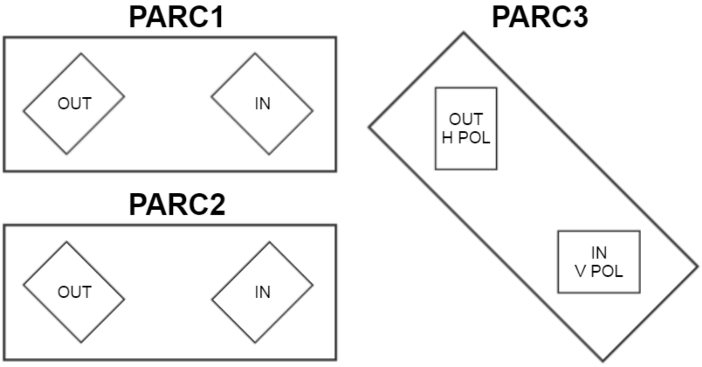

Figure 6.13: Sketch of the orientation of the PARCs located in the scenario to be used as references for the fully polarimetric measurement.

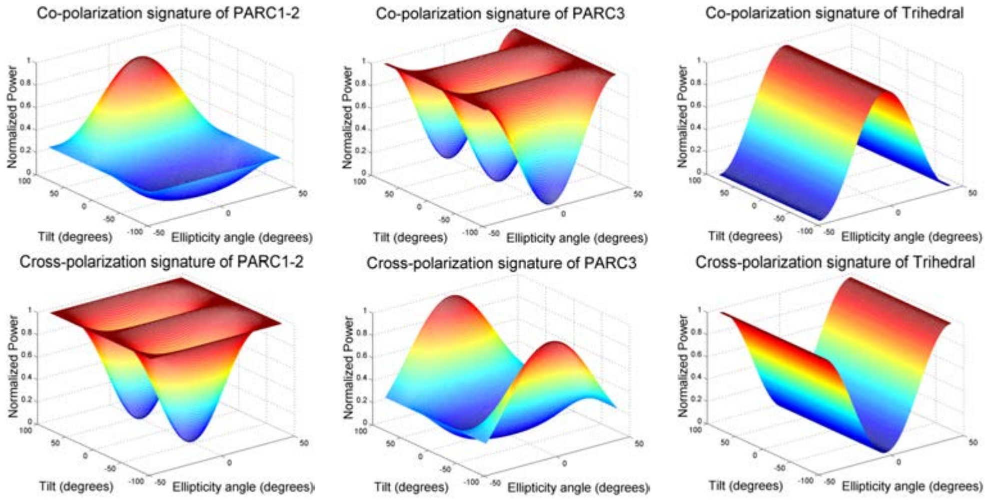

(a) **(b)** **(c)**

Figure 6.14: Theoretical polarimetric signature of: (a) PARC 1 and 2. (b) PARC 3. (c) Trihedral corner reflector.

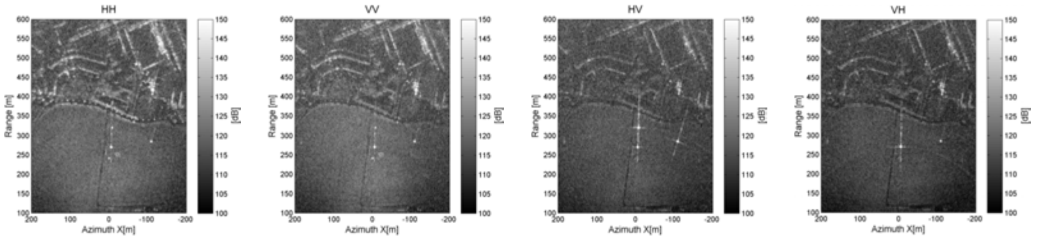

(a) **(b)** **(c)** **(d)**

Figure 6.15: SLC images of the different polarizations. (a) HH. (b) VV. (c) HV. (d) VH. Flight conditions: 150 m height, $v_{UAV} = 8.9m/s$.

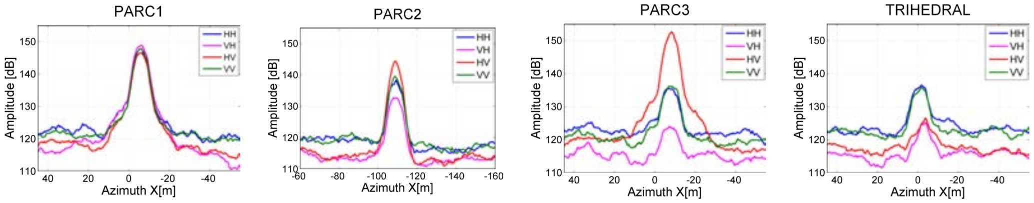

(a) **(b)** **(c)** **(d)**

Figure 6.16: Measured RCS of (a) PARC 1. (b) PARC 2. (c) PARC 3. (d) Trihedral corner reflector.

$$\begin{aligned} S_{P1} &= \begin{pmatrix} 0.81 & 0.69 \\ 1 & 0.78 \end{pmatrix}; \; S_{P2} = \begin{pmatrix} 0.44 & 1 \\ 0.23 & 0.49 \end{pmatrix}; \\ S_{P3} &= \begin{pmatrix} 0.1 & 1 \\ 0.02 & 0.15 \end{pmatrix}; \; S_{TRI} = \begin{pmatrix} 1 & 0.08 \\ 0.08 & 0.86 \end{pmatrix}. \end{aligned} \tag{6.3}$$

From the measured scattering matrix, the measured polarimetric signature of the calibrators is shown in Figure 6.17.

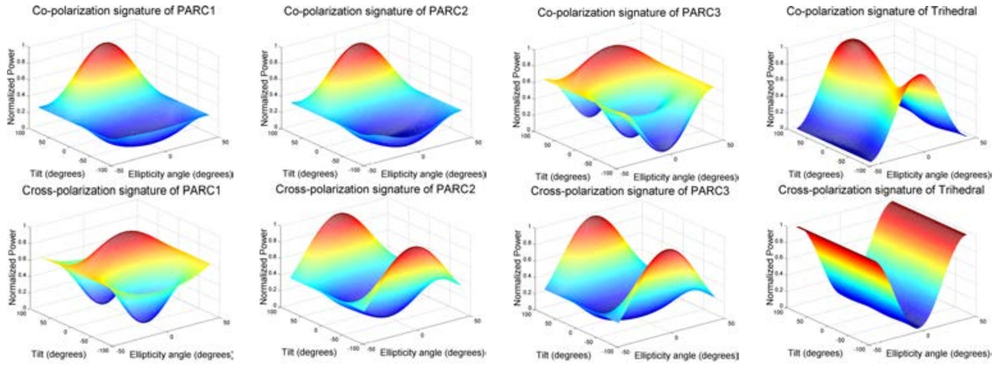

(a) **(b)** **(c)** **(d)**

Figure 6.17: Measured uncalibrated polarimetric signature of: (a) PARC 1. (b) PARC 2. (c) PARC 3. (d) Trihedral corner reflector.

Figures 6.16, 6.17 and the scattering matrices in Equation 6.3 show that the polarimetric response of the different calibrators generally corresponds to the theoretical behavior, but with some variations. These differences are, in part, due to the difficulty to perfectly point the calibrators to the expected flight path. As stated in Section 3.5 of Chapter 3, the high sensitivity of the PARCs response to alignment errors and the fluctuations in the signal amplification process make active calibrators unsuitable for long-time calibration purposes [76], [69]. Moreover, the reciprocity of the cross-polar channels is only ensured when perfectly orientated at exactly 45°, which is extremely difficult when flying with the ARBRES-X SAR system. The possible instabilities of the platform and the variation in the orientation of the antennas during the acquisition time can also degrade the polarimetric response. Because of that, the PARCs are not taken into account when trying to calibrate the system. Moreover, for targets with an important squint angle the polarization is rotated, as is the case of PARC 2. In this context, the measured uncalibrated response of the trihedral corner reflector is the only one that can give reliable information of the polarimetric response. In this case, the co-polar signature differs a little from the expected one while the cross-polar component perfectly matches the theoretical one.

As mentioned in Section 5.4 of Chapter 5, the system has important cross-talk effects that degrade the measured polarimetric data. As mentioned, this problem must be fixed at hardware level prior to the calibration. Future steps include the polarimetric calibration of the system, which is not a trivial problem. In our system, the length of the synthetic aperture is short and therefore, wide beam antennas (approximately 60° in our case) have to be used in order to obtain an image of suitable size. This implies a change of the polarization basis according to the illumination direction. This is not a problem in airborne and satellite SAR sensors where high-gain narrow beam antennas are used. As a consequence, this factor must be taken into account to calibrate polarimetrically the data.

6.3.3 Vertical flight in UAV MP SAR

During the last years, tomographic techniques for obtaining volume information of scatterers have progressed considerably [30], [31]. The tomograms can be used, for instance, to monitor vegetated areas or to estimate ground topography. However, in order to retrieve the vertical scattering distribution, it is necessary to use multiple passes of the SAR sensor at different positions. In the airborne case, it is extremely difficult to obtain equally spaced baselines between the different passes. Besides, the flight paths can suffer deviations from the ideal straight trajectory in the X, Y and Z axis, which extremely complicates the processing of the data. In this context, the use of the UAV MP has several advantages that make it suitable to perform tomographic images by means of exploiting the possibility of this platform to perform vertical flights to do vertical imaging in airborne SAR. With this strategy, the problems of the alignment and deviations of different flights might be overcome.

Figure 6.18 shows two representations of a vertical flight path performed by the UAV MP and taken from Google earth. In our experience, the ascending vertical flight of the UAV MP is very stable and does not suffer from important deviations from the ideal one. Moreover, the ascending velocity of the platform is maintained almost constant and the flight precision is equivalent to the horizontal stripmap acquisition mode.

In Figure 6.18 (b), it can be seen a pylon that is located at 197 m from the vertical flight trajectory. Besides, 2 PARCs have been placed in the scenario at 173 m and 226 m. Regarding the terrain of the scenario, it has an inclination of approximately 8% up to 300 m, where the road separating the agricultural field from the city begins. Figure 6.19 (a) shows the SLC image of the scenario obtained with the ARBRES-X SAR sensor during a normal horizontal flight. The yellow line in the image corresponds to the vertical profile

(a) (b)

Figure 6.18: Images of the scenario taken from Google Earth with the vertical flight path information. Ascending velocity of 2 m/s. (a) North-west orientation. (b) South-west orientation.

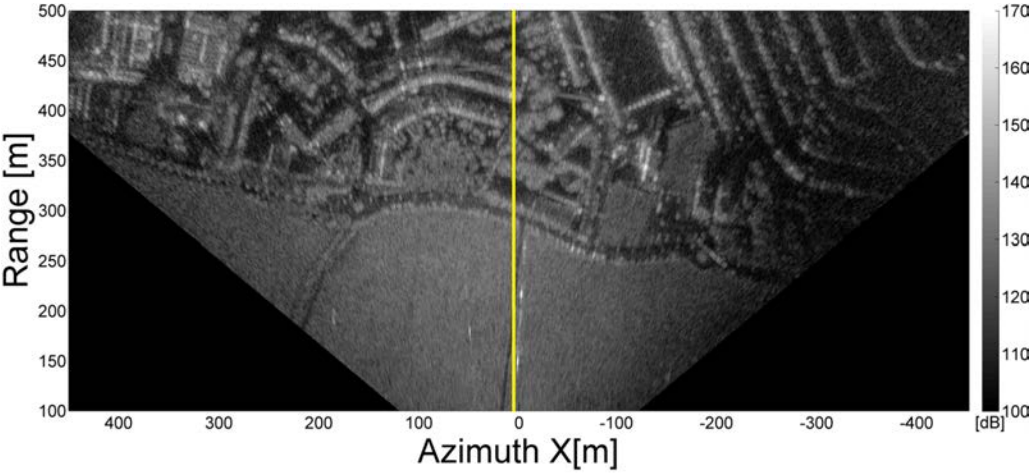

(a)

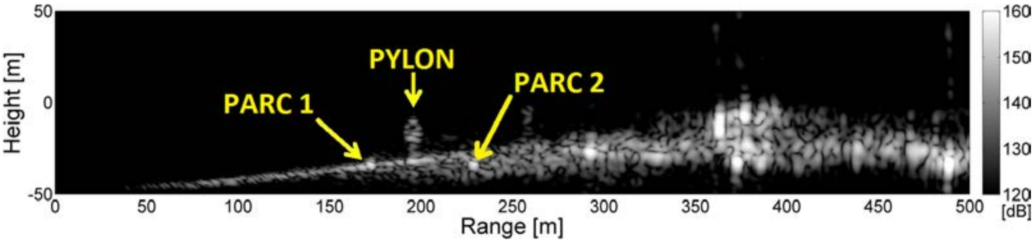

(b)

Figure 6.19: (a) SLC image of the scenario with flight conditions: 150 m height, $v_{UAV} = 8.9m/s$, VV Pol. (b) SLC image of the scenario during the vertical flight with flight conditions: $v_{UAV} = 2m/s$, VV Pol, 3 m aperture length. The profile corresponds to the yellow line shown on the SLC image in (a).

shown in Figure 6.19 (b), where the SLC obtained during the vertical flight is shown. The pylon located at 197 m can be perfectly seen in Figure 6.19 (b) and also PARC 1 and 2 at 173 m and 226 m, respectively. In the same way as in conventional SAR measurements, the resolution in elevation can be determined by Equation 3.1. Again, it depends on the range distance R, the length of the synthetic aperture in elevation L and the squint angle θ.

Table 6.2 summarizes the theoretical and measured resolutions for the 3 m aperture length. The theoretical azimuth resolutions for PARC 1 and 2 are 1.48 m and 1.96 m. Furthermore, the measured 3 dB azimuth resolutions are 1.93 m and 2.08 m for PARC 1 and 2. Again, considering the effect of the cross-range Hanning window, the measured resolutions are quite close to the theoretical ones.

Figure 6.19 (a) shows that the agricultural field of the scenario finishes approximately at 300 m and beyond this range distance starts the city. In Figure 6.19 (b), the contribution of all the scatterers covered by the antenna beamwidth corresponding to the urban area are collapsed at the same range. For that reason, there are a lot of bright pixels

Table 6.2: Azimuth resolution in vertical flight

	δ_{az} **Theoretical [m]**	δ_{az} **Measured [m]**
PARC 1	1.48	1.93
PARC 2	1.96	2.08

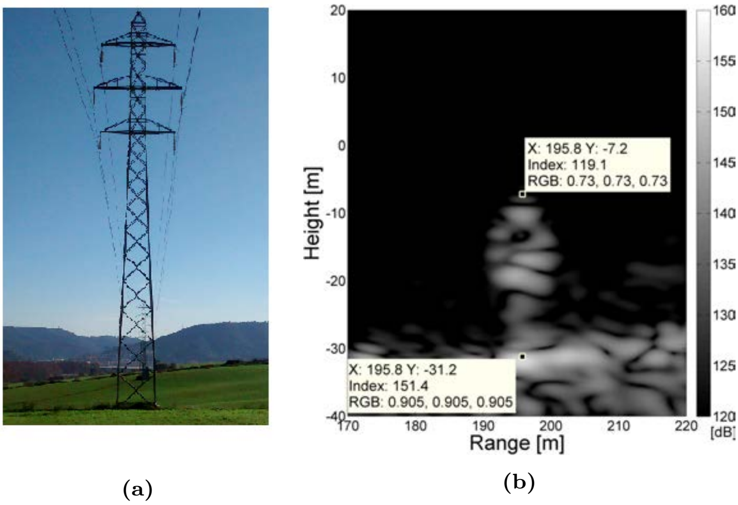

(a)

(b)

Figure 6.20: (a) Photograph of the pylon in the scenario. (b) Zoom to the pylon in the vertical aperture of the scenario obtained with the ARBRES-X SAR sensor.

between 350 m and 400 m that correspond to the buildings of the city. The slope of the terrain derived from the vertical aperture is of approximately 8% up to 300 m, what matches with the information obtained from topographic maps of the area.

The pylon isolated in the middle of the agricultural field constitutes a good reference to evaluate the performances of the vertical flight, since no other surrounding scatterers affect its reflectivity and has a considerable height. Figure 6.20 (a) shows a photograph of the pylon in the scenario where it can be seen that it has a typical pyramidal shape. It is a standard voltage tower that has a height of 24 m with a voltage of 132 KV. To analyze the response of the pylon in the focused image, Figure 6.20 (b) shows a zoom to the tower extracted from the image of the vertical aperture presented in Figure 6.19 (b). It can be observed that the markers located at the base and the top of the pylon in the SLC image present a height difference of 24 m, which perfectly matches the real height of the tower.

In the way it is performed, the vertical image is affected by left-right ambiguity. Nevertheless, the goal of this experiment is to set the basis to vertical tomography, where this ambiguity is solved by considering a given number of vertical flights. In addition, in the experiment, this ambiguity has a minimum effect in the imaged tower as it comes from a grass area.

6.3.4 Circular flight in UAV MP SAR

The aim of introducing a circular measurement in this chapter is to demonstrate the feasibility of acquiring SAR data with this type of trajectories with the UAV MP. The possibility of this platform to perform circular flights can be exploited to perform high resolution Circular SAR (CSAR) measurements in the future, where trajectories of 360° around a spotted region are used. If this is achieved, the possibility to perform tomographic imaging by means of circular trajectories instead of straight lines could also be assessed. In this sense, by obtaining different circular trajectories over an area several options would be possible, such as holographic representation of the scene by means of combining different tomograms [31], [107]. In our particular case, as a first approximation to these type of trajectories with the UAV MP, a partial segment of a circular flight has been processed and presented in this subsection, which allows to envisage the possibility to perform complete circular flights in the future.

Figure 6.21 (a) shows the flight path information of the partial segment of a circular flight taken from Google Earth and Figure 6.21 (b) shows the SLC image of the scenario obtained with the ARBRES-X SAR sensor during this trajectory. The aperture length is approximately 9.3 m and the platform height is approximately 50 m. In the focused image, the landing strip and the constructions of the airfield are perfectly seen, as well as the different paths, the agricultural field and the road with the two roundabouts.

Theoretically, the advantage of obtaining SAR images with circular flights is that it allows the maximum attainable resolution of a fraction of the wavelength [31]. In the SLC image obtained with the circular flight in Figure 6.21 (b), the area that theoretically has better resolution corresponds to the constructions in the airfield, such as the different buildings or the landing strip. Nevertheless, this is a preliminary result that has to be improved. Future work includes the implementation of SAR measurements with complete circular apertures endowing the system with narrow beam antennas. Furthermore, some calibrators will be placed in the near range to evaluate the obtained azimuth resolution.

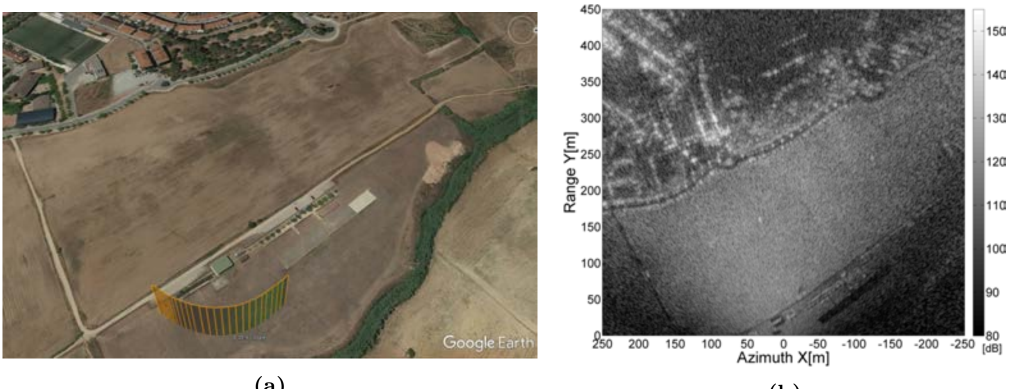

(a)

(b)

Figure 6.21: (a) Image of the scenario taken from Google Earth with the semicircular flight path. (b) SLC image of the scenario obtained with the ARBRES-X SAR sensor during the circular flight. Flight conditions: 50 m height, $v_{UAV} = 6.2m/s$, VV Pol.

6.4 Concluding remarks

In the present chapter the initial SAR capabilities of UAV MPs have been evaluated. To that end, the feasibility of the ARBRES-X SAR sensor integrated into a small multicopter platform has been demonstrated by performing several measurement campaigns in the RACBSA airfield. Furthermore, the main limitations and technical challenges of obtaining SAR data with this type of platforms have been assessed along this study.

The capability of the UAV MP to execute different types of trajectories has been exploited to evaluate the system performance and to obtain first preliminary results. It has been observed that the defocusing problem in the retrieved images is due to the deviation of the platform from the nominal trajectory and the flight instabilities. To overcome this undesired effect, it has been concluded that the use of a cost-effective, small-size IMU is a non-viable option. This is because of the lack of accuracy of these systems, which has forced us to discard the use of MOCO techniques to focus the image. Alternatively, an autofocus algorithm has been applied to refocus the SLC images, improving its quality for large apertures.

Otherwise, the inherent instability of the platform and the insufficient positioning accuracy of the GPS system together with the barometer make it extremely difficult to obtain interferometric results. The autofocus algorithm is well suited to compensate amplitude images, but the problem is not yet efficiently resolved with the phase in long apertures. Because of that, the interferometric measurements have been processed using small apertures, where the flight deviations are less important. Nevertheless, the first SAR interferogram obtained with a repeat-pass flight performed with a UAV MP has been presented.

In the future, the navigation system of the platform must be improved in order to operate the repeat-pass interferometric measurements. Nowadays, there are systems operating with Real Time Kinematic (RTK) GPS that permit an accuracy of few centimeters both in vertical and horizontal, as is the case of the DJI A3 Pro navigation system. Furthermore, as exposed in Subsection 6.3.1 of the present chapter, devoting some effort on the estimation and correction of time varying baseline errors from the interferometric SAR data constitutes another research line to improve the results. Moreover, if possible, a high precision cost-effective IMU integrable in the UAV MP would also be desirable to apply MOCO techniques.

On the other hand, a vertical and a partial segment of a circular aperture have been successfully performed obtaining SLC images of the scenario, which envisages the capability of the UAV MP to perform tomographic images and complete circular apertures in the future. Regarding the vertical flight, it has been observed that the ascending velocity of the platform is very stable and the trajectory does not suffer from important deviations from the nominal track, which makes the UAV MP a suitable alternative to perform tomographic images in the future.

One of the limitations of GB-SAR sensors is its dependence on the geometry of the scenario to illuminate the area under study. Sometimes, having the possibility to find the optimal position to place the GB-SAR sensor with the required orientation can be a problem. In the future, the use of UAV MPs can overcome this drawback allowing the monitoring of almost any site. In this sense, the use of SAR sensors integrated in UAV

MPs can be considered as an interesting alternative between ground based and airborne SAR sensors.

In conclusion, the UAV MP is a promising platform that opens new potentials for several applications, such as repeat-pass interferometry or differential tomography imaging with the realization of almost arbitrary trajectories.

Chapter 7

Main Conclusions and future research lines

This Ph.D. dissertation describes the research work performed during a period of more than 4 years (from March 2014 to September 2017) in the RSLab, within the Signal Theory and Communications (TSC) department at the UPC.
The purpose of this chapter is to summarize the main results and contributions presented along the manuscript as well as to provide some insights on the possible future research lines.

7.1 Main Conclusions

The encompassing objective of the present doctoral work has been part of the implementation and the subsequent evaluation of capabilities of two X-band SAR sensors. On the one hand, the RISKSAR-X radar designed to be operated at ground to monitor small-scale areas of observation and, on the other, the ARBRES-X sensor designed to be integrated into small UAVs. Despite its inherently dissimilar conception, the concurrence of both sensors has been evidenced along this manuscript. By taking advantage of the similarities between them, it has been possible to analogously assess both sensors to obtain conclusions, such as for instance when evaluating the effect of the azimuth miss-registration analyzed in Section 5.3.3 of Chapter 5. In this context, the common link has been the development of the polarimetric OtF operation mode in the RISKSAR-X, allowing this sensor to be operated equivalently to the ARBRES-X.

Regarding the RISKSAR-X sensor, several hardware contributions have been developed during part of this Ph.D. with the aim of improving the system performance. There are two of them that deserve special attention. On the one hand, the migration from the DDS to the PLL technology in the frequency generation unit has permitted the optimization of the transmitted signal and the endowment of a higher degree of flexibility to the system. By incorporating a microcontroller, which is accessible through a USB port, it can be configured the registers of the PLL, the frequency ramp generation, the trigger of the digitizer and the type of polarimetric acquisition by controlling the solid-state switch in the transmitter. This way, the system is able to operate in different operation modes as explained in Section 3.2 of Chapter 3. On the other hand, the introduction of the solid-state switch in transmission, together with two identical reception channels, has allowed the possibility to operate the system in the fully polarimetric OtF acquisition mode. The capability to synchronously switch between the two transmitting antennas while displacing the SAR sensor has allowed to reduce considerably the acquisition time.

The reduction of the relative long scanning time is of great interest since, as exposed in Chapter 4, the fact of having moving scatterers in the scenario that present a short term variable reflectivity during the scanning time may degrade the extracted parameters from the retrieved data and the GB-SAR image reconstruction. This changing reflectivity is mainly due to moving vegetation caused by the wind. In this context, in scenarios where the area of interest is surrounded or contains vegetation, the retrieved information can be deteriorated since pixels associated to moving scatterers also alter the reflectivity map of neighbouring pixels in the same radial range. During this doctoral activity, it has been studied the image blurring, the decorrelation and the coherence degradation introduced by this effect. It has been observed that periodic changes in scatterer reflectivity imply the apparition of cross-range replicas of the scatterer, while the random ones force image blurring and image decorrelation. A new term in the differential interferometric coherence γ_{blur} that takes into account the image blurring has been introduced [JA3]. Furthermore, the blurring effect could be also noticeable in airborne SARs, depending on the Doppler bandwidth and the frequency spreading of the energy of the scatterers.

All the effects that degrade the extracted parameters are an important drawback to GB-SAR systems, which are mainly used to detect and monitor changes in the scenario. For this reason it has been concluded that it is necessary to shorten the scanning time to reduce the cross-range image blurring. Nevertheless, despite an important reduction of the scanning time to seconds, the degradation of the retrieved parameters is not improved under strong wind conditions, so it is clearly preferable to take measurements under an stable atmosphere. This could be in part contradictory to the accepted definition of SAR, which is commonly claimed to be an all-weather imaging system.

Concerning the ARBRES-X SAR system, one of the main objectives pursued during this Ph.D. has been the integration of the sensor into a small UAV MP, overcoming restrictions of weight, size and aerodynamics of the platform [CA2], [CA4], [JA2]. The use of this type of platforms is expected to open up new possibilities in airborne SAR remote sensing, since it offers much more versatility than its predecessors. However, some limitations have been discovered while testing the prototypes. The most important could be the inherent motion errors of the UAV MP while flying compared with a fixed wings UAV, which forces the necessity to compensate the undesired motion errors to be able to obtain well focused SAR images. This was also a problem with the fixed wings UAVs, but in this type of platforms the fact is much more pronounced [100]. In this context, the application of MOCO techniques have been discarded since it has been determined that the accuracy of low cost, low weight and low size IMU used in these experiments is not enough to retrieve the errors of the platform. Hence, the solution to that problem has been found in the application of an autofocus algorithm. By means of the retrieved phase from different calibrators located in the illuminated scene, the errors of the platform in the three axis can be derived and subsequently used in a second iteration of the focusing process. Although acceptable results have been achieved with this method, see Chapter 6, the performance of the developed procedure could still be improved.

Another distinctive element of the UAV MP is the possibility to use the auto-pilot function with pre-defined flight strategies. This is quite interesting in airborne SAR observation as multiple types of trajectories can be carefully pre-programmed taking into account the area of interest. In this sense, maybe the most important application could be the use of this technology to perform repeat-pass interferometric measurements. During the course of the present doctoral work, much effort has been made to achieve this challenging objective. As a result, first experimental repeat-pass interfereometric results have been obtained with the UAV MP together with the ARBRES-X SAR sensor [JA2].

Nevertheless, important restrictions regarding the capabilities of the platform have been found during this process. Due to the lack of accuracy of the UAV MP navigation system, the velocity and the trajectory could not be the expected one, fact that degrades the interferometric process and, actually, any kind of measurements. This can provoke, for instance, non-aligned passes that decorrelate the obtained images, hindering the extraction of reliable interferometric information. Moreover, the vertical accuracy of the GPS together with the barometer is not enough to guarantee a constant flight altitude, being an important inconvenient when trying to maintain a non variable baseline between the two passes. Furthermore, the height accuracy of the system is normally far from the required one. In conclusion, the lack of accuracy of the navigation system together with the fact of having important undesired motion errors make this type of platforms a very preliminary technology that must be improved to obtain repeat-pass interferometric results. Furthermore, the methods and processes should be also improved in order to obtain better results.

The ARBRES-X SAR sensor has been endowed with fully polarimetric capabilities by applying the improvements developed to the RISKSAR-X radar, which is another example of the duality between both systems. Thus, by integrating the solid-state switch in the RF front-end and having two identical reception channels, the system is able to perform fully polarimetric measurements. Nevertheless, after analyzing the polarimetric correlation between different combinations of images, it has been determined that there are cross-talk effects due to the antennas that are degrading the performance of the sensor. In this sense, it has been concluded that, in order to obtain reliable fully polarimetric measurements, additional iterations of the system at hardware level must be conducted prior to the system calibration.

Chapter 6, which is based on the work presented in [JA2], shows different results obtained with the use of the ARBRES-X SAR system integrated in the UAV MP. In addition to the interferometric and polarimetric measurements, a vertical and a semicircular aperture have been successfully performed obtaining SLC images of the scenario. Vertical measurements may be a big improvement to the actual methodology used to obtain tomographic results, since it avoids the necessity to perform multiple passes that are extremely difficult to perfectly align. In this sense, the ascending velocity of the UAV MP is very stable and the trajectory does not suffer from important deviations from the nominal track. This way, the first profile of the scenario has been obtained with a vertical aperture performed by the UAV MP .

As a final conclusion, it can said that the UAV MP is a promising platform that opens new potentials for several applications, such as repeat-pass interferometry or differential tomography imaging with the realization of almost arbitrary trajectories. First contributions to that applications have been achieved during the realization of this doctoral activity, but the system still needs to be improved.

7.2 Original contributions

With the work described in this thesis, the impact of short term variable reflectivity in the GB-SAR imagery has been assessed. Furthermore, an initial evaluation of the SAR capabilities of UAV MP has been analyzed. Hence, part of the content of this thesis intends to contribute to the development of new strategies in the airborne SAR field. The main and original contributions to this thesis together with the reference to the corresponding publications are outlined below:

- *Fully polarimetric capabilities of the RISKSAR-X sensor in the OtF mode*
  The use of the continuous operation mode has led to an important reduction of the scanning time in GB-SAR sensors. By means of the hardware contributions developed to the sensor, it has been achieved the capability to perform fully polarimetric measurements in the OtF operation mode. Nevertheless, the system must be exhaustively calibrated in the future.
- *Definition of the new term* γ_{blur}
  A comprehensive mathematical analysis of the cross-range focusing process has been developed to understand the effect of short term variable reflectivity in the image reconstruction process. This is of key importance to analyze the impact of the blurring effect due to moving scatterers, which is taken into account by the new term introduced in the differential interferometric coherence γ_{blur} [JA3].

- *Integration of the ARBRES-X SAR sensor into a UAV MP*
  In the frame of this doctoral activity, one of the most challenging purposes was to integrate the SAR sensor into a small UAV MP, overcoming all the difficulties encountered throughout the process. After a lot of effort devoted to that objective, a first prototype of the system has been developed and tested [CA2], [CA4], [JA2].
- *Initial evaluation of SAR capabilities of UAV MPs*
  Different innovative flight strategies have been assessed with the ARBRES-X SAR system during the course of this research activity. The versatility of the platform to perform almost arbitrary trajectories has permitted to obtain several first experimental results. In this sense, obtaining repeat-pass interferometric results constitutes one of the most important challenges achieved. Furthermore, fully polarimetric measurements have been conducted, as well as vertical and circular apertures. The experimental results from vertical flights have permitted to figure out the possibility to perform tomographic measurements in a simple way than there is until now [JA2].
- *Development of the ARBRES Assistant tool*
  The different algorithms and codes developed during the course of the present doctoral activity have been collected in the ARBRES Assistant tool. It is of interest since it will permit to continue the research activity conducted with the ARBRES-X SAR system.

Part of these contributions have been collected in technical reports. References to these projects can be found in the list of publications at the end of this manuscript.

7.3 Future research lines

Future research lines move towards the improvement of the RISKSAR-X and the ARBRES-X SAR system, also including methods and procedures. During this doctoral research several open points have been identified as well as opportunities for further investigations. In this context, the following lines of research are highlighted:

- *MOCO techniques*
  Being informed about the evolution of high precision IMU could give the possibility to apply MOCO techniques in the future. If it would exist a cost-effective small IMU meeting the required accuracy, it would be possible to introduce the retrieved motion errors in the focusing process. Another possible solution could be the use of a RTK GPS together with the IMU, which ensures a centimeter accuracy. These solutions are particularly interesting since they avoid any kind of approximation in the focusing process and, furthermore, the use of the autofocus algorithm would not be necessary.
- *Improvement of the autofocus algorithm*
  Regarding the use of the autofocus algorithm, it has been concluded that there is still room to improve the procedure. On the one hand, the distribution of the calibrators in the scenario could be done in a more efficient way. If they would be distributed as far apart as possible from each other, it would be easier to compensate for the possible deviations in the entire image. Moreover, the different inaccuracies when solving the set of non-linear equations could be analyzed in order to improve the method. Finally, the fact of having discontinuities in the retrieved phase from

squinted targets due to the phase unwrapping could be studied and improved to minimize the error introduced for the approximations. Finally, the possibility to use different methods to solve the equations could be assessed.

- *The navigation system of the UAV MP*
  It has been observed that one of the main limitations when performing some measurements, such as for instance the repeat-pass interferometry, is the lack of accuracy of the navigation system. In the future, the navigation system of the platform must be improved. Nowadays, there are systems operating with RTK GPS that permit an accuracy of few centimeters both in vertical and horizontal, as is the case of the DJI A3 Pro navigation system. Furthermore, putting some effort on the estimation and correction of time varying baseline errors from the interferometric SAR data constitutes another research line to improve the interferometric results.

- *Azimuth spectral shift analysis*
  It has been concluded that the misalignment of the passes in the repeat-pass interferometric results provokes that the images are decorrelated due to a shift of the azimuth spectra after the rough coregistration. On the one hand, the fact of filtering the common bandwidth to remove the uncorrelated contributions that behave like noise could be analyzed. On the other hand, different techniques involving an azimuth shift of the spectrum to improve the coherence cold be analyzed.

- *Improvement of the antennas cross-talk of the ARBRES-X SAR sensor*
  After analyzing the polarimetric correlation between different combinations of different measurements, it has been concluded that in the actual version of the system the cross-talk between the antennas are altering the polarimetric measurements. In the future, this must be studied and improved at hardware level, generating a new version of the sensor that has eliminated this problem. A key point in this sense is the stabilization of the lightweight aluminum bar with the integrated patch antennas, which should be able to absorb any vibration of the platform and maintain the horizontal position with respect to the ground. After the system improvement, further steps also comprise an exhaustive calibration of the system.

- *Calibration of the RISKSAR-X and the ARBRES-X* sensors
  In order to ensure the extraction of reliable quantitative information from the two radars, the proper calibration of both sensors is mandatory in the future.

- *Vertical flights for tomographic imaging*
  By means of using vertical apertures, the basis to perform vertical tomography has been introduced. This can be performed by considering a given number of vertical flights. This represents a future flight strategy that could be done with the UAV MP.

- *Circular flights for tomographic imaging*
  A further possibility for tomographic imaging consists in performing acquisitions by means of circular trajectories like a CSAR. By illuminating an area with a circular trajectory and multiple passes at different heights, a 3-D imaging of an structure could be retrieved. This also represents a future flight strategy that could be done with the UAV MP.

- *ARBRES assistant*
  The tool developed to process the data acquired by the ARBRES-X SAR sensor still has room for improvement. All the codes are susceptible of being optimized and different functions can be added to make this assistant a more complete and powerful tool. An example of functions that might be added are the polarimetric calibration of the system or a simulator to evaluate the effect of the motion errors of the platform in the retrieved data.

Appendix A

Autofocus algorithm

This appendix is intended to comprehensively evaluate the efficiency of the autofocus algorithm. It is introduced for completeness to asses different simulations and conclusions that were out of the scope of the main dissertation.

In Section 5.3.1 of Chapter 5 a simulation applying the autofocus algorithm with errors in the three axis X, Y and Z has been analyzed. In the present appendix, the errors in each axis are assessed independently to evaluate the effect of each case in the focused images and to analyze the capability of the algorithm to compensate the undesired motion errors.

Figure A.1 (a) shows the simulated SLC image without any deviation error where it can be seen 5 PSs located at [0,200], [0,350], [0,450], [-50,300] and [-100,400] meters and called P1, P2, P3, P4 and P5, respectively. From now on this targets will be referred as PARCs, since they simulate its behavior. Moreover, Figure A.1 (c) shows the focused simulated image after introducing the deviation error in the X axis shown in Figure A.1 (b). As can be seen, for an error in the azimuth spacing of nearly 0.6 m the SLC image presents a certain degree of defocusing that is accentuated with the squint angle. For that reason, P5 at [-100,400] is much more affected by the X axis deviation error than P1 [0,200]. Considering the length of the apertures presented in this thesis of around 14 m, the radar is illuminating the scenario during 1.5 seconds to avoid undesired motion errors. This means that a velocity error of around 0.6 m/s during the aperture would degrade the focused image, which is a feasible error on the order of magnitude of the obtained with the platform.

Figure A.2 (a) shows the ideal with no motion errors and the measured slant range distance to P1, which are necessary to retrieve the X axis error. This last is shown in Figure A.2 (b), where can be observed in red that the retrieved error is not the expected one. Even approximating the curve to avoid discontinuities, the retrieved X error does not seem to be the expected. As the squinted targets are much more affected by the velocity errors, the same procedure is repeated with P5 and shown in Figure A.3. In this case, the retrieved error matches the one introduced in the simulation but it presents some discontinuities due to errors when extracting the phase from the pixel associated to the target. As mentioned in Section 5.3.1, the phase extracted from squinted targets have problems with the unwrapping process, reason for which the retrieved motion error must be approximated. Figure A.3 (b) shows in red the retrieved and approximated X error, which matches almost perfectly with the expected one.

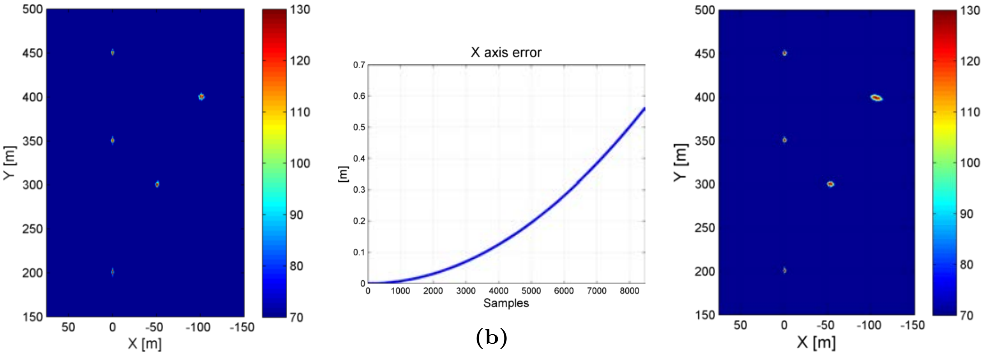

(a) **(b)** **(c)**

Figure A.1: SLC of a simulated aperture of 14 m with: (a) Ideal flight path. (c) Deviation errors in the X axis during the flight path. (b) Deviation error introduced in the X axis.

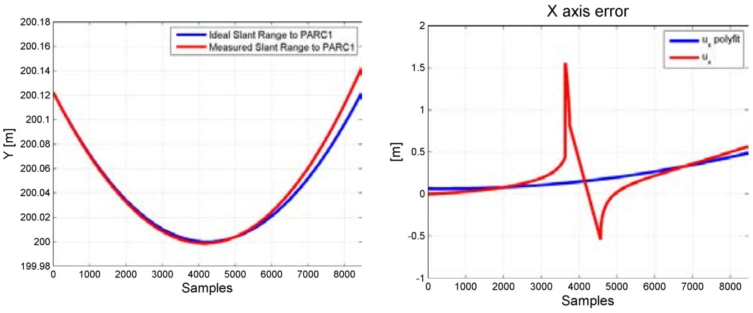

(a) **(b)**

Figure A.2: (a) Retrieved slant range distance from the sensor to PARC 1 [0,200]. (b) Retrieved motion error in the X axis.

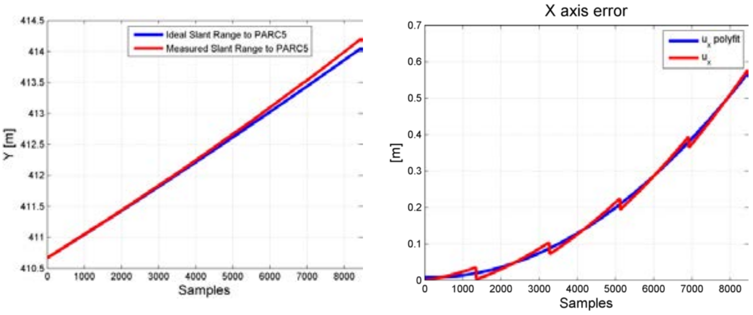

(a) **(b)**

Figure A.3: (a) Retrieved slant range distance from the sensor to PARC 5 [-100,400]. (b) Retrieved motion error in the X axis.

Figure A.4 shows the SLC images after introducing the compensation parameters in the focusing process with and without the approximation. As can be observed, the targets in Figure A.4 (a) present a blurring effect in the azimuth direction while the targets in Figure A.4 (b) are perfectly compensated. This means that the error introduced when approximating the curve is negligible.

Figure A.5 shows the cut in azimuth of the different PARCs, where the results for the different steps of the autofocus algorithm can be analyzed. In blue it is represented the cut of the simulated PARCs focused without any motion error and in red the cut is presented after introducing the deviations in the X axis. It is observable a considering spreading effect in the response of the simulated targets with squint, which means a loss of the azimuth resolution due to the simulated deviations. Contrarily, targets located at zero Doppler position are much less affected by the introduced errors in the X axis. In green and magenta it has been represented the response of the targets after applying the autofocus algorithm. Te green line shows the azimuth cut without approximating the retrieved u_x deviation and the magenta line after approximating it. As expected, when comparing the two responses in Figure A.5, the first one presents a higher value of floor noise for all the targets with differences of up to around 90 dB. Nevertheless, the

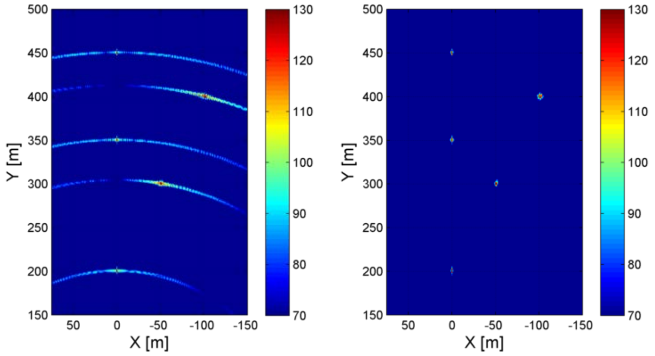

(a) (b)

Figure A.4: SLC of simulated aperture of 14 m after compensating X axis errors:(a) Without approximating retrieved parameters. (b) Approximating retrieved parameters.

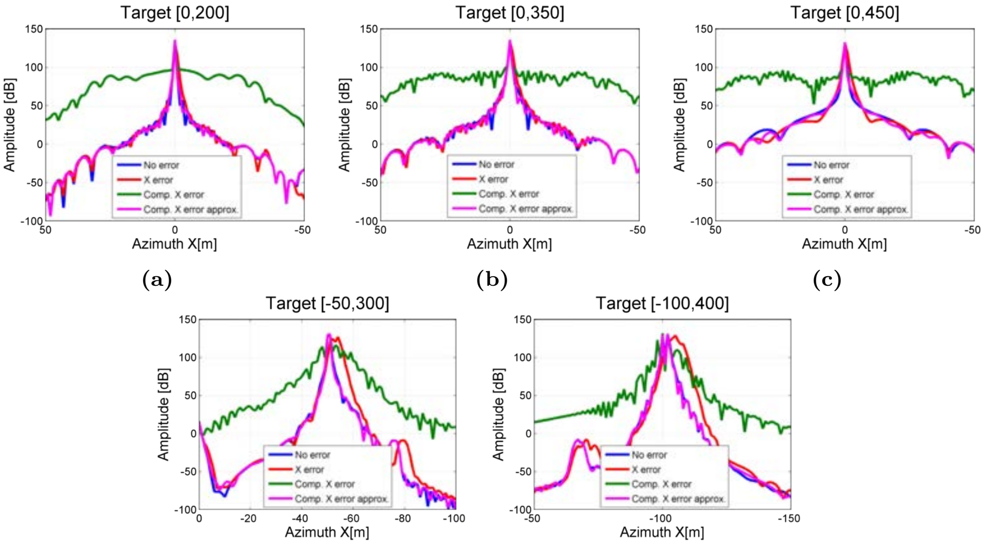

(a) (b) (c)

(d) (e)

Figure A.5: Cut in azimuth of:(a) PARC1 [0,200]. (b) PARC2 [0,350]. (c) PARC3 [0,450]. (c) PARC4 [-50,300]. (e) PARC5 [-100,400]. Blue: No deviation errors. Red: X deviation error. Green: Compensated error without approximating X deviation. Magenta: Compensated error approximating X deviation.

cut in azimuth of the targets after approximating the u_x parameter presents a perfect compensation of the errors without compromising the azimuth resolution, see magenta line.

After studying the effect of the errors applied in the X axis, the same analysis is conducted but introducing some deviations in height from the nominal trajectory. Figure A.6 (a) shows the simulated SLC image without any deviation while Figure A.6 (c) shows the focused simulated image after introducing the deviation error in the Z axis shown in

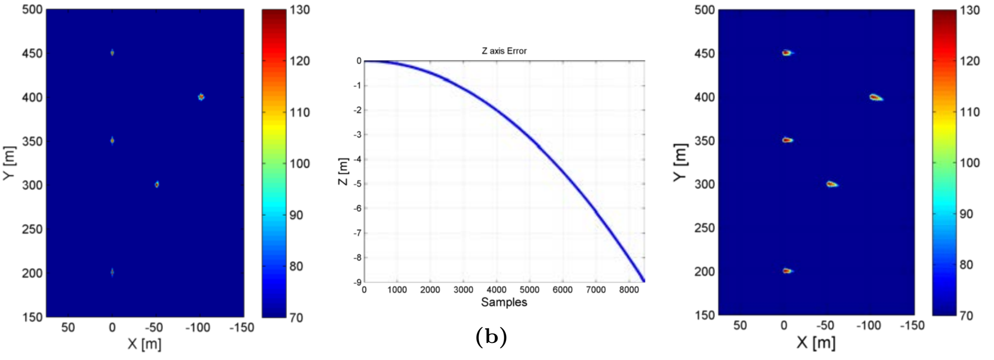

(a)

(b)

(c)

Figure A.6: SLC of a simulated aperture of 14 m with: (a) Ideal flight path. (c) Deviation errors in the Z axis during the flight path. (b) Deviation error introduced in the Z axis.

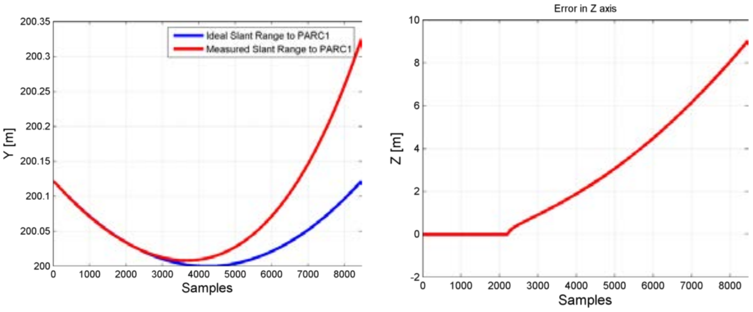

(a)

(b)

Figure A.7: (a) Retrieved slant range distance from the sensor to PARC 1 [0,200]. (b) Retrieved motion error in the Z axis.

Figure A.6 (b). Again, considering an aperture of 14 m, the introduced error in height is equivalent to descend 9 m in 1.5 seconds, which is too much considering the real attitude of the platform.

Figure A.7 (a) shows the ideal with no motion errors and the measured slant range distance to P1, which are necessary to retrieve the Z axis error. This last is shown in Figure A.7 (b). It can be seen that the retrieved error $u_z(t)$ is 0 for the first 2200 samples approximately, which corresponds to an error in height of roughly 0.6 m (almost half of the resolution cell). This is because small height errors does not affect too much to the focused image.

Figure A.8 shows the comparison between the SLC obtained without motion errors and the SLC obtained after compensating the Z axis deviations. As can be seen, the retrieved errors in height perfectly compensates the introduced errors, even though these ones are considerable. Figure A.9 shows the cut in azimuth of the different PARCs, where the results for the different steps of the autofocus algorithm can be analyzed. In blue it is represented the cut of the simulated PARCs focused without any motion error and in

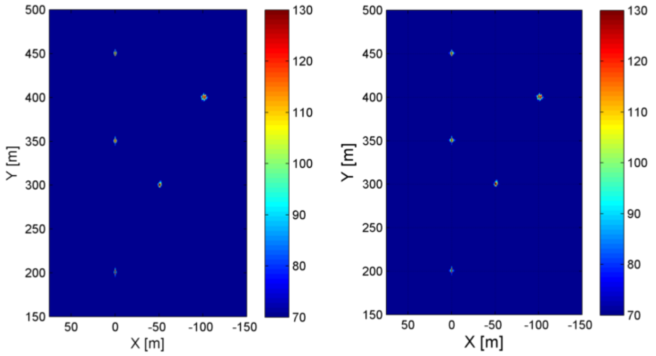

(a) (b)

Figure A.8: SLC of simulated aperture of 14 m: (a) Ideal flight path.(b) After compensating Z axis errors.

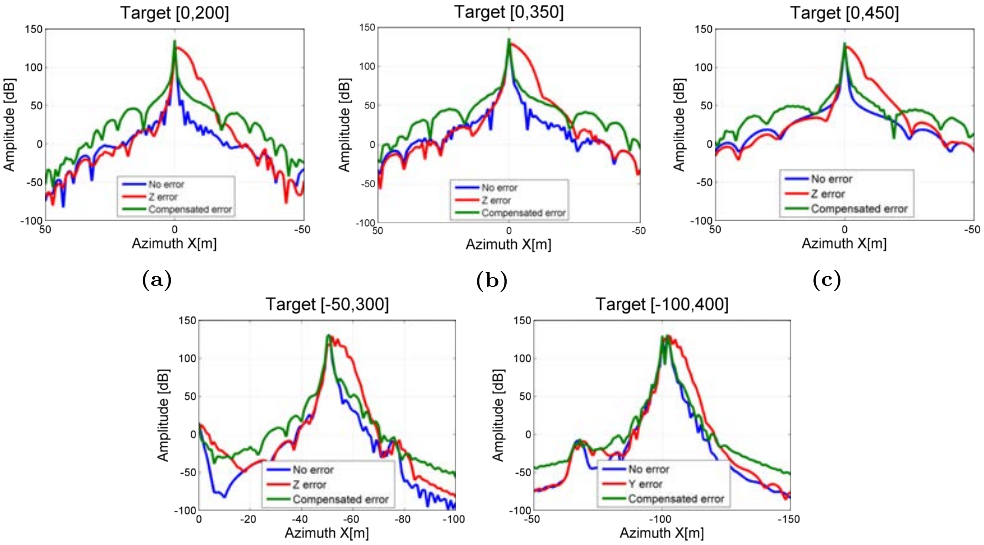

(a) (b) (c)

(d) (e)

Figure A.9: Cut in azimuth of: (a) PARC1 [0,200]. (b) PARC2 [0,350]. (c) PARC3 [0,450]. (c) PARC4 [-50,300]. (e) PARC5 [-100,400]. Blue: No deviation errors. Red: Z deviation error. Green: Compensating Z deviation.

red the cut is presented after introducing the deviations in the Z axis. It is observable a considering spreading effect in the response of the simulated targets, which means a loss of the azimuth resolution due to the simulated deviations. In green it has been represented the response of the targets after applying the autofocus algorithm. In this case, the cut in azimuth of the targets after compensating the height error does not present a perfect compensation of the errors, which degrades the azimuth resolution. The noise floor of the PARCs response is, in some cases, up to 30 dB above the ideal response.

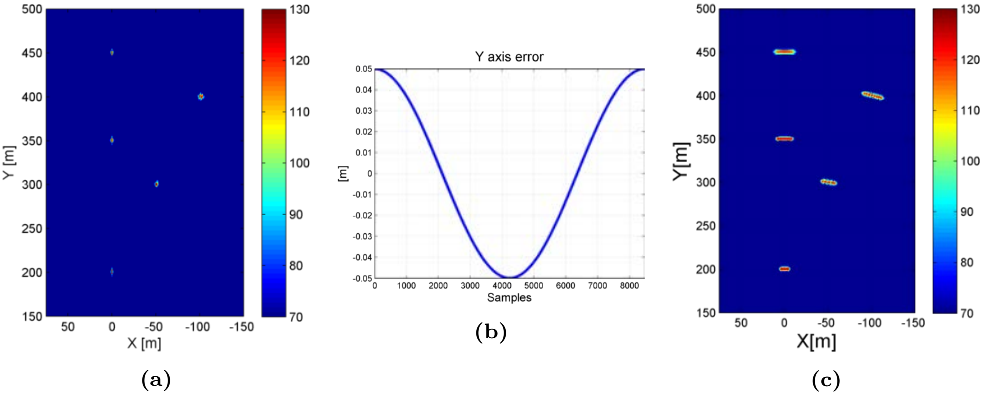

(a) (b) (c)

Figure A.10: SLC of a simulated aperture of 14 m with: (a) Ideal flight path. (c) Deviation errors in the Y axis during the flight path. (b) Deviation error introduced in the Y axis: oscillatory movement.

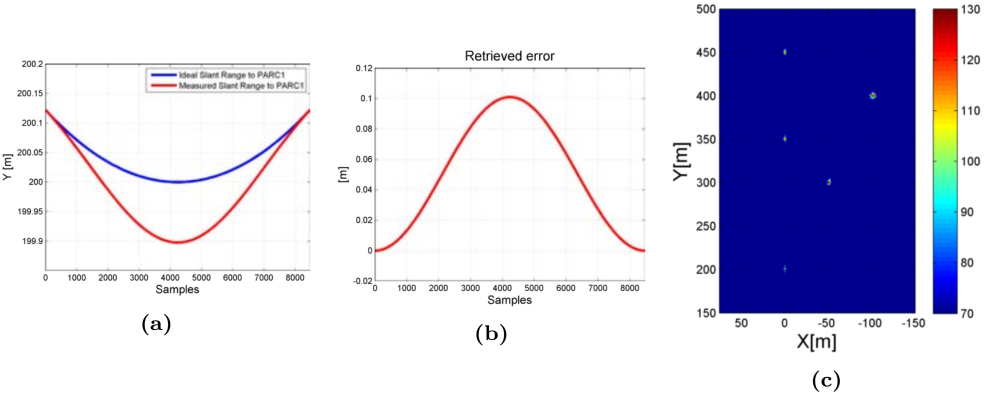

(a) (b) (c)

Figure A.11: (a) Retrieved slant range distance from the sensor to PARC 1 [0,200]. (b) Retrieved motion error in the Y axis. (c) SLC after compensating Y axis error.

During the realization of this doctoral activity it has been observed that the errors in the range direction are those that degrades the most the focused images. For that reason, the study of the autofocus algorithm in this direction deserves special attention. As shown in Figure 5.11 of Chapter 5, the location of the radar is displaced with respect to the center of gravity of the UAV. In Subsection 5.3.1 it was stated that this can provoke oscillatory movements like a pendulum while flying, which has to be taken into account. Figure A.10 shows (c) shows the focused image introducing one period of an oscillating error of 10 cm in the range direction, see Figure A.10 (b). This error, which considerably degrades the focusing process, is plausible considering the attitude and inertia of the UAV MP.

Figure A.12 (a) shows the ideal and the measured slant range distance to PARC 1, which are necessary to retrieve the Y axis error. The retrieved error and the focused image compensating it are shown in Figure A.12 (b) and Figure A.12 (c), respectively.

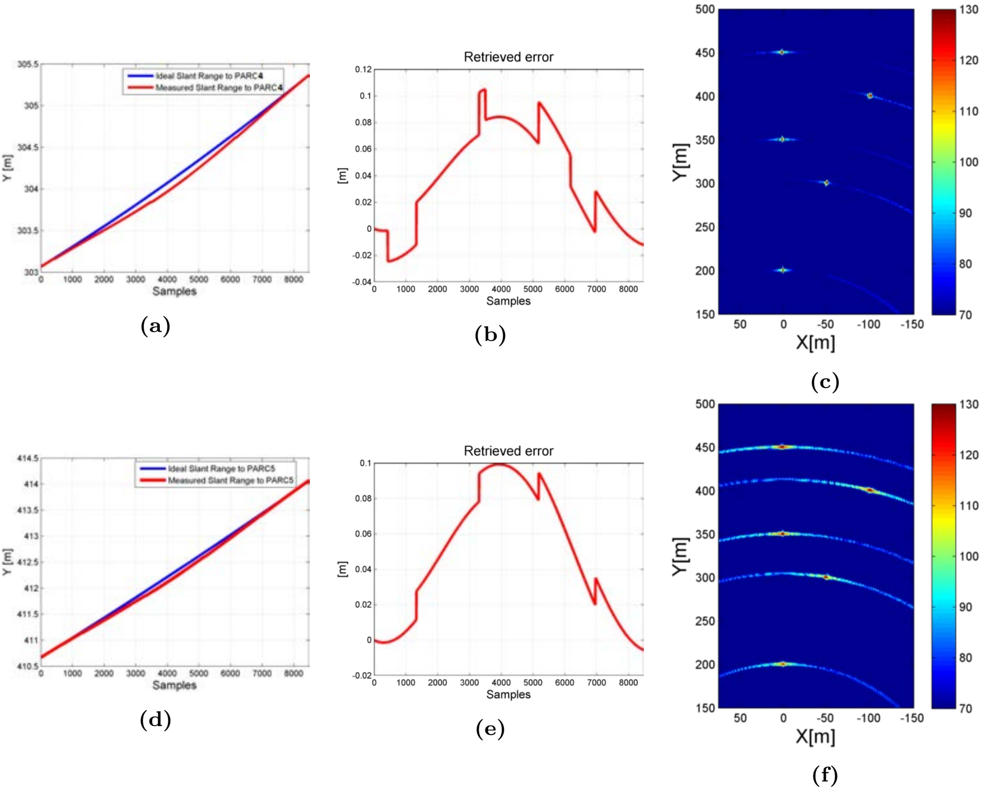

(a) (b) (c) (d) (e) (f)

Figure A.12: Retrieved slant range distance from the sensor to (a) PARC 4 and (d) PARC 5 located at [-50,300] m and[-100,400] m respectively. Retrieved motion error from (b) PARC 4 and (e) PARC 5. SLC compensated with retrieved error obtained from (c) PARC 4 and (f) PARC 5.

As can be observed, by selecting the targets with good quality of the phase the errors are well compensated. However, if the selected target to extract the information presents an important squint the retrieved error might be unusable, as it is shown in Figure A.12 where the phase history has been extracted from PARC 4 and PARC 5 located at [-50,300] and [-100,400], respectively.

Figure A.13 (c) shows the focused image introducing two periods of an oscillating error of 10 cm in the range direction, as it is shown in Figure A.13 (b). This error doubles the one introduced in the simulations of Figure A.10 shows (c). Figure A.14 (a) shows the ideal and the measured slant range distance to PARC 1, which are necessary to retrieve the Y axis error. The retrieved error and the focused image compensating it are shown in Figure A.14 (b) and Figure A.14 (c), respectively. Again, if the selected target to extract the information presents an important squint, the retrieved error will be unusable, as it is shown in Figure A.15 where the phase history has been extracted from PARC 4 and PARC 5 located at [-50,300] and [-100,400] respectively. Figure A.15 (c) and (f) show the SLC images obtained after compensating the motion errors with the retrieved information from the squinted targets. As can be observed, it is not the optimum solution.

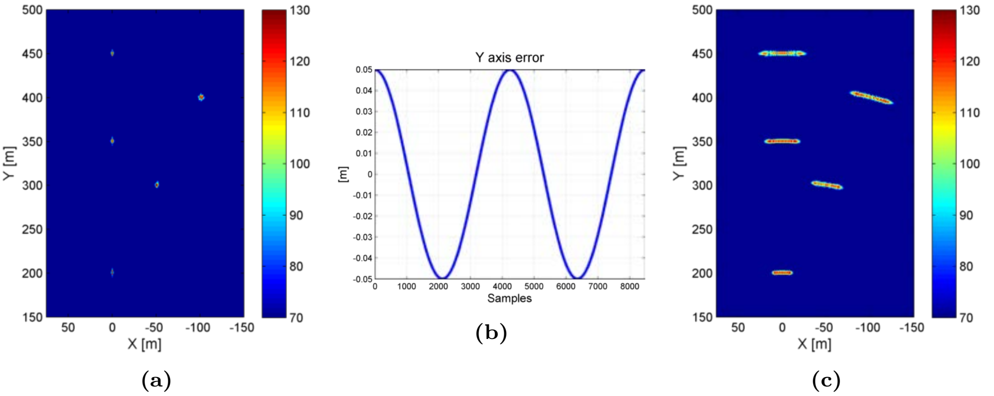

Figure A.13: SLC of a simulated aperture of 14 m with: (a) Ideal flight path. (c) Deviation errors in the Y axis during the flight path. (b) Deviation error introduced in the Y axis: oscillatory movement.

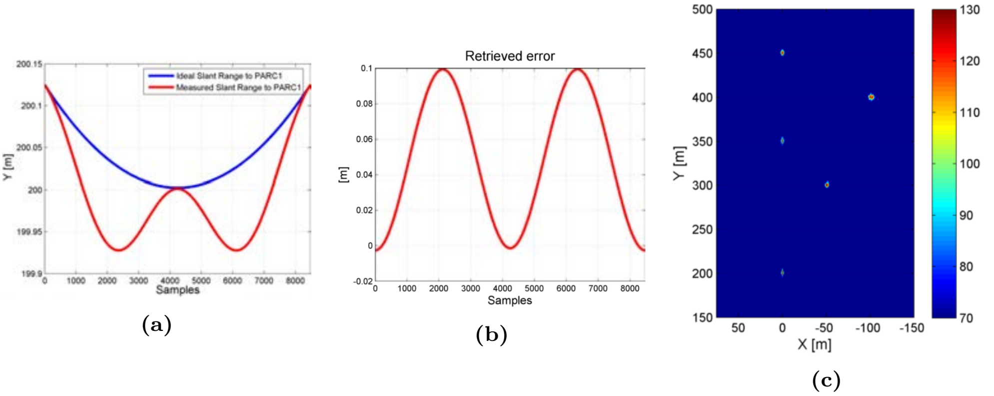

Figure A.14: (a) Retrieved slant range distance from the sensor to PARC 1 [0,200]. (b) Retrieved motion error in the Y axis. (c) SLC after compensating Y axis error.

Finally, Figure A.16 shows the cut in azimuth of the different PARCs, where the results for the different steps of the autofocus algorithm can be analyzed. In blue it is represented the cut of the simulated PARCs focused without any motion error and in red the cut is presented after introducing the oscillation of 1 period and 10 cm in the Y axis. Besides, in green it is observable the cut in azimuth after introducing the oscillation of 2 period and 10 cm. It is observable a considering spreading effect in the responses of the simulated targets, which means a loss of the azimuth resolution due to the simulated deviations. As expected, the response corresponding to the two periods present a higher degree of spreading in comparison with the response corresponding to one oscillation. In magenta and purple it has been represented the response of the targets after applying the autofocus algorithm for 1 and 2 periods of oscillation respectively. In this case, the cut in azimuth of the targets compensating the Y error are very similar to the ideal case.

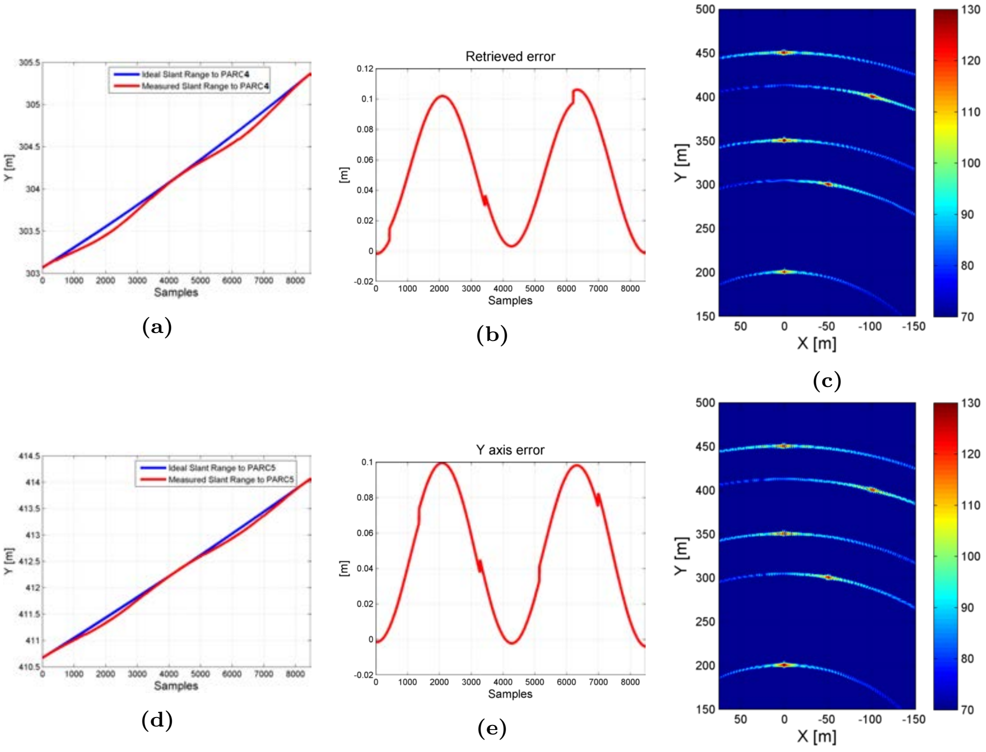

(a) (b) (c)

(d) (e) (f)

Figure A.15: Retrieved slant range distance from the sensor to (a) PARC 4 and (d) PARC 5 located at [-50,300] m and[-100,400] m respectively. Retrieved motion error from (b) PARC 4 and (e) PARC 5. SLC compensated with retrieved error obtained from (c) PARC 4 and (f) PARC 5.

Finally, it has to be taken into account that, in addition to the oscillatory movements, a deviation of the trajectory of the platform in the Y axis can occur. As seen in Figure 5.12, this deviation can be introduced by an error in the yaw angle of the platform. The last set of simulations consider a superposition of the oscillatory movement of the radar plus a deviation of the trajectory due to a constant error of the yaw angle of the platform. Figure A.17 (c) shows the focused image introducing two periods of an oscillating error of 10 cm in the range direction and an error in the yaw angle of the UAV, as it is shown in Figure A.17 (b).

Figure A.18 (a) shows the ideal and the measured slant range distance to PARC 1, which are necessary to retrieve the Y axis error. The retrieved error and the focused image compensating it are shown in Figure A.18 (b) and Figure A.18 (c), respectively. Again, if the selected target to extract the information presents an important squint, the retrieved error will be unusable, as it is shown in Figure A.19 where the phase history has been extracted from PARC 5 located at [-100,400]. Figure A.19 (c) show the SLC image obtained after compensating the motion errors with the retrieved information from the squinted target. As can be observed, it is not the optimum solution. Finally, Figure

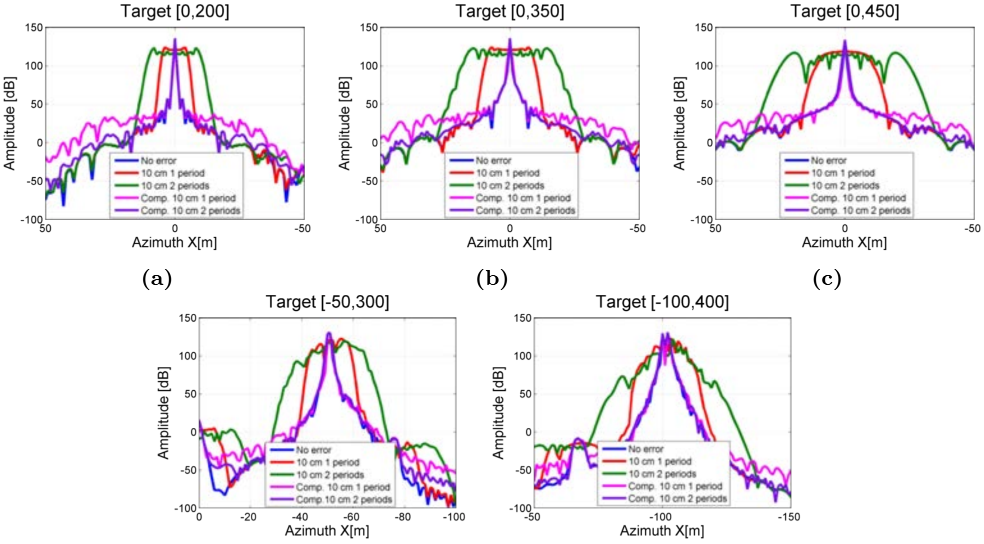

(a) **(b)** **(c)**

(d) **(e)**

Figure A.16: Cut in azimuth of: (a) PARC1 [0,200]. (b) PARC2 [0,350]. (c) PARC3 [0,450]. (c) PARC4 [-50,300]. (e) PARC5 [-100,400]. Blue: No deviation errors. Red: Y deviation error 10 cm 1 period. Green: Y deviation error 10 cm 2 periods. Magenta: Compensating Y deviation 10 cm 1 period. Purple: Compensating Y deviation 10 cm 2 periods.

A.20 shows the cut in azimuth of the different PARCs, where the results for the different steps of the autofocus algorithm can be analyzed. In blue it is represented the cut of the simulated PARCs focused without any motion error and in red the cut is presented after introducing the oscillatory and yaw errors in the Y axis. It is observable a considering spreading effect in the responses of the simulated targets. In green it has been represented the response of the targets after applying the autofocus algorithm. In this case, the cut in azimuth of the targets compensating the Y errors are very similar to the ideal case.

The last simulation exposed in the present appendix is intended to introduce to the system possible vibrations of the platform during the flight due to the rotors. To that purpose, it is considered a second order error superimposed to the error shown in Figure A.17 (b). This way, the error introduced simulates the oscillation of the sensor, the error in the yaw angle and the possible vibrations of the platform. Figure A.21 (a) and (c) show the SLC image before and after the introduction of the error, respectively. Moreover, the deviation error introduced in the Y axis is exposed in Figure A.21 (a). As can be seen in Figure A.22, the vibration introduced is on the order of few millimeters, which is enough to increase the noise floor of the response of the targets, appearing those characteristic tails in the same radial range of the focused image.

Finally, Figure A.24 shows the cut in azimuth of the different PARCs where the results for the different steps of the autofocus algorithm can be analyzed. In blue it is represented the cut of the simulated PARCs focused without any motion error and in red the cut is presented after introducing the oscillation plus the yaw error and the vibration in the Y axis. It is observable a considering spreading effect in the responses of the simulated

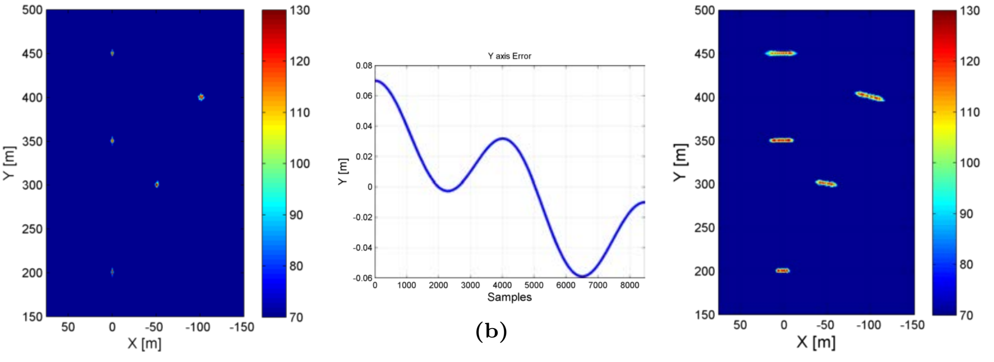

(a) (b) (c)

Figure A.17: SLC of a simulated aperture of 14 m with: (a) Ideal flight path. (c) Deviation errors in the Y axis during the flight path. (b) Deviation error introduced in the Y axis: oscillation + yaw error of the UAV.

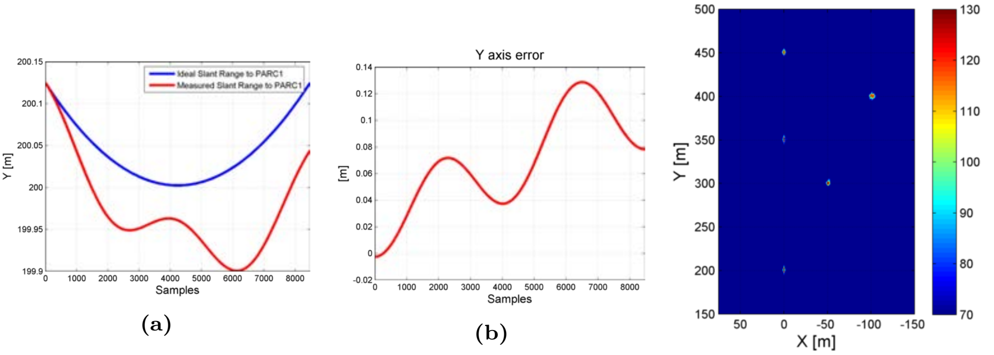

(a) (b) (c)

Figure A.18: (a) Retrieved slant range distance from the sensor to PARC 1 [0,200]. (b) Retrieved motion error in the Y axis. (c) SLC after compensating Y axis error.

targets, which means a loss of the azimuth resolution due to the simulated deviations. Besides, in green it has been represented the response of the targets after applying the autofocus algorithm. In this case, the cut in azimuth of the targets compensating the Y error present an increase of the noise floor level that is related with the vibrations introduced.

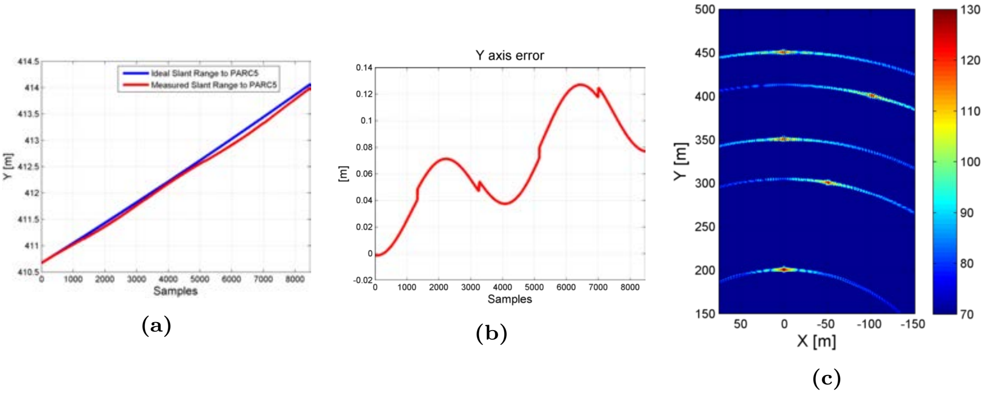

Figure A.19: (a) Retrieved slant range distance from the sensor to PARC 5 located at and[-100,400] m. (e) Retrieved motion error from PARC 5. (f) SLC compensated with retrieved error obtained from PARC 5.

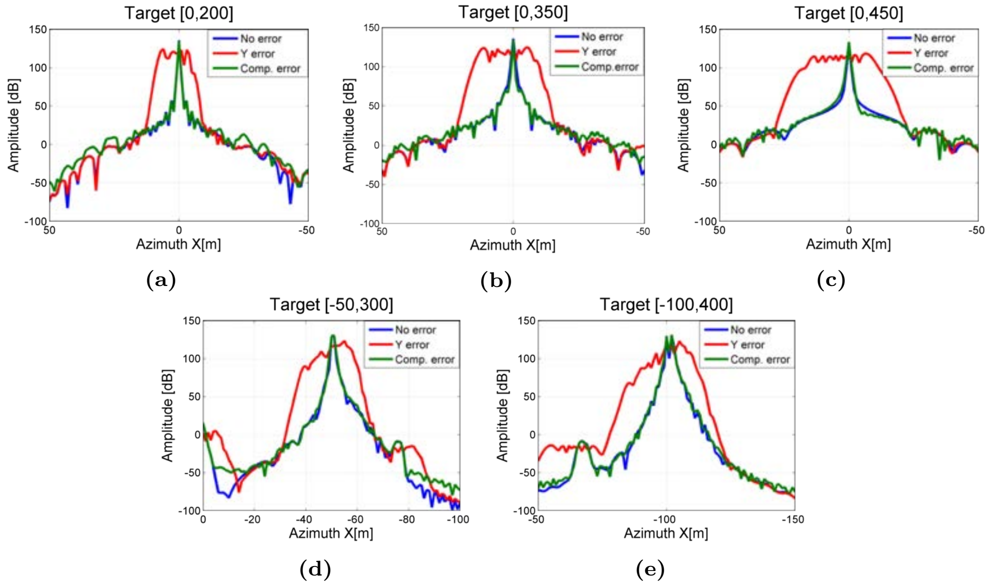

Figure A.20: Cut in azimuth of: (a) PARC1 [0,200]. (b) PARC2 [0,350]. (c) PARC3 [0,450]. (c) PARC4 [-50,300]. (e) PARC5 [-100,400]. Blue: No deviation errors. Red: Y deviation error. Green: Compensating Y deviation.

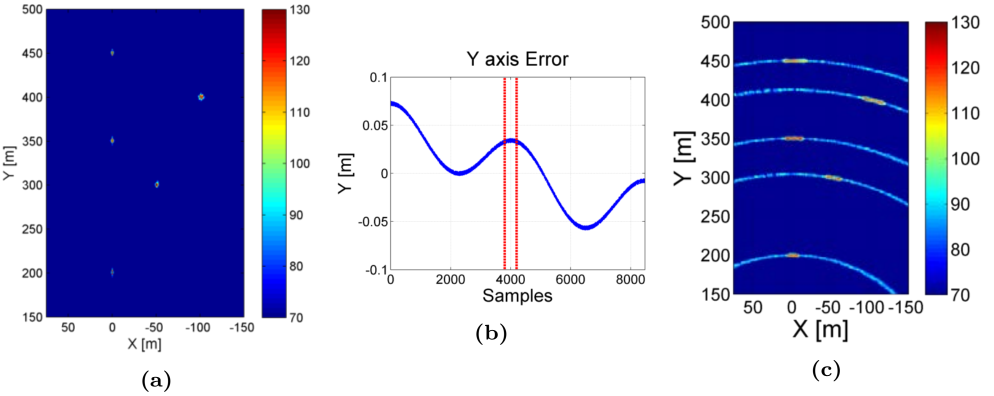

(a)

(b)

(c)

Figure A.21: SLC of a simulated aperture of 14 m with: (a) Ideal flight path. (c) Deviation errors in the Y axis during the flight path. (a) Deviation error introduced in the Y axis: oscillation + yaw error + vibration of the UAV.

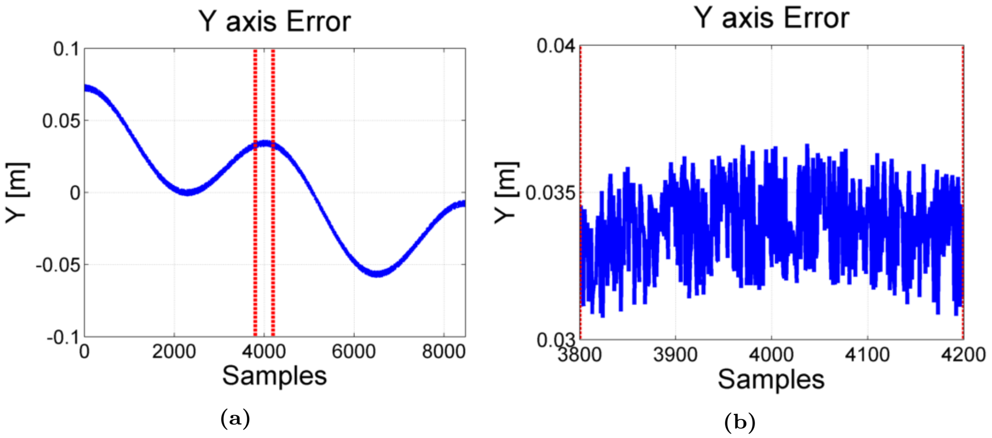

(a)

(b)

Figure A.22: (a) Deviation error introduced in the Y axis: oscillation + yaw error + vibration of the UAV. (b) Zoom to the error.

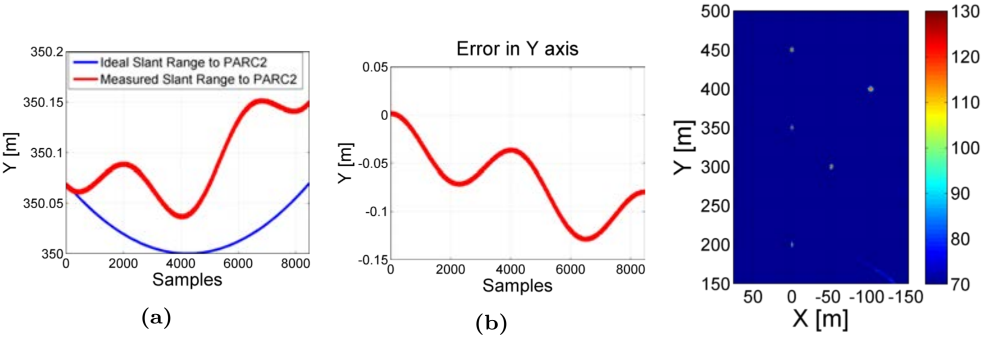

(a) (b) (c)

Figure A.23: (a) Retrieved slant range distance from the sensor to PARC 2 [0,350]. (b) Retrieved motion error in the Y axis. (c) SLC after compensating Y axis error.

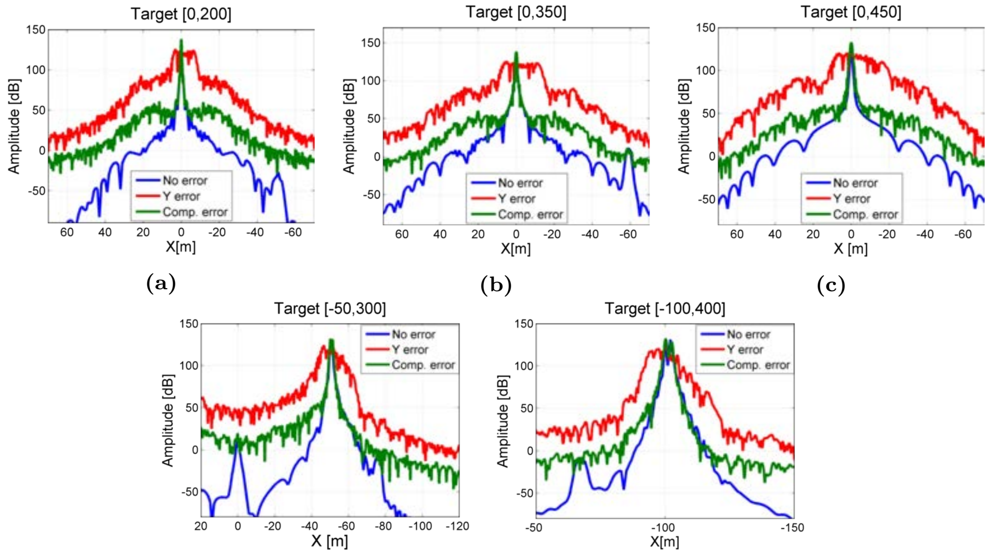

(a) (b) (c)

(d) (e)

Figure A.24: Cut in azimuth of: (a) PARC1 [0,200]. (b) PARC2 [0,350]. (c) PARC3 [0,450]. (c) PARC4 [-50,300]. (e) PARC5 [-100,400]. Blue: No deviation errors. Red: Y deviation error. Green: Compensating Y deviation.

Appendix B

Measurements with ARBRES

This appendix is intended to show other measurements performed with the ARBRES-X SAR system that have been excluded from the central explanation of the manuscript. Along the present appendix, different focused SLC images obtained from linear flights illuminating different areas of the RACBSA test site will be shown. Furthermore, other repeat-pass interferometric measurements that suffer the problems exposed in Chapters 5 and 6 are exposed.

B.1 SLC images of RACBSA

Figure B.1 (a) shows an image of the scenario taken from Google Earth where it can be seen the flight path performed by the UAV MP illuminating the radar towards South-East direction. Moreover, Figure B.1 (b) shows an image of the scenario obtained from an on-board camera. As it can be observed, this area contains agricultural fields, trees, dirt roads, and some urban areas at the left and in the farthest area of the image. Figure B.2 shows the SLC image of the scenario obtained with the ARBRES-X SAR sensor where the different elements of the scenario can be clearly distinguished. With the aim to better compare the retrieved focused image with the real scenario, Figure B.3 shows

(a) (b)

Figure B.1: South-East direction. (a) Image of the scenario taken from Google Earth with the linear flight path information. (b) Image of the scenario taken from an on-board camera.

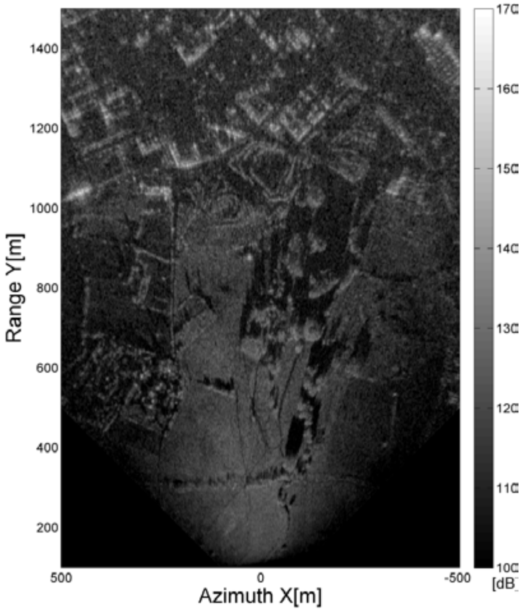

Figure B.2: SLC image of the scenario obtained with the ARBRES-X SAR sensor during the linear flight illuminating towards South-East direction. Flight conditions: 100 m height, $v_{UAV} = 8m/s$, Aperture=12.02 m, VV Pol.

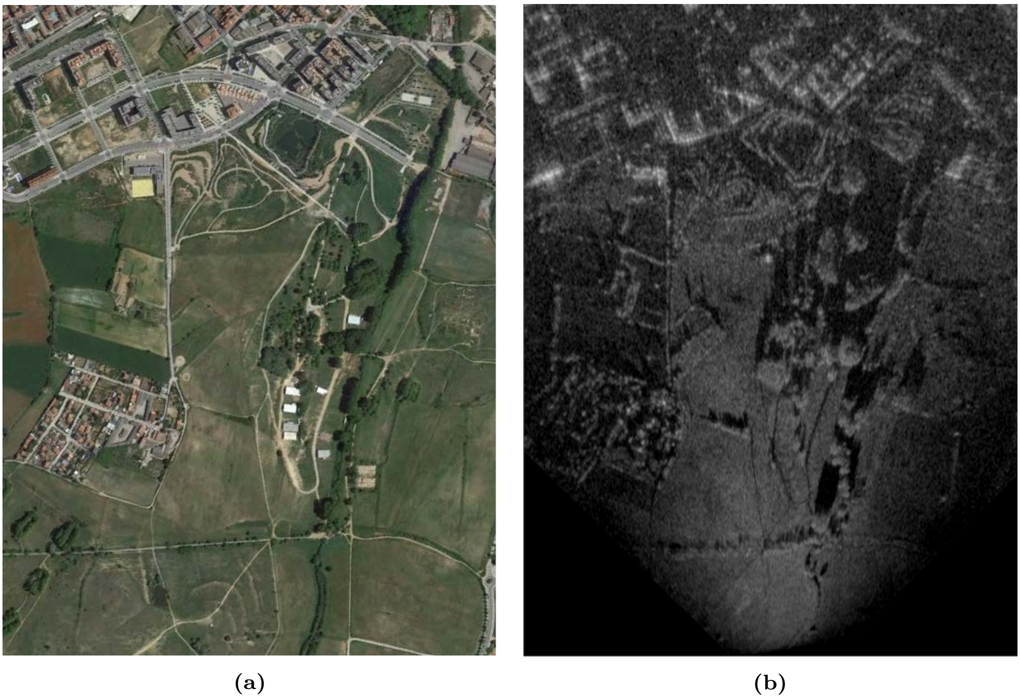

Figure B.3: Comparison between (a) Aerial photograph obtained from Google Earth and (b) SLC image obtained with the ARBRES-X SAR sensor illuminating South-East direction.

Figure B.4: North-East direction. (a) Image of the scenario taken from Google Earth with the linear flight path information. (b) Image of the scenario taken from an on-board camera.

the comparison of the image taken from Google Earth with the SLC.

Figures B.4 (a) and B.7 (a) show the flight paths of two different trajectories performed by the UAV MP illuminating the radar towards North-West direction. Otherwise, in Figure B.10 (a) it is illuminated the urban area of Ripollet. The latter is included because the platform altitude was 200 m, having a better perspective of the city than the flights at 150 m presented in Chapter 6. Moreover, Figures B.4 (b), B.7 (b) and B.10 (b) show an

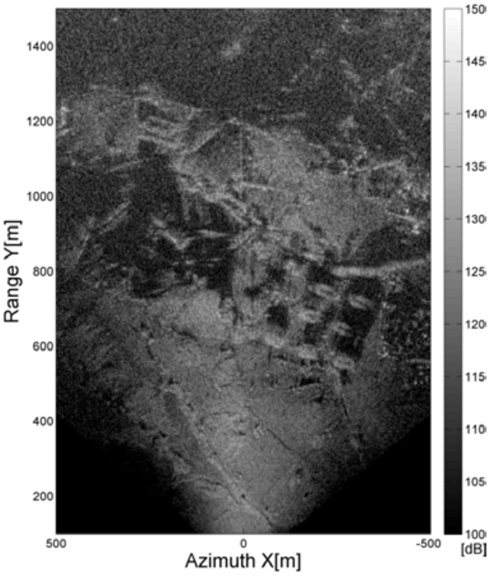

Figure B.5: SLC image of the scenario obtained with the ARBRES-X SAR sensor during the linear flight illuminating towards North-West direction. Flight conditions: 100 m height, $v_{UAV} = 8.9 m/s$, Aperture=13.4 m, VV Pol.

(a) **(b)**

Figure B.6: Comparison between (a) Aerial photograph obtained from Google Earth and (b) SLC image obtained with the ARBRES-X SAR sensor illuminating North-West direction.

image of the scenario obtained from the on-board camera while measuring. The focused SLC images obtained with the ARBRES-X SAR sensor are shown in Figures B.5, B.8

(a) **(b)**

Figure B.7: North-East direction. (a) Image of the scenario taken from Google Earth with the linear flight path information. (b) Image of the scenario taken from an on-board camera.

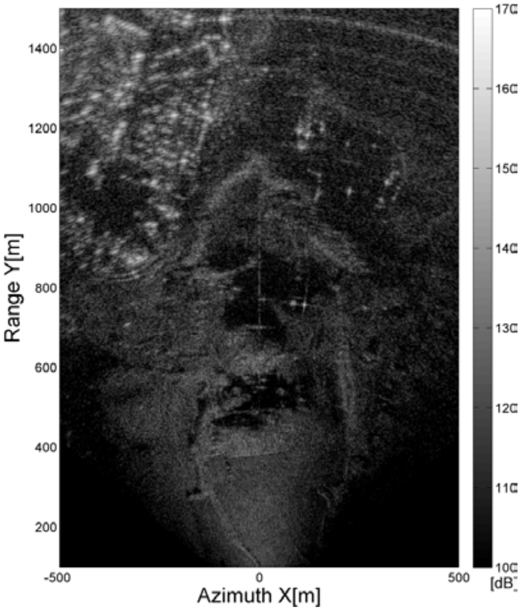

Figure B.8: SLC image of the scenario obtained with the ARBRES-X SAR sensor during the linear flight illuminating towards North-East direction. Flight conditions: 100 m height, $v_{UAV} = 7.5 m/s$, Aperture=5.64 m, VV Pol.

and B.11. Finally, Figures B.6, B.9 and B.12 show the comparison of the SLCs images with the images taken from Google Earth.

On the other hand, Figure B.13 shows the SLC images of Figure 6.3 (a'), (b') and (c') presented in Chapter 5 but with a larger grid, ranging from -850 m to 850 m in azimuth and up to 1 km in range. The aim of including these images is to better visualize the results shown in Section 6.2 of Chapter 5, evidencing for instance the importance of processing larger apertures to improve the SCR.

(a) (b)

Figure B.9: Comparison between (a) Aerial photograph obtained from Google Earth and (b) SLC image obtained with the ARBRES-X SAR sensor illuminating North-East direction.

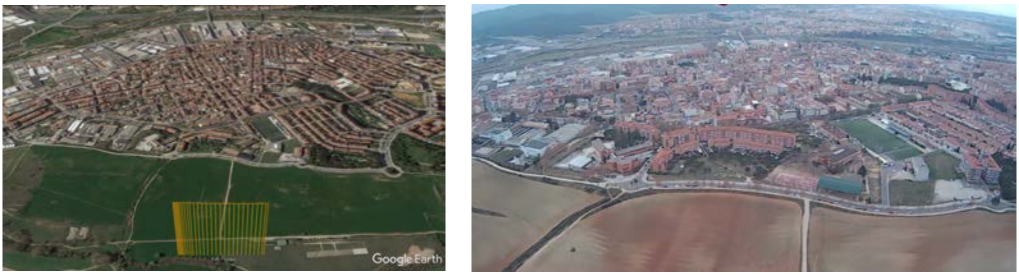

(a) (b)

Figure B.10: Urban area of Ripollet. (a) Image of the scenario taken from Google Earth with the linear flight path information. (b) Image of the scenario taken from the on-board camera.

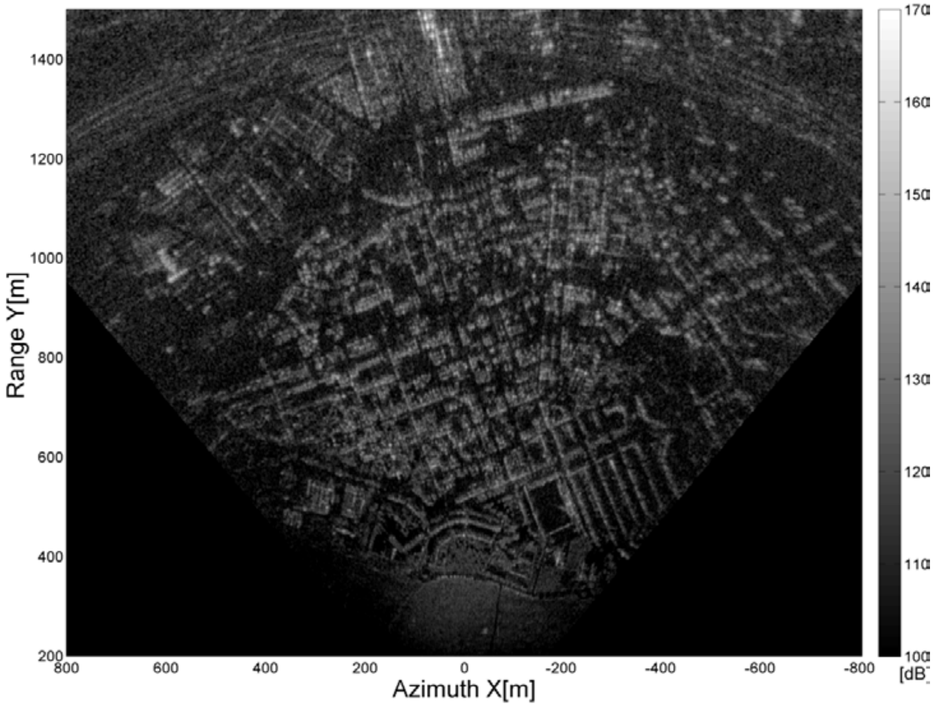

Figure B.11: SLC image of the scenario obtained with the ARBRES-X SAR sensor during the linear flight illuminating towards the urban area of Ripollet. Flight conditions: 200 m height, $v_{UAV} = 15.75m/s$, Aperture=11.84 m, VV Pol.

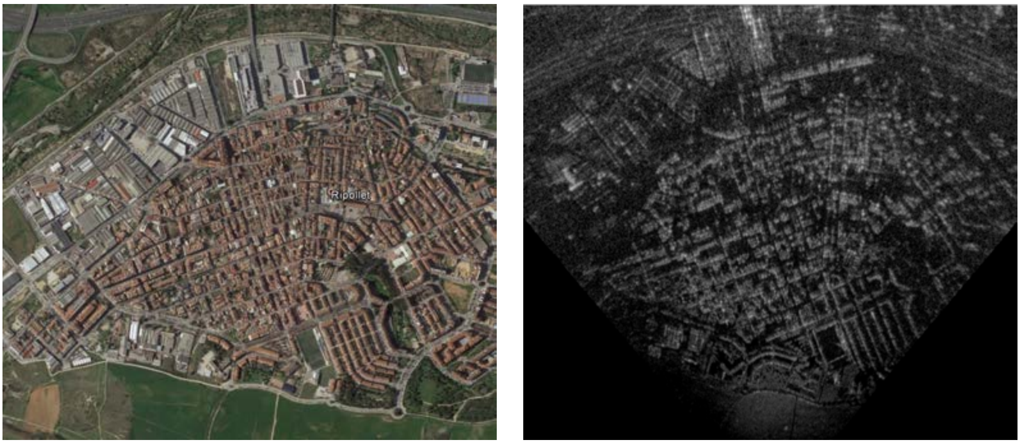

(a)

(b)

Figure B.12: Comparison between (a) Aerial photograph obtained from Google Earth and (b) SLC image obtained with the ARBRES-X SAR sensor illuminating towards the urban area of Ripollet.

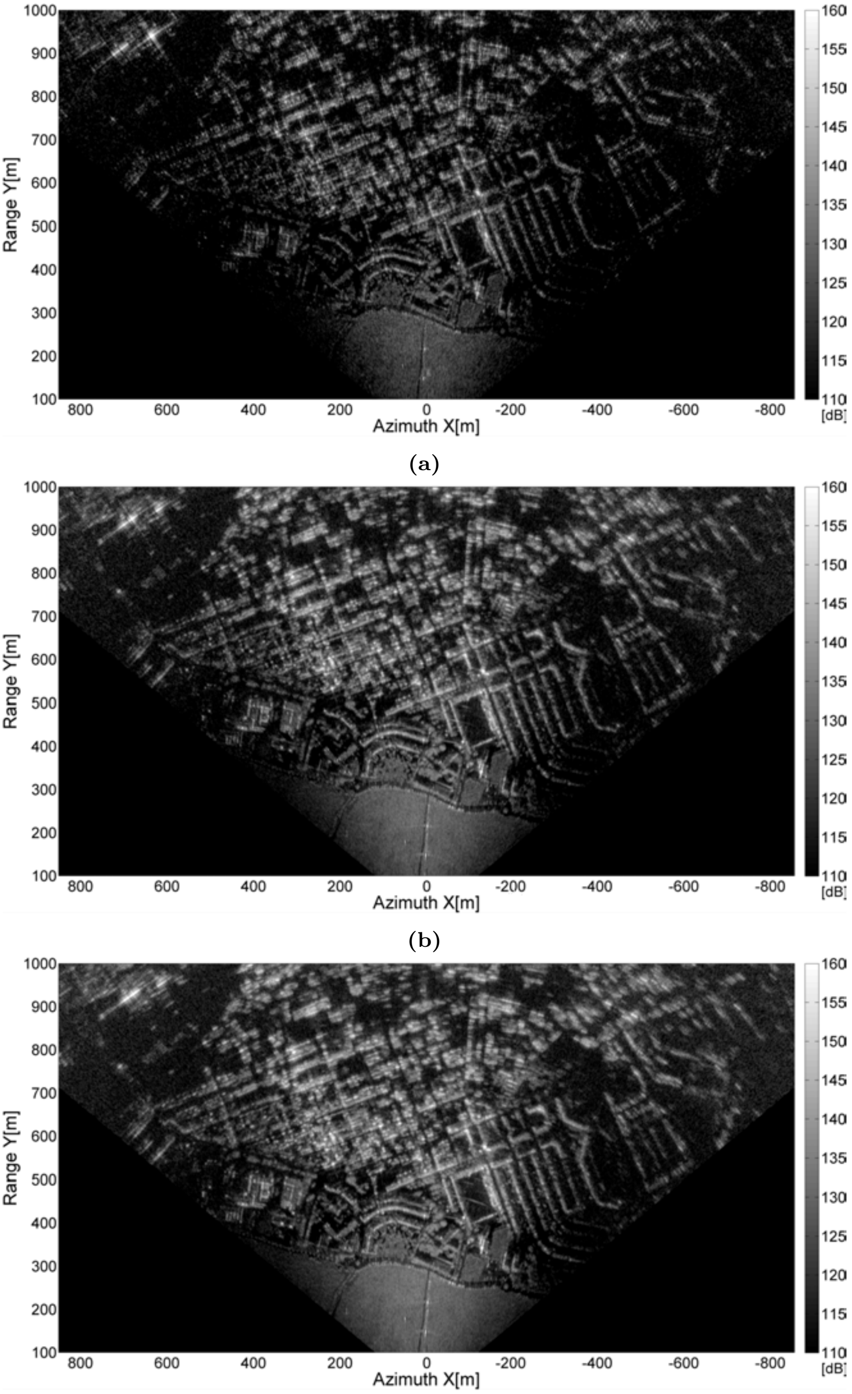

(a)

(b)

(c)

Figure B.13: SLC image of the urban area of Ripollet obtained with the ARBRES-X SAR sensor after applying the autofocus algorithm. Aperture lengths: (a) 13.4 m, (b) 40.6 m, (c) 55.6 m. Flight conditions: 150 m height, $v_{UAV} = 8.9 m/s$, VV Pol.

B.2 Repeat pass interferometric measurements

Along Chapters 5 and 6, the difficulties to obtain good interferometric measurements with UAV MPs have been evidenced. In this subsection, some interferograms obtained during different measurement campaigns are exposed.

Figures B.14 and B.15 show the interferometric results shown in Chapter 6 but focusing the images in Cartesian coordinates. In Figure B.14 the two SLC images corresponding to the different passes are processed considering the same velocity of the platform. Nevertheless, it has been commented in the manuscript the inaccuracy of the UAV MP to perform straight flights at constant velocities. Figure B.16 (a) and (b) show the velocity measured by the IOSD for the complete aperture of 96 m and the selected sub-aperture of 3.3 m, respectively. The vertical lines in Figure B.16 (a) delimit the selected sub-aperture of approximately 3.3 m. As can be observed, the sub-aperture corresponds to the beginning of the flight and has been chosen to minimize the decorrelation between both passes, since the passes would have more deviations from the ideal flight path as the platform advances. However, Figure B.16 (b) shows that there is a difference of approximately 0.11 m/s between the two passes, reason for which the velocity of the second pass has been readjusted to optimize the results in a later iteration of the focusing process, see Figure B.15.

As can be observed, the number of coherent pixels has increased after matching both images by adjusting the velocities, which is summarized in Table B.1 where the total number of pixels with coherence amplitude over 0.6 have increased by 6.4 %. This im-

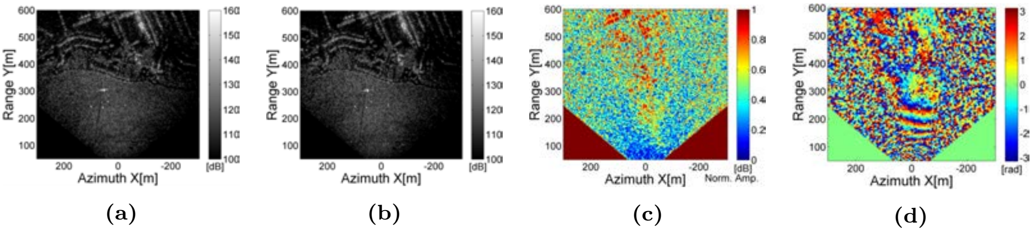

(a) (b) (c) (d)

Figure B.14: Cartesian coordinates. (a) SLC pass 1. (b) SLC pass2. (c) Coherence multilook 6 x 6 m. (d) Interferogram multilook 6 x 6 m. Flight conditions: 100 m height, 0.52 m mean baseline, VV Pol.

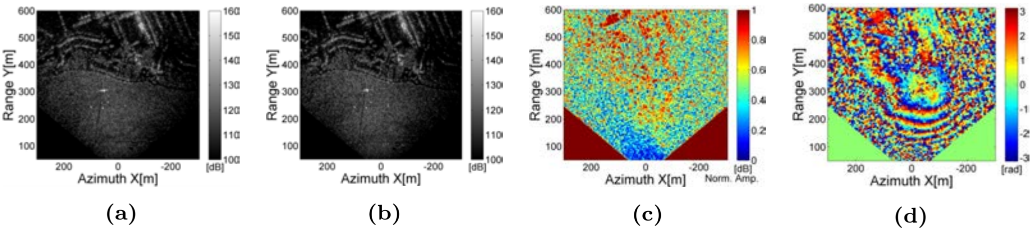

(a) (b) (c) (d)

Figure B.15: Cartesian coordinates and adjusting velocities. (a) SLC pass 1. (b) SLC pass2. (c) Coherence multilook 6 x 6 m. (d) Interferogram multilook 6 x 6 m. Flight conditions: 100 m height, 0.52 m mean baseline, VV Pol.

provement can be appreciated in the zoom shown in Figure B.17, where the fringes of the interferogram are better defined after adjusting the velocity of the second pass.

The same procedure has been performed in Polar coordinates obtaining similar results, as can be observed in Figures B.18, B.19 and B.20. This results are the ones presented in Chapter 6.

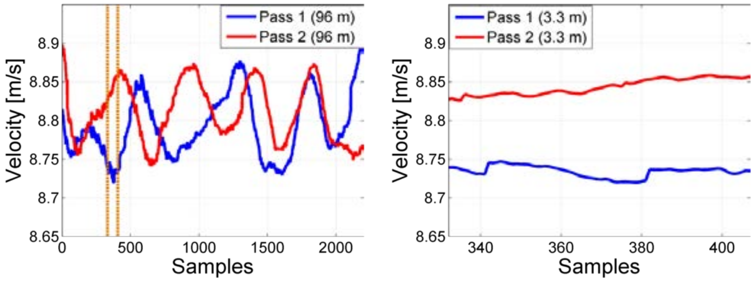

(a) (b)

Figure B.16: IOSD measured velocity. (a) Complete aperture of 96 m. (b) Processed sub-aperture of approximately 3.3 m.

Table B.1: Evaluation of the number of coherent pixels.

	Same velocity	Adjusting velocity
Pixels with coherence amplitude>0.6	382028	487936
% of total pixels	23.1	29.5

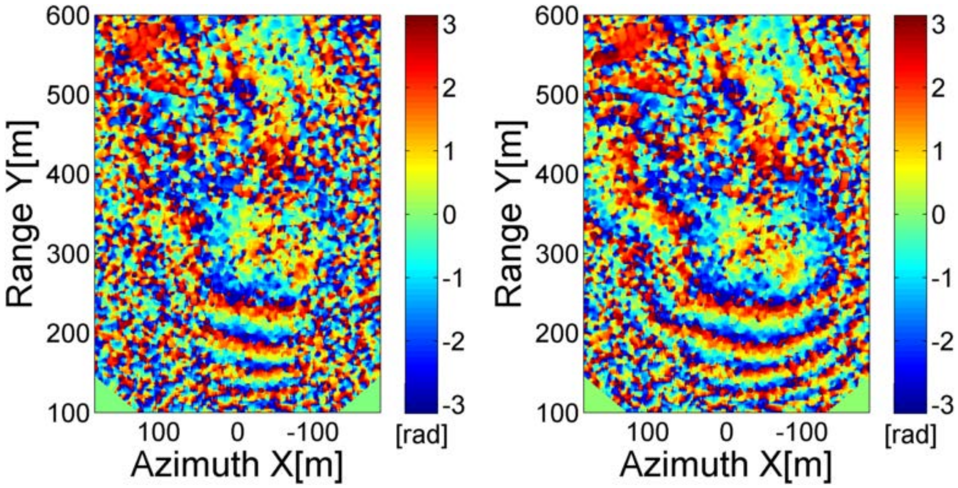

(a) (b)

Figure B.17: Zoom to the interferogram in Cartesian coordinates. Multilook 6 x 6 m. (a) Same velocity in both passes. (b) Adjusting velocity in pass 2.

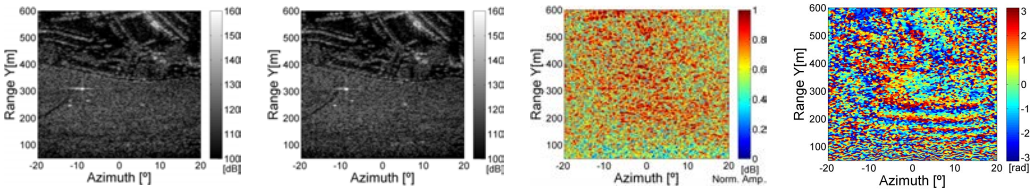

(a) (b) (c) (d)

Figure B.18: Polar coordinates. (a) SLC pass 1. (b) SLC pass2. (c) Coherence multilook 4 m x 0.4 deg. (d) Interferogram multilook 6 x 6 m. Flight conditions: 100 m height, 0.52 m mean baseline, VV Pol.

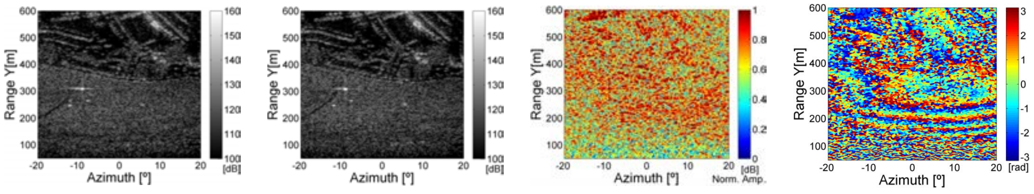

(a) (b) (c) (d)

Figure B.19: Polar coordinates and adjusting velocities. (a) SLC pass 1. (b) SLC pass2. (c) Coherence multilook 4 m x 0.4 deg. (d) Interferogram multilook 6 x 6 m. Flight conditions: 100 m height, 0.52 m mean baseline, VV Pol.

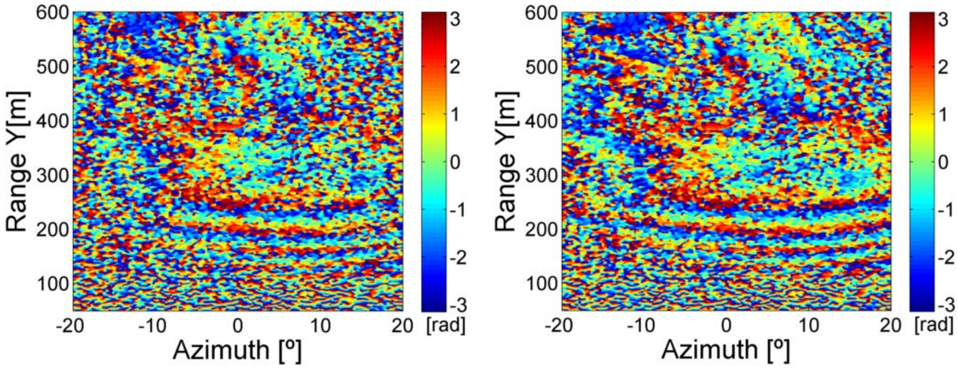

(a) (b)

Figure B.20: Zoom to the interferogram in Polar coordinates. Multilook 4 m x 0.4 deg. (a) Same velocity in both passes. (b) Adjusting velocity in pass 2.

Several attempts to obtain interferometric results have been conducted, but most of them have been unsuccessful due to the difficulties to perform perfectly aligned passes with the platform. This can be exemplified by selecting a different sub-aperture of the same measurement, obtaining results that change drastically. To illustrate this effect, it has been chosen, for instance, the sub-aperture shown in Figure B.21 where the measured mean baseline between the two passes is nearly 0. The results obtained in this case are shown in Figure B.22 and B.23.

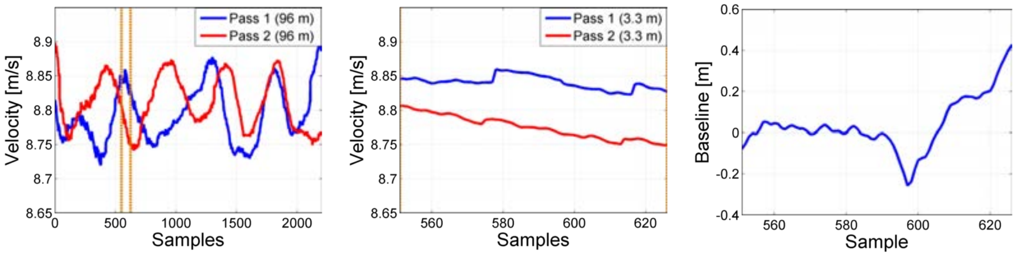

(a) (b) (c)

Figure B.21: IOSD measured velocity. (a) Complete aperture of 96 m. (b) Processed sub-aperture of approximately 3.3 m. (c) Baseline of the sub-aperture.

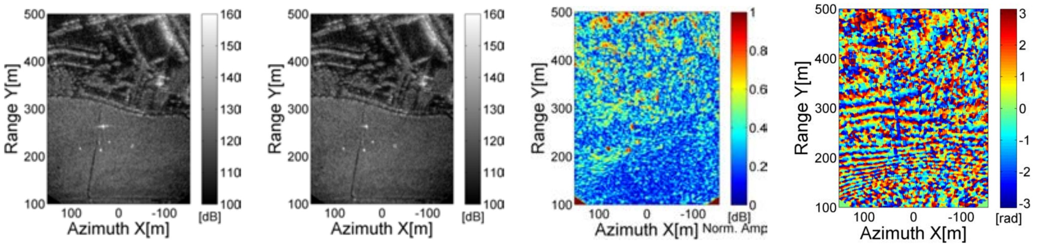

(a) (b) (c) (d)

Figure B.22: Cartesian coordinates. (a) SLC pass 1. (b) SLC pass2. (c) Coherence multilook 6 x 6 m. (d) Interferogram multilook 6 x 6 m. Flight conditions: 100 m height, 0.03 m mean baseline, VV Pol.

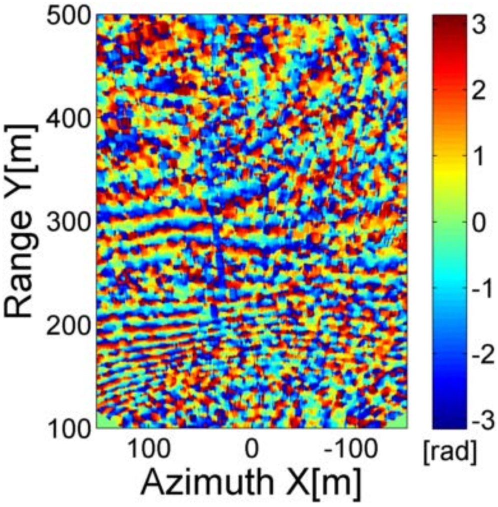

Figure B.23: Interferogram in Cartesian coordinates. Multilook 6 x 6 m.

Acronyms

ARBRES AiR-Based REmote Sensing
BPA Back Projection Algorithm
CNR Clutter-to-Noise Ratio
CPC Cross-polarization Phase Center
CRP Chirp Repetition Pulse
CSA Chirp Scaling Algorithm
CSAR Circular SAR
CW Continuous-Wave
DDS Direct Digital Synthesizer
DEM Digital Elevation Maps
DFT Discrete Fourier Transform
DInSAR Differential SAR Interferometry
CPD Cross Polarization Discrimination
EO Earth observation
FFT Fast Fourier Transform
FGU Frequency Generation Unit
FM Frequency Modulated
FMCW Frequency Modulated Continuous Wave
FP fully polarimetric
GB-SAR Ground-Based Synthetic Aperture Radar
GPS Global Positioning Satellite
HBT Heterojunction Bipolar Transistor
HS Horizontal Separation
IFFT Inverse Fast Fourier Transform
IMU Inertial Measurement Unit
JPL Jet Propulsion Laboratory

LNA Low Noise Amplifier

LO Local Oscillator

MMIC Monolithic Microwave Integrated Circuit

MOCO MOtion COmpensation

MP Multicopter Platform

MTI Moving Target Tndication

NASA National Aeronautics and Space Administration

NOAA National Oceanic and Atmospheric Administration

OtF On-the-Fly

PARC Polarimetric Active Radar Calibrator

PFD Phase-Frequency Detector

PID Proportional Integral Derivative

PLL Phase-Locked Loop

PolSAR Polarimetric SAR

PRF Pulse Repetition Frequency

PRI Pulse Repetition Interval

PS Permanent Scatterer

PT Prominent Target

PSD Power Spectral Density

PSI Persistent Scatterer Interferometry

RAR Real Aperture Radar

RACBSA Real Aero Club Barcelona-Sabadell

RC Range Compression

RCM Range Cell Migration

RCS Radar Cross Section

RF Radio Frequency

RGB Red, Green and Blue

RSLab Remote Sensing Laboratory

RTK Real Time Kinematic

RVPE Residual Video Phase Error

SAR Synthetic Aperture Radar

SCNR Signal-to-Clutter-and-Noise Ratio

SCR Signal-to-Clutter Ratio

SIR Signal to Interference Ratio

SP Single Polarimetric

SLC Single Look Complex

SNR Signal-to-Noise Ratio

SPDT Single Pole Double Throw

S&G *Stop&Go*

SLAR Side-Looking Airborne Radar

SLFM-CW Stepped Linear Frequency Modulated Continuous Wave

TDX TanDEM-X

TSC Signal Theory and Communications

TSX TerraSAR-X

UAV Unmanned Aerial Vehicle

UNFCCC United Nations Framework Convention on Climate Change

UPC Universitat Politècnica de Catalunya

USB Universal Serial Bus

VCO Voltage Controlled Oscillator

VNA Vector Network Analyzer

Nomenclature

Latin Letters

$a(t)$	Rectangular function	m/s
$A(\omega)$	Fourier transform of $a(t)$	Hz
B	Baseline	m
B_a	Doppler bandwidth	Hz
B_{rg}	Bandwidth of the transmitted signal	Hz
$B_{\|}$	Parallel baseline	m
$B_{\perp}$	Perpendicular baseline	m
$\mid B_{nc} \mid$	Critical baseline	m
c	Speed of light	m/s
c_k	Weight of S_k	
$[C_3]$	Covariance matrix 3x3	
d_x	Doppler frequency resolution	
E^r	Received elecric field vector	V/m
E^t	Transmitted elecric field vector	V/m
$E\{\cdot\}$	Statistical expectation	
f_0	Carrier frequency	Hz
$fi(t)$	Instantaneous frequency	Hz
$\mathcal{F}$	Fourier transform	
h	Target height	m
$h_{2\pi}$	Height of ambiguity	m
H	Platform altitude above ground	m
k	Wave number	rad/m
k_r	Distortion element in the receiver	
Kr	Transmitted signal chirp rate	Hz/s
L_{ant}	Length of the antenna	m
L_{sa}	Length of the synthetic aperture	m
m	Transmitted chirp period number	
M	Total number of antenna positions	
$[M]$	Measured matrix	
N	Total number of scatterers	
N_{chirp}	Total number of chirp pulses stored	
$N_{samples}$	Total number of samples stored for every chirp pulse	
$[N]$	Additive noise matrix	

$p(R, \beta)$	Pixel in the image in equivalent coordinate of the polar angle	
$p(R, \theta)$	Pixel in the image in polar coordinates	
$r_T(t)$	Distance from the sensor to a generic target	m
r_{T0}	Slant range at $t = 0$ (closest approach for fixed target	m
$r_{T_{CPC}}(t)$	r_T considering CPC rough coregistration	m
R_{OP}	Range distance from origin to pixel	m
$R_{OS}(m)$	Range distance from origin to scatterer	m
$\hat{R}_{OS}(m)$	Nominal range from origin to scatterer	m
$[R]$	Receiver distortion matrix	
$s_{IF}(t, m)$	Derramped signal in time domain	
$s_R(t, m)$	Received FMCW signal	
$s_T(t)$	Transmitted FMCW signal	
$S_{IF}(t, m)$	Derramped signal in frequency domain	
S_k	Response of canonical object k	
$[S]$	Scattering matrix	
t	Azimuth time (slow time)	s
t_0	Time of closest approach	s
T_p	Chirp duration	s
T_{PRF}	Pulse repetition time	s
T_{PRFeq}	Equivalent pulse repetition time between SG and OtF	s
$[T]$	Transmitter distortion matrix	
$[T_3]$	Coherency matrix 3x3	
u_r	Distortion element in the receiver	
u_x	Deviation of the platform in the X axis	m
u_y	Deviation of the platform in the Y axis	m
u_z	Deviation of the platform in the Z axis	m
v	Velocity of the platform	m/s
v_{eq}	Equivalent velocity of the platform between $S\&G$ and OtF	m/s
v_t	Distortion element in the transmitter	
w_r	Distortion element in the receiver	
$x_a(t)$	Antenna position in the X axis as a function of t	m
x_{PS}	Ideal position of the permanent scatterer in the X axis	m
x_T	Position of a generic target in the X axis	m
X	Along-track coordinate	m
$[X]$	Distortion matrix	
$y_A(m)$	Antenna position in the Y axis as a function of m	m
y_{PS}	Ideal position of the permanent scatterer in the Y axis	m
y_T	Position of a generic target in the Y axis	m
Y	Across-track coordinate	m
z_t	Distortion element in the transmitter	
z_{PS}	Ideal position of the permanent scatterer in the Z axis	m
z_T	Position of a generic target in the Z axis	m
Z	Elevation (height) coordinate	m

Greek Letters

α	Signal chirp rate	Hz/s
α_{KPSD}	Shape parameter of the KPSD model	
α_r	Distortion element in the receiver	
α_s	Tilt angle	rad
β	Equivalent coordinate of the polar angle θ	
γ	Complex coherence	
γ_t	Temporal decorrelation contribution to complex coherence	
γ_{other}	Other contributions to complex coherence	
γ_{th}	Thermal decorrelation contribution to complex coherence	
γ_{blur}	Blurring decorrelation contribution to complex coherence	
Γ	Complex reflectivity function	
δ_{az}	Azimuth resolution	m
δ_h	Height increment between two pixels	m
δ_r	Range increment between two pixels	m
δ_{rg}	Range resolution	m
Δx_{CPC}	Distance to compensate the center of phase in the x axis	m
Δy_{CPC}	Distance to compensate the center of phase in the y axis	m
Δ_{φ}	Increment of the azimuth illumination angle	rad
$\Delta R_{OS(m)}$	Range variation of the scatterer	m
Δt_{Lsa}	Observation time of a target	s
Δ_r	Range increment in line of sight	m
Δr_{CPC}	Range increment due to CPC	m
$\Delta\theta_{OS}(m)$	Squint variation of the scatterer	rad
θ	Squint angle	rad
θ_{OS}	Squint angle from origin to scatterer	rad
θ_0	Off-nadir look angle	rad
$\hat{\theta}_{OS}$	Nominal squint angle from origin to scatterer	rad
θ_{az}	Azimuth antenna beamwidth at -3 dB	rad
θ_{sa}	Narrow virtual bandwidth of the synthetic aperture	rad
λ	Carrier wavelength	m
$\sigma(m)$	Reflectivity of the target	
$\sigma_{\Delta r}$	Standard deviation of the range increment	m
$\tau_0(m)$	Round trip delay	s
τ_p	Pulse duration	s
$\phi(m)$	Phase of the target	rad
ϕ_{fe}	Flat earth term of interferometric phase	rad
ϕ_{int}	Interferometric phase	rad
$\phi_{\sigma 0}$	Phase due to reflectivity	rad
ϕ_{slc}	Phase of the single look complex image	rad
ϕ_{topo}	Topographic term of interferometric phase	rad
$\varphi(t)$	Azimuth phase as a function of t	rad
φ_{az}	Azimuth illumination angle of a target	rad
$\varphi_{CPC}(t)$	CPC phase compensation	rad

ω_0	Angular frequency	rad/s

Superscripts

$*$	Complex conjugate operator
$\dagger$	Transpose complex conjugate operator

List of Figures

List of Tables

Bibliography

[1] What are the characteristics of the Solar System that lead to the origins of life? NASA Science (Big Questions). NASA. [Online]. Available: http://solarsystem.nasa.gov/ (Cited on page 2.)

[2] Pidwirny, Michael. Surface area of our planet covered by oceans and continents. University of British Columbia, Okanagan. [Online]. Available: http://www.physicalgeography.net/fundamentals/8o.html (Cited on page 2.)

[3] Sweetlove, Lee. Number of species on Earth tagged at 8.7 million. Nature. Macmillan Publishers Limited. [Online]. Available: http://www.nature.com/news/2011/110823/full/news.2011.498.html (Cited on page 2.)

[4] 2016 World Population Data Sheet. Population Reference Bureau. [Online]. Available: http://www.prb.org/ (Cited on page 2.)

[5] R. L. Hooke, "On the efficacy of humans as geomorphic agents," 1994. (Cited on page 2.)

[6] E. W. Sanderson, M. Jaiteh, M. a. Levy, K. H. Redford, A. V. Wannebo, and G. Woolmer, "The Human Footprint and the Last of the Wild," *BioScience*, vol. 52, no. 10, pp. 891–904, 2002. (Cited on page 2.)

[7] The Earth as a System. International Geosphere-Biosphere Programme. [Online]. Available: https://web.archive.org/web/20100429213905/http://www.igbp.net/page.php?pid=101 (Cited on page 2.)

[8] The Achilles Heel of the Earth System. International Institute for Applied Systems Analysis. [Online]. Available: http://webarchive.iiasa.ac.at/Research/TNT/WEB/Publications/Abrupt_Changes/Abrupt_Changes.pdf (Cited on page 2.)

[9] J.-S. Lee and E. Pottier, "Polarimetric Radar Imaging: From Basics to Applications," in *Polarimetric Radar Imaging: From Basics to Applications*, 2009, p. 440. [Online]. Available: http://www.crcnetbase.com/doi/abs/10.1201/9781420054989.fmatt (Cited on pages 3, 8, 13, 14, 15, and 16.)

[10] J. C. Curlander and R. N. McDonough, *Synthetic aperture radar- Systems and signal processing(Book)*, 1991. (Cited on pages 3, 11, 12, and 37.)

[11] R. F. Hanssen, *Radar Interferometry - Data Interpretation and Error Analysis*, 2001, vol. 2, no. 8. [Online]. Available: http://link.springer.com/10.1007/0-306-47633-9 (Cited on pages 3 and 16.)

[12] D. Massonnet and K. L. Feigl, "Radar interferometry and its application to changes in the Earth's surface," p. 441, 1998. (Cited on pages 3, 16, and 50.)

[13] R. Bürgmann, P. A. Rosen, and E. J. Fielding, "Synthetic Aperture Radar Interferometry to Measure Earth's Surface Topography and Its Deformation," pp. 169–209, 2000. (Cited on pages 3 and 50.)

[14] F. Lombardini, "Differential tomography: a new framework for SAR interferometry," *IEEE Transactions on Geoscience and Remote Sensing*, vol. 43, no. 1, pp. 37–44, 2005. (Cited on page 4.)

[15] A. L. Gray and P. J. Farris-Manning, "Repeat-Pass Interferometry with Airborne Synthetic Aperture Radar," *IEEE Transactions on Geoscience and Remote Sensing*, vol. 31, no. 1, pp. 180–191, 1993. (Cited on pages 4 and 16.)

[16] J. C. Maxwell, *A dynamical theory of the electromagnetic field*, 1865, vol. 155, no. January. [Online]. Available: http://rstl.royalsocietypublishing.org/cgi/doi/10.1098/rstl.1865.0008 (Cited on page 8.)

[17] C. Hülsmeyer, "Verfahren, um entfernte metallische Gegenstände mittels elektrischer Wellen einem Beobachter zu melden," Germany Patent DE-165 546A, September 22, 1904. (Cited on page 8.)

[18] C. Wiley, "Pulsed Doppler Radar methods and apparatus," U.S. Patent 3.196.436, 7 20, 1954. (Cited on page 8.)

[19] C. a. Wiley, "Synthetic aperture radarsâĂŞa paradigm for technology evolution," *IEEE Trans. Aerospace Elec. Sys*, vol. 21, no. 3, pp. 440–443, 1985. (Cited on pages 8 and 11.)

[20] A. Reigber, R. Scheiber, M. Jager, P. Prats-Iraola, I. Hajnsek, T. Jagdhuber, K. P. Papathanassiou, M. Nannini, E. Aguilera, S. Baumgartner, R. Horn, A. Nottensteiner, and A. Moreira, "Very-high-resolution airborne synthetic aperture radar imaging: Signal processing and applications," in *Proceedings of the IEEE*, vol. 101, no. 3, 2013, pp. 759–783. (Cited on page 8.)

[21] P. Rosen, S. Hensley, I. Joughin, F. Li, S. Madsen, E. Rodriguez, and R. Goldstein, "Synthetic aperture radar interferometry," *Proceedings of the IEEE*, vol. 88, no. 3, pp. 333–382, 2000. (Cited on pages 8, 17, and 130.)

[22] D. Massonnet, M. Rossi, C. Carmona, F. Adragna, G. Peltzer, K. Feigl, and T. Rabaute, "The displacement field of the Landers earthquake mapped by radar interferometry," *Nature*, vol. 364, no. 6433, pp. 138–142, 1993. (Cited on pages 8, 16, and 17.)

[23] V. J. Zyl and Y. Kim, "Synthetic Aperture Radars (SAR) Imaging Basics," in *Synthetic Aperture Radar Polarimetry*, 2011, p. 334. [Online]. Available: http://descanso.jpl.nasa.gov/SciTechBook/series2/02Chap1{_}110106{_}amf.pdf (Cited on pages 8, 14, and 116.)

[24] M. Soumekh, *Synthetic Aperture Radar Signal Processing with MATLAB Algorithms*, 1999. [Online]. Available: http://www.amazon.com/Synthetic-Aperture-Signal-Processing-Algorithms/dp/0471297062 (Cited on pages 9, 13, 37, 39, and 95.)

[25] M. I. Skolnik, *Radar Handbook*, 2008. [Online]. Available: https://www.google.co.uk/?gfe{_}rd=cr{&}ei=hFKNVomPEu7S8Afcq5wI{#}q=radar+handbook+pdf (Cited on pages 9 and 10.)

[26] J. C. Bennett and K. Morrison, "Development of a ground-based, polarimetric synthetic aperture radar," in *Aerospace Applications Conference, 1996. Proceedings., 1996 IEEE*, vol. 4, 1996, pp. 139–146 vol.4. [Online]. Available: 10.1109/AERO.1996.499408 (Cited on page 9.)

[27] M. Pieraccini, G. Luzi, and C. Atzeni, "Terrain mapping by ground-based interferometric radar," *IEEE Transactions on Geoscience and Remote Sensing*, vol. 39, no. 10, pp. 2176–2181, 2001. (Cited on page 9.)

[28] A. Aguasca, A. Broquetas, J. J. Mallorqui, and X. Fabregas, "A solid state L to X-band flexible ground-based SAR system for continuous monitoring applications," *IEEE International IEEE International IEEE International Geoscience and Remote Sensing Symposium, 2004. IGARSS '04. Proceedings. 2004*, vol. 2, no. C, pp. 757–760, 2004. (Cited on page 9.)

[29] K. P. Papathanassiou and S. R. Cloude, "Single-baseline polarimetric SAR interferometry," *IEEE Transactions on Geoscience and Remote Sensing*, vol. 39, no. 11, pp. 2352–2363, 2001. (Cited on pages 9 and 16.)

[30] A. Reigber and A. Moreira, "First demonstration of airborne SAR tomography using multibaseline L-band data," *IEEE Transactions on Geoscience and Remote Sensing*, vol. 38, no. 5 I, pp. 2142–2152, 2000. (Cited on pages 9 and 138.)

[31] A. Moreira, P. Prats-iraola, M. Younis, G. Krieger, I. Hajnsek, and K. P. Papathanassiou, "A tutorial on synthetic aperture radar," *IEEE Geoscience and Remote Sensing Magazine*, vol. 1, no. march, pp. 6–43, 2013. (Cited on pages 9, 13, 14, 15, 17, 138, and 141.)

[32] F. M. Henderson and A. J. Lewis, *Principles and applications of imaging radar. Manual of remote sensing, volume 2*, 1998, vol. 2. (Cited on pages 9 and 13.)

[33] K. Tomiyasu, "Tutorial Review of Synthetic-Aperture Radar (SAR) with Applications to Imaging of the Ocean Surface," *Proceedings of the IEEE*, vol. 66, no. 5, pp. 563–583, 1978. (Cited on page 9.)

[34] R. Wang, O. Loffeld, H. Nies, S. Knedlik, M. Hägelen, and H. Essen, "Focus FMCW SAR data using the wavenumber domain algorithm," *IEEE Transactions on Geoscience and Remote Sensing*, vol. 48, no. 4 PART 2, pp. 2109–2118, 2010. (Cited on page 12.)

[35] A. Reigber, E. Alivizatos, A. Potsis, and A. Moreira, "Extended wavenumber-domain synthetic aperture radar focusing with integrated motion compensation," *Radar, Sonar and Navigation, IEE Proceedings*, vol. 153, no. 3, pp. 301–310, 2006. (Cited on page 12.)

[36] M. Y. Jin and C. Wu, "A SAR Correlation Algorithm Which Accommodates Large-Range Migration," *IEEE Transactions on Geoscience and Remote Sensing*, vol. GE-22, no. 6, pp. 592–597, 1984. (Cited on page 12.)

[37] R. Bamler, "A Comparison of Range-Doppler and Wavenumber Domain SAR Focusing Algorithms," *IEEE Transactions on Geoscience and Remote Sensing*, vol. 30, no. 4, pp. 706–713, 1992. (Cited on page 12.)

[38] R. K. Raney, H. Runge, I. G. Cumming, and F. H. Wong, "Precision SAR Processing Using Chirp Scaling," *IEEE Transactions on Geoscience and Remote Sensing*, vol. 32, no. 4, pp. 786–799, 1994. (Cited on page 12.)

[39] A. Moreira, J. Mittermayer, and R. Scheiber, "Extended chirp scaling algorithm for air- and spaceborne SAR data processing in stripmap and ScanSAR imaging modes," *IEEE Transactions on Geoscience and Remote Sensing*, vol. 34, no. 5, pp. 1123–1136, 1996. (Cited on page 12.)

[40] L. M. H. Ulander, H. Hellsten, and G. Stenström, "Synthetic-aperture radar processing using fast factorized back-projection," *IEEE Transactions on Aerospace and Electronic Systems*, vol. 39, no. 3, pp. 760–776, 2003. (Cited on pages 12 and 39.)

[41] A.F. Yegulalp, "Fast backprojection algorithm for synthetic aperture radar," *Proceedings of the 1999 IEEE Radar Conference. Radar into the Next Millennium (Cat. No.99CH36249)*, pp. 60–65, 1999. (Cited on pages 12 and 39.)

[42] C. Oliver and S. Quegan, *Understanding Synthetic Aperture Radar Images*, 1998, vol. 42. [Online]. Available: http://books.google.com/books?hl=en{&}lr={&}id=IeGKe40S77AC{&}oi=fnd{&}pg=PR17{&}dq=Understanding+Synthetic+Aperture+Radar+Images{&}ots=3bD3l68xbG{&}sig=nOMPKm5dIu7rlxt2fbmVhmegLE0 (Cited on page 12.)

[43] C. López Martínez, "Multidimensional speckle noise, modelling and filtering related to SAR data," *DLR Deutsches Zentrum fur Luft- und Raumfahrt e.V. - Forschungsberichte*, no. 35, pp. 1–262, 2004. (Cited on page 13.)

[44] S. V. Nghiem, S. H. Yueh, R. Kwok, and F. K. Li, "Symmetry properties in polarimetric remote sensing," *Radio Science*, vol. 27, no. 5, pp. 693–711, 1992. (Cited on page 14.)

[45] J. J. Van Zyl, "Calibration of Polarimetric Radar Images Using Only Image Parameters and Trihedral Corner Reflector Responses," *IEEE Transactions on Geoscience and Remote Sensing*, vol. 28, no. 3, pp. 337–348, 1990. (Cited on pages 15, 43, 115, and 116.)

[46] R. Bamler and P. Hartl, "Synthetic aperture radar interferometry Synthetic aperture radar interferometry," *Inverse Problems*, vol. 14, no. 4, p. 55, 1998. (Cited on page 16.)

[47] L. C. Graham, "Synthetic Interferometer Radar For Topographic Mapping," *Proceedings of the IEEE*, vol. 62, no. 6, pp. 763–768, 1974. (Cited on page 16.)

[48] H. A. Zebker and R. M. Goldstein, "Topographic mapping from interferometric synthetic aperture radar observations," *Journal of Geophysical Research*, vol. 91, no. B5, p. 4993, 1986. (Cited on pages 16 and 17.)

[49] R. M. Goldstein and H. A. Zebker, "Interferometric radar measurement of ocean surface currents," *Nature*, vol. 328, no. 6132, pp. 707 – 709, 1987. (Cited on pages 16 and 17.)

[50] R. M. Goldstein, H. a. Zebker, and C. L. Werner, "Satellite radar interferometry: Two-dimensional phase unwrapping," *Radio Science*, vol. 23, no. 4, pp. 713–720, 1988. (Cited on pages 16 and 18.)

[51] D. Massonnet, P. Briole, and A. Arnaud, "Deflation of Mount Etna monitored by spaceborne radar interferometry," *Nature*, vol. 375, no. 6532, pp. 567–570, 1995. (Cited on pages 16 and 17.)

[52] S. R. Cloude and K. P. Papathanassiou, "Polarimetric SAR interferometry," *IEEE Transactions on Geoscience and Remote Sensing*, vol. 36, no. 5, pp. 1551–1565, 1998. (Cited on page 16.)

[53] A. Ferretti, C. Prati, and F. Rocca, "Nonlinear subsidence rate estimation using permanent scatterers in\ndifferential SAR interferometry," *IEEE Transactions on Geoscience and Remote Sensing*, vol. 38, no. 5, pp. 2202–2212, 2000. (Cited on pages 16 and 17.)

[54] D. Ghiglia and M. Pritt, *Two-dimensional phase unwrapping: theory, algorithms, and software*, 1998. (Cited on page 16.)

[55] H. Breit, M. Eineder, J. Holzner, H. Runge, and R. Bamler, "Traffic Monitoring Using SRTM Along-Track Interferometry," in *Proceedings of the IEEE International Geoscience and Remote Sensing Symposium IGARSS*, vol. 2, 2003, pp. 1187–1189. (Cited on page 17.)

[56] C. E. Livingstone, I. Sikaneta, C. H. Gierull, S. Chiu, A. Beaudoin, J. Campbell, J. Beaudoin, S. Gong, and T. A. Knight, "An airborne synthetic aperture radar (SAR) experiment to support RADARSAT-2 ground moving target indication (GMTI)," *Canadian Journal of Remote Sensing*, vol. 28, no. 6, pp. 794–813, 2002. (Cited on page 17.)

[57] R. Romeiser, H. Breit, M. Eineder, H. Runge, P. Flament, K. De Jong, and J. Vogelzang, "Current measurements by SAR along-track interferometry from a Space Shuttle," *IEEE Transactions on Geoscience and Remote Sensing*, vol. 43, no. 10, pp. 2315–2323, 2005. (Cited on page 17.)

[58] R. M. Goldstein, H. Engelhardt, B. Kamb, and R. M. Frolich, "Satellite radar interferometry for monitoring ice sheet motion: application to an antarctic ice stream." *Science (New York, N.Y.)*, vol. 262, no. 5139, pp. 1525–1530, 1993. (Cited on page 17.)

[59] M. Fahnestock, R. Bindschadler, R. Kwok, and K. Jezek, "Greenland Ice Sheet Surface Properties and Ice Dynamics from ERS-1 SAR Imagery," *Science*, vol. 262, no. 5139, pp. 1530–1534, 1993. (Cited on page 17.)

[60] P. B. G. Dammert, M. Lepparanta, and J. Askne, “SAR interferometry over Baltic Sea ice,” *International Journal of Remote Sensing*, vol. 19, no. 16, pp. 3019–3037, 1998. (Cited on page 17.)

[61] J. O. Hagberg, L. M. H. Ulander, and J. Askne, “Repeat-pass SAR interferometry over forested terrain,” *IEEE Transactions on Geoscience and Remote Sensing*, vol. 33, no. 2, pp. 331–340, 1995. (Cited on page 17.)

[62] U. Wegmüller and C. Werner, “Retrieval of vegetation parameters with SAR interferometry,” *IEEE Transactions on Geoscience and Remote Sensing*, vol. 35, no. 1, pp. 18–24, 1997. (Cited on page 17.)

[63] G. Fornaro, G. Franceschetti, and R. Lanari, “Interferometric SAR phase unwrapping using Green’s formulation,” *IEEE Transactions on Geoscience and Remote Sensing*, vol. 34, no. 3, pp. 720–727, 1996. (Cited on page 18.)

[64] U. Spagnolini, “2-D phase unwrapping and instantaneous frequency estimation,” *IEEE Transactions on Geoscience and Remote Sensing*, vol. 33, no. 3, 1995. (Cited on page 18.)

[65] A. Aguasca, A. Broquetas, J. Mallorqui, and X. Fabregas, “A solid state L to X-band flexible ground-based SAR system for continuous monitoring applications,” *IGARSS 2004. 2004 IEEE International Geoscience and Remote Sensing Symposium*, vol. 2, 2004. (Cited on pages 24 and 87.)

[66] R. Iglesias, A. Aguasca, X. Fabregas, J. J. Mallorqui, D. Monells, C. Lopez-Martinez, and L. Pipia, “Ground-Based Polarimetric SAR Interferometry for the Monitoring of Terrain Displacement Phenomena–Part I: Theoretical Description,” *Selected Topics in Applied Earth Observations and Remote Sensing, IEEE Journal of*, vol. 8, no. 3, pp. 980–993, 2015. (Cited on page 24.)

[67] R. J. C. Middleton, “Dechirp-on-receive linearly frequency modulated radar as a matched-filter detector,” *IEEE Transactions on Aerospace and Electronic Systems*, vol. 48, no. 3, pp. 2716–2718, 2012. (Cited on pages 24, 37, and 88.)

[68] S. Rödelsperger, A. Coccia, D. Vicente, and A. Meta, “Introduction to the new metasensing ground-based SAR: Technical description and data analysis,” *International Geoscience and Remote Sensing Symposium (IGARSS)*, pp. 4790–4792, 2012. (Cited on page 26.)

[69] L. Pipia, “POLARIMETRIC DIFFERENTIAL SAR INTERFEROMETRY WITH GROUND-BASED SENSORS,” *Ph.D. dissertation*, vol. Universita, 2009. (Cited on pages 30, 37, 38, 41, 44, and 137.)

[70] J. Sanz-Marcos and J. Mallorqui, “Memory optimal configuration for efficient sar block-processing,” in *Proceedings European Conference on Synthetic Aperture Radar*. (Cited on page 36.)

[71] F. J. Harris, “On the use of windows for harmonic analysis with the discrete Fourier transform,” *Proceedings of the IEEE*, vol. 66, no. 1, pp. 51–83, 1978. (Cited on page 38.)

[72] N. Levanon and E. Mozeson, *Radar Signals*, 2004. (Cited on page 38.)

[73] J. W. McCorkle and M. Rofheart, “Order N^2 log(N) Backprojector Algorithm for Focusing Wide-Angle Wide-Bandwidth Arbitrary-Motion Synthetic Aperture Radar,” in *Radar Sensor Technology*, vol. SPIE 2747, 1996, pp. 25–36. [Online]. Available: http://opac.nebis.ch/ALEPH/2B5BMLRLIMDYIGQHXVPG4ULATX1PC3RPJRTNXXK1NX3B7V8F6F-09023/file/start-ids (Cited on page 39.)

[74] F. T. Ulaby and C. Elachi, “Radar polarimetry for geoscience applications,” *Norwood, MA, Artech House, Inc., 1990, 376 p. No individual items are abstracted in this volume.*, 1990. (Cited on page 44.)

[75] A. Freeman, “Sar Calibration: An Overview,” *IEEE Transactions on Geoscience and Remote Sensing*, vol. 30, no. 6, pp. 1107–1121, 1992. (Cited on page 44.)

[76] A. Freeman, Y. Shen, and C. L. Werner, “Polarimetric SAR Calibration Experiment Using Active Radar Calibrators,” *IEEE Transactions on Geoscience and Remote Sensing*, vol. 28, no. 2, pp. 224–240, 1990. (Cited on pages 44 and 137.)

[77] K. Sarabandi, F. T. Ulaby, and M. A. Tassoudji, “Calibration of Polarimetric Radar Systems With Good Polarization Isolation,” *IEEE Transactions on Geoscience and Remote Sensing*, vol. 28, no. 1, pp. 70–75, 1990. (Cited on pages 45, 48, and 119.)

[78] D. Leva, G. Nico, D. Tarchi, and J. Fortuny-Guasch, “Temporal analysis of a landslide by means of a ground-based SAR interferometer,” *IEEE Transactions on Geoscience and Remote Sensing*, vol. 41, no. 4 PART I, pp. 745–752, 2003. (Cited on page 50.)

[79] L. Pipia, X. Fabregas, A. Aguasca, and C. Lopez-Martinez, “Polarimetric temporal analysis of urban environments with a ground-based SAR,” *IEEE Transactions on Geoscience and Remote Sensing*, vol. 51, no. 4, pp. 2343–2360, 2013. (Cited on page 50.)

[80] P. Lombardo and J. Billingsley, “A new model for the Doppler spectrum of windblown radar ground clutter,” *Proceedings of the 1999 IEEE Radar Conference. Radar into the Next Millennium (Cat. No.99CH36249)*, 1999. (Cited on pages 50 and 71.)

[81] M. Pieraccini, L. Noferini, D. Mecatti, G. Macaluso, G. Luzi, and C. Atzeni, “Digital elevation models by a GBSAR interferometer for monitoring glaciers: The case study of Belvedere Glacier,” in *International Geoscience and Remote Sensing Symposium (IGARSS)*, vol. 4, no. 1, 2008. (Cited on page 50.)

[82] L. Noferini, T. Takayama, M. Pieraccini, D. Mecatti, G. Macaluso, G. Luzi, and C. Atzeni, “Analysis of ground-based SAR data with diverse temporal baselines,” *IEEE Transactions on Geoscience and Remote Sensing*, vol. 46, no. 6, pp. 1614–1623, 2008. (Cited on page 50.)

[83] L. Noferini, M. Pieraccini, D. Mecatti, G. Macaluso, C. Atzeni, M. Mantovani, G. Marcato, A. Pasuto, S. Silvano, and F. Tagliavini, “Using GB-SAR technique to monitor slow moving landslide,” *Engineering Geology*, vol. 95, no. 3-4, pp. 88–98, 2007. (Cited on page 50.)

[84] D. Tarchi, “Monitoring landslide displacements by using ground-based synthetic aperture radar interferometry: Application to the Ruinon landslide in the Italian

Alps," *Journal of Geophysical Research*, vol. 108, no. B8, p. 2387, 2003. (Cited on page 50.)

[85] A. Meta, P. Hoogeboom, and L. Ligthart, "Non-linear Frequency Scaling Algorithm for FMCW SAR Data," in *2006 European Radar Conference*, 2006, pp. 9–12. [Online]. Available: http://ieeexplore.ieee.org/xpl/freeabs{_}all.jsp?arnumber=4058244 (Cited on page 52.)

[86] B. Barber, "Some effects of target vibration on {SAR} images," *7th European Conference on Synthetic Aperture Radar*, vol. 44, no. 0, 2008. (Cited on page 55.)

[87] F. Rocca, "Modeling Interferogram Stacks," *IEEE Transactions on Geoscience and Remote Sensing*, vol. 45, no. 10, pp. 3289–3299, 2007. (Cited on page 56.)

[88] R. K. Raney, "WAVE ORBITAL VELOCITY FADE & SAR RESPONSE TO AZIMUTH WAVES." pp. 63–70, 1981. (Cited on page 56.)

[89] R. Touzi, A. Lopes, J. Bruniquel, and P. W. Vachon, "Coherence estimation for SAR imagery," *IEEE Transactions on Geoscience and Remote Sensing*, vol. 37, no. 1 PART 1, pp. 135–149, 1999. (Cited on page 57.)

[90] H. A. Zebker and J. Villasenor, "Decorrelation in interferometric radar echoes," *IEEE Transactions on Geoscience and Remote Sensing*, vol. 30, no. 5, pp. 950–959, 1992. (Cited on page 57.)

[91] L. Pipia, X. Fàbregas, A. Aguasca, and C. López-Martínez, "Atmospheric artifact compensation in ground-based DInSAR applications," *IEEE Geoscience and Remote Sensing Letters*, vol. 5, no. 1, pp. 88–92, 2008. (Cited on page 57.)

[92] R. Iglesias, A. Aguasca, X. Fabregas, J. J. Mallorqui, D. Monells, C. Lopez-Martinez, and L. Pipia, "Ground-Based Polarimetric SAR Interferometry for the Monitoring of Terrain Displacement Phenomena-Part II: Applications," *IEEE Journal of Selected Topics in Applied Earth Observations and Remote Sensing*, vol. 8, no. 3, pp. 1–14, 2014. (Cited on page 58.)

[93] R. Iglesias, X. Fabregas, A. Aguasca, J. J. Mallorqui, C. Lopez-Martinez, J. A. Gili, and J. Corominas, "Atmospheric phase screen compensation in ground-based sar with a multiple-regression model over mountainous regions," *IEEE Transactions on Geoscience and Remote Sensing*, vol. 52, no. 5, pp. 2436–2449, 2014. (Cited on page 58.)

[94] A. Martinez, A. Aguasca, M. Lort, and A. Broquetas, "Micrometric deformation imaging at W-Band with GBSAR," *European Journal of Remote Sensing*, vol. 49, pp. 719–733, 2016. (Cited on page 64.)

[95] A. Aguasca, R. Acevo-Herrera, A. Broquetas, J. J. Mallorqui, and X. Fabregas, "ARBRES: Light-weight CW/FM SAR sensors for small UAVs," *MDPI*, vol. 13, no. 3, pp. 3204–3216, 2013. (Cited on pages 84, 86, and 89.)

[96] O. Ponce, P. Prats-Iraola, M. Pinheiro, M. Rodriguez-Cassola, R. Scheiber, A. Reigber, and A. Moreira, "Fully polarimetric high-resolution 3-D imaging with circular SAR at L-band," *IEEE Transactions on Geoscience and Remote Sensing*, vol. 52, no. 6, pp. 3074–3090, 2014. (Cited on page 85.)

[97] R. Acevo-Herrera, A. Aguasca, J. J. Mallorqui, and X. Fabregas, “High-compacted FM-CW SAR for boarding on small UAVS,” in *International Geoscience and Remote Sensing Symposium (IGARSS)*, vol. 2, 2009. (Cited on page 86.)

[98] D. E. Wahl, P. H. Eichel, D. C. Ghiglia, and C. V. J. Jakowatz, “Phase gradient autofocus-a robust tool for high resolution SAR phase correction,” *IEEE Transactions on Aerospace and Electronic Systems*, vol. 30, no. 3, pp. 827–835, 1994. (Cited on page 95.)

[99] B. Fan, Z. Ding, W. Gao, and T. Long, “An improved motion compensation method for high resolution UAV SAR imaging,” *Science China Information Sciences*, vol. 57, no. C, pp. 1–13, 2014. (Cited on page 95.)

[100] A. Alabort and J. J. Mallorqui, “Development of Motion Compensation algorithms for airborne UAV SAR,” 2014. [Online]. Available: http://hdl.handle.net/2099.1/22022 (Cited on pages 95 and 147.)

[101] W. H. Press, S. a. Teukolsky, W. T. Vetterling, and B. P. Flannery, *Numerical recipes in C (2nd ed.): the art of scientific computing*, 1992, vol. 29, no. 4. [Online]. Available: http://www.jstor.org/stable/1269484?origin=crossref (Cited on page 97.)

[102] F. J. Harris, “On the use of windows for harmonic analysis with the discrete Fourier transform,” *Proceedings of the IEEE*, vol. 66, no. 1, pp. 51–83, 1978. (Cited on page 101.)

[103] A. Meta, P. Hoogeboom, and L. P. Ligthart, “Signal processing for FMCW SAR,” in *IEEE Transactions on Geoscience and Remote Sensing*, vol. 45, no. 11, 2007, pp. 3519–3532. (Cited on page 102.)

[104] S. Quegan, “A Unified Algorithm for Phase and Cross-Talk Calibration of Polarimetric Data-Theory and Observations,” *IEEE Transactions on Geoscience and Remote Sensing*, vol. 32, no. 1, pp. 89–99, 1994. (Cited on page 116.)

[105] F. Gatelli, A. M. Guarnieri, F. Parizzi, P. Pasquali, C. Prati, and F. Rocca, “The Wavenumber Shift in SAR Interferometry,” *IEEE Transactions on Geoscience and Remote Sensing*, vol. 32, no. 4, pp. 855–865, 1994. (Cited on page 130.)

[106] A. Reigber, P. Prats, and J. J. Mallorqui, “Refined estimation of time-varying baseline errors in airborne SAR interferometry,” in *International Geoscience and Remote Sensing Symposium (IGARSS)*, vol. 7, 2005, pp. 4799–4802. (Cited on page 133.)

[107] O. Ponce, P. Prats-Iraola, R. Scheiber, A. Reigber, A. Moreira, and E. Aguilera, “Polarimetric 3-D reconstruction from multicircular SAR at P-band,” *IEEE Geoscience and Remote Sensing Letters*, vol. 11, no. 4, pp. 803–807, 2014. (Cited on page 141.)

List of Publications

Journal Articles

[JA1] A. Martinez, A. Aguasca, **M. Lort**, and A. Broquetas, "Micrometric deformation imaging at W-Band with GBSAR," *European Journal of Remote Sensing*, pp. 719–733, 28th July 2016. (Cited on page 64.)

[JA2] **M. Lort**, A. Aguasca, C. Lopez-Martinez and T. Martinez Marin, "Initial evaluation of SAR capabilities in UAV Multicopter Platforms," *accepted for publication in IEEE Journal of Selected Topics in Applied Earth Observations and Remote Sensing*, pp. 1–14, 30th July 2017. (Cited on pages 123, 147, 148, and 149.)

[JA3] **M. Lort**, A. Aguasca, C. Lopez-Martinez and X. Fabregas, "Impact of Short term variable reflectivity scatterers on GB-SAR imagery," *submitted for publication to IEEE Journal of Selected Topics in Applied Earth Observations and Remote Sensing*, pp. 1–18, 30th July 2017. (Cited on pages 49, 146, and 148.)

Conference Articles

[CA1] T. Broquetas, J. Romeu, L. Jofre, A. Aguasca, M. Alonso, J. Abril, E. Nova, **M. Lort**, J. Parron, P. De Paco, G. Junkin and J. Marin, "Terasense: 94 GHz Short Range Real-Time Camera," in *XIX Simposium Nacional de la Union Cientifica Internacional de Radio, URSI*, Valencia, Spain, Sept. 2014. (Not cited.)

[CA2] **M. Lort**, A. Aguasca and X. Fabregas, "Interferometric and polarimetric X-band SAR sensor integrated in a small multicopter UAV," in *XXX Simposium Nacional de la Union Cientifica Internacional de Radio, URSI*, Pamplona, Spain, Sept. 2015. (Cited on pages 83, 147, and 149.)

[CA3] **M. Lort**, A. Aguasca, T. Broquetas and A. Martinez, "W-Band radar used as high resolution range profiler," in *XXX Simposium Nacional de la Union Cientifica Internacional de Radio, URSI*, Pamplona, Spain, Sept. 2015. (Cited on page 64.)

[CA4] **M. Lort** and A. Aguasca, "New potentials of integrating an interferometric and polarimetric SAR sensor in a small UAV multicopter platform," in *IEEE Young*

Professionals Conference, Barcelona, Spain, Dec. 2015. (Cited on pages 83, 147, and 149.)

[CA5] A. Martinez, **M. Lort**, A. Aguasca and T. Broquetas, “Submillimetric motion detection with a Ground Based Synthetic Aperture Radar at 94 GHz,” in *IET International Radar Conference*, Hangzhou, China, Oct. 2015. (Cited on page 64.)

[CA6] J. Romeu, S. Blanch, **M. Lort**, T. Broquetas, A. Aguasca, L. Jofre and A. Elias, “A study for a 94 GHz portable radar scanner for security screening,” in *XXXI Simposium Nacional de la Union CientÃŋfica Internacional de Radio, URSI*, Madrid, Spain, Sept. 2016. (Cited on page 64.)

Final Degree Projects Supervised

[MA1] A. Escartin, “SAR system development for UAV multicopter platforms,” Final Degree Project, Universitat Politècnica de Catalunya (UPC), June 2015. (Not cited.)

Participation in R&D Projects

CICYT TEC2011-28201-C02-01 Supported by the Spanish Interministerial Comission on Science and Technology (CICYT) under project TEC2011-28201-C02-01 entitled “SAR Multidimensional para la observación de la tierra: sistemas, procesado y aplicaciones”.

CONTRIBUTIONS TO GROUND-BASED AND UAV SAR SYSTEMS FOR EARTH OBSERVATION

The encompassing objective of the present doctoral work is the development and evaluation of two X-Band SAR sensors for Earth observation purposes; one of them has been designed to be operated on ground and the other to be integrated in a UAV MP. The manuscript is based on a transversal study ranging from the developed hardware contributions to the evaluation of processing strategies to diverse applications, passing by the utilization of the sensors in different measurement campaigns.